

JOHANNES GUTENBERG UNIVERSITÄT MAINZ

DOCTORAL THESIS

Structure, Dynamics and Vibrational
Spectroscopy of Interfacial Alkali
Nitrate Aqueous Solutions from *ab*
initio Molecular Dynamics

Author:

Gang HUANG

Supervisor:

Apl. Prof. Dr. Marialore
SULPIZI

*A thesis submitted in fulfillment of the requirements
for the degree of Doctor of Philosophy*

in the

Condensed Matter Theory Group
Institute for Physics

May 21, 2021

Declaration of Authorship

I, Gang HUANG, declare that this thesis titled, “Structure, Dynamics and Vibrational Spectroscopy of Interfacial Alkali Nitrate Aqueous Solutions from *ab initio* Molecular Dynamics” and the work presented in it are my own. I confirm that:

- This work was done wholly or mainly while in candidature for a research degree at this University.
- Where any part of this thesis has previously been submitted for a degree or any other qualification at this University or any other institution, this has been clearly stated.
- Where I have consulted the published work of others, this is always clearly attributed.
- Where I have quoted from the work of others, the source is always given. With the exception of such quotations, this thesis is entirely my own work.
- I have acknowledged all main sources of help.
- Where the thesis is based on work done by myself jointly with others, I have made clear exactly what was done by others and what I have contributed myself.

Signed:

Date:

“If a problem is worth looking at at all, then no mathematical technique is to be judged too sophisticated.”

David Ruelle

JOHANNES GUTENBERG UNIVERSITÄT MAINZ

Abstract

Condensed Matter Theory
Institute for Physics

Doctor of Philosophy

**Structure, Dynamics and Vibrational Spectroscopy of Interfacial Alkali
Nitrate Aqueous Solutions from *ab initio* Molecular Dynamics**

by Gang HUANG

The interfacial structure and dynamics of solutions containing alkali nitrates have been studied by Density Functional Theory-based Molecular Dynamics (DFTMD) simulations. In particular we have presented a detailed analysis of the Hydrogen Bond (HB) structure at the interface and have calculated the interface vibrational spectra in order to provide a molecular interpretation of available experimental data. When calculating the Vibrational Sum-Frequency Generation (VSFG) spectrum, we used a new approximation method. This method ignores the NR part of the spectrum and finally obtains the interface's nonlinear polarizability to infrared incident light through the velocity Auto-Correlation Function (ACF). Based on the calculation of Maximally-Localized Wannier Functions (MLWFs), the parameterization of the spatial gradient of the components of dipole moment and the polarization is realized. Therefore, the calculation of the correlation between the dipole moment and the polarization is transformed into the calculation of the velocity ACF. The theoretical value of the imaginary part of the nonlinear polarizability obtained by this method is the same as the experimental Phase Sensitive Sum-Frequency Generation (PS-SFG) spectrum result.

As a first system we have analyzed the behaviour of a salty interface containing LiNO_3 . Both the measured and calculated VSFG spectra shows a reduced intensity of the lower frequency portion region, when compared to the water/vapor interface. This reduction is attributed to the Hydrogen (H-) bonds established between the NO_3^- and the surrounding water molecules at the interface. This effects is only related to the presence of NO_3^- at the water surface and is not affected by the presence of alkali metal ions. I have shown that the use of simple models, such as small cluster is not suitable to reproduce the experimental spectra and cannot provide a microscopic interpretation of the spectra. Realistic models of the interface are required to address the perturbation of the ion at the water surface.

From the results of nonlinear susceptibilities, we conclude that these water molecules at the interfaces of LiI , NaI , and KI solutions are participating in weaker H-bonds, compared with those at the water/vapor interface. The origin of the characteristics comes from a unique distribution of I^- ions and alkali metal cations, which form a double layer over the thickness on the order of 5–10 Å.

For the bulk and interfacial systems, we calculated the correlation functions of the HB population, and obtained the reaction rate constants with the HB formation and breakage. To analyze the HB dynamics at the water/vapor interface, I proposed a new statistical scheme which is based on the interfacial HB population for the instantaneous interface. With the help of the HB population operator, one do not need to sample the molecules who are within the instantaneous interface, i.e., no need to identify the molecules on the interface and calculate the statistical average for the interesting physical quantities. Combining this method with molecule sampling on the interface, we can get more realistic and accurate HB dynamics for the water/vapor interface. The basic idea of this method is also applied to general interface systems, such as the solvation shells of ions in aqueous solutions. The difference between the HB dynamics outside the first solvation shell of the Li^+ and that of nitrate-water Hydrogen (H-) bonds at interfaces is not visible from the values of the HB relaxation time. For the interface of alkaline iodine solutions, we also find that the cations does not alter the H-bonding network outside the first hydration shell of the cations themselves. Through Solvation shell HB (SHB) dynamics, we obtained the HB dynamics for the H-Bonds between water molecules in and outside the ion's first solvation shell. Similarly, we also calculated the reorientation dynamics ($C_2(t)$) of the water molecules in the first solvation shells of ions. We found that the reorientation dynamics for the water molecules in the first solvation shell is significantly affected

by the ions. In contrast, the HB dynamics for the H-bonds between water molecules in the solvation shell and outside the shell are not sensitive to the ions' nature.

Acknowledgements

I wish to express my sincere gratitude to my supervisor, Prof. Dr. Marilore Sulpizi for her excellent guidance during my doctoral studies, and her detailed and valuable advice for my writing. I thank her for bringing me into interesting and novel areas of density functional theory-based molecular dynamics simulation and interface physics and chemistry. By communicating with her, I was implicitly and positively affected. She is rigorous in academic studies, optimistic and active, and has a wide range of interests. All these have kept in my heart and gave me greater confidence in future scientific research work.

I wish to thank Prof. Dr. Thomas Kühner, Dr. Giovanni Settanni, PD Dr. Peter Virnau, Dr. Hans Behringer and Prof. Dr. Thomas Speck at the institute for physics for leading me to the fundamental statistical physics and excellent lectures and discussions. I am grateful to Prof. Dr. Friederike Schmid and Prof. Dr. Kurt Binder for their talks and guidance.

I thank Prof. Dr. Harvey Meyer at the institute for nuclear physics. I feel very honored to be a teaching assistant in his quantum field theory course. I have benefited a lot from his wonderful teaching methods, exercises, and questions and answers with students in his class.

I am grateful to Rémi Khatib for programing skills and helpful guidance on the programs for calculating the VSFG spectra. I also thank Shuanhu Qi, Jiajia Zhou and Fei Yu for useful discussions on the calculation of response functions. I would like to thank Leila Salimi, Isidro Lorenzo Geadá, Santosh Kumar Meena and Anusha Lalitha, at the Institute for Physics, for their encouragement and assistance.

I thank Astrid Chase and Daniela Reibel for their enthusiastic and patient help during my stay at the University of Mainz. Thanks to Andreas Nussbaumer for providing technical support so that I can carry out the calculation smoothly.

I thank Prof. Honggang Luo, Prof. Haiping Fang and Prof. Haijun Zhou for their great help in my study during my doctoral studies. The cooperation and discussions with Guosheng Shi, Junming Shao, Bo Zhou and Chunlei Wang have benefited me a lot. I express my sincere thanks to them.

I thank Prof. Yuliang Jin for his support, trust and teachings over the past year.

I am grateful to my parents Yuhua Diao and Dehuai Huang, and my brother Jialiang, for their care, understanding and support for me for decades.

The financial supports of the China Scholarship Council and TRR146 are gratefully acknowledged.

Contents

Declaration of Authorship	iii
Abstract	viii
Acknowledgements	xi
1 Introduction	1
2 Methods	3
2.1 Modeling interfaces with <i>ab initio</i> molecular dynamics	3
2.2 Density functional theory	4
2.3 Born-Oppenheimer molecular dynamics	9
2.4 Vibrational density of states	11
2.5 Calculation of VSFG spectroscopy for water/vapor interfaces	11
2.5.1 Nonlinear susceptibility of water molecules at water/vapor in- terfaces	12
2.5.2 VSFG spectra from velocity ACFs	14
3 Experimental VSFG spectra of salty interfaces	17
4 Alkali nitrate clusters	19
4.1 Cluster of nitrate and water molecules	19
4.2 Cluster of alkali metal cation and water molecules	20
4.3 Clusters of alkali nitrate and water molecules	21
5 VSFG spectroscopy of water/vapor interface and solution/vapor in- terfaces	25
5.1 VSFG spectra of the interface of LiNO ₃ aqueous solutions	26
5.2 VSFG spectra of the interface of alkali iodine aqueous solutions	30
6 Hydrogen bond dynamics at water/vapor interfaces	35
6.1 Definitions of HB population and correlation functions	35
6.2 Dynamical properties of H-bonds in bulk water and at the water/vapor interfaces	40
6.3 Instantaneous interfacial HB dynamics	43
6.4 Summary	49
7 Hydrogen bond dynamics in electrolyte solutions	51
7.1 Ion-water HB dynamics at electrolyte/vapor interface	51
7.1.1 Lithium nitrate solutions	51
7.1.2 Alkali iodine solutions	53
7.1.3 Ion-water bond dynamics: breaking and reforming	56
7.2 Water-water hydrogen bond dynamics within the ions' solvation shells	59

7.3	Rotational anisotropy decay of water molecules at the water/vapor interface	61
7.4	Rotational anisotropy decay of water molecules in ions' solvation shells	67
7.5	Summary	70
8	Summary	71
A	Calculation of nonlinear optical susceptibilities	73
B	Computational details of the DFTMD simulations	77
C	Structural characterization of water clusters and solutions	79
C.1	Water clusters	79
C.2	Solution/vapor interfaces	82
C.3	Classification of water molecules based on H-bonds	84
D	Propensities of ions	87
D.1	Free energy of the water separated and the contact ion pair	87
D.2	Ion-surface distance	87
D.3	Surface tension increment	88
E	Thickness of the interface of aqueous solutions	91
E.1	Interfacial hydrogen bond dynamics	91
E.2	Thickness of the aqueous/vapor interfaces	93
F	HB dynamics and instantaneous interfaces	97
F.1	Relations between HB lifetime distributions	97
F.2	Hydrogen bond population operator	100
F.3	Reorientation dynamics of water molecules at solution/vapor interfaces	101
	Bibliography	103

List of Figures

2.1	The schematic of the VSFG process which involves IR and Raman transitions. The $\nu = 0$, $\nu = 1$ levels denote the ground and the first excited state of the oscillator[122], respectively. The dashed line denotes a virtual electronic state in the Raman transition.	12
2.2	The representation of the bond (a) and the molecular (b) frameworks. (from Ref. [120])	16
3.1	Experimental VSFG intensity of LiNO_3 solutions, compared with that of neat water. [135]	18
4.1	Geometry optimized structure of the clusters: (a) $[\text{NO}_3 \cdot (\text{H}_2\text{O})_3]^-$; (b) $\text{RNO}_3(\text{H}_2\text{O})_3$; (c) $\text{RNO}_3(\text{H}_2\text{O})_4$; (d) $\text{RNO}_3(\text{H}_2\text{O})_5$ ($\text{R}=\text{Li}, \text{Na}, \text{K}$). More structural properties are given in Appendix C.	19
4.2	VDOS for the two OH bonds in w1 (Fig. 4.1 (a)) of $[\text{NO}_3 \cdot (\text{H}_2\text{O})_3]^-$	20
4.3	The cluster $[\text{Li} \cdot (\text{H}_2\text{O})_4]^+$	20
4.4	RDFs $g_{\text{Li-O}}$ and $g_{\text{Li-H}}$ for the cluster $[\text{Li} \cdot (\text{H}_2\text{O})_4]^+$	20
4.5	(A) VDOS for the four water molecules (all water molecules) in the cluster $[\text{Li} \cdot (\text{H}_2\text{O})_4]^+$. (B) VDOS for the water molecules (three water molecules) bound to Li in the cluster $[\text{Li} \cdot (\text{H}_2\text{O})_4]^+$	21
4.6	(a)RDF $g_{\text{R-O}}$ for clusters $\text{RNO}_3(\text{H}_2\text{O})_3$ ($\text{R}=\text{Li}, \text{Na}, \text{K}$); (b)RDF $g_{\text{O-H}}$ for clusters $\text{RNO}_3(\text{H}_2\text{O})_3$ and $[\text{NO}_3 \cdot (\text{H}_2\text{O})_3]^-$ (no alkali metal cation, denoted as "R=").	22
4.7	VDOS for each water molecule in the cluster $\text{LiNO}_3(\text{H}_2\text{O})_n$: (a) $n = 3$; (b) $n = 4$; (c) $n = 5$. w1: H_2O bound to Li and H_2O ; w2: H_2O bound to nitrate and H_2O ; w3: H_2O bound to Li and nitrate; w4: H_2O bound to H_2O ; w5: H_2O only bound to Li.	22
4.8	VDOS for H_2O in clusters (a) $\text{LiNO}_3(\text{H}_2\text{O})_3$, (b) $\text{NaNO}_3(\text{H}_2\text{O})_3$ and (c) $\text{KNO}_3(\text{H}_2\text{O})_3$. w1: H_2O bound to R and H_2O ; w2: H_2O bound to nitrate and H_2O ; w3: H_2O bound to R and nitrate.	23
5.1	The salty water interface of LiNO_3 solution (top) and the water/vapor interface (bottom). The right panel shows that the Li^+ and the NO_3^- ions are separated by a water molecule at the salty interface.	25
5.2	Probability distributions of ions and water molecules for LiNO_3 water interface along the normal direction.	26
5.3	(a) The $\text{Im}\chi_{SSP}^{(2),\text{R}}$ and (b) $ \chi_{SSP}^{(2),\text{R}} ^2$ for water molecules at the interface of LiNO_3 solution.	27
5.4	VDOS $g_z(\nu)$ of water molecules at the interface of LiNO_3 solution (solid line) and at the water/vapor interface (dashed line). (a): $d = 1 \text{ \AA}$; (b): $d = 2 \text{ \AA}$; (c): $d = 5 \text{ \AA}$	27
5.5	VDOS for 6 water molecules bound to NO_3^- at the LiNO_3 solution/-vapor (LiNO_3 /vapor for short) interface (salty water) and that for 15 water molecules at the top layer ($d=1 \text{ \AA}$) of the neat water.	28

5.6	Free energy profile with respect to the distance r between Li^+ and the nitrogen in NO_3^- in the cluster $\text{LiNO}_3(\text{H}_2\text{O})_{30}$. <i>A</i> : configuration A where $r = 2.9$ Å; <i>B</i> : configuration B where $r = 4.3$ Å; <i>C</i> : the transition states.	29
5.7	Probability distributions $P(z)$, along the normal direction (z -axis), of Li^+ , I^- and O in LiI solution/vapor interface.	30
5.8	(a) RDF $g_{\text{Li-O}}$ and $g_{\text{Li-H}}$ for LiI–water interface. The first two peaks of $g_{\text{Li-O}}$ and $g_{\text{Li-H}}$: 1.97 and 4.12 Å, and, 2.61 and 4.73 Å, respectively. (b) RDF $g_{\text{I-O}}$ and $g_{\text{I-H}}$ for LiI–water interface. The first two peaks of $g_{\text{I-O}}$ and $g_{\text{I-H}}$: 3.62 and 5.28 Å; and, 2.69 and 4.11 Å, respectively. . .	32
5.9	(a) RDF $g_{\text{Na-O}}$ and $g_{\text{Na-H}}$ for NaI–water interface. The first two peaks of $g_{\text{Na-O}}$ and $g_{\text{Na-H}}$: 2.41 and 4.55 Å, and, 3.02 and 4.96 Å, respectively. (b) RDF $g_{\text{I-O}}$ and $g_{\text{I-H}}$ for NaI–water interface. The first two peaks of $g_{\text{I-O}}$ and $g_{\text{I-H}}$: 3.59 and 5.04 Å; and, 2.63 and 4.15 Å, respectively. . .	32
5.10	(a) RDF $g_{\text{K-O}}$ and $g_{\text{K-H}}$ for KI–water interface. The first two peaks of $g_{\text{K-O}}$ and $g_{\text{K-H}}$: 2.84 and 4.71 Å, and, 3.40 and 5.51 Å, respectively. (b) RDF $g_{\text{I-O}}$ and $g_{\text{I-H}}$ for KI–water interface. The first two peaks of $g_{\text{I-O}}$ and $g_{\text{I-H}}$: 3.59 and 5.43 Å; and, 2.65 and 4.10 Å, respectively. . .	32
5.11	(a) $\text{Im}\chi_{SSP}^{(2),R}$ and (b) $ \chi_{SSP}^{(2),R} ^2$ of the interface of the LiI solution (solid line) and the water/vapor interface (dashed line). The data for the water/vapor interface is calculated from the DFTMD simulation for the water interface with the same thickness (5 Å) (the same below). . .	33
5.12	(a) $\text{Im}\chi_{SSP}^{(2),R}$ and (b) $ \chi_{SSP}^{(2),R} ^2$ of the interface of the NaI solution (solid line) and the water/vapor (dashed line) interface.	33
5.13	(a) $\text{Im}\chi_{SSP}^{(2),R}$ and (b) $ \chi_{SSP}^{(2),R} ^2$ of the interface of the KI solution (solid line) and the water/vapor interface (dashed line).	33
5.14	$\text{Im}\chi_{XXZ}^{(2),R}$ and $\text{Im}\chi_{YYZ}^{(2),R}$ spectra for the whole KNO_3 interface of aqueous solution.	34
6.1	Dynamics of $r_{\text{OO}}(t)$ (top panel), $\cos\phi(t)$ (middle panel), and $h(t)$ (bottom panel) for a typical HB in a water cluster. The dashed lines show the interoxygen distance boundary $r_{\text{OO}}^c=3.5$ Å (top panel) and criterion of cosine of H–O \cdots O angle $\cos\phi^c$ with $\phi^c=30^\circ$ (middle panel), respectively.	36
6.2	Time dependence of $C_{\text{HB}}(t)$ for the simulated bulk water at 300 K with density $\rho = 1.00$ g/cm ³	37
6.3	The $C_{\text{HB}}(t)$ for bulk water, as computed from the ADH (solid line) and AHD (dashed line) criterion of H-bonds. Ref:[197]	38
6.4	Time dependence of $S_{\text{HB}}(t)$ for the simulated bulk water at 300 K with density $\rho = 1.00$ g/cm ³	39
6.5	Partial RDFs of the simulated bulk water.	40
6.6	Time dependence of (a) $n(t)$, $c(t)$ and (b) $k(t)$ of water–water H-bonds for <i>bulk</i> water.	41
6.7	Time dependence of (a) $n(t)$, $c(t)$ and (b) $k(t)$ of water–water H-bonds for the water/vapor <i>interface</i>	41
6.8	Time dependence of $k(t)$ of water–water H-bonds for (a) bulk water and (b) the water/vapor interface.	41
6.9	Time dependence of $k(t)$ for the water/vapor interface, according to Eq. 6.10. The inset shows the log-log plot of $k(t)$	42

6.10	Time dependence of $n(t)$ for bulk water and the water/vapor interface from (a) ADH (b) AHD criteria.	42
6.11	A slab of water (128 water molecules are included) with the instantaneous interface represented as a blue mesh on the upper and lower phase boundary. The normal is along the z -axis and the parameter d is the thickness of the interfacial layer. The grey surfaces are obtained by translating the interfaces to the interior of the slab along the z -axis (or the opposite direction) by d	44
6.12	The $C_{\text{HB}}^{(s)}(t)$ for the instantaneous interfacial H-bonds with different thickness (d), as computed from the (a) ADH and (b) AHD criteria of H-bonds.	45
6.13	The $C_{\text{HB}}(t)$ for the instantaneous interfacial H-bonds with different thickness d , as computed from the (a) ADH and (b) AHD criteria of H-bonds. These results are based on MS method. The sampling is performed every 4 ps.	46
6.14	Dependence of (a) the reaction rate constants k and k' and (b) the HB lifetime τ_{HB} on the interface thickness d , obtained by the IHB and MS methods, respectively. The corresponding k , k' and τ_{HB} in bulk water are also drawn with dashed lines as a reference. In panel a, the k of bulk water is represented by a <i>black dashed</i> line, and the k' is represented by a <i>blue dashed</i> line; in panel b, the τ_{HB} of bulk water is represented by a <i>black dashed</i> line. The ADH criterion of H-bonds is used and the least square fits are carried on the time region $0.2 \text{ ps} < t < 12 \text{ ps}$	47
7.1	Distribution of ions at the LiNO_3 solution/vapor interface. (A) Distances between ions and one of the instantaneous surfaces (blue meshes) for a slab of aqueous LiNO_3 solution. (B) Density distribution the Li^+ -surface and NO_3^- -surface distances at the LiNO_3 solution/vapor interface. The horizontal axis represents the distance between the ion and the instantaneous surface, which is defined in Eq. 7.1. The <i>distance</i> refers specifically to $d_{\text{X},1}$, the distance between the ion X and one of the instantaneous surfaces. Zero distance denotes the instantaneous surface of the interfacial system of LiNO_3 solution.	52
7.2	Time dependence of (a) $C_{\text{HB}}(t)$ and (b) $\ln S_{\text{HB}}(t)$ of all water-water (W-W) and nitrate-water (N-W) hydrogen bonds for the slab of LiNO_3 solution, as computed from the ADH (solid line) and AHD (dashed line) criterion of H-bonds. The W-W hydrogen bonds represents the H-bonds between all pairs of water molecules in the entire slab.	52
7.3	Distribution of ions at the LiI and NaI solution/vapor interface. (A) Density distribution the Li^+ -surface and I^- -surface distances at the LiI solution/vapor interface. (B) Density distribution the Na^+ -surface and I^- -surface distances at the NaI solution/vapor interface.	53
7.4	Distribution of ions at the KI solution/vapor interface. (A) Distances between ions and one of the instantaneous surfaces (grey meshes) for a slab of aqueous KI solution. (B) Density distribution the K^+ -surface and I^- -surface distances at the KI solution/vapor interface.	54

7.5	The $C_{\text{HB}}(t)$ of water–water hydrogen bonds in the solvation shell of (a) cations and (b) I^- at the interfaces of 0.9 M LiI, NaI and KI solutions, respectively. The solid and dashed line are for the instantaneous 1-Å water/vapor interface (see paragraph 6.3) and bulk water, respectively. The data for bulk water are calculated from water in the middle of the slab of LiI solution.	55
7.6	Time dependence of the $S_{\text{HB}}(t)$ of H-bonds at the interfaces of (a) LiI and (b) NaI solutions. The insets show the plots of $\ln S_{\text{HB}}(t)$	56
7.7	The $S_{\text{HB}}(t)$ of water–water (W–W) and nitrate–water (N–W) H-bonds at the interface of the LiNO_3 solution. The inset is the plot of $\ln S_{\text{HB}}(t)$. These results are calculated for the temporal resolution $t_t = 1$ fs. For the definition of t_t , see Appendix E.	57
7.8	Time dependence of the intermittent correlation functions $C_{\text{HB}}(t)$ of I^- –water (I^- –W) and water–water hydrogen bonds. A base-10 log scale is used for the x -axis.	58
7.9	Time dependence of the continuous correlation functions $S_{\text{HB}}(t)$ of I^- –water (I^- –W) and water–water hydrogen bonds.	58
7.10	Correlation function $C_{\text{HB}}^{(k)}(t)$ for H-bonds in solvation shells, based on the HB population $h^{(k)}(t)$, as computed from the (a) ADH and (b) AHD criteria of H-bonds. The $C_{\text{HB}}(t)$ (dashed line) in bulk water is also plotted in panel (a) and (b) respectively.	60
7.11	The $C_{\text{HB}}^{(k)}(t)$ for the solvation shell H-bonds with radius ($r_{\text{shell}} = 5.0$ Å), as computed from the (a) ADH and (b) AHD criteria of H-bonds. The $C_{\text{HB}}(t)$ (dashed line) in bulk water is also plotted in panel (a) and (b) respectively.	61
7.12	The $\ln S_{\text{HB}}^{(k)}(t)$ for H-bonds in the second solvation shells of Li^+ and I^- ions (in the water/vapor interface) as computed from the (a) ADH and (b) AHD criteria of H-bonds.	62
7.13	(A) Time dependence of $C_2(t)$ for water molecules at the water/vapor interface with different thickness in the range of 1 Å to 6 Å. (B) The dependence of decay time τ_2 on the thickness d in the exponential fitting ($t \in [0, 5]$ ps) of $C_2(t)$ for water molecules at the water/vapor interface.	63
7.14	Anisotropy decay of OH bonds in water molecules at the LiNO_3 solution/vapor interface. The water molecules considered are in instantaneous layer with $d = 2$ Å below the surface.	64
7.15	Distribution $P(n)$ of the number of H-bonds owned by a OH group at instantaneous layers with thickness d ($d = 1, \dots, 4$ Å). The red (black) line is for the LiNO_3 solution/vapor (water/vapor) interface.	64
7.16	Distribution $P(n)$ of the number of H-bonds owned by a OH group at instantaneous layers with thickness d ($d = 1, \dots, 6$ Å). The red (black) line is for the interfaces (bulk) phase.	65
7.17	[2105] Time dependence of $C_2(t)$ of OH bonds at the LiI solution/vapor (solid line) and the water/vapor (dashed line) interface. The water molecules considered are in instantaneous layer with $d = 2$ Å below the surface.	66
7.18	Distribution $P(n)$ of the number of H-bonds owned by a OH group at instantaneous layers with thickness d ($d = 1, \dots, 4$ Å). The red (black) line is for the LiI solution/vapor (water/vapor) interface.	66

7.19	Distribution $P(n)$ of the number of H-bonds owned by a OH group at instantaneous layers with thickness d ($d = 1, \dots, 6$ Å). The red (black) line is for the interfaces (bulk) phase.	67
7.20	The $C_2(t)$ for water molecules in the solvation shell of Li^+ , Na^+ , K^+ , I^- and nitrate ions at the alkali-nitrate (alkali-iodide) solution/vapor interfaces. For comparison, the $C_2(t)$ for bulk water (black line) is also shown.	68
7.21	RDFs for the alkali-nitrate solutions.	68
7.22	Dependence of τ_2 on the radius of the solvation shell of molecules and ions (water, Li^+ , Na^+ , K^+ , I^- and nitrate ions) in the slab of the alkali nitrate (iodide) solutions.	69
C.1	The nitrate O (ON)–water O (OW) and nitrate O–water H (HW) RDFs for $[\text{NO}_3 \cdot (\text{H}_2\text{O})_3]^-$. The peaks for the former are 1.93, 2.95 and 3.95 Å, and for the later are 2.95 and 4.80 Å.	81
C.2	The VDOS $g(\nu)$ for water molecules in the cluster $[\text{NO}_3 \cdot (\text{H}_2\text{O})_3]^-$ at 100 K.	81
C.3	The comparison between the VDOS for H and for a whole water molecule (w1, Fig. 4.1 a), in $[\text{NO}_3 \cdot (\text{H}_2\text{O})_3]^-$ at 300 K.	82
C.4	The dipole orientation distribution of water molecules at the water/-vapor and the LiNO_3 solution/vapor interfaces.	82
C.5	The RDFs $g_{\text{Li-OW}}(r)$, $g_{\text{Li-HW}}(r)$, $g_{\text{ON-OW}}(r)$ and $g_{\text{ON-HW}}(r)$ in bulk LiNO_3 solution.	83
C.6	The RDFs $g_{\text{Li-OW}}(r)$, $g_{\text{Li-HW}}(r)$, $g_{\text{I-OW}}(r)$ and $g_{\text{I-HW}}(r)$ for the interface of LiI solution.	83
C.7	(a) RDFs $g_{\text{X-O}}(r)$ ($\text{X}=\text{Li}^+$, Na^+ , K^+) and (b) the coordination number of Li^+ (Na^+ , K^+) ions at the interfaces of LiI (NaI , KI) solution. The coordination number $n_{\text{Li}^+}=4$, $n_{\text{Na}^+}=5$ and $n_{\text{K}^+}=6$	84
C.8	Four types of water molecules at the LiI solution/vapor interface, regarding the HB environments: (a) DDAA; (b) DDA; (c) DD'AA; (d) D'AA. The cyan balls denote I^- ions.	85
C.9	Time dependence of $C_2(t)$ for DD'A, DD'AA, and D'AA water molecules at the LiI solution/vapor interface.	86
D.1	Time dependence of K^+ –surface and I^- –surface distances for KI solution.	88
E.1	The calculated $ \chi_{SSP}^{(2),R} ^2$, of water molecules at the aqueous/vapor interfaces with different thickness.	93
E.2	The calculated $ \chi_{SSP}^{(2),R} ^2$, of water molecules at the interfaces of the LiI solution with different thickness.	93
E.3	The logarithms of the function $S_{\text{HB}}(t)$ for water-water H-bonds at interfaces with different thickness in the LiI solution.	94
E.4	The resolution dependence of the continuum lifetime τ_{HB} of water–water H-bonds at interfaces of different alkali-iodine solutions at 330 K, calculated for six temporal resolutions (t_t). [246–248]	94
E.5	The PBC's effect on the thickness-dependence of $C_2(t)$ for water molecules at the water/vapor interfaces.	95

- F.1 The H-bonds with lifetime τ in a certain configuration. At time t , we assume that there are totally n_{tot} H-bonds can be detected, and n_τ H-bonds are of lifetime τ , therefore, the fraction of H-bonds that have the lifetime τ in the configuration at time t is $P_{\text{tc}}(\tau) = n_\tau/n_{\text{tot}}$. Let τ take all the values in the interval $[0, \infty]$, we can get the HB lifetime distribution $P_{\text{tc}}(t)$ 98

List of Tables

4.1	The average length r_a of H-bonds (Li-O bonds) in the cluster $\text{LiNO}_3(\text{H}_2\text{O})_3$.	22
5.1	Peaks of $g_{\text{Li-O}}$ and $g_{\text{Li-H}}$ for the LiI solution. (unit: Å, the same below)	31
5.2	Peaks of $g_{\text{Na-O}}$ and $g_{\text{Na-H}}$ for the NaI solution.	31
5.3	Peaks of $g_{\text{K-O}}$ and $g_{\text{K-H}}$ for the KI solution.	31
6.1	The k and k' for bulk water (bulk) and the water/vapor interface (w/v). We carried on the short time region $0.2 \text{ ps} < t < 2 \text{ ps}$. The unit for k (k') is ps^{-1} , and that for τ_{HB} ($= 1/k$) is ps. (Same below.)	43
6.2	The k and k' for bulk water (bulk) and the water/vapor interface (w/v). We carried on the long time region $2 \text{ ps} < t < 12 \text{ ps}$	43
6.3	The k and k' for the interfacial HB dynamics of the water/vapor interface, through the IHB method, with ADH criteria. We carried on the longer time region $0.2 \text{ ps} < t < 12 \text{ ps}$ (same below).	48
6.4	The k and k' for the interfacial HB dynamics of the water/vapor interface through the IHB method, with AHD criteria.	48
6.5	The k and k' for the interfacial HB dynamics of the water/vapor interface through the MS method, with ADH criteria.	48
6.6	The k and k' for the interfacial HB dynamics of the water/vapor interface through the MS method, with AHD criteria.	48
7.1	The average of the continuum HB lifetimes $\langle \tau_a \rangle = \int_0^\infty S_{\text{HB}}(t)dt$ (unit: ps) in the first hydration shell of I^- ion and of alkali metal ion at the interface of three 0.9 M alkali-iodine solutions.	54
7.2	The relaxation time τ_R (unit: ps) of the $C_{\text{HB}}(t)$ for the interface of the LiI (NaI) solutions.	56
7.3	The k and k' for the water/vapor interface of the aqueous solution interfaces.	57
7.4	The dynamical properties of I^- -water and nitrate-water hydrogen bonds within ADH (AHD) criterion.	59
7.5	The radius r of hydration shells and corresponding relaxation times τ_2 at the interface of alkali-nitrate (alkali-iodide) solutions.	69
7.6	The peaks (unit: Å) of RDFs for the LiI/vapor, the LiNO_3 /vapor and the water/vapor interfaces (see Table C.5 and C.6).	70
C.1	The HB lengths r_a in $[\text{NO}_3 \cdot (\text{H}_2\text{O})_3]^-$ at 300 K.	79
C.2	The parameters of water molecules and H-bonds in $[\text{NO}_3 \cdot (\text{H}_2\text{O})_3]^-$ at 300 K.	79
C.3	The structural parameters of $\text{RNO}_3(\text{H}_2\text{O})_3$ from geometry optimization.	79
C.5	The lengths of H-bonds in $[\text{NO}_3 \cdot (\text{H}_2\text{O})_3]^-$. The indices of H atoms: H6, H7 in w1; H9, H10 in w2 and H12, H13 in w3.	80

C.4	The parameters of $\text{RNO}_3(\text{H}_2\text{O})_3$ at 300 K, obtained from the averaging during a DFTMD trajectory. For $\text{RNO}_3(\text{H}_2\text{O})_3$, R_{OH} and R'_{OH} denote the lengths of O-H bonds in which H atoms is H-bonded and is free, respectively.	80
C.6	The coordination number for ions in LiI (NaI) solution.	84
C.7	Biexponential fitting (2 ps) of $C_2(t)$ for water molecules in the LiI solution. The relative standard errors: $\Delta A/A \leq 10^{-2}$, $\Delta\tau_2/\tau_2 \leq 3 \times 10^{-2}$	86
F.1	The k and k' for the bulk water. We carried on the short time region $0.2 \text{ ps} < t < 2 \text{ ps}$. The unit for k (k') is ps^{-1} , and that for τ_{HB} ($= 1/k$) is ps. The $h(t)$ is bond-based.	101
F.2	The k and k' for the bulk water. We carried on the long time region $2 \text{ ps} < t < 12 \text{ ps}$. The unit for k (k') is ps^{-1} , and that for τ_{HB} ($= 1/k$) is ps. The $h(t)$ is bond-based.	101
F.3	The fitted parameters of anisotropy decay of water molecules at the LiI (NaI, KI) solution/vapor interface according to Eq. F.17 for the time range $[0, 10] \text{ ps}$. The standard errors: $\delta A_i \sim 0.01$, $\delta\tau_{2,i} \sim 0.1 \text{ ps}$ ($i = 1, 2$).	102
F.4	The fitted (single exponential) parameters of anisotropy decay of water molecules at the LiI (NaI, KI) solution/vapor interface according to Eq. F.17 for the time range $[0, 10] \text{ ps}$. The standard errors: $\delta A \sim 0.01$, $\delta\tau_2 \sim 0.1 \text{ ps}$	102

List of Abbreviations

ACF	A uto- C orrelation F unction
AIMD	<i>ab initio</i> M olecular D ynamics
BLYP	B eck- L ee- Y ang- P arr
BOMD	B orn- O ppenheimer M olecular D ynamics
CPMD	C ar- P arrinello M olecular D ynamics
DFT	D ensity F unctional T heory
DFTMD	D ensity F unctional T heory-based M olecular D ynamics
GGA	G eneralised G radient A pproximation
H-	H ydrogen
HB	H ydrogen B ond
HK	H ohenberg- K ohn
SHB	S olvation shell H ydrogen B ond
IHB	I nterface H ydrogen B ond
KS	K ohn- S ham
LDA	L ocal D ensity A pproximation
MD	M olecular D ynamics
MLWF	M aximally- L ocalized W annier F unctions
MP2	M oller- P lesset P erturbation
PBE	P erdew- B urke- E rnzherhof
PS	P hase- S ensitive
RDF	R adial D istribution F unction
SCF	S elf C onsistent F ield
VDOS	V ibrational D ensity O f S tates
VSFG	V ibrational S um- F requency G eneration
XC	eX change and C orrelation

Physical Constants

Avogadro constant	$N_{\text{A}} = 6.022\,141\,995 \times 10^{23} \text{ mol}$
Boltzmann constant	$k_{\text{B}} = 1.380\,650\,32 \times 10^{23} \text{ J K}^{-1}$
elementary charge	$e = 1.602\,176\,462\,6 \times 10^{-19} \text{ C}$
electron mass	$m_{\text{e}} = 9.109\,381\,887 \times 10^{-31} \text{ kg}$
molar gas constant	$R = 8.314\,459\,8 \text{ J mol}^{-1} \text{ K}^{-1},$
proton mass	$m_{\text{p}} = 1.672\,621\,581 \times 10^{-27} \text{ kg}$
Planck constant	$h = 6.626\,070\,15 \times 10^{-34} \text{ J s}$
reduced Planck constant	$\hbar = 1.054\,571\,817 \times 10^{-34} \text{ J s}$
speed of light in vacuum	$c = 299\,792\,458 \text{ m s}^{-1} \text{ (exact)}$

List of Symbols

f_i	activity coefficient of species i
Z_X	atomic number of atom X
\mathbf{R}	atomic coordinates
τ_a	average lifetime of H-bonds: $\langle \tau_a \rangle = \int_0^\infty t P_a(t) dt$
μ_i	chemical potential of component i
κ_i	decay rate of $C_2(t)$
n_X	coordination number of ion X
δ_1	difference between the first peaks' positions of the RDFs g_{X-O} and g_{X-H}
\mathbf{M}	dipole moment
$\mu^{i,l,\epsilon}$	dipole moment of the bond ϵ of the i -th water molecule in the lab frame
A	dipole polarizability (tensor)
D	direction cosine matrix
r	distance
μ	electric dipole vector
ϕ	electric potential
\mathbf{E}	electric field strength
$n(\mathbf{r})$	electron density
H_e	electronic many-body Hamiltonian
$E_I(\mathbf{R})$	energy of the nuclei
$V(\mathbf{r})$	external potential
V_{ee}	electron-electron repulsion energy
$T[n]$	electronic kinetic energy
$E_{\text{disp}}^{(2)}$	empirical two-body dispersion correction of energy
$E_{\text{disp}}^{(3)}$	empirical three-body nonadditivity dispersion correction of energy
F	Farady constant
ΔF_{AB}	free energy difference between configuration A and B
F_A	free energy of configuration A
$L_{\eta\kappa}$	Fresnel coefficients
ω_{SFG}	frequency of the sum-frequency generation beam
ω_{vis}	frequency of the incident visible beam
ω_{IR}	frequency of the incident infrared beam
$h(t)$	HB population operator
$h^{(d)}(t)$	HB population operator (it is 1 if the tagged pair are closer than r_{OO}^c)
$H(t)$	HB population operator (continuously)
$C_{\text{HB}}(t)$ (or $c(t)$)	HB population auto-correlation function
ω_I	highest nuclear phonon frequency
θ	H-O-H angle in a water molecule
β	hyperpolarizability; reciprocal temperature
$h^s(t)$	interfacial HB population operator
$j(t)$	integrated flux departing the HB configuration space at time t
I_{SFG}	intensity of the sum-frequency generation beam
I_{vis}	intensity of the incident visible beam

I_{IR}	intensity of the incident infrared beam
r_{OO}	interoxygen distance
ω_{e}	the lowest electronic frequency
r_{OO}^{c}	the maximum value of the interoxygen distance (in the definition of HB)
ϕ^{c}	the maximum value of the angle between the O–O axis and one of the O–H bonds (in the definition of HB)
m_i	molality (bulk or surface) of the ion i
N	number of water molecules
R_{OH}	O–H length in water molecule
$C_2(t)$	orientational anisotropy decay
Z	partition function
α	polarizability tensor
$\alpha^{i,l,\epsilon}$	polarizability of the bond ϵ of the i -th water molecule in the lab frame
$P_a(t)$	probability distribution of the first HB breaking in time t
$C_z(t)$	projected velocity auto-correlation function along z -axis
$x^{\text{l}}, y^{\text{l}}, z^{\text{l}}$	position coordinates in the lab frame
$x^{\text{m}}, y^{\text{m}}, z^{\text{m}}$	position coordinates in the molecular frame
$x^{\text{b}}, y^{\text{b}}, z^{\text{b}}$	position coordinates in the bond frame
$g_z(\nu)$	projected VDOS for selected atoms along z -axis
$g_{\text{A–B}}$	radial distribution function
k	rate constant of breaking a HB
k'	rate constant of reforming a HB
r_{X}	ratio of number of X to the number of H_2O among neighbors of a water molecule
θ_{SFG}	reflected angle of SFG beam w.r.t. the normal direction in the medium
$k(t)$	reactive flux
τ_{R}	relaxation time of HB population operator correlation function
$P_2(x)$	the second Legendre polynomial
$\chi^{(2),\text{R}}$	second-order resonant susceptibility
$\chi^{(2),\text{NR}}$	second-order nonresonant susceptibility
E_{KSDFIT}	self consistent KS energy
$\Delta\nu'$	shift of vibrational frequency
$h^{\text{k,X}}(t)$	solvation shell HB population operator
m_i^*	solvent molality
ν_i	stoichiometry of ion i
Γ_i	surface excess of component i
$K_{\text{p,X}}$	surface/bulk molar concentration ratio of ion X
γ	surface tension
$S_{\text{HB}}(t)$ (or $s(t)$)	survival probability of HB
t_t	temporal resolutions for calculating HB dynamics
a_i	thermodynamic activity of a chemical species i
K^{\ominus}	thermodynamic equilibrium constant
d	thickness of layer of interface (model)
τ	time for switching allegiance of a HB
$\hat{\mu}(t)$	unit vector of the transition dipole
$g(\nu)$	VDOS for selected atoms
z_i	valence of species i
\mathbf{v}	velocity of an atom
$C(t)$	velocity auto-correlation function
ν	vibrational frequency; vibrational quantum number

To my family.

Chapter 1

Introduction

Interfaces of water and electrolyte solutions exist in many biological and industrial chemical systems, and are essential for all kinds of physical [1–3] and chemical processes. [4–6] Many phenomena in biology and chemistry, such as adsorption, bubble formation, occur at aqueous interfaces. [7] Particularly, water/vapor interfaces are the most common liquid interface. [8] Water/vapor interfaces of aqueous solutions play a important role in environmental chemistry, biological systems, [9, 10] man-made systems [11–13] and atmospheric science. [14, 15] Ions at the water/vapor interface can undergo heterogeneous or interfacial reactions. [16–20] Therefore, the distribution of ions at water/vapor interfaces is essential for understanding the structure and dynamics of interfaces. The hydrogen (H-) bonding network [21–27] as well as electrostatic force, and van der Waals force are the main factors that determine the structure of interfaces. Salts change the H-bonding structure of water in the interfacial region. [7, 28, 29] The difference between anions’ distribution may have significant influence on the H-bonding network of interfacial water. [30]

Compared to bulk atoms or molecules, interfacial atomic or molecular layers generally have very different optical properties. Experimentally, in order to determine the structure of an interface, one can use Vibrational Sum-Frequency Generation (VSFG) spectroscopy. The VSFG spectroscopy utilizes a second-order nonlinear optical process and the resulting signal is very sensitive to surface ions and molecules of a submonolayer level. [30–34] This technique allows for detecting intramolecular vibrational modes, and molecular orientation by detecting polarization dependence of the VSFG signals. [35] Furthermore, the VSFG spectroscopy does not require ultrahigh-vacuum environment. [36] The advantage is its wide applicability to almost every interface as long as light can reach them. Therefore, the VSFG spectroscopy can be used to probe many types of interfaces, namely, liquid-liquid and solid-liquid interfaces. [11, 30, 37–42] With the electric dipole approximation, the VSFG process is forbidden in any centrosymmetric bulk medium, [43] such as isotropic liquids and glasses, but it is allowed at interfaces because of the broken inversion symmetry at the interfaces. [44] The VSFG spectroscopy can also be applied to metal and semiconductor surfaces. [45, 46] The VSFG spectra suggest that the interfacial H-bonding between water molecules is changed by the presence of salt, especially the anions. [28] Molecular-level properties of interfacial materials arising from interactions between water and minerals, such as swelling, wetting, hydrodynamics can also be studied by the VSFG spectroscopy. [47]

However, the quantitative interpretation of the VSFG spectra is not straightforward, because the VSFG intensity is influenced by several factors, including ions’ concentration, molecular orientation and distribution and local field correction. [30]

Although there is some general consensus on the fact that anions propensity inversely correlates with the order of the Hofmeister series, namely $\text{CO}_3^{2-} > \text{SO}_4^{2-} > \text{F}^- > \text{Cl}^- > \text{Br}^- > \text{NO}_3^- > \text{I}^- > \text{ClO}_4^- > \text{SCN}^-$, [48–51] the driving force and the

microscopic details of the solvation structure are still debated. In terms of the Gibbs adsorption equation, the traditional theory predicts that no atomic ions will exist at interfacial regions of solutions. However, Molecular Dynamics (MD) simulations have shown that more polarizable anions (e.g., larger halide anions) are present in the surface region. [52, 53] Tian and coworkers [54] also have predicted that some ions, such as I^- and Br^- , could accumulate at the interface. The surface tension has been used to infer the composition of water/vapor interface, since the surface tension of the water/vapor interface is generally altered by dissolved substance. [55]

Recently considerable attention has been given to the nitrate ions in aqueous phase for their ubiquitous and diverse role in atmospheric aerosols, polluted water, and the remote troposphere. [56, 57] In order to clarify the variations of the structural and dynamical properties of water containing ions with high surface propensity, MD simulations are a valuable tool, which can provide detailed information on the structure and dynamics of water in a simple and well-known system like alkali metal nitrate and alkali metal halide solutions. [58] In recent years, MD simulations have been used for calculating properties, such as the depth profile of ion concentrations of interfaces, [52, 53] and the VSFG spectra of electrolyte solution surfaces, [33, 41, 59, 60] but the results depend heavily on the molecular model and interaction potentials used. [61–64] In this thesis, we use Density Functional Theory-based Molecular Dynamics (DFTMD) simulations to compute the interfacial VSFG spectra of electrolyte solutions and to provide their molecular interpretation. The advantage of DFTMD is that it does not require a priori parameterization and it is capable to include polarization effects, [65] also including electronic polarization. DFTMD at the gradient corrected level, and also including dispersion corrections [66–70] has been shown to provide an accurate description of the vibrational properties at interface. [71]

The thesis is organized as follows. In Chapter 2, we present the methods of *ab initio* Molecular Dynamics and one of its implementations—the DFT and the method to calculate the VSFG spectra. In Chapter 3, we showed the experimental VSFG spectra of salty interfaces. In Chapter 4, we present the results of the Vibrational Density Of States (VDOS) for water clusters including alkali metal nitrates, which are calculated for interpreting the vibrational characteristics of water molecules in a special water/vapor interface—the water clusters. The theoretical results of VSFG spectra of water/vapor interfaces of alkali metal nitrate solutions are included in Chapter 5. Chapter 6 focuses on the Hydrogen Bond (HB) dynamics of water/vapor interfaces, and the rotational anisotropy decay of water at interfaces of alkaline iodine solutions. Finally, we studied the solution and its HB dynamics, the reorientation dynamics of water molecules, and the configuration of water molecules near ions. In addition to the alkali nitrate solutions, we also simulated and analyzed the alkali iodide solutions and its interface, which have similar properties in many aspects. This part of the content is mainly contained in Chapter 7. The conclusions are summarized in chapter 8.

Chapter 2

Methods

In this chapter, we describe the methods to study the structure and dynamics of water and aqueous solutions. We use DFTMD simulations to calculate the theoretical VSFG spectra. Our motivations for adopting DFTMD simulations are manifold. In general, by using DFTMD, (1) Structure and reactivity can be treated in a consistent way; (2) Efficient treatments of basis sets and long range interactions in the DFT do extend the simulation capabilities to thousands of atoms, i.e. it allows realistic models for interfaces; (3) They provide information on the structural organization of the solvent in the interfaces. In particular, the interface of the solution contains a large number of water molecules and a HB network composed of H-bonds between them. As Stillinger said, "Since hydrogen bonding is the most important interaction in liquid water and since these interactions are cooperative (that is, nonadditive), it is insufficient for the purposes of computer simulation to use the potential energy function for dimers alone." [72] Paragraph 2.1 to 2.3 will give an introduction to the basic ideas of AIMD and DFT as well as the BOMD we adopted. Paragraph 2.4 and 2.5 will introduce the analysis methods used in this paper, including the method of calculating VDOS from velocity autocorrelation and the method of calculating SFG spectrum from velocity correlation function.

2.1 Modeling interfaces with *ab initio* molecular dynamics

Modern theoretical methodology, aided by the advent of high speed computing, has advanced to a level where the microscopic details of dynamical processes in condensed phases can be treated on a relatively routine basis. One common theoretical approaches for obtaining these microscopic details of the system is the MD method. In the MD simulations, the classical Newtonian equations of motion for a system are solved numerically starting from a prespecified initial state, and subject to a set of boundary conditions appropriate to the problem. The MD methodology allows both equilibrium thermodynamic and dynamical properties of a system at finite temperature to be computed, while simultaneously providing a view of the microscopic motion of individual atoms in the system. [73]

Despite the success of classical molecular dynamics simulations, they have some limitations. First, charges are treated as static parameters, therefore electronic polarization effects are not included. The so-called polarizable models, [74–76] in which charges and induced dipoles are allowed to fluctuate in a changing environment, have been proposed to overcome this problem. While they have considerable success, they also have serious limitations, including a lack of transferability and standardization. [77] Second, force fields assume a pre-specified connectivity among the atoms, therefore, they suffer from an inability to describe chemical bond-forming and -breaking.

This problem can be treated using techniques such as the empirical valence bond method [78] or other semi-empirical approaches. Unfortunately, these methods are also not transferable and, therefore, need to be reparametrized for each type of reaction and may end up biasing the reaction path in undesirable ways.

To overcome these limitations of force field based approaches, *ab initio* molecular dynamics (AIMD) simulation techniques [79–85] can be used. The AIMD combines finite temperature dynamics with forces obtained from electronic structure calculations performed ‘on the fly’ as the MD simulation proceeds. [84] Because the electronic structure is treated explicitly in the AIMD calculations, many-body forces, electronic polarization and bond-forming and -breaking events are described with the accuracy of the electronic structure representation. Moreover, the AIMD method can be easily extended to incorporate nuclear quantum effects via the Feynman path integral approach, [86, 87] leading to the *ab initio* path integral technique. [88–90]

The AIMD method have been used to study a wide variety of chemically interesting problems in areas such as chemical reactivity, H-bonds for the interfacial structure, pKa, and vibrational spectroscopy. AIMD applications include calculations of the structure and dynamics of water and other H-bonded liquids, proton transport in aqueous and condensed phase environments, structure, proton order/disorder and dynamical properties of ice, structure of liquid silicates and glasses, mechanisms of polymer knotting, Ziegler-Natta industrial catalysis and other surface catalytic processes. More recently, the AIMD methods have started to impact the biological sciences and have been applied in calculations of nuclear magnetic resonance chemical shifts in drug-enzyme complexes, structure of nucleic acids, exploration of the design of possible biomimetics and structure, dynamics and binding mechanisms in myoglobin. In many of these applications, new physical phenomena have been revealed, which could not have been uncovered using empirical models, often leading to new interpretations of experimental data and even suggesting new experiments to perform. [77]

To study the heterogeneous environment at water interface, AIMD is particularly suitable for the following reasons: (1) AIMD is only relying on the atomic coordinates of the model system \mathbf{R} , and not on any adjustable parameter, i.e., the interatomic forces $\mathbf{F}_I = -\nabla_{\mathbf{R}_I} V(\mathbf{R})$, where $V(\mathbf{R})$ is the potential energy, [91] are determined using the first principle electronic structure methods on the fly; (2) New phenomena that are not foreseen before starting the simulation can simply happen if necessary. Therefore, AIMD is also a good predictive tool. However, as a drawback, the AIMD simulations are expensive and can nowadays be performed on size-limited system of 100–1000 atoms for up to a few hundred ps.

2.2 Density functional theory

In most currently performed AIMD simulations, the dynamics is performed within the so-called Born-Oppenheimer approximation. Since the mass of an electron is much smaller than that of any nuclei, there is a strong separation of timescales between the electronic and nuclear motion. We assume that the kinetic energy of nuclei is zero and their potential energy is constant in each moment of the dynamics. Therefore, the electrons can be treated independently at constant nuclear coordinates \mathbf{R} . Applying Born-Oppenheimer approximation, the potential energy $V(\mathbf{R})$ is written as

$$V(\mathbf{R}) = \langle \Psi_0 | H_e | \Psi_0 \rangle + E_I(\mathbf{R}), \quad (2.1)$$

where $|\Psi_0\rangle$ is the ground state, $E_I(\mathbf{R})$ is the energy of the nuclei, and H_e is the electronic many-body Hamiltonian, which depends on the electronic coordinates but parametrically on the nuclear degrees of freedom,

After the Born-Oppenheimer approximation, a formidable task is to solve the electronic, non-relativistic, time independent many-body Schrödinger equation

$$H_e|\Psi_0\rangle = \epsilon_0(\mathbf{R})|\Psi_0\rangle. \quad (2.2)$$

This is a high-dimensional eigenvalue problem, and it is still time consuming. One great solution to the electronic structure problem (to solve the electronic, non-relativistic, time independent many-body Schrödinger equation) is the DFT. [92, 93]

DFT can be used to map the problem of a interacting electron gas onto that of a single particle in an effective non-local potential. [80] It provides a favorable compromise between computational cost and accuracy.

Hohenberg and Kohn (HK) proved that the total energy of a many-electron system is a unique functional of the electron density $n(\mathbf{r})$. The first HK theorem proves that there exists a one-to-one correspondence between the ground state electronic density $n_0(\mathbf{r})$ and an external potential $v(\mathbf{r})$, i.e., the electron density n determines all properties of a non-degenerate ground state of an atom or molecule (for a degenerate ground state the density n determines the energy). (If we want to solve variationally for the ground state energy of a system with $H = T + V_{ee} + \sum_{i=1}^N v(i)$) the HK theorem says that there exists a valid functional $Q[n]$ that delivers the sum of the electronic kinetic energy $T[n]$ and electron-electron repulsion energy $V_{ee}[n]$ of each trial electron density n . [94]

The electronic density $n(\mathbf{r})$ which depends on just 3 electronic degrees of freedom, become the central quantity in DFT in place of the complex $3N_e$ -dimensional many-body wave-function.

The second HK theorem states that the total energy in the electronic density space satisfies

$$E^{\text{DFT}}[n_0] = \psi_0 H_e \psi_0 \leq \psi' H_e \psi' = E^{\text{DFT}}[n'], \quad (2.3)$$

for which the equality holds iff $n_0 = n'$. (variational principle) One try to choose different n to optimize $E^{\text{DFT}}[n]$, the quantum expectation value of $H_e[n]$, thus to determine $E^{\text{DFT}}[n_0]$, i.e.

$$E^{\text{DFT}}[n_0] = \min_{\psi} \psi H_e \psi = \min_n \psi[n] H_e[n] \psi[n] = \min_n E^{\text{DFT}}[n], \quad (2.4)$$

Eq. (2.2) can be solved by iteratively diagonalizing $H_e[n]$ within a self consistent field (SCF) procedure.

Assuming atomic units and considering the physical relevant Coulomb interaction, the total Hamiltonian is

$$\begin{aligned} H_e &= \frac{1}{2} \sum_{i=1}^{N_e} \nabla_i^2 + \sum_{i<j}^{N_e} \frac{1}{|\mathbf{r}_i - \mathbf{r}_j|} + \sum_{I,i}^{N,N_e} \frac{Z_I}{|\mathbf{R}_I - \mathbf{r}_i|} \\ &= \hat{T} + \hat{U} + \hat{V}, \end{aligned} \quad (2.5)$$

where Z_I is the atomic number of atom I , \hat{T} is the operator of kinetic energy of electrons, \hat{U} is the electron-electron interaction and $\hat{V} = \sum_i v(\mathbf{r}_i)$ is the electron-nuclei operator.

In DFT, we obtain the ground state energy of a many-electron system as minimum of an energy functional

$$E^{\text{DFT}}[n(\mathbf{r})] = T[n(\mathbf{r})] + U[n(\mathbf{r})] + V[n(\mathbf{r})]. \quad (2.6)$$

The next problem is how to provide an explicit form for the three terms appearing in Eq. (2.6). The solution is the Kohn-Sham approach to DFT. A reference system with the same electron density as the density for the full interacting system and without electron-electron repulsion is introduced. For such reference system, the kinetic energy functional is

$$T_s[n(\mathbf{r})] = -\frac{1}{2} \sum_{i=1}^{N_e} \int d\mathbf{r} \psi_i^*(\mathbf{r}) \nabla^2 \psi_i(\mathbf{r}) = T_s[\{\psi_i[n(\mathbf{r})]\}], \quad (2.7)$$

and the electronic density can be written as

$$n(\mathbf{r}) = \sum_{i=1}^{N_{\text{occ}}} f_i \psi_i(\mathbf{r}) \psi_i^*(\mathbf{r}), \quad (2.8)$$

in which N_{occ} is the number of occupied orbitals and f_i the occupation number of the i th state, so that

$$\sum_{i=1}^{N_{\text{occ}}} f_i = N_e, \quad (2.9)$$

and $\psi_i(\mathbf{r})$ is the wave-function of the i -th state.

The total energy functional of the Kohn-Sham (KS) system is

$$\begin{aligned} E^{\text{KS}}[n(\mathbf{r})] &= E^{\text{KS}}[\{\psi_i[n(\mathbf{r})]\}] \\ &= T_s[\{\psi_i[n(\mathbf{r})]\}] + U_H[n(\mathbf{r})] + V[n(\mathbf{r})] + E_{\text{XC}}[n(\mathbf{r})] \end{aligned} \quad (2.10)$$

$$\begin{aligned} &= -\frac{1}{2} \sum_{i=1}^N f_i \int d\mathbf{r} \psi_i^*(\mathbf{r}) \nabla^2 \psi_i(\mathbf{r}) + \frac{1}{2} \int d\mathbf{r} \int d\mathbf{r}' \frac{n(\mathbf{r})n(\mathbf{r}')}{|\mathbf{r} - \mathbf{r}'|} \\ &\quad + \int d\mathbf{r} v_{\text{ext}}(\mathbf{r})n(\mathbf{r}) + E_{\text{XC}}[n(\mathbf{r})], \end{aligned} \quad (2.11)$$

where $E_{\text{XC}}[n(\mathbf{r})] \equiv (T[n(\mathbf{r})] - T_s[\{\psi_i[n(\mathbf{r})]\}]) + (U[n(\mathbf{r})] - U_H[n(\mathbf{r})])$ is the exchange and correlation (XC) energy functional and $v_{\text{ext}} = \delta V[n(\mathbf{r})]/\delta n(\mathbf{r})$ is the external potential. The energy functional $E_{\text{XC}}[n(\mathbf{r})]$ is the only unknown part of the total energy functional. This definition of XC energy functional shows that a significant part E_{XC} is due to correlation effects of the kinetic energy, that is expressed explicitly only with the reduced 2-particle density matrix.

Directly minimizing Eq. (2.10) is not straightforward because $T_s[\{\psi_i[n(\mathbf{r})]\}]$ is an explicit orbital functional. However, it is more appropriate to make $E_{\text{KS}}[\{\psi_i[n(\mathbf{r})]\}]$ stationary by the following Euler-Lagrange equation. It is possible to use the variational principle to derive the corresponding Euler-Lagrange equation of the non-interacting system within the potential v_{ext} . The KS scheme permits to map the full interacting many-body problem, with the electron-electron interaction \hat{U} onto an equivalent fictitious single-body problem, with an effective potential operator $\hat{V}_{\text{KS}} = \hat{U}_s + \hat{V}_H + \hat{V}_{\text{XC}}$.

If we figure out a way to approximate the V_{XC} accurately, we will have a much less demanding set of equations to solve than those of the true system. [95] Using the variational principle is possible to derive the corresponding Euler-Lagrange equation

of the reference system (non-interaction system) within the potential v . To determine the set of wave-functions ψ_i which minimize the KS energy functional , we can iteratively solve the equation

$$[T_s[n(\mathbf{r})] + V_H[n(\mathbf{r})] + V[n(\mathbf{r})] + E_{XC}[n(\mathbf{r})]]\psi_i(\mathbf{r}) = \varepsilon_i\psi_i(\mathbf{r}), \quad (2.12)$$

where ε_i is the eigenvalue of each equation, V_H is the Hartree potential of the electrons:

$$V_H = e^2 \int \frac{n(\mathbf{r})n(\mathbf{r}')}{|\mathbf{r} - \mathbf{r}'|} d\mathbf{r}', \quad (2.13)$$

and the exchange and correlation potential

$$V_{XC} = \frac{\delta E_{XC}[n(\mathbf{r})]}{\delta n(\mathbf{r})}. \quad (2.14)$$

Given the explicit form of the exchange and correlation functional E_{XC} , the exchange and correlation potential V_{XC} can be determined, and thus electron density $n(\mathbf{r})$. Thus the KS equation must be solved self-consistently.

The simplest density functional approximation is the Local Density Approximation (LDA). In LDA, the exchange and correlation energy of an electronic system is

$$E_{XC}[n(\mathbf{r})] = \int \varepsilon_{XC}(\mathbf{r})n(\mathbf{r})d\mathbf{r}, \quad (2.15)$$

and

$$\frac{\delta E_{XC}[n(\mathbf{r})]}{\delta n(\mathbf{r})} = \frac{\partial n(\mathbf{r})\varepsilon_{XC}(\mathbf{r})}{\partial n(\mathbf{r})}, \quad (2.16)$$

where

$$\varepsilon_{XC}(\mathbf{r}) = \varepsilon_{XC}^{\text{hom}}[n(\mathbf{r})]. \quad (2.17)$$

The LDA is accurate for systems with slowly varying charge densities. It has a tendency to favor more homogeneous systems and over-binds solids and molecules. The dielectric and piezoelectric constant calculated from the LDA are approximately 10% over estimated. The limitations of the LDA suggest that care must be taken into its applications. For example, the independent particle picture breaks down in strongly correlated systems, where the LDA is very inaccurate. Furthermore, the LDA does not take into account variation of the electronic density and van der Waals interactions, [95] so it does not give a very accurate description of H-bonding. H-bonding is essential for a correct description of water and interfaces with water, therefore, a functional beyond the LDA is needed in the description of hydrogen-bonded systems, including water.

For any density that varies sufficiently slowly, an expansion of a functional f in gradients should have increasing accuracy:

$$f[n] = \int d^3r [an(\mathbf{r}) + bn(\mathbf{r})|\nabla n(\mathbf{r})|^2 + \dots]. \quad (2.18)$$

But the gradient expansion of the exchange-correlation energy does not always improve results, sometimes it leads to divergences. Therefore, a more general approach which is called Generalised Gradient Approximation (GGA) is considered. An approach to improve the LDA is to include gradient corrections , in which E_{XC} is a functional of density and its gradient:

$$E_{XC}^{\text{GGA}}[n(\mathbf{r})] = \int \varepsilon_{XC}(n(\mathbf{r}))n(F_{XC}[n(\mathbf{r}), |\nabla n(\mathbf{r})|])d\mathbf{r}, \quad (2.19)$$

where $F_{\text{XC}}[n(\mathbf{r})]$ is a correction chosen to satisfy conditions for E_{XC} . The XC energy depends locally on the gradient of the density ∇n as well as the density n . There are several forms of the GGAs.

The GGA is usually the best compromise between speed and accuracy in large systems. For solids, the most commonly used functional with the GGA is the one proposed by Perdew, Burke and Ernzerhof (PBE). [96] Another popular GGA functional is the BLYP functional. The electron densities of electric dipole and quadrupole moments are not uniform in space. Physically, GGAs include information on the spatial variation in the electron densities, and thus they can create functionals with better flexibility to describe dipole and quadrupole moments. Therefore, GGAs generally describe the dipole and quadrupole moments of the monomer quite well. However, they somewhat overestimate polarizabilities, the predicted dipolar polarizability (also called dipole polarizability) being typically 10% too large.

Dispersion is a general term referring to weak, long-range correlations in electronic structure. It includes van der Waals interactions, which originates from the coupling of the electric field generated by fluctuations in the electronic density at position \mathbf{r} in the system with the density at another point \mathbf{r}' . [97] These interactions are not well modelled by any mean-field level of theory, the *ab initio* wave-function theory such as second-order Moller-Plesset perturbation theory (MP2), or standard DFT functionals, eg. LDA, GGAs, etc. The mean-field theory does not include the electron correlation effect, MP2 theory usually overestimate the binding energies and underestimates intermolecular equilibrium distances, and all the gradient corrected DFT are unable to describe dispersion interactions, because they can not describe the long-range electron correlation. In the last two decades, a series of empirical corrections have been proposed which can improve the structural properties without more computational cost. [66–69, 98–100] Among such empirical approaches we choose the DFT-D3 correction which can be used in our application to interfaces with water. [69, 101]

In the DFT-D3 correction, also used in this thesis, the input parameters are cut-off radii and dispersion coefficients, and they can be calculated by KS-DFT methods using extended atomic orbital basis sets. The use of structure dependent dispersion coefficients, i.e., functional coordination number, to interpolate between dispersion coefficients of atoms in different chemical environments, increases the accuracy. Moreover, no atom connectivity information is required and all the properties are calculated only from Cartesian coordinates and atomic numbers. [69]

If the three-body nonadditivity terms are considered, as well as the pairwise terms, the total energy is given by

$$E_{\text{DFT}} = E_{\text{KS-DFT}} + E_{\text{disp}}^{(2)} + E_{\text{disp}}^{(3)}, \quad (2.20)$$

where $E_{\text{KS-DFT}}$ is the usual self-consistent KS energy obtained from the chosen density functional, $E_{\text{disp}}^{(2)}$ is the empirical two-body dispersion correction term and $E_{\text{disp}}^{(3)}$ is the three-body nonadditivity term. $E_{\text{disp}}^{(2)}$ is given by

$$E_{\text{disp}}^{(2)} = \sum_{\text{AB}} \sum_{n=6,8,10,\dots} s_n \frac{C_n^{\text{AB}}}{R_{\text{AB}}^n} f_{\text{dmp},n}(r_{\text{AB}}), \quad (2.21)$$

where \sum_{AB} denotes the sum over all atom pairs in the system, C_n^{AB} is the averaged n -order dispersion coefficients ($n = 6, 8, 10, \dots$) for atom pair AB, r_{AB} is the inter-nuclear distance of atom pair AB, and $f_{\text{dmp},n}(r_{\text{AB}})$ is the damping function used to

avoid near-singularities for small distance R between nuclei. The damping function in Eq. (2.21) is given by

$$f_{\text{dmp},n}(r_{\text{AB}}) = \frac{1}{1 + 6(r_{\text{AB}}/(s_{r,n}R_0^{\text{AB}}))^{-\alpha_n}}, \quad (2.22)$$

where $s_{r,n}$ is the order-dependent scaling factor of the cutoff radii R_0^{AB} , which is the most important parameter that has to be adjusted for each density functional and α_n is a parameter which can be adjusted manually such that the dispersion correction is smaller than 1% of $\max(|E_{\text{disp}}|)$ for typical covalent bond distances. In the Ref. [69] $s_{r,6}$ is optimized by a least-squares fitting procedure and $s_{r,8}$ is fixed to 1 for all density functionals.

The leading non-additive dispersion term for three atoms A, B and C is

$$E_{\text{disp}}^{(3)} = \frac{C_9^{\text{ABC}}(3\cos\theta_a\cos\theta_b\cos\theta_c + 1)}{(r_{\text{AB}}r_{\text{BC}}r_{\text{CA}})^2}, \quad (2.23)$$

where θ_a , θ_b and θ_c are the internal angles of the ΔABC , and C_9^{ABC} is the triple-dipole constant defined by

$$C^{\text{ABC}} = \frac{3}{\pi} \int_0^\infty \alpha^{\text{A}}(i\omega)\alpha^{\text{B}}(i\omega)\alpha^{\text{C}}(i\omega), \quad (2.24)$$

which can be approximated by a geometric mean

$$C^{\text{ABC}} \approx -\sqrt{C_6^{\text{AB}}C_6^{\text{AC}}C_6^{\text{BC}}}, \quad (2.25)$$

since the total three-body contribution is typically 5–10% of $E_{\text{disp}} = E_{\text{disp}}^{(2)} + E_{\text{disp}}^{(3)}$.

2.3 Born-Oppenheimer molecular dynamics

In computational material science, the most popular AIMD simulation methods are the Born-Oppenheimer Molecular Dynamics (BOMD) and Car-Parrinello Molecular Dynamics (CPMD) methods. In the BOMD, the potential energy $E[\{\psi_i\}; \mathbf{R}]$ is minimized at each MD step with respect to $\{\psi_i(\mathbf{r})\}$ under the orthonormality condition

$$\langle \psi_i(\mathbf{r}) | \psi_j(\mathbf{r}) \rangle = \delta_{ij}. \quad (2.26)$$

Thus the Lagrangian density is

$$\begin{aligned} L_{\text{BO}}(\{\psi_i\}; \mathbf{R}_I) = & \frac{1}{2} \sum_{I=1}^N M_I \dot{\mathbf{R}}_I^2 - \min_{\{\psi_i\}} E[\{\psi_i\}; \mathbf{R}_I] \\ & + \sum_{i,j} \Lambda_{ij} (\langle \psi_i | \psi_j \rangle - \delta_{ij}), \end{aligned} \quad (2.27)$$

in which Λ is the Hermitian Lagrangian multiplier matrix. By the Euler-Lagrange equations one obtains the equations of motion

$$\begin{aligned} M_I \ddot{\mathbf{R}}_I &= -\nabla_{R_I} [\min_{\{\psi_i\}} E[\{\psi_i\}; \mathbf{R}_I] |_{\langle \psi_i | \psi_j \rangle = \delta_{ij}}] \\ &= -\frac{\partial E}{\partial \mathbf{R}_I} + \sum_{i,j} \Lambda_{ij} \frac{\partial}{\partial \mathbf{R}_I} \langle \psi_i | \psi_j \rangle \\ &\quad - 2 \sum_i \frac{\partial \langle \psi_i |}{\partial \mathbf{R}_I} \left(\frac{\delta E}{\delta \langle \psi_i |} - \sum_j \Lambda_{ij} | \psi_j \rangle \right) \end{aligned} \quad (2.28)$$

The term $-\frac{\partial E}{\partial \mathbf{R}_I}$ is the Hellmann-Feynman force, and the term $\sum_{i,j} \Lambda_{ij} \frac{\partial}{\partial \mathbf{R}_I} \langle \psi_i | \psi_j \rangle$, i.e., the wave-function force F_{WF} , [102] is a constraint force due to the orthonormality constraint. The last term comes from the fact that there is always an implicit dependence on the atomic positions through the expansion coefficient $c_{ij}(\mathbf{r})$ that is defined by

$$\psi_i(\mathbf{r}) = \sum_j c_{ij}(\mathbf{r}) \phi_j(\mathbf{r}), \quad (2.29)$$

where the KS orbitals are assumed to be real.

The CPMD is an alternative method to the BOMD, which includes the electrons in a single state. [103] In the CPMD, a coupled electron-ion dynamics is performed. The CP Lagrangian is

$$\begin{aligned} L_{CP}(\{\psi_i\}; \mathbf{R}, \dot{\mathbf{R}}) &= \frac{\mu}{2} \sum_i \langle \dot{\psi}_i | \dot{\psi}_i \rangle + \frac{1}{2} \sum_{I=1}^N M_I \dot{\mathbf{R}}_I^2 - E[\{\psi_i\}; \mathbf{R}] \\ &\quad + \sum_{i,j} \Lambda_{ij} (\langle \psi_i | \psi_j \rangle - \delta_{ij}), \end{aligned} \quad (2.30)$$

where the electronic degrees of freedom carries a fictitious mass parameter μ , and are characterized by orbital velocities $\{\dot{\psi}_i\}$. Applying the Euler-Lagrangian equations leads the equations of motion:

$$\begin{aligned} M_I \ddot{\mathbf{R}}_I &= -\nabla_{R_I} [E[\{\psi_i\}; \mathbf{R}] |_{\langle \psi_i | \psi_j \rangle = \delta_{ij}}] \\ &= -\frac{\partial E}{\partial \mathbf{R}_I} + \sum_{i,j} \Lambda_{ij} \frac{\partial}{\partial \mathbf{R}_I} \langle \psi_i | \psi_j \rangle \end{aligned} \quad (2.31)$$

$$\begin{aligned} \mu \ddot{\psi}_i(\mathbf{r}, t) &= -\frac{\partial \langle \psi_i |}{\partial \mathbf{R}_I} \left(\frac{\delta E}{\delta \langle \psi_i |} + \sum_j \Lambda_{ij} | \psi_j \rangle \right) \\ &= -\hat{H}_e \langle \psi_i | + \sum_j \Lambda_{ij} | \psi_j \rangle, \end{aligned} \quad (2.32)$$

where $-\delta E / \delta \psi_i$ are the electronic forces to propagate the electronic degrees of freedom in time within a fictitious Newtonian dynamics. No SCF cycle is required to quench the electrons to the Born-Oppenheimer surface and to force them to evolve adiabatically with respect to the nuclei.

To ensure the adiabatic energy-scale separation of the nuclear and the electronic degrees of freedom, i.e. to prevent energy transfer between them, the highest nuclear phonon frequency ω_I must be much smaller than the lowest electronic phonon frequency ω_e . The condition $\omega_I \ll \omega_e$ is ensured by a proper choice of the fictitious mass μ . The fictitious mass determines the computational accuracy.

Which method is to favor depends largely on the definition of accuracy, as well as on the particular application. In the applications in this thesis, we use the BOMD

method, as implemented in CP2K package. [104, 105] In the BOMD (1) the nuclear positions are propagated in time followed Newton’s equations of motion with the electronic ground state energy as the potential energy surface; (2) the time evolution of the atomic coordinates is performed with the velocity Verlet algorithm. [106]

Since there is no explicit electron dynamics, the maximum integration time step is simply given by the one intrinsic to nuclear motion, i.e., $\tau_e^{\text{BO}} \approx \tau_n$. In BOMD, the time step can be even larger if the nuclear dynamics becomes fairly slow. [107] But in order to resolve vibrations in molecular systems, the time step must be decreased to less than 1 fs in this thesis. [84]

2.4 Vibrational density of states

In order to obtain information on the vibrational properties of a molecular systems, it is possible to use the velocities auto-correlation functions (ACFs), as calculated from the AIMD trajectories. The obtained Vibrational Density Of States (VDOS) can provide information on the local environments on the OH-stretching mode of water molecules. For a system comprised of N atoms, the velocity ACF $C(t)$ for a molecule is [63, 108, 109]

$$C(t) = \frac{\langle \sum_{i=1}^N \mathbf{v}_i(t) \cdot \mathbf{v}_i(0) \rangle}{\langle \sum_{i=1}^N \mathbf{v}_i(0) \cdot \mathbf{v}_i(0) \rangle}, \quad (2.33)$$

where $\langle \dots \rangle$ denotes the average over starting times, t is the time interval, and \mathbf{v}_i denotes the velocity of the i -th atom. The VDOS $g(\nu)$ for selected atoms, which is a function of the vibrational frequency ν of atoms, is expressed in terms of the FT of the velocity ACF of the atoms. [110] In equilibrium, $C(-t) = C(t)$, and $g(\nu)$ is a real function, i.e.,

$$g(\nu) = \sqrt{\frac{2}{\pi}} \int_0^\infty dt \cos(2\pi\nu t) C(t). \quad (2.34)$$

Single components of the velocities ACFs can be also calculated. For example in the case of an interface it may be of interest to look at z -component (where z is the direction perpendicular to the surface), we can calculate the Fourier transform $g_z(\nu)$ of the ACF of the vertical component of atomic velocity. $g_z(\nu)$ can be calculated by Eq. (2.34), if we replace $C(t)$ by

$$C_z(t) = \frac{\langle \sum_{i=1}^N v_{i,z}(t) v_{i,z}(0) \rangle}{\langle \sum_{i=1}^N \mathbf{v}_i(0) \cdot \mathbf{v}_i(0) \rangle}, \quad (2.35)$$

where $v_{i,z}$ is the vertical component of the velocity of the i -th atom. The VDOS $g_z(\nu)$ for water molecules is used to extract the O-H stretch along the vertical direction to the averaging water/vapor interface.

2.5 Calculation of VSFG spectroscopy for water/vapor interfaces

As we introduced in Chapter 1, the VSFG spectroscopy is a powerful tool for extracting structural and dynamical information on surfaces and interfaces. It can be applied to any interface as long as light can reach it, also including liquid/metal interfaces [111–115] and buried interfaces; [116, 117] It can probe liquid interface with molecular sensitivity. [118–120] Therefore, VSFG spectroscopy can yield structural information about water/vapor interfaces which could not be obtained with other techniques.

2.5.1 Nonlinear susceptibility of water molecules at water/vapor interfaces

VSFG The VSFG is a coherent nonlinear optical process in which incident laser beams with frequency and wave vector (ω_1, \mathbf{k}_1) and (ω_2, \mathbf{k}_2) produce a signal with frequency and wave vector $(\omega_1 + \omega_2, \mathbf{k}_1 + \mathbf{k}_2)$ (Fig. 2.1). In this process, the fields arise from the polarization induced over a macroscopically large volume superposition coherently. The VSFG signal intensity is proportional to the square of the resonant and non-resonant terms:

$$\begin{aligned} I_{\text{SFG}}(\omega) &\propto |\chi^{(2)}(\omega)|^2 \\ &= |\chi^{(2),\text{R}}(\omega) + \chi^{(2),\text{NR}}(\omega)|^2, \end{aligned} \quad (2.36)$$

where $\chi^{(2)}$ is a third-rank tensor called second-order nonlinear susceptibility, or hyperpolarizability for a molecule[121], and it is responsible to the SFG process. $\chi^{(2),\text{R}}$ is the vibrationally resonant term, while $\chi^{(2),\text{NR}}$ is the nonresonant term. Because

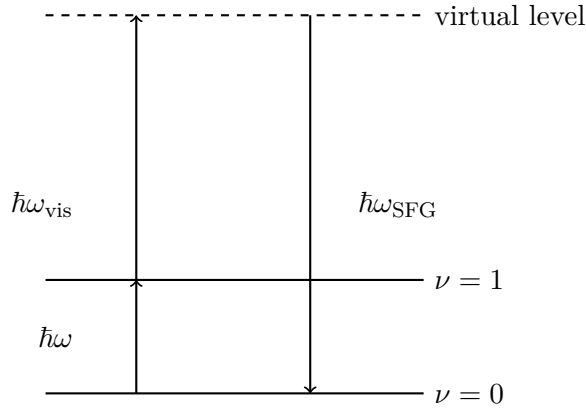


FIGURE 2.1: The schematic of the VSFG process which involves IR and Raman transitions. The $\nu = 0$, $\nu = 1$ levels denote the ground and the first excited state of the oscillator[122], respectively. The dashed line denotes a virtual electronic state in the Raman transition.

experiments usually employed visible and SFG frequencies are far from resonant conditions, $\chi^{(2),\text{NR}}$ can be considered totally off-resonant and therefore insensitive to the laser beams' frequencies involved. Therefore, we can neglect the frequency dependence of the non-resonant term. The molecular information is contained in the resonant signal. The resonant susceptibility $\chi^{(2),\text{R}}(\omega)$ is given by

$$\chi_{\eta\xi\kappa}^{(2),\text{R}}(\omega) = \frac{-i}{\hbar} \int_0^\infty dt e^{i\omega t} \text{Tr}[\rho, \mu_\kappa] \alpha_{\eta\xi}(t), \quad (2.37)$$

where the index η , ξ and κ are one of x, y and z labels of the laboratory coordinate frame. In Eq. (2.37) $\rho = e^{-\beta H}/Z$ for a system with Hamiltonian H and partition function Z at reciprocal temperature $\beta = 1/k_B T$; μ_κ is the κ -th component of the system electric dipole and $\alpha_{\eta\xi}$ is the $\eta\xi$ -th component of the polarizability tensor. [123] Besides the vibrational resonance, $\chi^{(2),\text{R}}$, which reflects the vibrational and orientational characteristics of the surface species, the VSFG signal also includes the contribution from the non-resonant signal background $\chi^{(2),\text{NR}}$, due to static hyperpolarizability of the interface itself. [43] For example, there are strong non-resonant second-order nonlinear responses [115, 124, 125] of the interface in the case of some metal(-oxide). Generally, experiments employ visible light and VSFG frequencies far

from resonant conditions, therefore, the non-resonant term $\chi^{(2),\text{NR}}$ is approximately off-resonant to the light frequencies involved. [126]

Microscopic expression of molecular hyperpolarizability As the electric field is increased, the description of the induced dipole moment $\boldsymbol{\mu}$ should include the normally insignificant nonlinear terms. We can express the induced dipole moment as

$$\boldsymbol{\mu} = \boldsymbol{\mu}_0 + \alpha \mathbf{E} + \beta \mathbf{E} \mathbf{E}. \quad (2.38)$$

The VSFG spectra are determined by the frequency-dependent hyperpolarizability in molecular level description. The frequency-dependent hyperpolarizability can be expressed as a sum of resonant and non-resonant terms:

$$\beta_{\eta\xi\kappa}(\omega_{\text{SFG}}, \omega_{\text{vis}}, \omega) = \beta_{\eta\xi\kappa}^{\text{R}} + \beta_{\eta\xi\kappa}^{\text{NR}}, \quad (2.39)$$

where η , ξ and κ are space-fixed axes. The resonant term of the frequency-dependent hyperpolarizability is

$$\beta_{\eta\xi\kappa}^{\text{R}}(\omega_{\text{SFG}}, \omega_{\text{vis}}, \omega) = \sum_{v',v} \frac{\langle v | \alpha_{\eta\xi} | v' \rangle \langle v' | \mu_{\kappa} | v \rangle}{(\omega_{v'} - \omega_v) - \omega - i\gamma_{v'v}} \rho_v, \quad (2.40)$$

where the subscripts η , ξ and κ denote body-fixed axes, $\omega_{v'} - \omega_v$ is the vibrational energy gap, ρ_v is the thermal distribution function of the initial vibrational states v , $\alpha_{\eta\xi}$ is the $\eta\xi$ -th component of the molecular dipole polarizability, μ_{κ} is the κ -th component of the molecular dipole moment, and $\gamma_{v'v}$ is the damping rate. Since (Appendix A)

$$\int_0^\infty dt e^{-it[(\omega_{v'} - \omega_v) - \omega - i\gamma_{v'v}]} = \frac{-i}{(\omega_{v'} - \omega_v) - \omega - i\gamma_{v'v}}, \quad (2.41)$$

we can rewrite Eq. (2.40) as

$$\begin{aligned} \beta_{\eta\xi\kappa}^{\text{R}} &= i \int_0^\infty dt \sum_{v',v} e^{-i[(\omega_{v'} - \omega_v) - \omega - i\gamma_{v'v}]t} \langle v | \alpha_{\eta\xi} | v' \rangle \langle v' | \mu_{\kappa} | v \rangle \rho_v \\ &= i \int_0^\infty dt \sum_{v',v} e^{i\omega t} \langle v | e^{iHt} \alpha_{\eta\xi} e^{-iHt} | v' \rangle \langle v' | \mu_{\kappa} | v \rangle \rho_v \\ &= i \int_0^\infty dt e^{i\omega t} \langle \alpha_{\eta\xi}(t) \mu_{\kappa}(0) \rangle, \end{aligned} \quad (2.42)$$

where H is the Hamiltonian of the system without external field. Eq. (2.42) indicates that the resonant term $\beta_{\eta\xi\kappa}^{(2),\text{R}}$ is the Fourier-Laplace transformation of the quantity $\langle \alpha_{\eta\xi}(t) \mu_{\kappa}(0) \rangle$, i.e., the ensemble average of the time correlation function $\alpha(t) \mu_r(0)$. The damping rate $\gamma_{v'v}$ is not explicitly included in Eq. (2.42), because the dephasing is incorporated in the time development of the off-diagonal matrix elements of $\alpha_{\eta\xi}(t)$ and $\mu_{\kappa}(0)$.

The tensor elements $\chi_{\eta\xi\kappa}^{(2),\text{R}}$ is microscopically represented as the average sum of first-order hyperpolarizability of the constituent molecules β in the space-fixed frame

$$\chi_{\eta\xi\kappa}^{(2),\text{R}} = \left\langle \sum_i^N \sum_{pqr} D_{\eta p}(\Omega_i) D_{\xi q}(\Omega_i) D_{\kappa r}(\Omega_i) \beta_{pqr} \right\rangle \quad (2.43)$$

where $D(\Omega_i)$ is the direction cosine matrix of the i -th molecule, projecting β onto the space-fixed frame. [127]

The Fresnel Factors Because of screening and dipole-dipole coupling, the local electric fields felt by molecules is different from the macroscopic fields. [125] The SFG signal depends on the magnitude of the local electric fields of the interacting optical beams at the interfaces. While the magnitude of the local electric fields is related to both the intensity of the incident beams and the linear refractive indices of the different layers (bulk) of the sample.[118] The Fresnel coefficients define the magnitude of the electric fields at the interface. Therefore, to find out the magnitude of the local electric fields, we need to evaluate the Fresnel factors. The SFG intensity I_{SFG} , is proportional to the intensities of the incident visible and infrared beams, I_{vis} , I , and to the square of the second-order nonlinear susceptibilities, $\chi_{\eta\xi\kappa}^{(2)}(\omega_{\text{SFG}})$, of the interface:

$$\chi_{\eta\xi\kappa}^{(2)}(\omega_{\text{SFG}}) \propto \left| \sum_{\eta,\xi,\kappa} L_{\eta\eta}(\omega_{\text{SFG}}) \chi_{\eta\xi\kappa}^{(2)}(\omega_{\text{SFG}}) L_{\xi\xi}(\omega_{\text{vis}}) L_{\kappa\kappa}(\omega) \right|^2 \sec^2(\theta_{\text{SFG}}) I_{\text{vis}} I \quad (2.44)$$

where η, ξ, κ are the Descartes coordinates of the reference frame; $\omega_{\text{SFG}} = \omega_{\text{vis}} + \omega$ is the frequency of SFG beam; $L_{\eta\eta}$, $L_{\xi\xi}$ and $L_{\kappa\kappa}$ are the Fresnel coefficients; θ_{SFG} is the reflected angle of SFG beam with respect to the normal direction in the medium.

2.5.2 VSFG spectra from velocity ACFs

In this paragraph I review the derivation an expression for the calculation of the sum frequency generation spectra of water interfaces that is based on the projection of the atomic velocities on the local normal modes, such an approach permits one to obtain the SFG signals from suitable velocity ACFs, reducing the computational cost to that of the accumulation of a molecular dynamics trajectory, and therefore cutting the overhead costs associated with the explicit calculation of the dipole and polarizability tensor. Moreover, the method permits to interpret the peaks in the spectrum in terms of local modes. The components of the resonant term $\chi_{\eta\xi\kappa}^{(2),\text{R}}$ of the second order susceptibility can be calculated according to the classical formula [30, 126, 128]

$$\chi_{\eta\xi\kappa}^{(2),\text{R}} = \frac{-i}{k_{\text{B}} T \omega} \int_0^\infty dt e^{i\omega t} \langle \dot{A}_{\eta\xi}(t) \dot{M}_{\kappa}(0) \rangle \quad (2.45)$$

where k_{B} is the Boltzmann constant, ω is the frequency of the IR beam, \mathbf{M} (A) is the dipole moment (dipole polarizability) of the system, and $\langle \dots \rangle$ denotes the average over all starting time points.

The total dipole moment and dipole polarizability derivatives for the system can be expressed in terms of the water and bond contributions:

$$\dot{A} = \sum_{i=1}^N \sum_{\epsilon} \dot{\alpha}^{i,1,\epsilon} \quad (2.46)$$

$$\dot{\mathbf{M}} = \sum_{i=1}^N \sum_{\epsilon} \dot{\mu}^{i,1,\epsilon} \quad (2.47)$$

where $\mu^{i,1,\epsilon}$ ($\alpha^{i,1,\epsilon}$) is the dipole moment (polarizability) of the bond ϵ of the i -th water molecule, the superscript (1) denote these quantities are measured in the lab frame,

and N is the total number of the water molecules. Therefore, the correlation function in Eq. (2.45) can be written as

$$\begin{aligned} \langle \dot{A}_{\eta\xi}(t) \dot{M}_{\kappa}(0) \rangle &= \sum_{i=1}^N \sum_{\epsilon} \langle \dot{\alpha}_{\eta\xi,i,\epsilon}^1(t) \dot{\mu}_{\kappa,i,\epsilon}^1(0) \rangle \\ &+ \sum_{i=1}^N \sum_{\epsilon} \langle \dot{\alpha}_{\eta\xi,i,\epsilon}^1(t) \dot{\mu}_{\kappa,i,-\epsilon}^1(0) \rangle \\ &+ \sum_{i,j=1;i \neq j}^N \sum_{\epsilon,\epsilon'} \langle \dot{\alpha}_{\eta\xi,i,\epsilon}^1(t) \dot{\mu}_{\kappa,i,\epsilon'}^1(0) \rangle. \end{aligned} \quad (2.48)$$

In Eq. (2.48), the first term of the right-hand side is the bond auto-correlation, the second term accounts for the correlation between the two bonds in the same water molecule, and the third term for the correlation between bonds in two different water molecules.

We assume that the bond elongation are small compared to the total bond length and stretching frequencies of the bond are much larger than frequencies of bond reorientation, for example, the libration. Therefore, we can approximately write $\dot{\mu}(0)$ by

$$\begin{aligned} \dot{\mu}_{\kappa}(0) &= \sum_i^{x,y,z} \mathbf{D}_{\kappa i}(0) \dot{\mu}_i(0) \\ &= \sum_i^{x,y,z} \mathbf{D}_{\kappa i}(0) \left(\sum_j^{x,y,z} \frac{d\mu_i}{dr_j} \frac{dr_j}{dt} \Big|_{t=0} \right) \\ &= \sum_i^{x,y,z} \mathbf{D}_{\kappa i}(0) \frac{d\mu_i}{dr_z} v_z(0), \end{aligned} \quad (2.49)$$

where $\mathbf{D}_{\kappa i}$ is the direction cosine between the laboratory-fixed κ axis and the molecular-fixed i axis, and $v_z = \frac{dr_z}{dt} \Big|_{t=0}$ is the projection of the velocity on the bond axis.

Similarly, for the dipole polarizability, we have

$$\dot{\alpha}_{\eta\xi}(t) = \sum_{i,j}^{x,y,z} \left(\mathbf{D}_{\eta i}(t) \frac{\partial \alpha_{ij}}{\partial r_z} \mathbf{D}_{\xi j}(t) \right) v_z(t). \quad (2.50)$$

The Eq. (2.49) and Eq. (2.50) simplify the calculation of the $\langle \dot{A}_{\eta\xi}(t) \dot{M}_{\kappa}(0) \rangle$ in Eq. (2.45), because $v_z(t)$ and $\mathbf{D}(t)$ can be readily determined from the DFTMD trajectory, and $\frac{d\mu_i}{dr_z}$ and $\frac{\partial \alpha_{ij}}{\partial r_z}$ can be parameterized. [118, 129]

We used three different frameworks: the lab framework (x^l, y^l, z^l), the molecular framework (x^m, y^m, z^m) and the bond framework (x^b, y^b, z^b) (see Fig. 2.2). In the lab framework, the z^l -axis is perpendicular to the interface. The molecular frame will be used to decompose the signal into normal modes of water monomers. For the j -th molecule, the z^m axis is along the bisector of the H-O-H angle, the x^m axis is in the molecular plane, and the y^m axis is out of the molecular plane. [120]

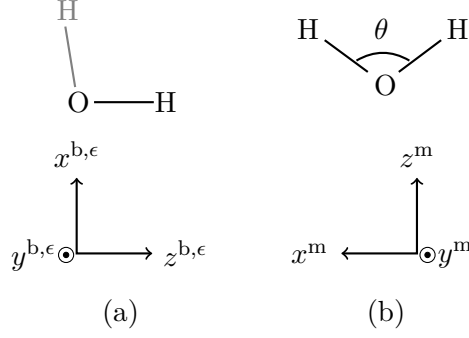


FIGURE 2.2: The representation of the bond (a) and the molecular (b) frameworks. (from Ref. [120])

In the bond framework, $z^{b,\epsilon}$ axis is along the bond ϵ of a molecule, $z^{b,\epsilon}$ is in the molecular plane and $y^{b,\epsilon}$ is out of the molecular plane.

$$\dot{\alpha}^{l,\epsilon} = \mathbf{D}^m \mathbf{D}^{b,\epsilon} \left(\frac{\partial \alpha^b}{\partial r} \dot{r}^\epsilon \right) (\mathbf{D}^{b,\epsilon})^T (\mathbf{D}^m)^T, \quad (2.51)$$

$$\dot{\mu}^{l,\epsilon} = \mathbf{D}^m \mathbf{D}^{b,\epsilon} \left(\frac{\partial \mu^b}{\partial r} \dot{r}^\epsilon \right). \quad (2.52)$$

The direction cosine matrix $\mathbf{D}^{b,\epsilon=1}$ and $\mathbf{D}^{b,\epsilon=-1}$ can be expressed as

$$\mathbf{D}^{b,1} = \begin{pmatrix} \cos \frac{\theta}{2} & 0 & -\sin \frac{\theta}{2} \\ 0 & 1 & 0 \\ \sin \frac{\theta}{2} & 0 & \cos \frac{\theta}{2} \end{pmatrix}, \quad \mathbf{D}^{b,-1} = \begin{pmatrix} -\cos \frac{\theta}{2} & 0 & \sin \frac{\theta}{2} \\ 0 & 1 & 0 \\ \sin \frac{\theta}{2} & 0 & \cos \frac{\theta}{2} \end{pmatrix}, \quad (2.53)$$

where θ is the H-O-H angle in a water molecule. We can use \mathbf{D}^m to transform the coordinates in a molecular framework to coordinates in the lab framework. Because the orientation of water molecules is changing during the simulation, \mathbf{D}^m is time dependent.

Based on the DFTMD simulations, we can implement the parameterization of $\frac{\partial \mu_k}{\partial r_z}$ and $\frac{\partial \alpha_{ij}}{\partial r_z}$ and calculate the correlation function $\langle \dot{A}_{\eta\xi}(t) \dot{M}_\kappa(0) \rangle$ through the velocity auto-correlation function. This approximation for estimating the susceptibility retains the details of the interface, including the full electronic structure. And it reduces the computational cost for a total calculation with the instantaneous evaluation of the molecular dipoles and polarizabilities.[130] The parametrization of $\frac{\partial \mu_k}{\partial r_z}$ and $\frac{\partial \alpha_{ij}}{\partial r_z}$ is based on the calculation of Maximally Localized Wannier Functions (MLWF) [131] and can be done through the approach developed by Salanne *et al.*[132] and Khatib *et al.*[120] The implementation of this parametrization is given in Appendix A.

Chapter 3

Experimental VSFG spectra of salty interfaces

In this chapter, we give the experimental results obtained on salty solutions containing alkali cations and nitrate (iodide) anions. [133–135]

From the experimental data of surface tension dependence on solute concentration $d\gamma/dm_2$ at low electrolyte concentrations (≤ 1.5 M), [136–139] the relation of the surface/bulk molar concentration ratio K_p [140] among Li^+ , Na^+ and K^+ is:

$$0 = K_{p,\text{Na}^+} < K_{p,\text{K}^+} < K_{p,\text{Li}^+}. \quad (3.1)$$

i.e., Na^+ is the most surface-excluded in the water solution RNO_3 , K^+ is less excluded, and Li^+ is the least excluded cation. (See Appendix D.3 for details.) In modeling the interfaces of aqueous solutions of alkali metal nitrates, we decided to start with LiNO_3 , because the Li^+ ion is the least excluded of the vapor-liquid interface among the alkali metal ions.

Hua *et al.* [135] have recently measured the VSFG spectra of water/vapor interface of LiNO_3 salt solutions in the OH stretching region ($3000\text{--}3800\text{ cm}^{-1}$) using Heterodyne Detected VSFG spectroscopy. [141–143] The experimental result of the VSFG intensity of the alkali nitrate interfaces is given by in Fig. 3.1. At a difference with the spectra for the water interface, in the spectra of LiNO_3 solutions, a depletion of the 3200 cm^{-1} peak is observed, with an enhancement of the 3400 cm^{-1} peak. A similar behaviour had been observed for the interface of NaNO_3 and $\text{Mg}(\text{NO}_3)_2$ solutions. [134, 135] It has been suggested that this depletion of the 3200 cm^{-1} peak, and in some cases the enhancement of the 3400 cm^{-1} peak, is an indication that nitrate ions reside at the interface. On the other hand the small cations should have little surface propensity. It has also been argued that the positive electric field found at the interface of NaCl , NaI and NaNO_3 salt solutions is due to the formation of an ionic double layer between anions located near the surface and their counter-cations (e.g. Na^+) located further below. In Phase-Sensitive (PS) VSFG experiments the magnitude of the induced change in the $\text{Im}\chi^{(2)}$ spectra comparatively to that of the neat water suggested that NO_3^- has a surface propensity just in between I^- and Cl^- . [144, 145]

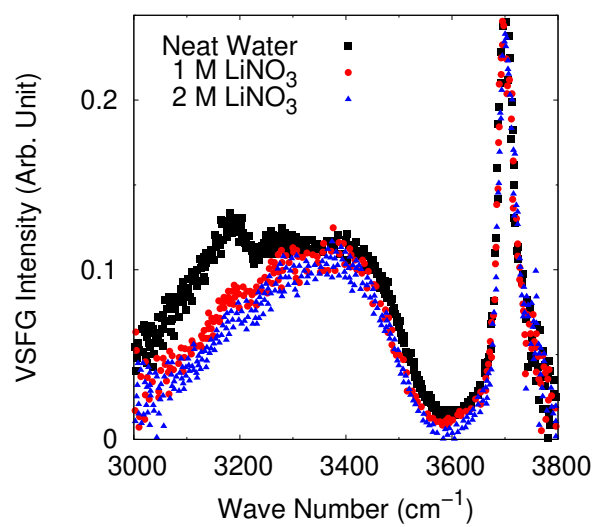


FIGURE 3.1: Experimental VSFG intensity of LiNO_3 solutions, compared with that of neat water. [135]

Chapter 4

Alkali nitrate clusters

There are two ways of obtaining highly specific information on solvation structures: studying gas-phase clusters consisting of ions surrounded by a few water molecules [146, 147], and exciting and detecting a dissolved prob molecule [148]. Due to the experimental difficulties, most information on the dynamics of aqueous solvation shells was obtained from MD simulations. [149, 150] In this chapter, DFTMD simulations of the gas phase clusters including alkali cations, nitrate ions and a few water molecules have been used to obtain these specific information and to understand the effects of alkali cations and nitrate anions on hydrogen bonding. [151, 152] VDOS is used to extract the vibrational signatures for the water molecules in these systems. In the first two paragraphs the effect of the anion and the cation are separately investigated. The two clusters, $[\text{NO}_3 \cdot (\text{H}_2\text{O})_3]^-$ and $[\text{Li} \cdot (\text{H}_2\text{O})_4]^+$, are used to study the structural and dynamical properties of water clusters with nitrate ions and with alkali cations at $T = 300$ K. In paragraph 4.3, the effects of the alkali metal cations and the nitrate anion are discussed within clusters containing both cations and anions and an increasing number of water molecules.

4.1 Cluster of nitrate and water molecules

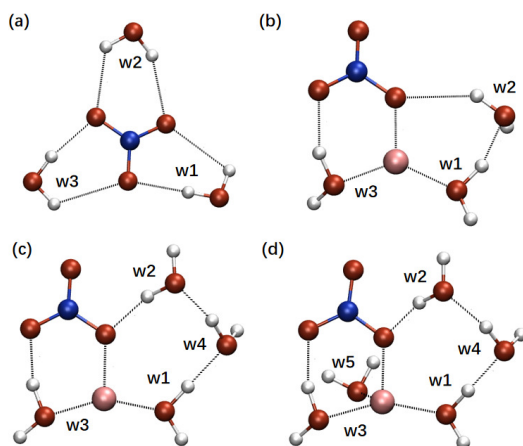


FIGURE 4.1: Geometry optimized structure of the clusters: (a) $[\text{NO}_3 \cdot (\text{H}_2\text{O})_3]^-$; (b) $\text{RNO}_3(\text{H}_2\text{O})_3$; (c) $\text{RNO}_3(\text{H}_2\text{O})_4$; (d) $\text{RNO}_3(\text{H}_2\text{O})_5$ ($\text{R}=\text{Li}, \text{Na}, \text{K}$). More structural properties are given in Appendix C.

First, we consider the nitrate–water cluster, $[\text{NO}_3 \cdot (\text{H}_2\text{O})_3]^-$. The symmetric isomer of the cluster, as shown in Fig. 4.1 (a), is obtained by geometry optimization at the BLYP/TZV2P level of theory. According to the definition of the H-bond, [153, 154] there are three H-bonds in it, i.e., only one of the two OH bonds is H-bonded to

NO_3^- in each water molecule. Therefore, the two OH bonds in each water molecule exhibit different vibrational features. Fig. 4.2 shows the difference of VDOS for the OH bonds in the cluster. For each water molecule, one OH bond is vibrating in the frequency range 3680–3700 cm^{-1} , while the other in the frequency range 3380–3440 cm^{-1} . The difference of frequencies between the vibrational modes is about $\Delta\nu = 250 \text{ cm}^{-1}$.

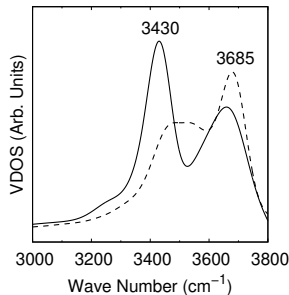


FIGURE 4.2: VDOS for the two OH bonds in w1 (Fig. 4.1 (a)) of $[\text{NO}_3 \cdot (\text{H}_2\text{O})_3]^-$.

Additionally, we label the three water molecules as w1, w2, and w3, respectively (Fig. 4.1 (a)). For the three water molecules, we find some differences in the structural parameters. Table C.5 gives the calculated lengths of H-bonds in the cluster $[\text{NO}_3 \cdot (\text{H}_2\text{O})_3]^-$. The average differences Δd between the H-bonds and the quasi-H-bonds are 0.69 Å (Table C.2).

4.2 Cluster of alkali metal cation and water molecules

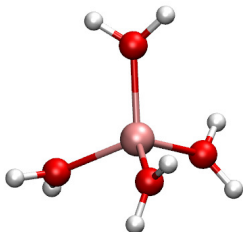


FIGURE 4.3: The cluster $[\text{Li} \cdot (\text{H}_2\text{O})_4]^+$.

To find the effects of alkali cations on the structural properties of water, we investigate the cluster $[\text{Li} \cdot (\text{H}_2\text{O})_4]^+$ (Fig. 4.3). We concentrate on two aspects: the radial distribution function (RDF), and the VDOS for water molecules of this cluster.

The sharp peaks in the RDF given in Fig. 4.4 show that the solvation shell of Li^+ is bound to all the four water molecules. The peak for g_{LiO} is at 2.02 Å, and for g_{LiH} is at 2.69 Å.

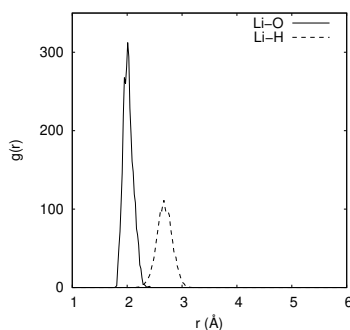


FIGURE 4.4: RDFs $g_{\text{Li-O}}$ and $g_{\text{Li-H}}$ for the cluster $[\text{Li} \cdot (\text{H}_2\text{O})_4]^+$.

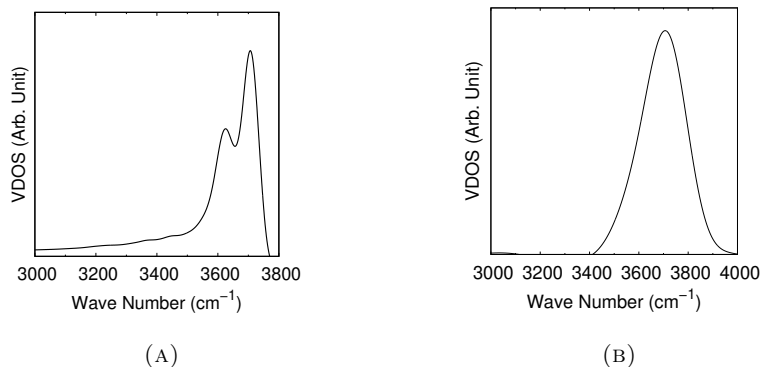


FIGURE 4.5: (A) VDOS for the four water molecules (all water molecules) in the cluster $[\text{Li} \cdot (\text{H}_2\text{O})_4]^+$. (B) VDOS for the water molecules (three water molecules) bound to Li in the cluster $[\text{Li} \cdot (\text{H}_2\text{O})_4]^+$.

The VDOS for water molecules in the cluster $[\text{Li} \cdot (\text{H}_2\text{O})_4]^+$ is calculated from a 20-ps trajectory, during which one water molecule escaped from the bonding of the Li and then formed a new HB to another water molecule. First, Fig. 4.5 (A) shows that, in this case, there are two types of OH stretching modes in the cluster $[\text{Li} \cdot (\text{H}_2\text{O})_4]^+$: free OH stretch which peaks at 3705 cm^{-1} and bonded OH stretch at 3625 cm^{-1} . However, the water molecules just bound to Li has two degenerate free O-H stretching modes. The VDOS for water molecules only bound to Li (Fig. 4.5 (B)) shows that these water molecules only have free OH stretch, since there is only a broad stretching mode at 3705 cm^{-1} .

4.3 Clusters of alkali nitrate and water molecules

As a first minimal model system for the interfaces of alkali nitrate solution, we consider alkali nitrate water clusters including 3 to 5 waters. The idea is to investigate the effect of the alkali nitrate on the vibrational properties of those water molecules which are directly H-bonded to the ions. In our simulations, the clusters are geometry optimized and the most stable configurations are determined (Fig. 4.1 (b), (c) and (d)). The first interesting result is that for all the clusters containing 3 to 5 water molecules, a contact ion pair is maintained during the 300 K simulation trajectories where a *direct* interaction involves the cation and one of the nitrate oxygen's.

In the $\text{LiNO}_3(\text{H}_2\text{O})_3$ cluster, there are three H-bonds and three Li-O bonds. The average lengths of them are given in Table 4.1. We use HB1, HB2 and HB3 to denote the HB between w1 and w2, w2 and NO_3^- , and w3 and NO_3^- , respectively (Fig. 4.1 (b)). Both the average lengths of HB1 and HB3 are very close to each other and both of them are smaller than those of HB2. Since both w1 and w2 are bound to Li^+ , we calculate an average value $\bar{d}_{\text{HB}} = 1.81 \text{ \AA}$ of the lengths of HB1 and HB3. The difference between length of HB2 and \bar{d}_{HB} is $\delta d_{\text{HB}} = 0.19 \text{ \AA}$. By testing the difference of environment of each H-bonds, we obtain that δd_{HB} comes from the difference between Li-O and H-bonds.

Besides, the RDF between the alkali (Li^+ , Na^+ or K^+) and the water O (panel a) and the nitrate O – water H (panel b) are reported in Fig. 4.6. The sharp peaks in the RDF (Fig. 4.6 (b)) show that the nitrate is solvated and in particular a stronger HB is formed in the presence of the cation.

TABLE 4.1: The average length r_a of H-bonds (Li-O bonds) in the cluster $\text{LiNO}_3(\text{H}_2\text{O})_3$.

Bonds	r_a (Å)
HB1	1.83 ± 0.14
HB2	2.00 ± 0.25
HB3	1.79 ± 0.16
O(w1)-Li	1.95 ± 0.09
O(w3)-Li	1.92 ± 0.07
nitrate O-Li	1.91 ± 0.08

The vibrational features associated to the small clusters are calculated from the VDOS and reported in Fig. 4.8. In the frequency range $3000\text{--}3800\text{ cm}^{-1}$, each water molecule has two vibrational bands. In addition to the free OH peak at 3700 cm^{-1} , we see that the HB band is characterized by quite strong *red-shifted* peaks around 3200 cm^{-1} . These red-shifted peaks are associated to water molecules which are bound either to the cation or to both cation and anion and are different with respect to the peaks associated to the water molecules which only bound to the nitrate in the simple cluster $[\text{NO}_3 \cdot (\text{H}_2\text{O})_3]^-$ (3430 cm^{-1} , see Fig. 4.2).

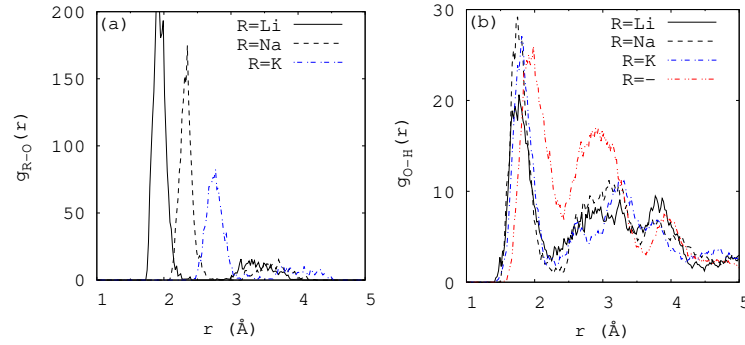


FIGURE 4.6: (a)RDF g_{R-O} for clusters $\text{RNO}_3(\text{H}_2\text{O})_3$ ($\text{R} = \text{Li}, \text{Na}, \text{K}$); (b)RDF g_{O-H} for clusters $\text{RNO}_3(\text{H}_2\text{O})_3$ and $[\text{NO}_3 \cdot (\text{H}_2\text{O})_3]^-$ (no alkali metal cation, denoted as "R=").

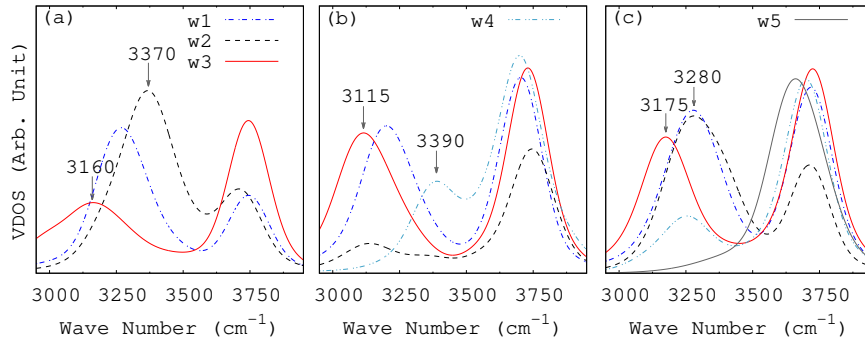


FIGURE 4.7: VDOS for each water molecule in the cluster $\text{LiNO}_3(\text{H}_2\text{O})_n$: (a) $n = 3$; (b) $n = 4$; (c) $n = 5$. w1: H_2O bound to Li and H_2O ; w2: H_2O bound to nitrate and H_2O ; w3: H_2O bound to Li and nitrate; w4: H_2O bound to H_2O ; w5: H_2O only bound to Li.

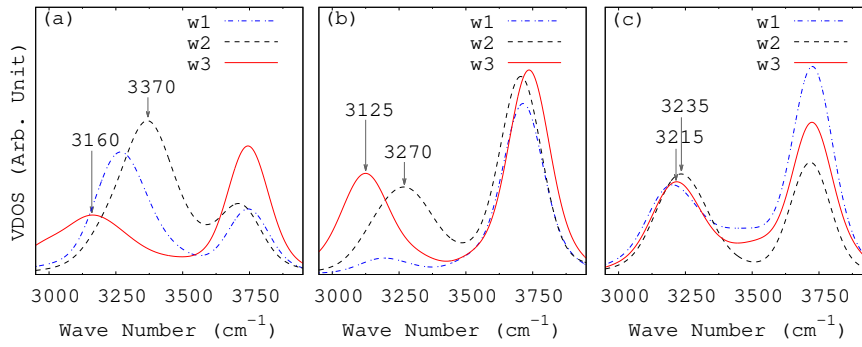


FIGURE 4.8: VDOS for H_2O in clusters (a) $\text{LiNO}_3(\text{H}_2\text{O})_3$, (b) $\text{NaNO}_3(\text{H}_2\text{O})_3$ and (c) $\text{KNO}_3(\text{H}_2\text{O})_3$. w1: H_2O bound to R and H_2O ; w2: H_2O bound to nitrate and H_2O ; w3: H_2O bound to R and nitrate.

To explore the effect of adding some additional water molecules to the cluster, we considered the clusters $\text{RNO}_3(\text{H}_2\text{O})_n$ ($n=4, 5$; $\text{R}=\text{Li}, \text{Na}, \text{K}$). The most stable configurations are shown in Fig. 4.1 (c) and (d), and the corresponding VDOS for the water molecules are shown in Fig. 4.7 (b) and (c) for the clusters $\text{LiNO}_3(\text{H}_2\text{O})_n$ ($n=4$ and 5). We find that the OH stretching peaks in the HB region are also quite red-shifted. The red shift is particularly strong for the water molecules which are directly interacting with the Li and those which are simultaneously bound to the Li and to the nitrate O's (e.g. w3).

We also calculate the effects of other alkali metal cations, namely Na^+ and K^+ . The calculated VDOS for water molecules in clusters $\text{NaNO}_3(\text{H}_2\text{O})_3$ and $\text{KNO}_3(\text{H}_2\text{O})_3$ are shown in Fig. 4.8 (b) and (c), respectively. As in the case of $\text{LiNO}_3(\text{H}_2\text{O})_3$, the HB bands are also characterized by red-shifted peaks around 3200 cm^{-1} . In addition, the peaks in the OH-stretching region are also compatible with infrared predissociation (IRPD) spectra which have been recorded for the $[\text{Li} \cdot (\text{H}_2\text{O})_{3-4} \text{Ar}]^+$ clusters [155–157] and for $[\text{Na} \cdot (\text{H}_2\text{O})_{4-7}]^+$ and $[\text{K} \cdot (\text{H}_2\text{O})_{4-7}]^+$ clusters, [158] although there no nitrate is present and only the effect of the cation was investigated.

To summarize, the vibrational spectra from the clusters clearly point to red-shifted peaks which are not recorded in the vibrational sum-frequency generation spectra at the water/vapor interface for the LiNO_3 solution. In other words, these clusters are not really representative of the solvation structures presents in the LiNO_3 solution. Therefore, these small clusters cannot be directly used to describe the topmost layer of the LiNO_3 solution, and we need to build more realistic models to capture the main features the interface. In particular, according to the cluster picture one would be tempted to rule out the possibility of a contact ion pair at the interface.

Chapter 5

VSG spectroscopy of water/vapor interface and solution/vapor interfaces

In Chapter 4, we investigated the VDOS for water clusters containing nitrate ions and alkali metal ions. We found that small clusters cannot be directly used to model interfaces of aqueous solutions, and we need to build more realistic ones to capture the main features of interfaces. In this chapter, we will analyze the structure and dynamics of salty solutions containing an alkali cation and a nitrate (iodide) ion and to provide a microscopic interpretation of recent experimental results. [133–135]

The goal of this chapter is to find the origin of the main characteristics of the VSG spectra of the LiNO_3 solution, and provide a molecular picture to interpret the recorded spectra. To achieve this goal, we simulate a water/vapor interface including Li^+ and NO_3^- , as shown in Fig. 5.1, and extract the vibrational spectroscopic properties of the water/vapor interface of LiNO_3 solution.

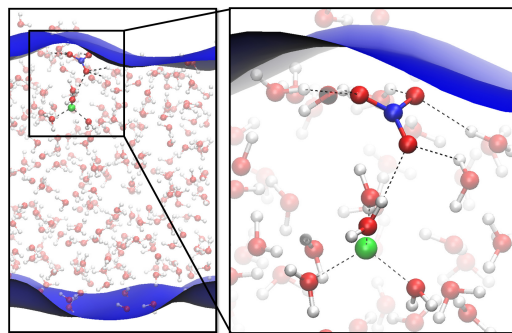


FIGURE 5.1: The salty water interface of LiNO_3 solution (top) and the water/vapor interface (bottom). The right panel shows that the Li^+ and the NO_3^- ions are separated by a water molecule at the salty interface.

We consider a model for the interface where a slab of 256 water molecules containing one Li^+ and one NO_3^- ($\text{LiNO}_3(\text{H}_2\text{O})_{256}$) is included in a periodic simulation box of $19.70 \times 19.70 \times 40.00 \text{ \AA}^3$ at 300 K. The slab is 20 \AA thick and infinite in the x and y direction, while the separation between the periodic slabs in the z direction is 20 \AA . The LiNO_3 was inserted at one of the two interfaces, with the NO_3^- residing in the topmost layer and the Li^+ residing somewhat deeper at about 5 \AA from the surface. In this way we have a model with one *salty* interface and one *neat* interface which can be used as a reference. To provide the interpretation to the above experimental results, the following analysis tools are used: (1) VDOS; (2) calculation of the nonlinear susceptibility; (3) reconcile of the interface and cluster picture. In paragraph 5.1, the

VSFG spectroscopy of the alkali nitrate interfaces of aqueous solutions is calculated, to find the connection between these two kind of models: the interface and cluster picture. Additionally, to study the effect of cations, the interfaces of alkali-iodine solutions are also studied in paragraph 5.2.

5.1 VSFG spectra of the interface of LiNO_3 aqueous solutions

It has been often put forward the idea that in nitrate solution anion and cation are paired at the interface and form a double layer. Based on the relatively high propensity of NO_3^- for the interface [56, 159] we decided to start the simulations with the anion at the water surface and to investigate the possibility that LiNO_3 forms a stable water-separated ion pair at the interface. The idea that nitrate anions form water-separated pair where the Coulomb interaction is shielded was already suggested for divalent cation nitrate. [56] The first result is that such model system is stable and the NO_3^- remains within the topmost water layer during all the simulation time. This result can be found in the probability distribution along z -axis of the simulation box, as shown in Fig. 5.2. This is in agreement with previous simulation results based on polarizable classical force field [160] and also with some DFTMD work on nitric acid, which was also found stable at the interface. [161] Moreover, the Li^+ remains relatively close to the surface, in a water sub-layer forming a water separated ion pair with the NO_3^- at the interface.

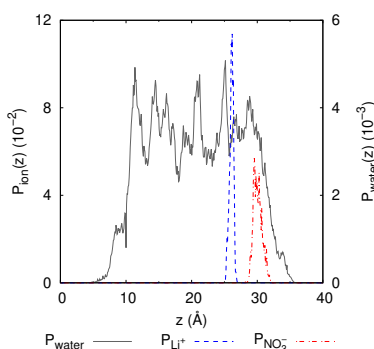


FIGURE 5.2: Probability distributions of ions and water molecules for LiNO_3 water interface along the normal direction.

We have calculated the susceptibility for the two interfaces, namely the one containing the LiNO_3 pair (salty interface) and the neat one which does not include any ion. The calculated imaginary part is reported in panel (a) and the intensity in panel (b) of Fig. 5.3. The calculated intensity spectra show a depletion of the 3200 cm^{-1} region as in the experiments. The same feature is also shown in the imaginary part. Also the calculated spectra show that the free OH region is less intense in the salty interface with respect to the water/vapor interface.

To find the microscopic origin of the depression of the lower frequency region, we have also decomposed the salty water interface VDOS into the contributions coming from the different water molecules.

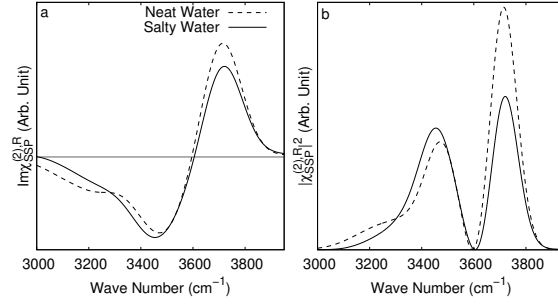


FIGURE 5.3: (a) The $\text{Im}\chi_{SSP}^{(2),R}$ and (b) $|\chi_{SSP}^{(2),R}|^2$ for water molecules at the interface of LiNO_3 solution.

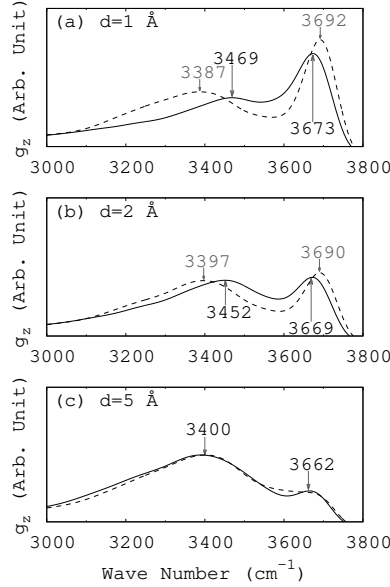


FIGURE 5.4: VDOS $g_z(\nu)$ of water molecules at the interface of LiNO_3 solution (solid line) and at the water/vapor interface (dashed line). (a): $d = 1 \text{ \AA}$; (b): $d = 2 \text{ \AA}$; (c): $d = 5 \text{ \AA}$.

The VDOS $g_z(\nu)$ for the water molecules at the interface, which is calculated from the Fourier Transform (FT) of the auto-correlation function of velocity of the atoms in the z-axis projection, gives a rough value of the thickness of the interface d . Using 1, 2 and 5 \AA thicknesses, we have defined three different interfacial regions. For the LiNO_3 solution, $g_z(\nu)$ of the salty and neat water interfaces in the slab is reported in Fig. 5.4. When $d = 1 \text{ \AA}$, water molecules at the solution surface have lower free OH stretching frequency than that in pure water. This means that there are less water molecules with free OH stretch at the interface of LiNO_3 solution than at the water-vapor interface. It compares very well with the experimental result of the surface propensity of nitrate anions in water solution. [133] Meanwhile, compared to the result of pure water, the H-bonded band of the VDOS for the salty interface has a blue shift of $\Delta\nu \approx 80 \text{ cm}^{-1}$. As we increase the value of d , the difference between pure water and salt water VDOS is gradually reduced. For example, when $d = 2 \text{ \AA}$, the amount of blue shift $\Delta\nu$ is reduced to 55 cm^{-1} (Fig. 5.4 (b)); when $d = 5 \text{ \AA}$, the amount of blue shift is almost zero (Fig. 5.4 (c)). This indicates that the ions' (Li^+ , Na^+ , K^+ and NO_3^-) effects can be found only on the water molecules in the top $\sim 5\text{-}\text{\AA}$ layer of the interface. As the thickness of the interfacial water layer included in $g_z(\nu)$ increases, the free OH signal is depressed and at the same time the H-bonded OH

bands for the salty and neat water interfaces become more similar.

To explore the reason for the blue shift of the H-bonded OH stretch in the interface system, we also calculated the VDOS $g(\nu)$ for the 6 water molecules in the subsystems $\text{NO}_3^-(\text{H}_2\text{O})_6$ (The structure of this cluster is shown in Fig. 5.1). Compared to the VDOS for H-bonded water molecules at the water-vapor interface, a blue shift of $\Delta\nu' \approx 80 \text{ cm}^{-1}$ on the vibrational modes of water molecules is found at the interface (Fig. 5.5). It indicates that a HB with nitrate acceptor is weaker than that with water acceptor, since the amount of O–H frequency shift reflects the strength of the H-bonds[127, 162]. This feature agrees with experimental result obtained by Jubb et.al. [134] The OH stretching band at 3394 cm^{-1} (300 K) also agrees with that of liquid pure water (3400 cm^{-1} . [163]) Since the value of $\Delta\nu'$ is almost equal to the value of $\Delta\nu$ at $d = 1 \text{ \AA}$, we conclude that the blue shift of the VDOS at the salty water interface is mainly caused by the H-bonds between the uppermost nitrate and water molecules at the salty interface.

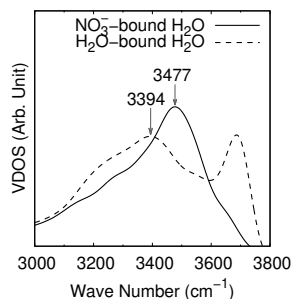


FIGURE 5.5: VDOS for 6 water molecules bound to NO_3^- at the LiNO_3 solution/vapor ($\text{LiNO}_3/\text{vapor}$ for short) interface (salty water) and that for 15 water molecules at the top layer ($d=1 \text{ \AA}$) of the neat water.

First, there are two reasons to support the view that NO_3^- is located at the top layer of the surface. (1) The reduced intensity of the free OH peak can be explained by that NO_3^- is at the surface. The 3700 cm^{-1} -peak is the character of free OH stretch in water molecules with their dipole moment pointing to the vapor phase. [39, 164] NO_3^- binds to water molecules from the water surfaces which have less free OH, therefore reduce the intensity of the free OH peak. (2) Those water molecules directly H-bonded to the NO_3^- ion show an higher frequency band with respect to the neat water at the interface, which explain the increased intensity of the 3400 cm^{-1} band.

Second, the statement that Li^+ and NO_3^- are separated is confirmed by Ref. [165, 166], which show that the alkali metal cations are of *small* composite partition coefficients ($k_{p,K^+} = 0.00 \pm 0.03$, $k_{p,\text{Na}^+} = 0.05 \pm 0.17$, $k_{p,\text{Li}^+} = 0.14 \pm 0.18$), i.e., these cations are more surface-excluded than NO_3^- ($k_{p,\text{NO}_3^-} \approx 1.0$). How do we reconcile the interface picture and the cluster picture? In the small clusters (with 3, 4 and 5 water molecules) the contact ion pair is the most stable configuration, while at the interface the water *separated* configuration is the most stable. This suggests that a sufficiently large number of water molecules is required to stabilize a water separated ion pair where the NO_3^- anion still reside at the surface. To verify this idea we extracted a relatively large cluster with 30 water molecules from the full interface, centered around the Li^+ ion and we simulate it in the gas phase. For this medium size cluster we calculated the free energy difference between the water separated and the contact ion pair. The details of the calculation is given in Appendix D.1. The blue-moon ensemble method [167–169] is used to calculate the free energy as a function of a

parameter: the distance r between alkali metal cation and the nitrogen of NO_3^- in $\text{LiNO}_3(\text{H}_2\text{O})_{30}$. In Fig. 5.6, we find that there are two minima in the free energy at $r = 2.9 \text{ \AA}$ (configuration A) and $r = 4.3 \text{ \AA}$ (configuration B). Li^+ and NO_3^- are bonded in configuration A, but are water-separated in configuration B. The free energy difference $\Delta F_{AB} = F_A - F_B = 0.3 \text{ kcal/mol}$. The energy barrier between C and A (B) is: $\Delta F_{CA} = 1.2 \text{ kcal/mol}$ ($\Delta F_{CB} = 1.5 \text{ kcal/mol}$). Configuration B is more stable than A. For the water molecules in interface system, NO_3^- resides on the surface and Li^+ in the layer below, separated from NO_3^- by water molecules. Therefore, no obvious red-shift induced by alkali metal cation and nitrate is obtained in the VSFG spectrum. Our results show that as the number of waters increases, the first solvation shell around the Li^+ is stabilized and the water separated ion pair is equally stable as the contact ion.

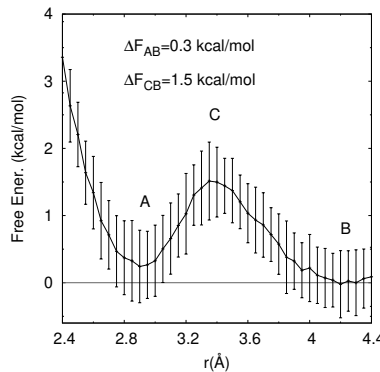


FIGURE 5.6: Free energy profile with respect to the distance r between Li^+ and the nitrogen in NO_3^- in the cluster $\text{LiNO}_3(\text{H}_2\text{O})_{30}$. A: configuration A where $r = 2.9 \text{ \AA}$; B: configuration B where $r = 4.3 \text{ \AA}$; C: the transition states.

Finally, in the salty interface, one single water is constantly shared between the Li^+ and the NO_3^- and indeed this water shows a vibrational peak with a very pronounced red shift. This clearly reminds the water peak we already observed in the small clusters, however if the full interface is considered its signature do not emerge from the spectra, as it can be seen in Fig. 5.3.

From the three arguments above, our conclusion is thus that in the VSFG spectra we do only see the changes induced by the NO_3^- at the interface. This points to a clear 3400 cm^{-1} band in the vibrational spectra. The Li^+ resides in the sub-layer forming a water separated ion pair at the interface.

Until now, we have analyzed the behaviour of a salty interface containing LiNO_3 . Both the measured and calculated VSFG spectra show a reduced intensity of the lower frequency portion of the HB region, namely around 3200 cm^{-1} , when compared to the water/vapor interface. This reduction can be attributed to the H-bonds which are established between the NO_3^- and the surrounding water molecules at the interface. This effect is only related to the presence of NO_3^- at the water surface and is not affected by the presence of Li^+ ions. Indeed we have shown that although Li^+ can reside relative close to the water surface, also forming a water mediated ion pair with NO_3^- , its effect on the VSFG spectrum is not visible. The water which mediate the interaction between the NO_3^- and Li^+ would produce a red-shifted peak in small water cluster, but its influence is not visible neither in the calculated or the measured VSFG spectra. We have also shown that the very simple models, such as small clusters are not suitable to reproduce the experimental spectra and cannot provide a microscopic interpretation of the spectra. A realistic model of the interface is required to address

the perturbation of the ion on the water surface. Besides, how do other ions, such as Li^+ , Na^+ , and K^+ , etc., affect the VSFG spectra of the interface? To test our method and explain the experimental observations, we constructed the interface of lithium iodide, sodium iodide, and potassium iodide solutions and calculated the VSFG spectra. Experiments have proved that iodide ions have similar properties to nitrate ions in many aspects. For example, they tend to interface and are easily polarized. On the other hand, when we analyze the effects of cations, the model containing iodide ions is more simplified than the model containing nitrate ions.

5.2 VSFG spectra of the interface of alkali iodine aqueous solutions

Direct investigations of the dynamics of simple ions, such as I^- and Br^- , at water interfaces, by the x-ray photoelectron spectroscopy [170] and MD simulations [55, 171] have shown that these ions could accumulate at the interface. To provide a molecular interpretation of the recorded spectra we perform here *ab initio* molecular dynamics simulation of salty solutions containing alkali cations and iodine.

A model for the electrolyte solution/vapor interface is built, in which a slab of 118 water molecules containing two Li^+ cations and two I^- anions is included in a period simulation box of $15.60 \times 15.60 \times 31.00 \text{ \AA}^3$ at 330 K. This model corresponds to a 0.9 M solution. The slab is about 20 \AA thick and infinite in the x and y direction, while the separation between the periodic slabs in the z direction is about 20 \AA . In the initial configuration, the LiI was inserted at one of the two interfaces, with the I^- residing in the topmost layer and the Li^+ residing somewhat deeper at about 5 \AA from the surface. Using the same method, we also constructed interface models of NaI solution and KI solution for DFT simulations. In all the cases the systems were equilibrated for 30 ps and then a production time of 60 ps was considered for the analysis.

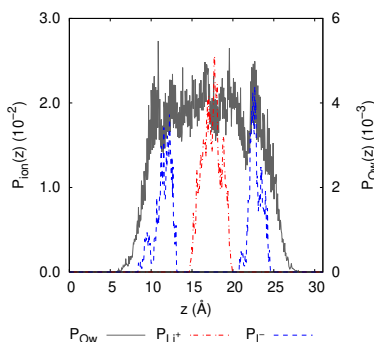


FIGURE 5.7: Probability distributions $P(z)$, along the normal direction (z -axis), of Li^+ , I^- and O in LiI solution/vapor interface.

Structural Properties First, we have calculated the probability distributions of Li^+ , I^- and O with respect to the normal direction (z -axis) of the LiI solution surface. The results are given by Fig. 5.7, where we see that I^- anions prefer to be located at the surface of the solution, while the Li^+ cations prefer to stay below the surface. This result is consistent with the calculations from Ishiyama and Morita [60, 63] on a similar system.

The effects of Li^+ and I^- on the organization of water molecules are shown in Li–water (Fig. 5.8 (a)) and I–water RDFs (Fig. 5.8 (b)), respectively. In Fig. 5.8, the

first two peaks of $g_{\text{Li-O}_w}$ and $g_{\text{Li-H}_w}$ are located at 1.97 Å and 4.12 Å, and, 2.61 Å and 4.73 Å, respectively. Here we consider the *difference* δ_1 between the first peaks' positions of $g_{\text{X-O}}$ and $g_{\text{X-H}}$. Thus, one can determine the differences of the peaks' positions, which are shown in Table 5.1. The difference δ_1 between the first peaks, 0.67 Å, is shorter than the OH group length R_{OH} in a water molecule which is about 0.98 Å, i.e.,

$$\delta_1 < R_{\text{OH}}. \quad (5.1)$$

This relation reflects that all the water molecules around the Li^+ have their O atom facing Li^+ . Similarly, we find from Fig. 5.8 (b) that the distance δ_1 between the first peaks of the two RDFs is 0.93 Å, and it can be seen that δ_1 is slightly equal to R_{OH} , i.e.,

$$\delta_1 \approx R_{\text{OH}}. \quad (5.2)$$

This shows that for the water molecules around the I^- , only one H atom forms an I-H bond with the I^- . This relation also implies that I^- is essentially at the outermost layer of the solution interface. This is consistent with many of the previous results from MD simulations [52, 172] and experimental results for the increase in surface tension relative to neat water for aqueous solutions of sodium halide salts.[53, 173–175]

TABLE 5.1: Peaks of $g_{\text{Li-O}}$ and $g_{\text{Li-H}}$ for the LiI solution. (unit:Å, the same below)

$g_{\text{Li-O}}$	$g_{\text{Li-H}}$	δ_1
1.97	2.64	0.67
4.12	4.73	0.61
6.13	6.93	0.80

TABLE 5.2: Peaks of $g_{\text{Na-O}}$ and $g_{\text{Na-H}}$ for the NaI solution.

$g_{\text{Na-O}}$	$g_{\text{Na-H}}$	δ_1
2.41	3.02	0.61
4.55	4.96	0.41
6.48	7.20	0.72

TABLE 5.3: Peaks of $g_{\text{K-O}}$ and $g_{\text{K-H}}$ for the KI solution.

$g_{\text{K-O}}$	$g_{\text{K-H}}$	δ_1
2.84	3.40	0.56
4.71	5.51	0.80
6.78	7.49	0.71

For NaI and KI interfaces, the effects can be seen from Fig. 5.9 and 5.10. For Na^+ and K^+ , the relation $\delta_1 < R_{\text{OH}}$ remains, i.e., $\delta_1 = 0.61$ Å for Na^+ and $\delta_1 = 0.56$ Å for K^+ . For iodide ions, the relation $\delta_1 \approx R_{\text{OH}}$ still holds (See Fig. 5.9 (a) and 5.10 (a), and Table 5.2 and 5.3). For I^- in NaI interface, $\delta_1 = 0.96$ Å; and for I^- in KI interface, $\delta_1 = 0.94$ Å (See Fig. 5.9 (b) and 5.10 (b)). Therefore, these structural properties are similar to that in LiI interface, except the larger solvation shells.

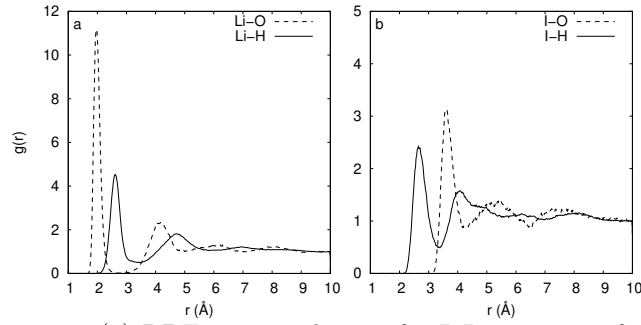


FIGURE 5.8: (a) RDF $g_{\text{Li-O}}$ and $g_{\text{Li-H}}$ for LiI-water interface. The first two peaks of $g_{\text{Li-O}}$ and $g_{\text{Li-H}}$: 1.97 and 4.12 Å, and, 2.61 and 4.73 Å, respectively. (b) RDF $g_{\text{I-O}}$ and $g_{\text{I-H}}$ for LiI-water interface. The first two peaks of $g_{\text{I-O}}$ and $g_{\text{I-H}}$: 3.62 and 5.28 Å; and, 2.69 and 4.11 Å, respectively.

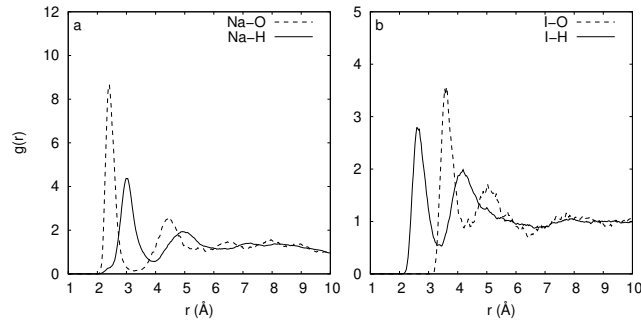


FIGURE 5.9: (a) RDF $g_{\text{Na-O}}$ and $g_{\text{Na-H}}$ for NaI-water interface. The first two peaks of $g_{\text{Na-O}}$ and $g_{\text{Na-H}}$: 2.41 and 4.55 Å, and, 3.02 and 4.96 Å, respectively. (b) RDF $g_{\text{I-O}}$ and $g_{\text{I-H}}$ for NaI-water interface. The first two peaks of $g_{\text{I-O}}$ and $g_{\text{I-H}}$: 3.59 and 5.04 Å; and, 2.63 and 4.15 Å, respectively.

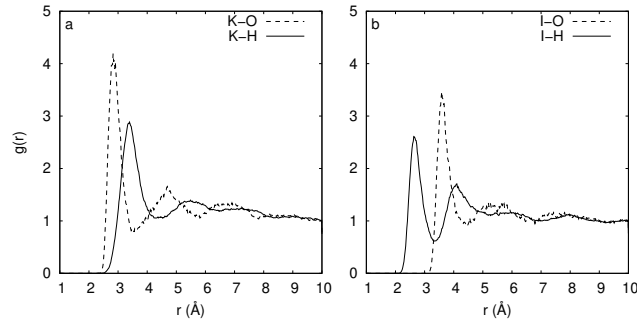


FIGURE 5.10: (a) RDF $g_{\text{K-O}}$ and $g_{\text{K-H}}$ for KI-water interface. The first two peaks of $g_{\text{K-O}}$ and $g_{\text{K-H}}$: 2.84 and 4.71 Å, and, 3.40 and 5.51 Å, respectively. (b) RDF $g_{\text{I-O}}$ and $g_{\text{I-H}}$ for KI-water interface. The first two peaks of $g_{\text{I-O}}$ and $g_{\text{I-H}}$: 3.59 and 5.43 Å; and, 2.65 and 4.10 Å, respectively.

VSG spectra The calculated VSG spectra for LiI, NaI and KI interfaces, are shown in Fig. 5.11 to 5.13. In all the cases there is one free OH stretching band (3600–3800 cm^{-1}) and one bonded OH stretching band (3000–3600 cm^{-1}). For all the three cations the sign of $\text{Im}\chi^{(2),\text{R}}$ is positive for the free OH peak while it is negative in the hydrogen bonded region. This result is consistent with the VSG spectrum calculated in paragraph 5.1, i.e., (1) the anion–water H-bonds at interfaces decrease the amount of free stretching OH bonds (2) the free stretching peak in the intensity of VSG

decrease and the H-bonded stretching peak is shifted at the interfaces of LiNO_3 (or alkali-iodine) solution.

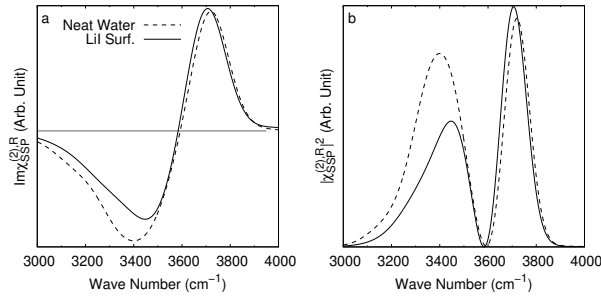


FIGURE 5.11: (a) $\text{Im}\chi_{SSP}^{(2),R}$ and (b) $|\chi_{SSP}^{(2),R}|^2$ of the interface of the LiI solution (solid line) and the water/vapor interface (dashed line). The data for the water/vapor interface is calculated from the DFTMD simulation for the water interface with the same thickness (5 Å) (the same below).

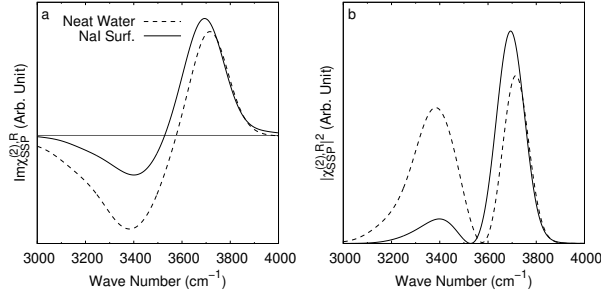


FIGURE 5.12: (a) $\text{Im}\chi_{SSP}^{(2),R}$ and (b) $|\chi_{SSP}^{(2),R}|^2$ of the interface of the NaI solution (solid line) and the water/vapor (dashed line) interface.

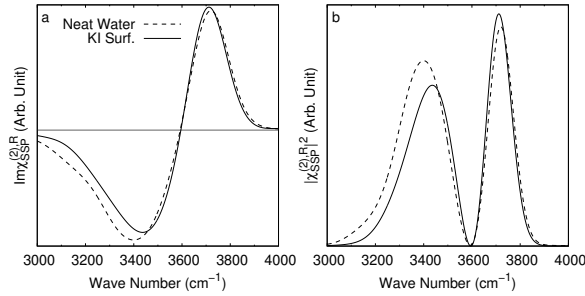


FIGURE 5.13: (a) $\text{Im}\chi_{SSP}^{(2),R}$ and (b) $|\chi_{SSP}^{(2),R}|^2$ of the interface of the KI solution (solid line) and the water/vapor interface (dashed line).

Compared with the water/vapor interface, the OH-bonded peak of $|\chi_{SSP}^{(2),R}|^2$ for the NaI solution is blue-shifted, which is consistent with experimental results on the NaI solution. [28, 54, 134, 176] The H-bonded OH-stretching peak of $|\chi_{SSP}^{(2),R}|^2$ for LiI and KI solutions are also blue-shifted. These results support the idea that I^- is a strong structure-breaking anion. Secondly, the bonded OH-stretching region of the NaI solution is narrower than that of pure water. This result has also been obtained for the interface of LiNO_3 solution. The retained high frequencies of these bonded OH-stretching peaks indicate that these molecules at the interfaces of these solutions are participating in weak H-bonding. The introduction of I^- salts, caused a slight

decrease in the strong H-bonding region at 3200 cm^{-1} and relatively an increase in the weak H-bonding region at 3400 cm^{-1} . This result is consistent with experimental results in Ref. [134, 176].

Because of surface isotropy of the solutions, [177] the $\chi_{SSP}^{(2),R}$ can be calculated either through $\chi_{XXZ}^{(2),R}$, or $\chi_{YYZ}^{(2),R}$. In our simulation, both of them give very similar results. Here we report the comparison between $\text{Im}\chi_{XXZ}^{(2),R}$ and $\text{Im}\chi_{YYZ}^{(2),R}$ for the KI solution in Fig. 5.14. They should be very close to each other, because the interfaces have rotational symmetry about the z-axis. It can be seen that indeed the calculated spectra are very close to each other. From the results of the nonlinear susceptibilities, we conclude that water molecules at the interfaces of the LiI, NaI, and KI solutions are participating in weaker H-bonds, compared with those at the water/vapor interface. The simulation results permit to interpret the features present in the experimental spectra, which can be explained as consequence of the double layer formed by I^- ions on the topmost water layer and the alkali in the sublayer (bulk in our relatively small simulation box).

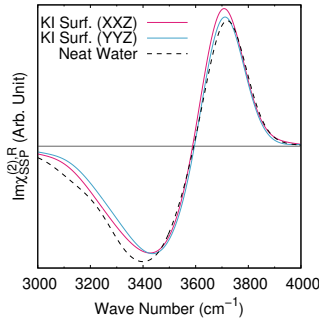


FIGURE 5.14: $\text{Im}\chi_{XXZ}^{(2),R}$ and $\text{Im}\chi_{YYZ}^{(2),R}$ spectra for the whole KNO_3 interface of aqueous solution.

In view of the close relationship between the HB network and the VSFG spectra of the solution interface, we will continue to study the properties of the water/vapor interface and the solution/vapor interface from the perspectives of HB dynamics and reorientation of water molecules in Chapters 6 and 7.

Chapter 6

Hydrogen bond dynamics at water/vapor interfaces

Hydrogen bonds play a critical role in the behaviour of bulk water,[21, 178, 179] water near interfaces,[180] and aqueous solutions. [181] There are many methods to study the HB dynamics in water, solutions or interfaces, such as molecular dynamics simulation,[180, 182–185] neutron scattering, IR spectroscopy,[186, 187] etc. In this chapter, we will introduce the general concepts and methods of HB dynamics [178, 188, 189] used to analyze the structure and dynamic properties of bulk water and the water/vapor interface.

6.1 Definitions of HB population and correlation functions

Luzar and Chandler [188] have pioneered the analysis of the HB dynamics of pure water, and subsequently such analysis has been also extended to more complex systems, e.g., electrolytes, [150] protein and micellar surfaces. [190] There are temporal, geometric[191] and energetic criteria [192] to define HB. Here we use the geometric one. Two water molecules are H-bonded if their interoxygen distance between of specific tagged pair of water molecules is less than cutoff radius r_{OO}^c and the O-H \cdots O angle is less than cutoff angle ϕ^c . [153, 154, 193] The value r_{OO}^c corresponds to the first-minimum position of the O–O Radial Distribution Function (RDF) of water. [192] The choice for the cutoff angle ϕ^c for water-water molecules is obtained by studying the average number of H-bonds, as a function of ϕ^c . [194] We call this definition of HB the Acceptor-Donor-Hydrogen (ADH) criterion. To compare the impact of different HB definitions on HB dynamics, we also use another definition of HB in our analysis. When the distance between the oxygen atoms of two water molecules is less than r_{OO}^c , and the oxygen-hydrogen-oxygen included angle is greater than cutoff angle θ^c , then we say that there is a HB between the two molecules. We denote this definition as the Acceptor-Hydrogen-Donor (AHD) criterion. In this thesis, we use $r_{\text{OO}}^c = 3.5\text{\AA}$ both for ADH and AHD criteria, $\phi^c = 30^\circ$ for ADH criterion, and $\theta^c = 120^\circ$ for AHD criterion.

The configuration criterion above allows us to define a variable $h[r(t)] = h(t)$, the HB population. Here an instantaneous configuration $r(t)$ denotes the positions of all the atoms in the system at time t . [188] The $h(t)$ has a value 1 when the particular tagged pair of molecules are bonded, and 0 otherwise. The fluctuation or deviation in a dynamical variable $A(t)$ from its time-independent equilibrium average $\langle A \rangle$, is defined by [189]

$$\delta A = A(t) - \langle A \rangle.$$

Since the probability that a specific pair of molecules is bonded in a large system is extremely small, i.e., the time average of h is zero, or $\langle h \rangle = 0$, then

$$\delta h(t) = h(t).$$

Therefore, $h(t)$ describe the fluctuation $\delta h(t)$ of the HB population.

While the equilibrium average of $\delta h(t)$ is zero, we can obtain useful information by considering the equilibrium correlations between fluctuations at different times. The correlation between $\delta h(t)$ and $\delta h(0)$ can be written as

$$\langle \delta h(0) \delta h(t) \rangle = \langle h(0) h(t) \rangle - \langle h \rangle^2 = \langle h(0) h(t) \rangle,$$

where the averaging $\langle \dots \rangle$ is to be performed over the ensemble of initial conditions.

In this paragraph, we will use the following three correlation functions to describe the HB dynamics of the water/vapor interface: the HB population auto-correlation function $C_{\text{HB}}(t)$, the continuum HB population correlation function (survival probability) $S_{\text{HB}}(t)$ and the reactive flux $k(t)$. [195]

HB population auto-correlation function $C_{\text{HB}}(t)$ We use the auto-correlation function $C_{\text{HB}}(t)$ ($c(t)$ for short) of the HB population to describe the structural relaxation of H-bonds:

$$C_{\text{HB}}(t) = \langle h(0) h(t) \rangle / \langle h \rangle. \quad (6.1)$$

With the aid of the ergodic principle, the ensemble average $\langle \dots \rangle$ is implemented by time average. The $\langle h \rangle$ is the probability that a pair of randomly chosen water molecules in the system is H-bonded at any time t . As examples, the dynamics of the interoxygen distance $r_{\text{OO}}(t)$, the cosine of H–O \cdots O angle $\cos\phi(t)$ and the $h(t)$ for a HB in a DFTMD simulated water cluster $(\text{H}_2\text{O})_n$ ($n=5$) at 300 K is displayed in Fig. 6.1, respectively.

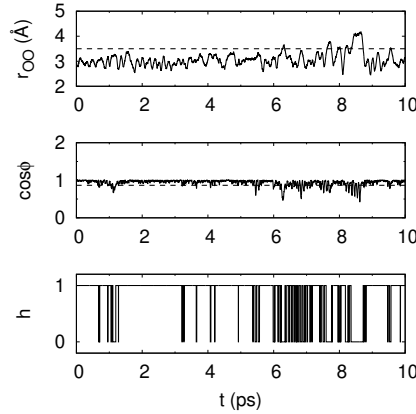


FIGURE 6.1: Dynamics of $r_{\text{OO}}(t)$ (top panel), $\cos\phi(t)$ (middle panel), and $h(t)$ (bottom panel) for a typical HB in a water cluster. The dashed lines show the interoxygen distance boundary $r_{\text{OO}}^c = 3.5 \text{ Å}$ (top panel) and criterion of cosine of H–O \cdots O angle $\cos\phi^c$ with $\phi^c = 30^\circ$ (middle panel), respectively.

In a large system that consist of many water molecules, the probability that a specific pair of water molecules are H-bonded is extremely small. Therefore, the $C_{\text{HB}}(t)$ relaxes to zero, when t is large enough. The $C_{\text{HB}}(t)$ measures correlation in $h(t)$ independent of any possible bond breaking events. This function is similar to

one of the intermittent HB correlation functions, introduced by Rapaport,[195] and can be studied by a continuous function, probability densities. From $C_{\text{HB}}(t)$, the HB relaxation time can be computed by

$$\tau_{\text{R}} = \frac{\int t C_{\text{HB}}(t) dt}{\int C_{\text{HB}}(t) dt}. \quad (6.2)$$

The $C_{\text{HB}}(t)$ for the simulated bulk water is shown in Fig. 6.3 (For computational details, see Appendix B). We can obtain the relaxation time from Eq. 6.2: $\tau_{\text{R}} = 14.01$ ps for ADH definition, and $\tau_{\text{R}} = 14.16$ ps for AHD definition.

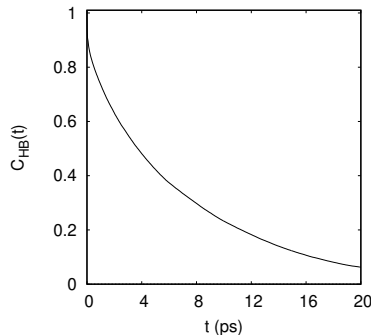


FIGURE 6.2: Time dependence of $C_{\text{HB}}(t)$ for the simulated bulk water at 300 K with density $\rho = 1.00$ g/cm³.

The method of water-water pair based HB dynamics used in this section has been frequently used in previous literature.[150, 188, 196] The basis is the population operator $h(t)$ of the HB formed between two water molecules. The function $C_{\text{HB}}(t)$ is interpreted as the probability that the HB between a certain pair of water molecules is intact at time t , if the pair of water molecules are H-bonded at time zero.

Besides $h(t)$, here we also discuss the definition of another possible definition of the HB population operator $\tilde{h}(t)$. When a pair of water molecules a and b are H-bonded, the oxygen atom in each water molecule can act both as a donor and an acceptor. In particular, a pair of water molecules can form 4 different forms of H-bonds. In other words, if the role of H atoms between the pair of water molecules changes, but they still form H-bonds, we think that an old HB is broken and a new HB is formed. The calculated results of the correlation functions (still denoted by $C_{\text{HB}}(t)$) of $\tilde{h}(t)$ of water molecules in bulk water is shown in Fig. 6.3. Comparing Fig. 6.2 and Fig. 6.3, we found that there are some differences in the correlation functions of the two definitions $h(t)$ and $\tilde{h}(t)$, because hydrogen exchange is considered in the O–H pair-based HB population $\tilde{h}(t)$, but not in the water–water pair-based HB population $h(t)$. In Fig. 6.3, we plotted $C_{\text{HB}}(t)$ for bulk water, using ADH and AHD criteria of HB. We found that the difference from different choice of HB population is not affected by the HB criteria. In the following, we will use the HB population $h(t)$ based on molecular pairs, i.e., water–water molecule pairs, or ion–water molecule pairs, unless otherwise specified.

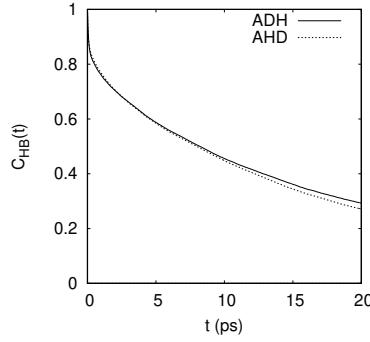


FIGURE 6.3: The $C_{\text{HB}}(t)$ for bulk water, as computed from the ADH (solid line) and AHD (dashed line) criterion of H-bonds. Ref:[197]

Because the thermal motion can cause distortions of H-bonds from the perfectly tetrahedral configuration, water molecules show a librational motion on a time scale of ~ 0.1 ps superimposed to rotational and diffusional motions (> 1 ps), which causes a time variation of interaction parameters. A new HB population $h^{(d)}(t)$ was also defined to obviate the distortion of real HB dynamics due to the above geometric definition. [150, 192] The $h^{(d)}(t)$ is 1 when the interoxygen distance of a particular tagged pair of water molecules is less than $r_{\text{OO}}^c = 3.5$ Å at time t and 0 otherwise. The difference between the operators $h^{(d)}(t)$ and $h(t)$ is that those molecular pairs that meet the condition of $h^{(d)}(t) = 1$ may not meet the condition of $h(t) = 1$. That is, the H-bonds between the tagged molecular pairs that satisfy the condition $h^{(d)}(t) = 1$ may have been broken, but they may more easily form H-bonds again. The function

$$C_{\text{HB}}^{(d)}(t) = \langle h(0)h^{(d)}(t) \rangle / \langle h \rangle \quad (6.3)$$

is the probability that the specific two water molecules are located in reformable region ($r_{\text{OO}} < r_{\text{OO}}^c$) at time t , if they were H-bonded at time zero. The correlation function

$$n(t) = \langle h(0)[1 - h(t)]h^{(d)}(t) \rangle / \langle h \rangle \quad (6.4)$$

represents the probability at time t that a tagged pair of initially H-bonded water molecules are unbonded but remain separated by less than r_{OO}^c . In the above formula, $1 - h(t)$ describes the breaking of a HB at time t after its formation at time $t = 0$.

The probability at time t that a pair of water molecules bonded by H-bonds at the initial moment does not be bonded but the distance between their oxygen atoms is still less than r_{OO}^c is calculated according to

$$n(t) = \int_0^t dt' k_{\text{in}}(t'), \quad (6.5)$$

where $k_{\text{in}}(t) = -\langle \dot{h}(0)[1 - h(t)]h^{(d)}(t) \rangle / \langle h \rangle$ is the restricted rate function.

Continuum HB population correlation function $S_{\text{HB}}(t)$ Another scheme to describe the HB dynamics is the continuum HB population correlation function $S_{\text{HB}}(t)$ ($s(t)$ for short), or survival probability [150] for a newly generated HB. It is defined as

$$S_{\text{HB}}(t) = \langle h(0)H(t) \rangle / \langle h \rangle, \quad (6.6)$$

where $H(t) = 1$ if the tagged pair of molecules, remains *continuously* H-bonded till time t and 0 otherwise. It describes the probability that an initially H-bonded molecular pair remains bonded at all times up to t . [198] The $S_{\text{HB}}(t)$ for the simulated bulk water according to the formula 6.6 is shown in Fig. 6.4.

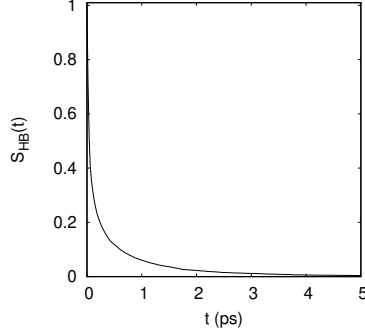


FIGURE 6.4: Time dependence of $S_{\text{HB}}(t)$ for the simulated bulk water at 300 K with density $\rho = 1.00 \text{ g/cm}^3$.

The average continuum HB lifetime $\langle \tau_a \rangle$ is calculated by the integration of $S_{\text{HB}}(t)$ over t (For detailed derivation, see Appendix F.1.) :

$$\langle \tau_a \rangle = \int_0^\infty dt S_{\text{HB}}(t). \quad (6.7)$$

The time derivative of $S_{\text{HB}}(t)$

$$P_a(t) = -\frac{dS_{\text{HB}}(t)}{dt} \quad (6.8)$$

represents the first passage time probability density of H bonds. $P_a(t)$ is also called probability distribution of HB lifetimes, [199–202] or histogram of HB lifetimes.[203, 204] It denotes the probability of the first HB breaking in time t after it has been detected at $t = 0$, i.e.,

$$S_{\text{HB}}(t) = \int_t^\infty P_a(t') dt'. \quad (6.9)$$

Reactive Flux $k(t)$ The rate of relaxation to equilibrium is characterized by the reactive flux correlation function,

$$k(t) = -\frac{dC_{\text{HB}}(t)}{dt}, \quad (6.10)$$

i.e., $\langle j(0)[1 - h(t)] \rangle / \langle h \rangle$, where $j(0) = -dh/dt|_{t=0}$ is the integrated flux departing the HB configuration space at time $t = 0$ (For detailed derivation, see Appendix F.2.). The reactive flux $k(t)$ quantifies the rate that an initially present HB breaks at time t , independent of possible breaking and reforming events in the interval from 0 to t . Therefore, $k(t)$ measures the effective decay rate of an initial set of H-bonds. [189, 205]

We assume that each HB acts independently of other H-bonds, [188, 206] and due to detailed balance condition, we can obtain

$$\tau_{\text{HB}} = \frac{1 - \langle h \rangle}{k}, \quad (6.11)$$

where k is the rate constant of breaking a HB (forward rate constant). [207, 208] For an aqueous interface, the probability of exactly a tagged molecule pair forming a HB is very low, that is, $\langle h \rangle \ll 1$. Therefore, k is related to the average HB lifetime by $\tau_{\text{HB}} = 1/k$. We use k' to represent the rate constant from the HB *on* state to the HB *off* state for a tagged pair of molecules (backward rate constant). Therefore, the reaction time constant τ_{re} is

$$\tau_{\text{re}} = \frac{1}{k + k'}. \quad (6.12)$$

6.2 Dynamical properties of H-bonds in bulk water and at the water/vapor interfaces

The bulk water system and the interface between pure water and vacuum, i.e., the water/vapor interface, are ideal model systems for testing our algorithms. For bulk water, we can compare the results of the method in this paragraph with the results of previous works.[188, 209] After the validation for bulk water, we will show in this paragraph the results of the HB dynamics of the water/vapor interface.

All simulations in this chapter were performed at 300 K within the canonical (NVT) ensemble. The length of the trajectory is 60 ps of physical time. The simulated bulk water consisted of 128 water molecules in a periodic cubic box of length $L = 15.64 \text{ \AA}$, which corresponds to a density of 1.00 g cm^{-3} . The simulated water/vapor interface consisted of 128 water molecules in a periodic box with size $15.64 \times 15.64 \times 31.28 \text{ \AA}^3$.

Correlation functions $c(t)$, $n(t)$ and $k(t)$ First, we calculated the basic structural properties of the simulated bulk water. The RDFs $g_{\text{OO}}(r)$ and $g_{\text{OH}}(r)$ for bulk water system are shown in Fig. 6.5. The correlation functions $C_{\text{HB}}(t)$ from the trajectory

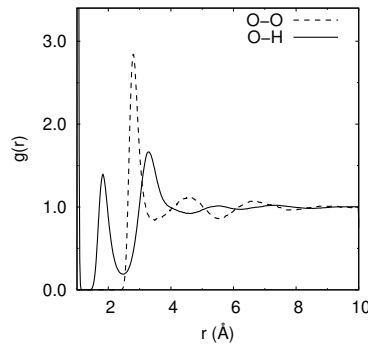


FIGURE 6.5: Partial RDFs of the simulated bulk water.

of a simulation calculated according to formula 6.1 with ADH (solid line) and AHD (dashed line) definition of H-bonds are shown in Fig. 6.6 a. The reactive flux $k(t)$ calculated according to formula 6.10 (see Fig. 6.6b) is very consistent with the result in [210]. For bulk water, there exists a ~ 0.2 -ps transient period, during which $k(t)$ quickly changes from its initial value. [205] However, at longer times, the $k(t)$ is independent of the HB definitions. The calculation results in Fig. 6.6 (b) show that when t is large enough, the difference in $k(t)$ caused by different HB definitions is relatively small. Therefore, the long time decay of $k(t)$ reflects the general properties of H-bonds, and calculating the reactive flux HB correlation functions is a more rigorous way to obtain the nature of H-bonds. [206]

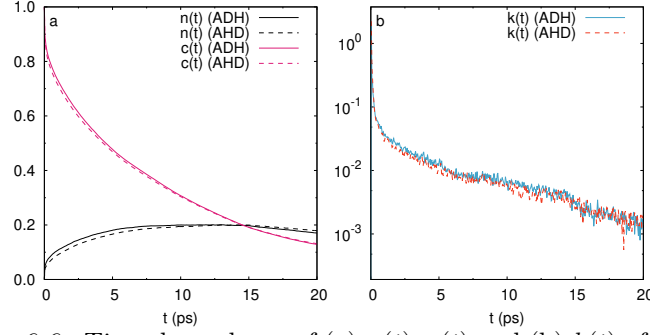


FIGURE 6.6: Time dependence of (a) $n(t)$, $c(t)$ and (b) $k(t)$ of water–water H-bonds for *bulk* water.

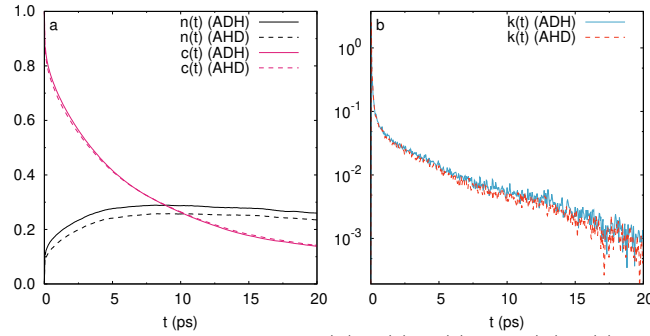


FIGURE 6.7: Time dependence of (a) $n(t)$, $c(t)$ and (b) $k(t)$ of water–water H-bonds for the water/vapor *interface*.

Let's now discuss the result for the water/vapor interface. We reported correlation functions $c(t)$ and $n(t)$ in Fig. 6.7 (a) and the reactive flux $k(t)$ in Fig. 6.7 (b). In both bulk and interface cases, $k(t)$ quickly changes from its initial value on a time scale of less than 0.2 ps. This value can be seen from Fig. 6.8, which redraws the $k(t)$ in Fig. 6.6 and Fig. 6.7 in double logarithmic coordinates and compares them.

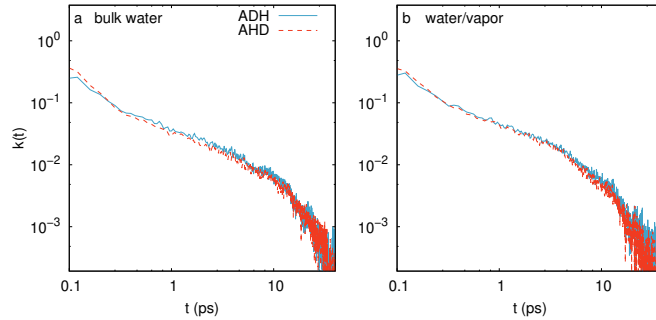


FIGURE 6.8: Time dependence of $k(t)$ of water–water H-bonds for (a) bulk water and (b) the water/vapor interface.

For the water/vapor interface, we focus on the reactive flux $k(t)$, which had been used in the study of HB dynamics of liquid water. [188, 197] The $k(t)$ calculated from the trajectory of water molecules in simulations, is reported in Fig. 6.9. In the water/vapor interface, $k(t)$ quickly changes from its initial value in transient period (~ 0.2 ps, see the inset of Fig. 6.9). Beyond this transient period, $k(t)$ decays to zero monotonically, and the slope of the $\ln k(t)$ increases monotonically with t (see Fig. 6.9). These two properties have been found for bulk water using the SPC water model by Luzar and Chandler. [188] This log-log plot of the $k(t)$ shows that, as in bulk water, this decay behaviour does not coincide with a power-law decay for the

water/vapor interface. This result is also the same as that of the classical molecular simulation of pure water. [178, 210]

The functions $n(t)$ calculated according to Eq. 6.5 for bulk water and the water/vapor interface are shown in Fig. 6.10. It shows that the overall trend of $n(t)$ does not depend on the choice of HB definition. i.e., as t increases, $n(t)$ increases rapidly from 0, and it reaches a maximum value at $t \approx 10$ ps, and then gradually decreases. We also find that the maximum value of $n(t)$ for the water/vapor interface is slightly higher than that in bulk water. It can be seen that $n(t)$ for the water/vapor interface is always greater than that in bulk water, whether we take the definition of ADH or AHD. We interpret this result as the fact that at time t , there is a greater probability that H-bonds at the interface are broken compared to H-bonds in bulk water.

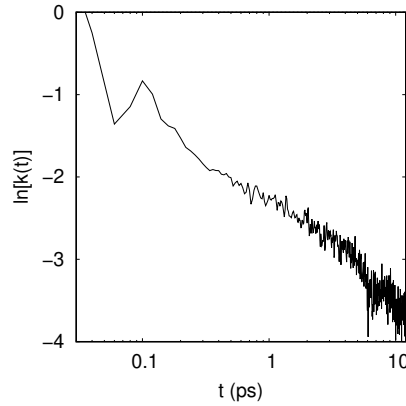


FIGURE 6.9: Time dependence of $k(t)$ for the water/vapor interface, according to Eq. 6.10. The inset shows the log-log plot of $k(t)$.

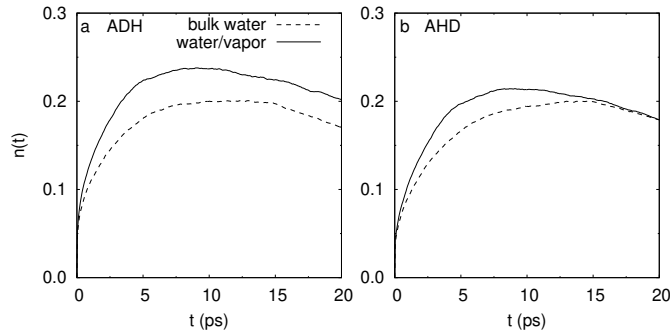


FIGURE 6.10: Time dependence of $n(t)$ for bulk water and the water/vapor interface from (a) ADH (b) AHD criteria.

Reaction rate constants k and k' Khaliullin and Kühne have studied the H-bonding kinetics of bulk water using the AIMD simulations.[197] Based on the HB population operators $h(t)$ and $h^{(d)}(t)$, and correlation functions $n(t)$ and $k(t)$, they have used the simulation data to obtain the ratio k/k' in bulk water, and then the lifetime and relaxation time of the HB. Here, we use the DFTMD simulations to study the HB dynamics at the water/vapor interface. We can obtain the optimal solution range of k and k' from the relationship between the reactive flux and the HB population correlation function $c(t)$ and $n(t)$, and the two rate constants k and k' , i.e.,

$$k(t) = kc(t) - k'n(t). \quad (6.13)$$

We found the optimal value of the rate constants, k and k' , by a least squares fit of the calculated data $k(t)$, $c(t)$ and $n(t)$ beyond the transition phase. The function $c(t)$ was regarded as a P -dimensional column vector composed by $(c(1), c(2), \dots, c(P))^T$, and denoted as \mathbf{c} , with $c(i)$ representing the value of the correlation $c(t)$ at $t = i$. Similarly, the functions $n(t)$ and $k(t)$ were also viewed as P -dimensional column vectors and can be denoted as \mathbf{n} and \mathbf{k} , respectively. Therefore, k and k' were determined from the matrix $\mathbf{A} = \begin{bmatrix} \mathbf{c} & \mathbf{n} \end{bmatrix}$, i.e.,

$$\begin{bmatrix} k \\ -k' \end{bmatrix} = (\mathbf{A}^T \mathbf{A})^{-1} \mathbf{A}^T \mathbf{k}. \quad (6.14)$$

For bulk water and the water/vapor interface, the optimal k and k' are reported in Table 6.1 and 6.2.

TABLE 6.1: The k and k' for bulk water (bulk) and the water/vapor interface (w/v). We carried on the short time region $0.2 \text{ ps} < t < 2 \text{ ps}$. The unit for k (k') is ps^{-1} , and that for τ_{HB} ($= 1/k$) is ps. (Same below.)

Criterion	k (bulk)	k' (bulk)	τ_{HB} (bulk)	k (w/v)	k' (w/v)	τ_{HB} (w/v)
ADH	0.30	0.99	3.38	0.32	0.77	3.10
AHD	0.29	1.15	3.47	0.31	0.89	3.18

TABLE 6.2: The k and k' for bulk water (bulk) and the water/vapor interface (w/v). We carried on the long time region $2 \text{ ps} < t < 12 \text{ ps}$.

Criterion	k (bulk)	k' (bulk)	τ_{HB} (bulk)	k (w/v)	k' (w/v)	τ_{HB} (w/v)
ADH	0.12	0.04	8.72	0.16	0.07	6.37
AHD	0.11	0.05	9.50	0.16	0.09	6.47

To obtain the forward and backward rate constants (k and k'), we performed the fitting in different time region $0.2 < t < 2 \text{ ps}$ and $2 < t < 12 \text{ ps}$, respectively. We note that in the larger time region, i.e., $2 < t < 12 \text{ ps}$, the value of HB lifetime τ_{HB} is larger than that in shorter time region, $0.2 < t < 2 \text{ ps}$, no matter for bulk water or for the water/vapor interface. A larger τ_{re} value means that the distance between a water molecule and another water molecule stays within $r_{\text{OO}}^c = 3.5 \text{ \AA}$ for a longer time. For the long time region, these values of the k are comparable in magnitude to that obtained by Ref. [197]

6.3 Instantaneous interfacial HB dynamics

To study the HB dynamics for the water/vapor interface, we first determine the instantaneous interface and then define the interfacial HB population operator. Based on these two definitions, we derived the correlation functions and reaction rate constants, for interfacial layers. Using these quantities we discussed the change in the HB dynamics at the interface with the interface layer's thickness.

Instantaneous Interfaces As Willard and Chandler mentioned, due to molecular motions, interfacial configurations change with time, and the identity of molecules

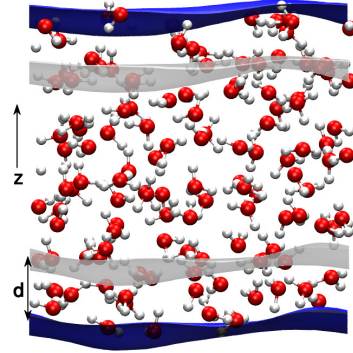


FIGURE 6.11: A slab of water (128 water molecules are included) with the instantaneous interface represented as a blue mesh on the upper and lower phase boundary. The normal is along the z -axis and the parameter d is the thickness of the interfacial layer. The grey surfaces are obtained by translating the interfaces to the interior of the slab along the z -axis (or the opposite direction) by d .

that lie at the interface also change with time, generally useful procedures for identifying interfaces must take into account these motions. [211] To determine the instantaneous interface of the system, we adopted their proposed method based on spatial density. The coarse-grained density at space-time point (\mathbf{r}, t) can be expressed as polynomial

$$\bar{\rho}(\mathbf{r}, t) = \sum_i \phi(|\mathbf{r} - \mathbf{r}_i(t)|; \xi) \quad (6.15)$$

where $\mathbf{r}_i(t)$ is the position of the i th particle at time t and the sum is over all such particles, and

$$\phi(\mathbf{r}; \xi) = (2\pi\xi^2)^{-3/2} \exp(-r^2/2\xi^2) \quad (6.16)$$

is a normalized Gaussian functions for a 3-dimensional system, where r is the magnitude of \mathbf{r} , and ξ is the coarse-graining length. Equation 6.16 is introduced to improve the accuracy of the interface, such that we can extend the domain and make it a single unicom, i.e., no cavity exists in the domain. With the parameter ξ set, the interfaces can be defined to be the 2-dimensional manifold $\mathbf{r} = \mathbf{s}$ such that

$$\bar{\rho}(\mathbf{s}; t) = \rho_c \quad (6.17)$$

where ρ_c is a reference density. This interface is a function of time as molecular configurations changes with time, that is $\mathbf{s}(t) = \mathbf{s}(\{\mathbf{r}_i(t)\})$.

After the surface (instantaneous interface) is defined, we can define an instantaneous interface layer for any non-uniform fluid system. Specifically, for the simulated water/vapor interface system in the cuboid simulation box, we can get another two-dimensional manifold $\mathbf{s}_0(t)$ by moving the surface $\mathbf{s}(t)$ determined above along the system's normal coordinate to a certain distance d (two grey surfaces are shown in Fig. 6.11). We use these two surfaces as the two boundaries of the interface. In other words, at any time point t , the volume between the two surfaces $\mathbf{s}(t)$ and $\mathbf{s}_0(t)$ is defined as an *instantaneous interface*, or *instantaneous interface layer*. Here, we use d to denote the thickness of the interface. As we change the value of d , we can get interfaces with different thicknesses. Different values of d give us different layering strategies for the interface system. See Fig. 6.11 as an example.

Below we will combine the instantaneous interface and Luzar-Chandler's HB population operator [188] to select the H-bonds at the water/vapor interface. The dynamics of these H-bonds will vary with the thickness d of the interface. By investigating the characteristics of HB dynamics for these interfaces, we can obtain the dynamical characteristics of various solution/vapor interfaces.

Interfacial hydrogen bond population Once we have determined the instantaneous surface $\mathbf{s}(t) = \mathbf{s}(\{r_i(t)\})$, we can define *interfacial H-bonds*. Now we define the interface HB population operator $h^{(s)}[r(t)]$ as follows: It has a value 1 when the particular tagged molecular pair are H-bonded, *and* both molecules are inside the instantaneous interface with a thickness d , and zero otherwise. The definition of $h^{(s)}[r(t)]$ is critical to help us to efficiently obtain the H-bonds' dynamic characteristics of the interfacial layer with a given thickness d . In this paragraph, we discuss H-bonds based on water molecule pairs.

Similar to the correlation function $C_{\text{HB}}(t)$ in Eq. 6.1, which describes the fluctuation of the general H-bonds, we define the correlation function $C_{\text{HB}}^{(s)}(t)$ that describes the fluctuation of the interfacial H-bonds:

$$C_{\text{HB}}^{(s)}(t) = \langle h^{(s)}(0)h^{(s)}(t) \rangle / \langle h^{(s)} \rangle. \quad (6.18)$$

Similarly, we define correlation functions

$$n^{(s)}(t) = \langle h^{(s)}(0)[1 - h^{(d,s)}(t)]h^{(d,s)}(t) \rangle / \langle h^{(s)} \rangle, \quad (6.19)$$

and

$$k^{(s)}(t) = -\frac{dC_{\text{HB}}^{(s)}}{dt}. \quad (6.20)$$

Using these new correlation functions, we can determine the reaction rate constant of breaking and reforming and the lifetimes of interfacial H-bonding. We will discuss the dependence of the correlation functions $C_{\text{HB}}(t)$, $C_{\text{HB}}^{(s)}(t)$, and the reaction rates k and k' on the interface thickness d in the next two paragraphs.

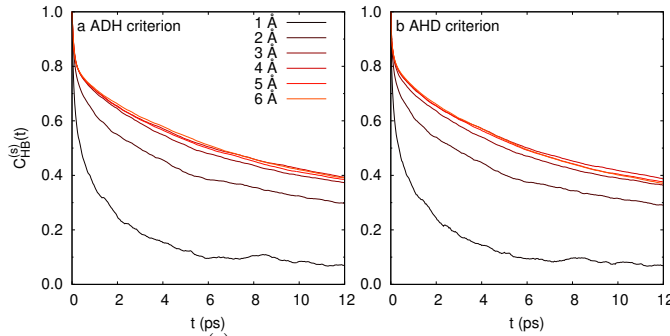


FIGURE 6.12: The $C_{\text{HB}}^{(s)}(t)$ for the instantaneous interfacial H-bonds with different thickness (d), as computed from the (a) ADH and (b) AHD criteria of H-bonds.

Depth-dependence of $C_{\text{HB}}^{(s)}(t)$ For the water/vapor interface, we used two geometric criteria of H-bonds to calculate the $h^{(s)}(t)$ and therefore correlation function $C_{\text{HB}}^{(s)}(t)$. The calculation results of the $C_{\text{HB}}^{(s)}(t)$ are shown in Fig. 6.12. We find that the HB dynamics is faster at the water/vapor interface when compared to bulk. As

d increases, we get slower and slower HB dynamics. This feature means that as d increases, the interface's HB dynamics will converge and eventually tend to bulk water's hydrogen bond dynamics. This behavior is independent of the HB definition as shown by the comparison of the results in panel (a) and (b) of Fig. 6.12.

For comparison, we also calculate the HB dynamics of water molecules at the interface obtained by selecting molecules located at the interface. We call this method Molecule Sampling (MS) (See Appendix E.1 for details). In this method, we first select molecules at the interface at each moment and then make a statistical average of the calculated correlation functions. Specifically, to determine which water molecules staying in the interface layer, we sample at regular intervals, and then calculate the correlation function $C_{\text{HB}}(t)$ for the water molecules in the interface layer and their a statistical average. As the thickness d changes, the $C_{\text{HB}}(t)$ for the interface will change. Figure 6.13 shows how the function $C_{\text{HB}}(t)$ changes with the thickness d . The panel (a) and (b) use HB definition criterion ADH, and AHD, respectively. Comparing Fig. 6.12 and Fig. 6.13, we found that when we use the method of MS at the interface, the dependence of the correlation function $C_{\text{HB}}(t)$ on the interface thickness is consistent with that of $C_{\text{HB}}^{(s)}(t)$ for large d . Moreover, regardless of the AHD definition or the ADH definition of the HB, this conclusion is basically valid.

Beside the correlation functions $C_{\text{HB}}(t)$ or $C_{\text{HB}}^{(s)}(t)$ for the interface, we will further examine the correlation functions $C_{\text{HB}}(t)$, $n(t)$, $k(t)$ ($C_{\text{HB}}^{(s)}(t)$, $n^{(s)}(t)$, $k^{(s)}(t)$), and the rate constants k , k' .

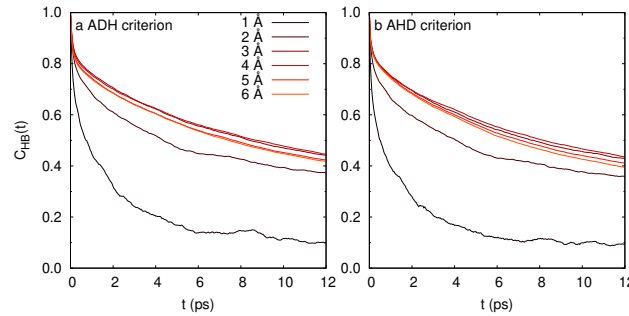


FIGURE 6.13: The $C_{\text{HB}}(t)$ for the instantaneous interfacial H-bonds with different thickness d , as computed from the (a) ADH and (b) AHD criteria of H-bonds. These results are based on MS method. The sampling is performed every 4 ps.

Depth-dependence of k and k' To find the reaction rate constants k and k' , we also have two choices. We can use the correlation functions $C_{\text{HB}}^{(s)}(t)$, $n^{(s)}(t)$ and $k^{(s)}(t)$; We can also first select the water molecules at the instantaneous interface at each time point t , and start from the corresponding correlation functions $C_{\text{HB}}(t)$, $n(t)$ and $k(t)$ of the H-bonds of these selected water molecules. Figure 6.14 compares the rate constants (k and k') and the lifetime τ_{HB} obtained by the two different methods, i.e., the Instantaneous Interfacial Hydrogen Bond (IHB) and MS methods. We see that, whether it is k , k' or τ_{HB} , their changing *trend* with the thickness d of the interface is only slightly affected by the calculation methods. To illustrate this point more clearly, we compare the k , k' and τ_{HB} obtained under the two methods. We listed more detailed data in Table 6.3 to 6.6.

As we can see from Fig. 6.14, when the thickness d is large enough ($d_0 \sim 4$ Å), these two constants agree well quantitatively. This result shows that the two extreme statistical methods (see Appendix E.1) for the HB dynamics of the interface did not

produce much difference for the time scale (10^2 ps) and the scale (10^2 Å) of the simulation box.

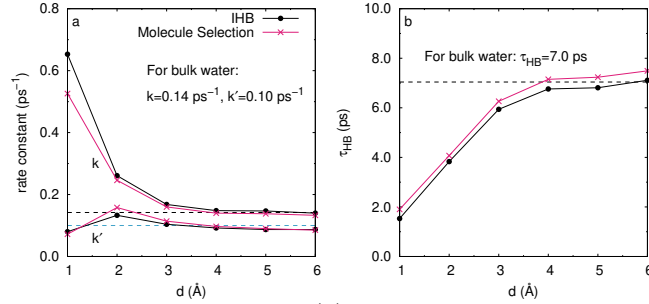


FIGURE 6.14: Dependence of (a) the reaction rate constants k and k' and (b) the HB lifetime τ_{HB} on the interface thickness d , obtained by the IHB and MS methods, respectively. The corresponding k , k' and τ_{HB} in bulk water are also drawn with dashed lines as a reference. In panel a, the k of bulk water is represented by a *black dashed* line, and the k' is represented by a *blue dashed* line; in panel b, the τ_{HB} of bulk water is represented by a *black dashed* line. The ADH criterion of H-bonds is used and the least square fits are carried on the time region $0.2 \text{ ps} < t < 12 \text{ ps}$.

We also found that when we focus on the molecules in the interface layer whose thickness is less than d_0 , the values of the reaction rate constants slightly depend on the method we use. That is, the k obtained by the IHB method is relatively larger than by the MS method, and k' is smaller. Since $\tau_{\text{HB}} = 1/k$, large k directly leads to a relatively shorter HB lifetime. This result is related to our definition of IHB, and it is the same as our expectation: The definition of interfacial H-bonds (or $h^{(s)}(t)$) makes the HB break rate on the interface artificially increased. At the same time, the MS method retains the original rate constant of H-bonds, but it may include the contribution of bulk water molecules to the rate constant. That is why the MS method slightly underestimate the k .

In Fig. 6.14, the k , k' and τ_{HB} for the *bulk* water are also drawn with dashed lines as a reference. Comparing the above-mentioned physical quantities for the water/vapor interface and bulk water, we found that when the interface thickness d is larger than d_0 , no matter which statistical method is used, the value of the calculated reaction rate constants of the interface water is *greater* than that in bulk water. Therefore, since the HB lifetime can be calculated by the relation $\tau_{\text{HB}} = 1/k$, the value of τ_{HB} for water molecules at the water/vapor interface is smaller than that for bulk water.

Furthermore, we have found from Fig. 6.14 that as the interface thickness d increases, the values of k and k' also tend to the values of rates in bulk water at the same condition. These results are obtained by the least squares method in the same interval (0.2–12 ps). This verifies that the IHB method can get as good results as the method of MS for $d > d_0$. Because the method of IHB is easier to operate, it can be used to calculate the HB dynamics and thus HB lifetime for the water/vapor interface when d is larger than d_0 . For the water/vapor interface, d_0 is approximately 4 Å or equals to the size of 2–3 water molecules. This result coincides with the previous theoretical results based on MD simulation[127, 212, 213] and VSFG spectroscopy[214, 215], which have shown that isotropic properties are already present at sub-nanometer distances from the surface of ordered hydrophobic monolayers. They suggested a "healing length" of about 3 Å with the bulk-phase properties of water recovered within the top few monolayers. We also noticed that the method of MS depends on our sampling rate on the trajectory of the simulated system, while the

IHB method does not require such sampling. Therefore, the IHB method is a more convenient method to determine the HBD at the water/vapor interface.

Finally, because the real HB dynamical properties of interface molecules are between the results of the above two methods, we can approximate the interfacial HB dynamics, by either the IHB and the MS method if the thickness of the interface is large enough.

TABLE 6.3: The k and k' for the interfacial HB dynamics of the water/vapor interface, through the IHB method, with ADH criteria. We carried on the longer time region $0.2 \text{ ps} < t < 12 \text{ ps}$ (same below).

$d \text{ (\AA)}$	$k \text{ (ps}^{-1}\text{)}$	$k' \text{ (ps}^{-1}\text{)}$	$\tau_{\text{HB}} (= 1/k) \text{ (ps)}$
1.0	0.653	0.080	1.53
2.0	0.261	0.133	3.83
3.0	0.168	0.104	5.94
4.0	0.148	0.092	6.76
5.0	0.147	0.087	6.81
6.0	0.139	0.087	7.17

TABLE 6.4: The k and k' for the interfacial HB dynamics of the water/vapor interface through the IHB method, with AHD criteria.

$d \text{ (\AA)}$	$k \text{ (ps}^{-1}\text{)}$	$k' \text{ (ps}^{-1}\text{)}$	$\tau_{\text{HB}} (= 1/k) \text{ (ps)}$
1.0	0.661	0.080	1.51
2.0	0.265	0.133	3.77
3.0	0.172	0.102	5.82
4.0	0.148	0.090	6.74
5.0	0.149	0.084	6.72
6.0	0.144	0.078	6.93

TABLE 6.5: The k and k' for the interfacial HB dynamics of the water/vapor interface through the MS method, with ADH criteria.

$d \text{ (\AA)}$	$k \text{ (ps}^{-1}\text{)}$	$k' \text{ (ps}^{-1}\text{)}$	$\tau_{\text{HB}} (= 1/k) \text{ (ps)}$
1.0	0.526	0.072	1.90
2.0	0.246	0.158	4.07
3.0	0.160	0.114	6.26
4.0	0.140	0.097	7.15
5.0	0.138	0.090	7.24
6.0	0.133	0.085	7.49

TABLE 6.6: The k and k' for the interfacial HB dynamics of the water/vapor interface through the MS method, with AHD criteria.

$d \text{ (\AA)}$	$k \text{ (ps}^{-1}\text{)}$	$k' \text{ (ps}^{-1}\text{)}$	$\tau_{\text{HB}} (= 1/k) \text{ (ps)}$
1.0	0.610	0.083	1.64
2.0	0.235	0.142	4.62
3.0	0.138	0.102	7.22
4.0	0.141	0.098	7.07
5.0	0.120	0.078	8.40
6.0	0.119	0.071	8.39

6.4 Summary

In this chapter, we have introduced the HB population operators, interfacial HB population operators, and various correlation functions $C_{\text{HB}}(t)$, $S_{\text{HB}}(t)$, $n(t)$, and $k(t)$ based on this operator. The HB dynamics calculations for bulk water and the water/vapor interface are based on these correlation functions. The $C_{\text{HB}}(t)$ describes the relaxation of H-bonds. The $S_{\text{HB}}(t)$ gives the average lifetime $\langle\tau_a\rangle$ of the continuous H-bonds. The $n(r)$ describes the probability that a HB is broken but still separated by cutoff radius r_{OO}^c . Based on DFTMD simulations, starting from the functions $C_{\text{HB}}(t)$, $n(t)$, and $k(t)$, we have calculated the reaction rate constants k and k' for HB rupture and regeneration for bulk water and the water/vapor interface.

We have studied the HB dynamics for instantaneous interfaces using two different statistical methods, the new IHB and MS. We have found that as the interface thickness increases, the HB reaction rate constants tend to the rate constants in bulk water. From above results for the water/vapor interface, we conclude that from the perspective of HB dynamics, the thickness of the water/vapor interface is about 3 Å. This value is smaller than that obtained from the SFG spectra (Ref. paragraph 5.1), and this result has reference significance for our study of the influence of ions on the H-bonds outside the solvation shell of ions. As the presence of ions in the solution affects the HB network, we will analyze these effects in the next chapter.

Chapter 7

Hydrogen bond dynamics in electrolyte solutions

In this chapter, we explore the effects of nitrate ions, iodide ions and alkali metal cations on the HB dynamics and water reorientation dynamics at the interface of alkali nitrate solutions and alkali iodine solutions. In paragraphs 7.1, we discuss the ion-water HB dynamics for the whole interface. Then in paragraph 7.2, we study the HB dynamics and HB lifetime specifically in the solvation shells of ions. In paragraphs 7.3 and 7.4, we focus on the reorientation dynamics of water molecules at the interfaces and in the solvation shells of ions in the solutions. All simulations in this chapter were performed at the DFT (BLYP + D) level and at 300 K within the canonical NVT ensemble. The length of each trajectory is about 60 ps. For each solution, we have performed DFTMD simulations for the solution/vapor interface and bulk system, respectively. The detailed parameter settings of different systems can be found in Appendix B.

7.1 Ion-water HB dynamics at electrolyte/vapor interface

7.1.1 Lithium nitrate solutions

We simulated a LiNO_3 solution/vapor interface including Li^+ and NO_3^- , as shown in Fig. 7.1(A) (water molecules are not shown). For computational details, see Appendix. B The correlation functions $C_{\text{HB}}(t)$ and $S_{\text{HB}}(t)$ for both nitrate–water (N–W) and water–water (W–W) hydrogen bonds in the slab are shown in Fig. 7.2 (a) and (b), respectively. For both HB definitions, we found that the decay of $C_{\text{HB}}(t)$ and $S_{\text{HB}}(t)$ for N–W hydrogen bonds is much faster than that for W–W hydrogen bonds. From the relation 6.7, the faster relaxation of $S_{\text{HB}}(t)$ implies that the N–W hydrogen bonds have shorter lifetime than the W–W hydrogen bonds in bulk phase. The calculation results obtained from the simulations are in good agreement with numerous experimental and simulation results. [133, 173, 182, 216] It means that nitrate has structure-breaking ability, or compared with W–W interaction, that the N–W interaction is weaker.

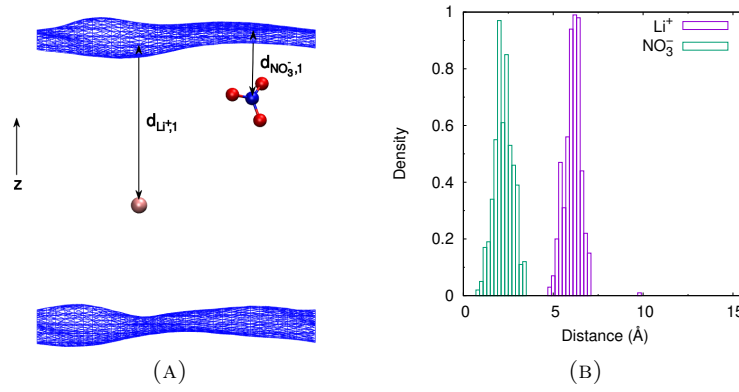


FIGURE 7.1: Distribution of ions at the LiNO_3 solution/vapor interface. (A) Distances between ions and one of the instantaneous surfaces (blue meshes) for a slab of aqueous LiNO_3 solution. (B) Density distribution the Li^+ -surface and NO_3^- -surface distances at the LiNO_3 solution/vapor interface. The horizontal axis represents the distance between the ion and the instantaneous surface, which is defined in Eq. 7.1. The *distance* refers specifically to $d_{X,1}$, the distance between the ion X and one of the instantaneous surfaces. Zero distance denotes the instantaneous surface of the interfacial system of LiNO_3 solution.

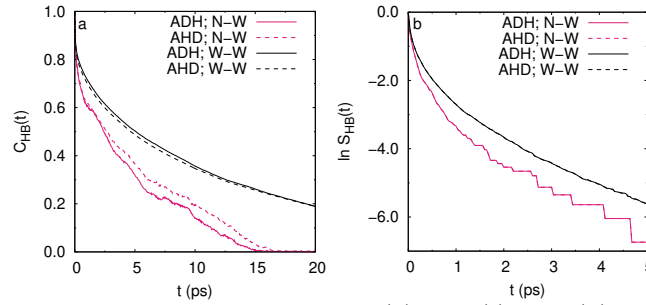


FIGURE 7.2: Time dependence of (a) $C_{\text{HB}}(t)$ and (b) $\ln S_{\text{HB}}(t)$ of all water-water (W-W) and nitrate-water (N-W) hydrogen bonds for the slab of LiNO_3 solution, as computed from the ADH (solid line) and AHD (dashed line) criterion of H-bonds. The W-W hydrogen bonds represents the H-bonds between all pairs of water molecules in the entire slab.

Since the structure-breaking ability of ions is closely related to surface propensity, we speculate that the rate of relaxation of the correlation functions ($C_{\text{HB}}(t)$ and $S_{\text{HB}}(t)$) of N-W bonds may be related to the distribution of NO_3^- ions at various depths under the surface. Therefore, we calculated the distribution of ions at different depths relative to the instantaneous interfaces of the LiNO_3 solution.

For the DFTMD trajectory of a solution interface, we can now get instantaneous surface (see blue meshes in Fig. 7.1 (A)). For any molecule or ion X in such a solution/vapor interface, we can define its distance from the instantaneous surface. We assume that the z -axis is the normal direction, then the distances between the particle and the instantaneous surfaces are:

$$d_{X,1}(t) = z_{X,1}^{\text{surf}}(t) - z_X(t), \quad (7.1)$$

$$d_{X,2}(t) = z_X(t) - z_{X,2}^{\text{surf}}(t), \quad (7.2)$$

where z_X is the coordinate of the particle X in the normal direction at time t , $z_{X,i}^{\text{surf}}(t)$ is the z coordinate of the surface position corresponding to particle X at time t , and the subscripts $i = 1$ and 2 respectively identify the lower and upper instantaneous surfaces. As an example, Fig. 7.1 (A) shows the distance, $d_{\text{Li}^+,1}$ ($d_{\text{NO}_3^-,1}$), between Li^+ (NO_3^-) ions and one of the instantaneous surfaces at a certain moment.

Figure 7.1 (B) shows the probability density of the distance between the ion and the instantaneous surface for the LiNO_3 solution/vapor interface. We found that when the system reaches an equilibrium state, the Li^+ ion is stable within a few angstroms below the instantaneous interface, while the NO_3^- ion resides near the surface. When the system is in equilibrium ($t > 10$ ps), the distance $d_{\text{NO}_3^-,1}$ is around 2 Å, which indicates that the nitrate ion is in the top layer of the instantaneous interface.

The result for the HB dynamics are in agreement with what we have learn in paragraph 5.1 from the vibrational spectroscopy. From the calculation of the VSFG spectrum of the LiNO_3 solution/vapor interface and the VDOS of water molecules in the water cluster $\text{NO}_3^-(\text{H}_2\text{O})_3$, we have shown that (1) Compared with the water/vapor interface, the VSFG spectrum of the LiNO_3 solution/vapor interface has a blue-shifted HB band (see Fig. 5.3); (2) The vibration frequency of water molecules from the LiNO_3 interface is higher than that at the water/vapor interface (see Fig. 5.4). The two conclusions above indicate that nitrate ions have the surface propensity. Here, the probability distribution of the nitrate ion in the slab shows that the average position of the nitrate ion relative to the solution/vapor interface is 2 Å, which is consistent with the conclusion from the VSFG spectra and VDOS calculations.

7.1.2 Alkali iodine solutions

We also calculated the distribution of ions at different depths at the instantaneous interface for the alkali iodine solutions. Figure 7.3–7.4 shows the density of the distance between the anion (cation) and the instantaneous surface in the simulated solution/vapor interface of LiI, NaI and KI solution, respectively. As an example, the distances between ions and one of the instantaneous surfaces (grey meshes) for a slab of aqueous KI solution are shown in Fig. 7.4 (A). We found that, the I^- ion resides near the surface, while alkali metal ions does not have such a strong tendency toward the surface.

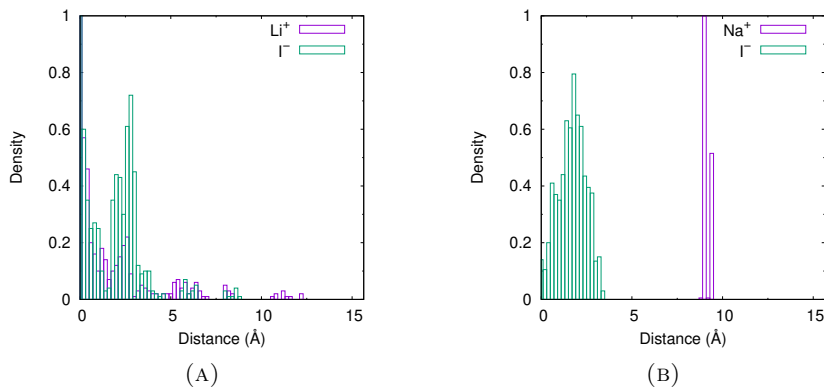


FIGURE 7.3: Distribution of ions at the LiI and NaI solution/vapor interface. (A) Density distribution the Li^+ –surface and I^- –surface distances at the LiI solution/vapor interface. (B) Density distribution the Na^+ –surface and I^- –surface distances at the NaI solution/vapor interface.

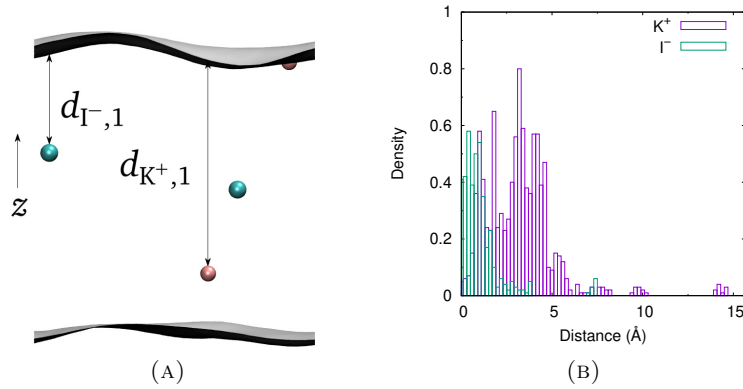


FIGURE 7.4: Distribution of ions at the KI solution/vapor interface. (A) Distances between ions and one of the instantaneous surfaces (grey meshes) for a slab of aqueous KI solution. (B) Density distribution the K^+ -surface and I^- -surface distances at the KI solution/vapor interface.

The experimental data of the concentration dependence of surface tension $d\gamma/dm_2$ of solutions containing Li^+ , Na^+ and K^+ ions also show that they do not have the strong surface propensity of I^- ions (see Chapter 3). Therefore, they did not show apparent surface propensity on the time scale of our current simulations. The ions propensity for the water surface can also be seen from the change of the distance of the ion relative to the interface over time. For example, Fig. D.1 shows the change of the distance between each ion in the KI solution and the interface over time. It illustrates that the fluctuation of the distance of I^- ions from the interface is smaller than the fluctuation of the distance of K^+ ions from the interface.

TABLE 7.1: The average of the continuum HB lifetimes $\langle\tau_a\rangle = \int_0^\infty S_{HB}(t)dt$ (unit: ps) in the first hydration shell of I^- ion and of alkali metal ion at the interface of three 0.9 M alkali-iodine solutions.

	I^- -shell	cation-shell	bulk water	w/v interface
LiI	0.22	0.24	0.25	0.23
NaI	0.24	0.28	0.25	0.23
KI	0.20	0.23	0.25	0.23

To investigate ions' effects, we calculated the HB population correlation functions at the water/vapor interface and we compared it to that in the ions' solvation shells at aqueous electrolyte interfaces. We consider the $C_{HB}(t)$ and $S_{HB}(t)$, from which the HB relaxation time τ_R and the HB lifetime τ_a can be calculated, respectively. Table 7.1 lists the continuum HB lifetime in the first hydration shell of I^- ion and of alkali metal ion at interfaces of alkali-iodine solutions: LiI, NaI and KI. For reference, we also give the τ_a for bulk water and the water/vapor interface in the third and fourth column, respectively. The continuum HB lifetime τ_a in the solvation shell of alkali metal (iodine) ions is larger (smaller) than that of H-bonds at the water/vapor interface. For LiI solution, the water molecules bound to the cation ion Li^+ , on average, have a continuum HB lifetime $\tau_{HB} \sim 0.24$ ps, which is longer than that of molecules bound to I^- or at the water/vapor interface. Besides, we found that τ_a for the I^- -shell is smaller than that for water/vapor interface in general.

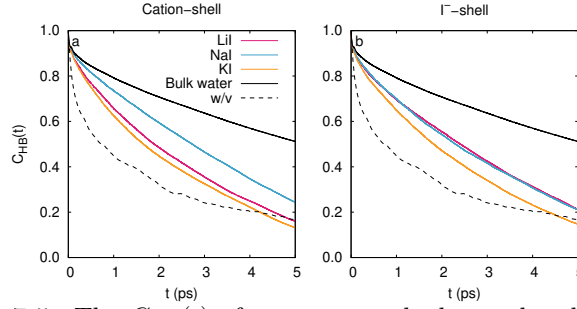


FIGURE 7.5: The $C_{HB}(t)$ of water–water hydrogen bonds in the solvation shell of (a) cations and (b) I^- at the interfaces of 0.9 M LiI, NaI and KI solutions, respectively. The solid and dashed line are for the instantaneous 1-Å water/vapor interface (see paragraph 6.3) and bulk water, respectively. The data for bulk water are calculated from water in the middle of the slab of LiI solution.

Fig. 7.5 (a) and (b) show that the $C_{HB}(t)$ of H-bonds within the alkali cations and I^- decay faster than those in bulk water. The interface of LiI solution contains H-bonds between water molecules similar to those in bulk water, i.e., water molecules participating in these H-bonds are not in the solvation shell of ions. This result is consistent with the observation of femtosecond midinfrared pump-probe experiments on the O–H stretch vibration of water molecules in aqueous solution, that changing the nature of the cation does not affect the dynamics of solvating water.[147] It is also in agreement with the following *ab initio* simulation results: water molecules that directly surround the cation, the O–H groups point away from the cation and form O–H \cdots O hydrogen bonds with bulk water molecules.[147, 217, 218] From Fig. 7.5 (b), we found that for all three alkali-iodine solutions, the $C_{HB}(t)$ for hydration shell water molecules of I^- decays faster than that for molecules in bulk water. The simulation produces similar result as Omta and coworker’s experiments of femtosecond pump-probe spectroscopy, which demonstrate that anions (SO_4^{2-} , ClO_4^- , etc) have no influence on the dynamics of bulk water, even at high concentration up to 6 M.[219, 220] Here, we have found that the cations Li^+ and Na^+ do not alter the H-bonding network outside the first hydration shell of cations. It is concluded that no long-range structural-changing effects for alkali metal cations.

Besides, the correlation function $C_{HB}(t)$ for the instantaneous interface layer of thickness $d = 1$ Å in pure water is also shown in Fig. 7.5. Its ultrafast relaxation process shows that the effects of ions (alkali cations and I^-) are not as obvious as that of the water/vapor interface.

Effects of the ion concentration To investigate the effect of the ion concentration we considered one additional system with higher concentration, namely 1.8 M.

We calculated the $C_{HB}(t)$ for the interfaces of the alkali-iodine solutions, and the relaxation time τ_R for each of them can be determined according to formula 6.2. Here, the *interface* means *all* the water molecules in each model. The τ_R for the interfaces of the LiI (NaI) solutions are given in Table 7.2. Generally, they are in the range 1–10 ps. The values of τ_R decrease as the concentration of the solutions increases.

The concentration dependence of the $S_{HB}(t)$ was also calculated. Figure 7.6 (a) (7.6 (b)) gives the $S_{HB}(t)$ for the interfaces of 0.9 M and 1.8 M LiI (NaI) solutions. This result indicates that, for the interface of alkali-iodine solution, the continuum HB lifetime decrease as the concentration of LiI (or NaI) solution increase. This can be explained as following: As the ion concentration increases, more iodide ions gather on the surface. The *ratio* of the number of iodide ions to the number of other water

TABLE 7.2: The relaxation time τ_R (unit: ps) of the $C_{HB}(t)$ for the interface of the LiI (NaI) solutions.

concentration	τ_R (LiI)	τ_R (NaI)
0	11.50	11.50
0.9 M	7.04	10.60
1.8 M	4.40	1.96

molecules among the neighbors of the surface water molecules is set to r_{I^-} . For the water molecules in the first solvation shell of the cation, the ratio of the number of cations to other water molecules in its neighbors is set to r_{cation} . Water molecules below the surface are surrounded by more water molecule neighbors than molecules at the interface. Since the upper half of the surface is vacuum and the cations here do not aggregate on the surface. Therefore, $r_{I^-} > r_{cation}$, so the influence of the cation on the HB relaxation is not as strong as the influence of the I^- ion on the surface. We believe that this fact is the reason that the HB relaxation of the water molecules at the interface becomes faster as the alkali iodide concentration increases. Therefore, the HB relaxation of the interface and the lifetime of H-bonds at the interface will be more dominated by the concentration of ions accumulated at the interface.

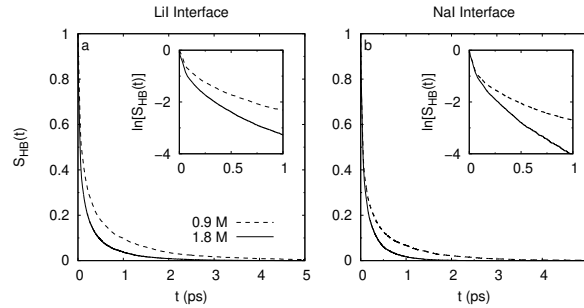


FIGURE 7.6: Time dependence of the $S_{HB}(t)$ of H-bonds at the interfaces of (a) LiI and (b) NaI solutions. The insets show the plots of $\ln S_{HB}(t)$.

To summarize, we have investigated the effect of alkali-nitrate and alkali-iodide on the HB dynamics of water molecules at solution/vapor interfaces, obtained from *ab initio* simulations. N-W's $C_{HB}(t)$ and $S_{HB}(t)$ decay faster than W-W's, which proves that the N-W hydrogen bonds is weaker than W-W ones. The result we obtained from VSFG spectra in paragraph 5.1 is that the blue shift of the HB band in the $\text{Im}\chi^{(2)}$, or, the nitrate ion in the solution tends to be distributed on the surface, which is also consistent with the smaller relaxation time given by the correlation functions $C_{HB}(t)$ and $S_{HB}(t)$. Compared with the water/vapor interface, the characteristic relaxation time of H-bonds between water molecules at the interface of the alkali metal salt solution as a whole becomes smaller and increases with the increase of the solute concentration.

7.1.3 Ion-water bond dynamics: breaking and reforming

For the water/vapor interface and the aqueous electrolyte solution/vapor interfaces, we have performed the same analysis described in Chapter 6 where the $k(t) = -dc(t)/dt$ is decomposed into two terms: $kc(t)$ and $-k'n(t)$. The optimal values of coefficients k and k' given for these interfaces have been listed in Table 7.3. These

values are comparable in magnitude to those obtained by Ref. [197] for bulk water. It can be seen from Table 7.3 that the HB breaking rate (k) at the water/vapor interface is the same as that at the solution interface, but the HB reforming rate constant (k') is smaller than that at the solution interface by 30% to 50%. [HERE WE NEED SOME MORE UNDERSTANDING AND COMPARISON WITH THE LITERATURE. WHY? WAS THIS RESULT ALREADY KNOWN IN THE LITERATURE? ANY EXPLANATION?] Correspondingly, we find the HB relaxation times for the three interfaces are: $\tau = 1/(k + k') \sim 2.0\text{--}2.5$ ps; while for the water/vapor interface, the relaxation time is $\tau \sim 3.3$ ps.

TABLE 7.3: The k and k' for the water/vapor interface of the aqueous solution interfaces.

Interface	k (ps ⁻¹)	k' (ps ⁻¹)	τ_R (ps)
water/vapor	0.10 ± 0.02	0.20 ± 0.02	11.50
LiI	0.10 ± 0.04	0.30 ± 0.05	5.33
NaI	0.20 ± 0.10	0.30 ± 0.05	5.77
KI	0.10 ± 0.04	0.40 ± 0.10	6.96

As for the effect of the interface on the HB dynamics in alkali-iodine solutions, we also calculate the survival probability for interfaces with different sizes of thickness. The result for the LiI solution/vapor interface shows that H-bonds at the water/vapor interface decay faster than that in bulk water. The logarithm of $S_{HB}(t)$ is given in Fig. E.3 in Appendix E, in which the thickness of the alkali-iodine solutions can be determined. As the interface thickness increases, the $S_{HB}(t)$ converges to a fixed curve, which characterizes the HB dynamics of the solution/vapor interface. In particular, it gives the average continuum HB lifetime in bulk solution.

Nitrate water solutions First, let us take a look at the changes in H-bonds of water molecules by nitrate ions in bulk solution. The $\ln S_{HB}(t)$ for the water–water hydrogen bonds and nitrate–water hydrogen bonds at the interface of the LiNO_3 solution is shown in Fig. 7.7. The $\ln S_{HB}(t)$ shows that the nitrate–water bonds are weaker than water–water bonds, i.e., nitrate ions accelerate the HB dynamics in water.

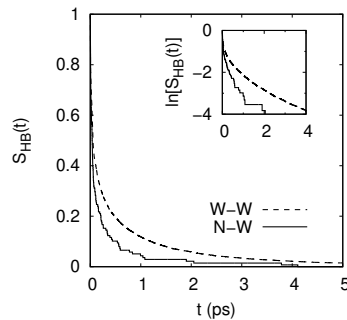


FIGURE 7.7: The $S_{HB}(t)$ of water–water (W–W) and nitrate–water (N–W) H-bonds at the interface of the LiNO_3 solution. The inset is the plot of $\ln S_{HB}(t)$. These results are calculated for the temporal resolution $t_t = 1$ fs. For the definition of t_t , see Appendix E.

The difference between nitrate–water and water–water hydrogen bonds is also analyzed in terms of the survival probability $S_{HB}(t)$, [153, 188, 193] reported in Fig. 7.7. The integration of $S_{HB}(t)$ from 0 to $t_{\max} = 5.0$ ps, [221] gives the approximate

lifetime τ_a . [222] The values of τ_a depend on the temporal resolution t_t , during which the H-bonds that break and reform are treated as intact. [206] Here, we choose the temporal resolution as $t_t = 1$ fs. Then, Fig. 7.7 gives $\tau_a = 0.20$ ps for nitrate–water hydrogen bonds at the interface, and $\tau_a = 0.42$ ps for water–water hydrogen bonds. This result of τ_a is consistent with the experimental result of Kropman and Bakker ($\tau_a = 0.5 \pm 0.2$ ps) for water–water hydrogen bonds. [223] The smaller value of τ_a for nitrate–water hydrogen bonds implies that the nitrate–water hydrogen bonds are weaker than bonds between water molecules. This is consistent with the VDOS analysis and the blue-shifted frequency (of 55 cm^{-1} towards the blue) of the OH stretching in the nitrate–water HB (see Fig. 5.5).

Iodine water solutions Hydrogen bonds between water molecules and other species also play decisive role in chemical and biological systems. For this type of HB, some results obtained by molecular simulations have been published. For example, the HB dynamics of surfactant–water and water–water hydrogen bonds at the interface has been analyzed by Chanda and Bandyopadhyay.[183] Similar analyse for nitrate–water is also done by Yadav, Choudhary and Chandra by first-principles MD simulations.[224] In the case of water–water hydrogen bonds, the cutoff radius $r_{\text{OO}}^c = 3.5 \text{ \AA}$ is the position of the first minimum of the oxygen–oxygen RDF (see Fig. 6.5).

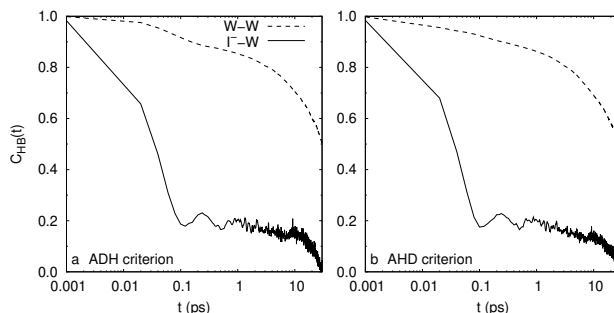


FIGURE 7.8: Time dependence of the intermittent correlation functions $C_{\text{HB}}(t)$ of I^- –water (I^- –W) and water–water hydrogen bonds. A base-10 log scale is used for the x -axis.

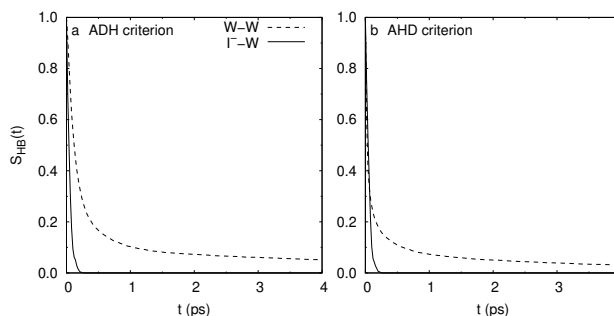


FIGURE 7.9: Time dependence of the continuous correlation functions $S_{\text{HB}}(t)$ of I^- –water (I^- –W) and water–water hydrogen bonds.

For the anion–oxygen (X–O) bonds, we can use the similar criteria. The cutoff values for X–oxygen distance are obtained from the positions of the first minimum of the X–oxygen RDF, i.e., $R_{\text{XO}}^c = 3.7$ and 4.1 \AA , for $\text{X} = \text{nitrate O}$ (see Fig. 7.21) and $\text{X} = \text{I}^-$ (see Fig. 5.8). We have used $\phi^c = 30^\circ$ for the angular cutoff.[198] The function $C_{\text{HB}}(t)$ of I^- –water and water–water bonds describes the structural relaxation of these H-bonds. The $C_{\text{HB}}(t)$ are shown in Fig. 7.8, and the results of the

continuous correlation functions for both definitions (ADH and AHD criterions) for the H-bonds are shown in Fig. 7.9 for I^- -water bonds. The results of water-water hydrogen bonds are also included for comparison in both Fig. 7.8 and 7.9. For both ADH and AHD definitions of H-bonds, it is found that the I^- -water bonds show faster dynamics than water-water bonds (consistent to previous MD results by Chowdhuri and Chandra).^[198]

The time scales of the relaxation of the I^- -water bonds are obtained for both definitions. In Table 7.4, we have included the average lifetimes $\langle\tau_a\rangle$ for I^- -water and nitrate-water bonds. We have performed the fitting in the time region $0.2 \text{ ps} < t < 12 \text{ ps}$ to calculate the forward and backward rate constants for HB reactive flux. No matter from ADH or AHD criteria, the average lifetime $\langle\tau_a\rangle$ of I^- -water bonds is shorter than that of NO_3^- -water bonds. In addition, based on the HB population operator for ion-molecule pairs, we also calculated the HB lifetime $1/k$ for these two hydrogen bonds. The results show that the lifetime of the I^- -water bonds is only half of lifetime of NO_3^- -water bonds. Therefore, from the perspective of HB dynamics, we can draw the following conclusion: I^- -water bonds and NO_3^- -water bonds are both weaker than water-water bonds. In particular, the I^- -water bonds is slightly weaker than the NO_3^- -water ones.

TABLE 7.4: The dynamical properties of I^- -water and nitrate-water hydrogen bonds within ADH (AHD) criterion.

Quantities	I^- -water	NO_3^- -water
$\langle\tau_a\rangle$ (ps)	0.10 (0.11)	4.35 (7.91)
$1/k$ (ps)	2.80 (2.40)	4.15(6.02)

7.2 Water-water hydrogen bond dynamics within the ions' solvation shells

We will extend the IHB dynamics (see paragraph 6.3) to H-bonds around ions in aqueous solutions. Similar to the determination of the instantaneous surface, we can define an interface for molecules or ions in aqueous solutions, i.e., their first solvation shell. Below we will combine the interface defined by the first solvation shell of ions, and Luzar-Chandler's HB population ^[188] to calculate the HB dynamics for the H-bonds between water molecules in the second solvation shell of ions. From characteristics of HB dynamics in the solvation shells, we can obtain the effect of various ions on structure and dynamics of aqueous solutions.

Solvation shell HB population Given the solvation shell $\mathbf{k}(t) = \mathbf{k}(\{\mathbf{r}_i(t)\})$, we can define the Solvation shell H-Bonds (SHBs). We use the parameter r_{shell} to denote the radius of the solvation shell. We define the solvation shell HB population operator $h^{(\mathbf{k},\text{X})}(t) = h^{(\mathbf{k},\text{X})}[r(t)]$ as follows: It has a value 1 when the particular tagged molecular pair are H-bonded *and* one of the water molecules are inside the solvation shell of species X with a radius r_{shell} , and zero otherwise. The definition of $h^{(\mathbf{k},\text{X})}(t)$ is similar to $h^{(\text{s})}(t)$ in paragraph 6.3 for studying the interfacial H-bonds, and it is used to obtain the dynamic characteristics of H-bonds in the solvation shell of species X with radius r_{shell} .

Similar to the definitions of the correlation function $C_{\text{HB}}^{(\text{s})}(t)$, which we have defined in Eq. 6.18, for the H-bonds in an instantaneous interface layer, for a given r_{shell} , we

define the correlation function $C_{\text{HB}}^{(k,X)}(t)$ that describes the fluctuation of the solvation shell H-bonds for ion X:

$$C_{\text{HB}}^{(k,X)}(t) = \langle h^{(k,X)}(0)h^{(k,X)}(t) \rangle / \langle h^{(k,X)} \rangle. \quad (7.3)$$

(When not considering specific ions, we denote $C_{\text{HB}}^{(k,X)}(t)$ as $C_{\text{HB}}^{(k)}(t)$ for short.) Similarly, we define a correlation function

$$n^{(k,X)}(t) = \langle h^{(k,X)}(0)[1 - h^{(k,X)}(t)]h^{(d,k,X)} \rangle / \langle h^{(k,X)} \rangle, \quad (7.4)$$

and a reactive flux function

$$k^{(k,X)}(t) = -\frac{dC_{\text{HB}}^{(k,X)}(t)}{dt}. \quad (7.5)$$

Using these correlation functions, we can determine the rate constants of breaking and reforming and the lifetimes for the solvation shell H-bonding. The results are given in next paragraphs.

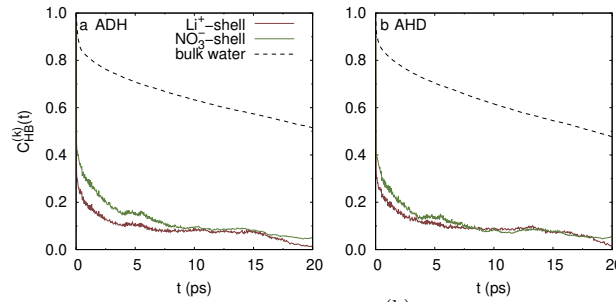


FIGURE 7.10: Correlation function $C_{\text{HB}}^{(k)}(t)$ for H-bonds in solvation shells, based on the HB population $h^{(k)}(t)$, as computed from the (a) ADH and (b) AHD criteria of H-bonds. The $C_{\text{HB}}(t)$ (dashed line) in bulk water is also plotted in panel (a) and (b) respectively.

Alkali-nitrate solution We calculated the HB dynamics for the H-bonds between water molecules in the first solvation shell and molecules in the second solvation shell. The choice of the shell radius comes from the RDFs (see Fig. 7.21). Figure 7.2 (a) shows that nitrate–water hydrogen bonds, or H-bonds in the first solvation shell of nitrate, is significantly weaker than water–water hydrogen bonds. And from the VDOS for the $\text{Li}^+(\text{H}_2\text{O})_4$ cluster (see Fig. 4.5 (A)), we know that Li^+ -bound water has a red-shifted peak, i.e., the Li^+ -water bonds slow down the vibrational relaxations of water–water hydrogen bonds in the solvation shell of Li^+ . If the above two properties were still valid outside the first solvation shell of the nitrate or Li^+ ions, then we could conclude that the H-bonds outside the first solvation shell of nitrate will be weaker than that outside the first solvation shell of Li^+ ion, i.e., the relaxation time of $C_{\text{HB}}^{(k,\text{NO}_3^-)}(t)$ will be significantly less than the relaxation time of $C_{\text{HB}}^{(k,\text{Li}^+)}(t)$. However, as we can see from Fig. 7.10 (a) and (b), the relaxation of $C_{\text{HB}}^{(k,\text{NO}_3^-)}(t)$ is almost the same as that of $C_{\text{HB}}^{(k,\text{Li}^+)}(t)$, or the former will not be faster than the latter. Specifically, Fig. 7.10 shows that the relaxation process of H-bonds between the water molecules in NO_3^- -shell and those outside the shell is *not* faster than the relaxation process of H-bonds between the water molecules in and outside the Li^+ -shell. In general, this result implies that the HB strength between water

molecules in the ions' hydration shells and those outside the shells are not affected by the nature of the ions evidently. In other words, the order of the strength of the H-bonds does not significantly affect the surrounding H-bonds.

Alkali-iodine solutions We have done DFTMD simulations for LiI, NaI, KI bulk system and interface system respectively. The probability distributions of ions in the solution/vapor interface of LiI and NaI solutions with respect to the depth of ions in the solutions are calculated. The distributions in Fig. 7.3–7.4 indicate that I^- ions prefer to staying at the topmost layer of surface of solutions. The probability distribution shows that I^- ions tend to the surface of solutions, while Na^+ and Li^+ tend to stay in bulk phase. This result is consistent with the calculations from Ishiyama and Morita[60, 63]. We choose LiI solution to calculate HB correlation function $C_{\text{HB}}^{\text{k}}(t)$, and the results are shown in Fig. 7.11. Like the LiNO_3 solution, the relaxation functions $C_{\text{HB}}^{(\text{k},\text{Li})}(t)$ and $C_{\text{HB}}^{(\text{k},\text{I})}(t)$ are very close to each other. This result shows that the presence of ions has no significant effect on the relaxation of H-bonds outside the first solvation shell.

Moreover, the $S_{\text{HB}}^{(\text{k},\text{Li})}(t)$ and $S_{\text{HB}}^{(\text{k},\text{I})}(t)$ have no significant difference. This result also implies that Li^+ ions have not significantly affected the relaxation process of H-bonds between the water molecules in the second solvation shells. Comparing the results in Fig. 4.7 in Chapter 4, we can summarize the influence of lithium ions on the dynamics of water molecules in the cluster (solution) as follows: Although in water molecule clusters, the vibration frequency of the water molecules directly connected to the Li^+ ion has a redshift, the HB relaxation between water molecules in the second solvation shell of the ion is almost no longer significantly affected by the ion.

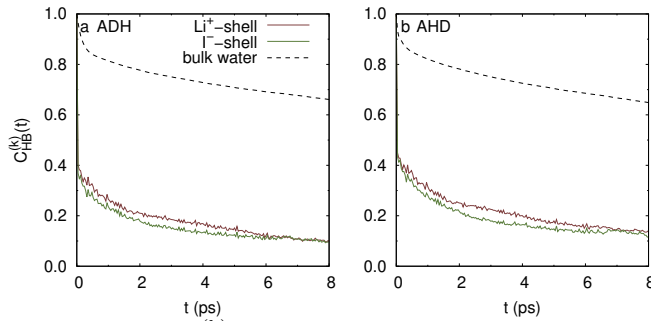


FIGURE 7.11: The $C_{\text{HB}}^{\text{k}}(t)$ for the solvation shell H-bonds with radius ($r_{\text{shell}} = 5.0 \text{ \AA}$), as computed from the (a) ADH and (b) AHD criteria of H-bonds. The $C_{\text{HB}}(t)$ (dashed line) in bulk water is also plotted in panel (a) and (b) respectively.

7.3 Rotational anisotropy decay of water molecules at the water/vapor interface

The effect of ions on the dynamics of water molecules can also be characterized by rotational anisotropy decay of water molecules. The pump-probe polarization anisotropy monitors electronic alignment.[225, 226] The anisotropy decay can be determined from experimental signal in two different polarization configurations—parallel and perpendicular polarizations, by[227, 228]

$$R(t) = \frac{I_{\parallel}(t) - I_{\perp}(t)}{I_{\parallel}(t) + 2I_{\perp}(t)} \quad (7.6)$$

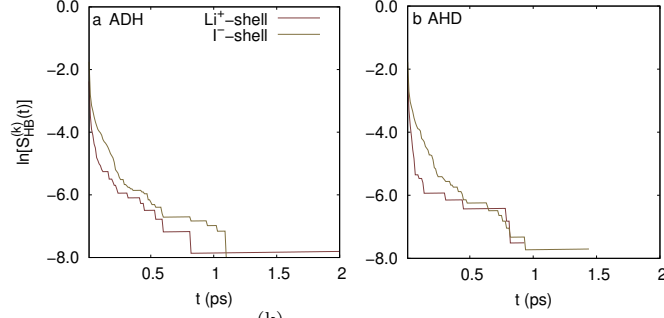


FIGURE 7.12: The $\ln S_{\text{HB}}^{(k)}(t)$ for H-bonds in the second solvation shells of Li^+ and I^- ions (in the water/vapor interface) as computed from the (a) ADH and (b) AHD criteria of H-bonds.

where $I_{\parallel}(t)$ is the absorption change when the probe laser pulse is parallel to the pump laser pulse, $I_{\perp}(t)$ is the absorption change when the probe laser pulse is perpendicular to the pump, and t is the time between pump and probe laser pulses. The effects of ion environment on structure and dynamics of water are obtained by comparing the second-order Legendre polynomial, i.e., $P_2(x) = \frac{1}{2}(3x^2 - 1)$, orientational correlation function of the transition dipole. The anisotropy decay can also be obtained by simulations, and calculated by the third-order response functions. [229, 230] If the anisotropy decay is only due to the orientational relaxation of water molecules and within the Condon approximation[231], it is directly related to the orientational correlation function $C_2(t)$ [232–235]

$$R(t) = \frac{2}{5}C_2(t). \quad (7.7)$$

The $C_2(t)$ is given by the rotational time-correlation function

$$C_2(t) = \langle P_2(\hat{u}(0) \cdot \hat{u}(t)) \rangle, \quad (7.8)$$

where $\hat{u}(t)$ is the time dependent unit vector of the transition dipole, and $\langle \rangle$ indicate equilibrium ensemble average.[129, 236] In our simulations, we concentrate on water molecules and consider a unit vector that is directed along the OH bond.

Water/vapor interface For the water/vapor interface, using the method introduced in paragraph 6.3, we first obtained the instantaneous interface with thickness $d = 1, \dots, 6 \text{ \AA}$. Then for each thickness, the method of molecule sampling (see paragraph 6.3) is used to obtain the $C_2(t)$ for the water molecules at the water/vapor interface. The result is shown in Fig. 7.13.

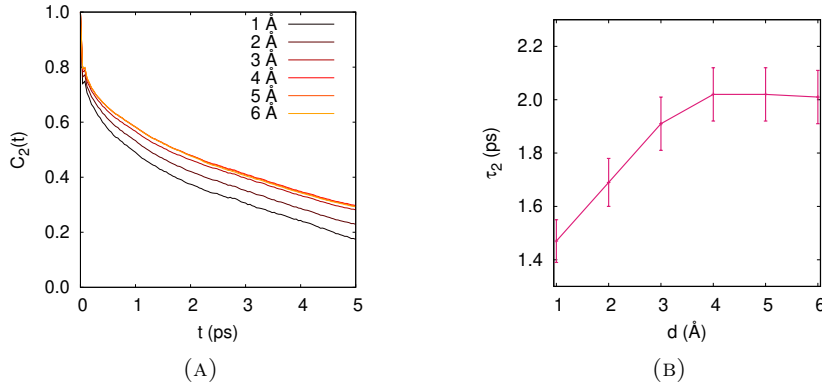


FIGURE 7.13: (A) Time dependence of $C_2(t)$ for water molecules at the water/vapor interface with different thickness in the range of 1 Å to 6 Å. (B) The dependence of decay time τ_2 on the thickness d in the exponential fitting ($t \in [0, 5]$ ps) of $C_2(t)$ for water molecules at the water/vapor interface.

Here we introduce a fitting with an exponential and provide a decay time τ_2 , i.e.:

$$C_2(t) = Ae^{-t/\tau_2}, \quad (7.9)$$

with $A = 1.0$ for all thickness values ($d = 1, \dots, 6$ Å), and the thickness dependence of τ_2 is shown in Fig. 7.13 (B). We see that when the interface thickness d is small, the decay time τ_2 increases linearly with d . That is, the orientation relaxation process of OH bonds in the thinner interface is faster than in the thicker interface. Similar to the correlations $C_{HB}(t)$ and $S_{HB}(t)$ for interfacial water molecules, as the interface thickness increases, the τ_2 converges to a fixed value, which characterizes the decay time of the orientation relaxation process of OH bonds in bulk water. Therefore, we have reached a conclusion that the orientation of OH in the water/vapor interface relaxes faster than in bulk water. From the convergence trend of τ_2 in Fig. 7.13, we found that at the interface with a thickness greater than 3 Å, the OH orientation relaxation of the water/vapor interface is no longer different from bulk water.

Therefore, starting from the instantaneous interface, we reach a consistent conclusion on the issue of estimating the thickness of the water/vapor interface, no matter from the perspective of OH reorientation relaxation or from HB dynamics.

Lithium nitrate solution The anisotropy decay of OH bonds in water molecules at 0.4 M LiNO₃ solution/vapor interface is shown in Fig. 7.14. This result implies that the reorientation relaxation rate of water molecules at the interface of the alkali nitrate solution is very close to that at the water/vapor interface.

We also introduced the fitting with an exponential according to Eq. 7.9. As we known in paragraph 5.1, the LiNO₃ was inserted at one of the two interfaces, we have a model with one salty interface and one neat interface which can be used as a reference. We obtained $A = 0.70 \pm 0.01$ for both the salty and neat interface, and $\tau_2 = 3.88 \pm 0.09$ ps and 4.04 ± 0.09 ps for the salty and neat water interface, respectively. Therefore, the close reorientation decay time (τ_2) for the salty interface and the water/vapor interface is also obtained from this fitting.

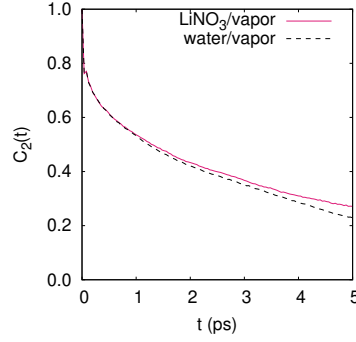


FIGURE 7.14: Anisotropy decay of OH bonds in water molecules at the LiNO₃ solution/vapor interface. The water molecules considered are in instantaneous layer with $d = 2$ Å below the surface.

To understand the reason of the difference between the alkali nitrate solution/-vapor interface and the water/vapor interface, we consider the water dangling OH bonds (or free OH bonds) at the interfaces. First, we define a new quantity n , which denotes the the number of H-bonds owned by a OH group at a given instantaneous interface. The distribution can be calculated by

$$P(n) = \frac{\sum_j^J N_{l,j}}{\sum_j^J \sum_{i=1}^M N_{i,j}}, \quad (7.10)$$

where $N_{l,j}$ denotes the number of OH bonds which own l HBs at the j -th sampling time, and $l = 1, \dots, l_{\max}$, l_{\max} is the largest number of HBs that a OH bond can form. For the solution/vapor interface, we use $l_{\max} = 5$.

For the LiN solution/vapor interface, the distribution $P(n)$ is shown in Fig. 7.15(a)–(d).

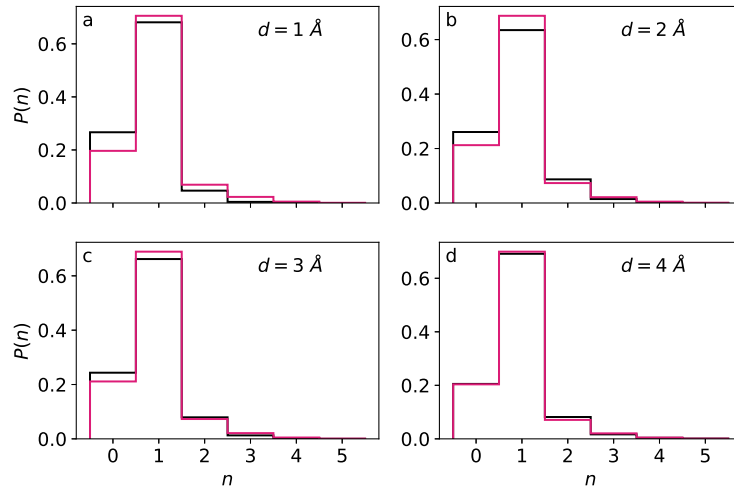


FIGURE 7.15: Distribution $P(n)$ of the number of H-bonds owned by a OH group at instantaneous layers with thickness d ($d = 1, \dots, 4$ Å). The red (black) line is for the LiNO₃ solution/vapor (water/vapor) interface.

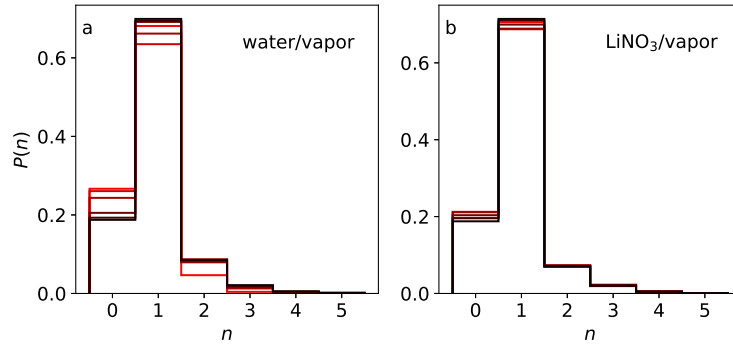


FIGURE 7.16: Distribution $P(n)$ of the number of H-bonds owned by a OH group at instantaneous layers with thickness d ($d = 1, \dots, 6$ Å). The red (black) line is for the interfaces (bulk) phase.

From Fig. 7.15 and 7.16, we found the following features: (1) For thinner layers (Fig. 7.15(a)(b)(c), i.e., $d \leq 3$ Å), $P(n=0)$ for LiNO₃ solution/vapor interface is smaller than that for the water/vapor interface. This result implies that there are less water dangling OH bonds at the LiNO₃ solution/vapor interface, compared to the water/vapor interface. (2) The $P(n=1)$ for LiNO₃/vapor interface is larger for d is thin enough. This means that the water at the topmost interface layer are more H-bonded than those at the water/vapor interface. (3) In particular, for $d = 2$ Å, we have $P(n=2)$ for LiNO₃ is larger than $P(n=2)$ for water/vapor interface, which is approximately zero. This character means that for water/vapor interface there are less possibility for a OH bond to form *two* H-bonds at the topmost instantaneous layer. (4) From the distribution $P(n)$, we again obtain the consistent result, i.e., when $d > 3$ Å, the difference between LiNO₃/vapor interface and water/vapor interface disappears. Both distributions converge to $P(n)$ for bulk water.

These results demonstrate that the structural properties in the instantaneous layer with $d \leq 3$ Å is the main source of interfacial properties, such as HB lifetime, anisotropy decays and SFG spectroscopy.

Alkali-iodine solutions We also calculated $C_2(t)$ for the LiI solution/vapor interface (the whole slab). The results of $C_2(t)$ for these solution/vapor interfaces are shown in Fig. 7.17. It decays significantly faster than $C_2(t)$ at the water/vapor interface, indicating that H-bonds at the LiI solution/vapor interface are orientated more frequently than that of the water/vapor interface. From the single exponent fitting by Eq. 7.9, we obtained $A = 0.73 \pm 0.02$ (0.77 ± 0.02) and $\tau_2 = 2.1 \pm 0.1$ ps (2.7 ± 0.1 ps) for the LiI interface (the water/vapor interface). It shows that LiI accelerate the dynamics of molecular reorientation of water molecules at the interface.

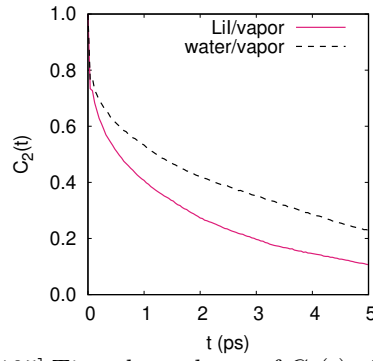


FIGURE 7.17: [2105] Time dependence of $C_2(t)$ of OH bonds at the LiI solution/vapor (solid line) and the water/vapor (dashed line) interface. The water molecules considered are in instantaneous layer with $d = 2$ Å below the surface.

From Fig. 7.17, we can find that water molecules at the LiI solution/vapor interface have larger reorientation relaxation rate than that at the water/vapor interface.

The distribution of the number of HBs per OH bond for LiI solution/vapor interface is also calculated and analyzed. For the LiI solution/vapor interface, the distribution $P(n)$ is shown in Fig. 7.18(a)–(d).

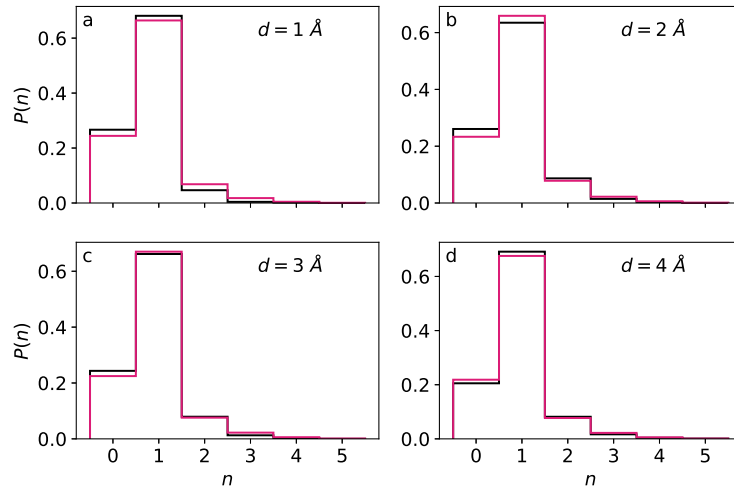


FIGURE 7.18: Distribution $P(n)$ of the number of H-bonds owned by a OH group at instantaneous layers with thickness d ($d = 1, \dots, 4$ Å). The red (black) line is for the LiI solution/vapor (water/vapor) interface.

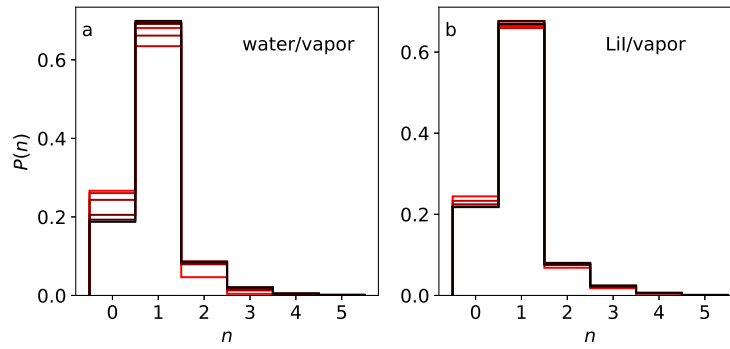


FIGURE 7.19: Distribution $P(n)$ of the number of H-bonds owned by a OH group at instantaneous layers with thickness d ($d = 1, \dots, 6$ Å). The red (black) line is for the interfaces (bulk) phase.

(1) From both Fig. 7.18 and Fig. 7.19, we found that the ratio of water dangling OH bonds for the LiI/vapor interface is smaller than that for the water/vapor interface. (2) We can also find that when $d > 3$ Å the distribution $P(n)$ does not change anymore. (3) At top layer, $P(1)$ is larger than that for water/vapor interface, this result implies that OH bonds are bonded to ions. From the probability distribution of ions for LiI solution/vapor interface, see Fig. 7.3, which shows that I^- ions has more propensity for surface than Li^+ cations. We conclude that there are more O-H \cdots I bonds at the LiI solution/vapor interface than in bulk phase. (4) We can find that $P(0)$ of the LiI solution/vapor interface is larger than that of the water/vapor interface, this implies that at the LiI/vapor interface, the O-H \cdots I bonds replace the role of H-bonds at these layers.

Therefore, the increasing density of O-H \cdots I bonds, and decreasing density of water dangling OH bonds is the two clear structural propensities of alkali iodide solution/vapor interface.

7.4 Rotational anisotropy decay of water molecules in ions' solvation shells

In this paragraph, we answer the question whether the water molecules in the first solvation hydration shell of different ions have different orientation dynamics.

We calculated the anisotropy decay of water molecules in ions' hydration shells in alkali-nitrate (alkali-iodide) solution/vapor interfaces. The calculated average of $C_2(t)$ is shown in Fig. 7.20. It is obtained by averaging the $C(t)$'s for 6 different trajectories. The radius of the hydration shell of nitrate O, Li^+ , and water molecules are taken as 4.0, 2.8 and 3.5 Å, respectively. These values are obtained from the position of the first minimum of the RDFs $g_{NN-OW}(r)$ (NN: Nitrate Nitrogen), $g_{Li-OW}(r)$ and $g_{OW-OW}(r)$, for bulk alkali nitrate solution, as shown in Fig. 7.21. To avoid that the considered molecules diffuse out of the first solvation shell, we only consider trajectories with a duration of 10 ps.

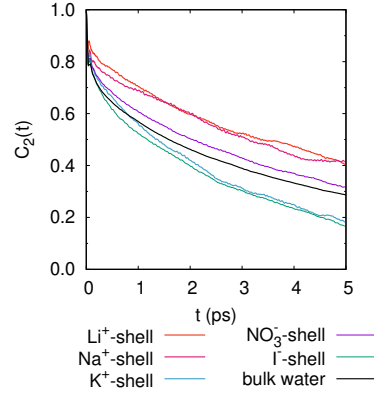


FIGURE 7.20: The $C_2(t)$ for water molecules in the solvation shell of Li^+ , Na^+ , K^+ , I^- and nitrate ions at the alkali-nitrate (alkali-iodide) solution/vapor interfaces. For comparison, the $C_2(t)$ for bulk water (black line) is also shown.

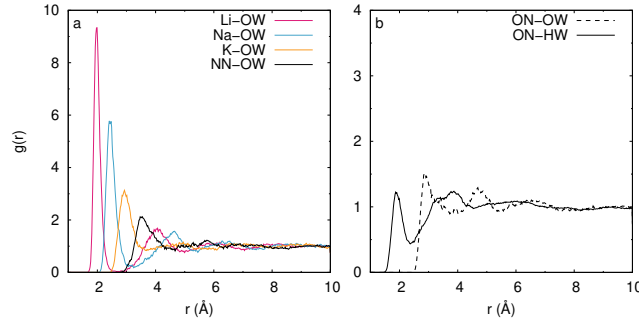


FIGURE 7.21: RDFs for the alkali-nitrate solutions.

For the NaNO_3 solution/vapor interface, the average values of the $C_2(t)$ are also shown in Fig. 7.20. The radius of the hydration shell of nitrate O, Na^+ , and water molecules are taken as 4.0, 3.2 and 3.5 Å, respectively. (Also in this case, these values are obtained from the RDFs $g_{\text{NN-OW}}(r)$, $g_{\text{Na-OW}}(r)$ and $g_{\text{OW-OW}}(r)$, see Fig. 7.21.)

Finally we also did the same calculation of $C_2(t)$ for the KNO_3 solution/vapor interface. The average values of $C_2(t)$ are shown in Fig. 7.20. The radius of the hydration shell of nitrate O, K^+ , and water molecules are taken as 4.0, 3.6 and 3.5 Å, respectively. (Also in this case, these values are obtained from the RDFs $g_{\text{NN-OW}}(r)$, $g_{\text{K-OW}}(r)$ and $g_{\text{OW-OW}}(r)$, see Fig. 7.21.)

From the above calculation of $C_2(t)$, we found that in the interfacial systems of alkali metal nitrate solution, nitrate ions always accelerate the reorientation dynamics of water molecules in the hydration shells of nitrate ions. However, the reorientation dynamics of water molecules in the hydration shells of alkali metal ions may slow down (for LiNO_3 and NaNO_3 solutions, respectively) or accelerate (for the KNO_3 solution), due to the presence of alkali metal ions.

For the dynamic process in a short time, we found a relation between the reorientation relaxation time and the radius of hydration shell. Using a single exponential fit of the decay function $C_2(t)$ we obtained the values of τ_2 as reported in Table 7.5. The anisotropy decay is a single exponential given by

$$C_2(t) = e^{-t/\tau_2}.$$

It can be seen that the reorientation relaxation time τ_2 of the water molecules in the hydration shell decreases with the increase of the radius of the hydration shell, as

shown in Fig. 7.22. We also give a linear regression function (solid line) to fit this relation, obtained from the data from alkali nitrate (iodide) solutions. The relation between orientation relaxation time τ_2 and the radius is as following:

$$\tau_2(r) = -ar + b, \quad (7.11)$$

where $a = -1.5 \pm 0.5$ and $b = 8.6 \pm 1.7$.

TABLE 7.5: The radius r of hydration shells and corresponding relaxation times τ_2 at the interface of alkali-nitrate (alkali-iodide) solutions.

ion (molecule)	r (Å)	τ_2 (ps)
Li^+	2.8	4.57(3)
Na^+	3.2	4.35(2)
K^+	3.6	2.37(2)
H_2O	3.5	2.92(2)
NO_3^-	4.0	3.32(2)
I^-	4.3	2.22(2)

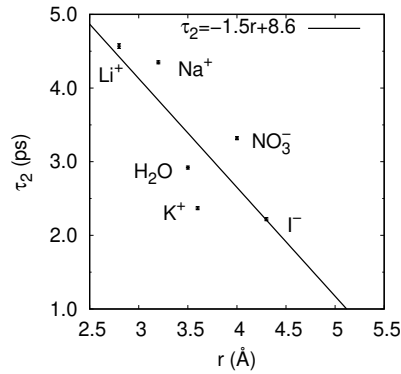


FIGURE 7.22: Dependence of τ_2 on the radius of the solvation shell of molecules and ions (water, Li^+ , Na^+ , K^+ , I^- and nitrate ions) in the slab of the alkali nitrate (iodide) solutions.

Using the same approach as above, we calculated τ_2 with a single exponential fitting. We also found that τ_2 of the water molecules in the hydration shell decreases with the increase of the radius of the solvation shell (see the data for I^- in Table 7.5).

To explain the $C_2(t)$ for the LiNO_3 and LiI solution/vapor interfaces, we list the peaks of RDFs for the LiI /vapor, the LiNO_3 /vapor and the water/vapor interfaces (see Fig. 7.6). We found that there is a correlation between reorientation and the strength of the H-bonds: The N-W and W-W hydrogen bonds have very close local structure, while the iodide-water (I^- -W) HB is of significantly different local structure. This result can be found from the larger value (3.61 Å and 2.66 Å, see the first two rows in Table 7.6) of the first peaks' locations in $g_{\text{I-OW}}$ and $g_{\text{I-HW}}$, and close first peak locations for ON-OW and OW-OW RDFs (2.80 Å and 2.79 Å, see the 3rd and 5th row in Table 7.6). The difference between water molecules with OW-OW and ON-OW bonds is discussed in paragraph C.3.

TABLE 7.6: The peaks (unit: Å) of RDFs for the LiI/vapor, the LiNO₃/vapor and the water/vapor interfaces (see Table C.5 and C.6).

$g(r)$	1st peak	2nd peak
I-OW	3.61	-
I-HW	2.66	4.07
ON-OW	2.80	-
ON-HW	1.83	3.30
OW-OW	2.79	-
OW-HW	1.83	3.25

7.5 Summary

We have investigated effects of alkali-nitrate and alkali-iodide on the HB dynamics of water molecules at solution/vapor interfaces. Nitrate–water’s HB dynamics decay faster than water–water’s, which proves that the nitrate–water hydrogen bonds is weaker than water–water bonds. The result from calculated VSFG spectra is that the blue shift of the HB band in the nonlinear susceptibility, or, the nitrate ion in the solution tends to be distributed on the surface, which is consistent with the smaller relaxation time given by the HB population correlation functions $C_{HB}(t)$ and $S_{HB}(t)$.

From a detailed analysis of the dynamics of water molecules in the second solvation shell of ions, we found that the HB relaxation between water molecules in the second solvation shell of the ion is almost no longer significantly affected by the ion.

The rotational anisotropy decay of water molecules at the water/vapor and solution/vapor interfaces was investigated to understand the effects of ions on the dynamics of water at interfaces. The main result is: the ratio of free OH bonds for the water/vapor interface is the most important factor that affect the decay rate of the reorientation relaxation of water molecules. Single exponential decay is a good model for water molecules at the interface of the alkali-iodine solutions, and the faster anisotropy decay of water molecules at the interface is the effects of free OH stretch and Hydrogen–Iodide (H–I) bond at the interface. This difference of HB structure from the water/vapor interface is the source of the HB dynamics as well as the $\text{Im}\chi^{(2)}$ spectrum of the interface of alkali-iodine solutions.

Chapter 8

Summary

Using DFTMD simulations, we have analyzed the interfacial structure and dynamics of electrolyte solutions containing alkali nitrates. In particular we have presented a detailed analysis of the VSFG spectra, HB dynamics, reorientation dynamics of water molecules at the solution/vapor interfaces. We have calculated the interface vibrational spectra in order to provide a molecular interpretation of available experimental data. In view of the similarity between iodide ion and nitrate ion in the Hofmeister sequence, we also did the same calculation for the electrolyte solutions of alkali metal iodides. It is expected that a general understanding of the dynamical properties in solutions containing larger anions such as nitrate and iodide will be obtained.

As a first system we have analyzed the behaviour of a salty interface containing LiNO_3 . Both measured and calculated VSFG spectra shows a reduced intensity of the lower frequency portion region, when compared to the water/vapor interface. This reduction is attributed to the H-bonds established between the NO_3^- and the surrounding water molecules at the interface. This effects is only related to the presence of NO_3^- at the water surface and is not affected by the presence of alkali metal ions. Indeed we have shown that although the Li^+ can reside relative close to the water surface, also forming a water mediated ion pair with NO_3^- , its effect on the VSFG spectrum is not visible. The water molecule which mediate the interaction between the NO_3^- and the Li^+ would produce a red-shifted peak in small water cluster, but its influence is not visible neither in the VSFG spectra. To verify this conclusion, the free energy of different configurations was calculated for larger water clusters in CP2K by the Blue-Moon method. The results give consistent results: $\text{Li}^+ - \text{NO}_3^-$ ion pairs separated by a water molecule have lower free energy than the configuration in which Li^+ is in direct contact with NO_3^- .

We have also shown that the use of simple models, such as small cluster is not suitable to reproduce the experimental spectra and cannot provide a microscopic interpretation of the VSFG spectra. Realistic models of the interface are required to address the perturbation of ions on the water surface. The elucidated mechanism is possibly more general to anions which have high surface propensity for the solution/vapor interface, as for example other molecular ions.

From the results of nonlinear susceptibilities, which shows bonded OH-stretching peaks with higher frequencies, we conclude that the water molecules at the interfaces of LiI , NaI , and KI solutions are participating in weaker H-bonds, compared with those at the water/vapor interface. This conclusion is based on the DFTMD simulations, and the origin of the characteristics come from a unique distribution of I^- ions and alkali metal cations, which form a double layer [177] over the thickness on the order of 5 Å (see Appendix E).

For bulk system, based on the Luzar-Chandler HB population operator, we calculated the correlation functions $C_{\text{HB}}(t)$, $n(t)$, and $k(t)$, and obtained the reaction

rate constants with the HB formation and breakage, and then obtained the information about the HB lifetime. As we did in paragraph 7.1, we studied the population operators of nitrate ion–water hydrogen bond and iodide ion–water hydrogen bond and their correlation functions.

Based on the DFMD simulations, the MS method can *partially* gives information on the HB breaking and reforming rates through the water/vapor interface and therefore partially shows how much the interface affects the dynamics of H-bonds in water. This method *underestimates* the HB breaking rate constant of the water/vapor interface. We have provided a method based on the *instantaneous* interface and the new-defined *interfacial HB population* operator to obtain the interfacial HB dynamics of instantaneous water/vapor interfaces. Using the correlation functions based on IHB population operator, we directly calculated the HB dynamics of water layer with a certain thickness under the instantaneous surface. The IHB method allows us to avoid choosing which molecules reside in the interfacial layer and it also can provide partial information on the HB breaking and reforming rates at the interface. However, it *overestimates* the HB breaking rate constant. The calculation results in these two extreme cases indicate that the HB breaking and reforming rate constants in the water layer *below* the surface tends to be uniform (see Fig.6.14 a) as the thickness of the water layer increases. Therefore, the real HB dynamical characteristics at the water/vapor interface are derived from the two extreme cases. In particular, the result gives an estimate of the *thickness* ($\sim 3 \text{ \AA}$) of the water/vapor interface.

The combination of the methods of MS and IHB is extended to the solution interface. It has been confirmed that different ions in the electrolyte solution interface have their own unique distributions in the normal direction of the interface. Therefore, the thickness of the solution is greater than the thickness of the water/vapor interface. In addition, we also regarded the solvation shell of an ion as an interface, and defined the *SHB population* operator, which is an extension to the IHB population.

The difference between the HB dynamics for H-bonds between the first and the second solvation shell of the Li^+ and for nitrate-water H-bonds at the interface is not visible from the values of the HB relaxation time. They reflect the difference between HB dynamics in bulk water and at the water/vapor interface. For the alkaline iodide solution/vapor interfaces, we find that the cations does not alter the H-bonding network outside the first hydration shell. It is concluded that no long-range structural-changing effects for alkali metal cations. Moreover, we use the SHB method to calculate the HB dynamics for water molecules between the first and the second solvation shell. As far as the types of ions (Li^+ , Na^+ , K^+ , NO_3^- and I^- ions) are concerned, the HB dynamics for water molecule pairs does not vary significantly with the type of ions.

Finally, by calculating the rotational anisotropy decay, we obtain a main result: the average ratio of free OH bonds is the most important factor that affect the decay rate of the reorientation relaxation of water molecules. Faster rotational anisotropy decay is a quite good model for water molecules at the interface of aqueous alkali-iodine solutions, which is the result of a different HB types (D'AA) from the usual HB type (DDAA) in bulk water. This effect on anisotropy decay is due to the H–I bond at the interface. Since the iodide's surface propensity is high, this difference of HB structure from the water/vapor interface changed the $\text{Im}\chi^{(2),\text{R}}$ spectrum and the HB dynamics of the interface of alkali-iodine solution.

Appendix A

Calculation of nonlinear optical susceptibilities

Definitions and relations 1. Definition of double product of a m -order tensor A and a n -order tensor B is a tensor with order $m + n - 2$.

$$A : B = A_{ij} B_{lm} \delta_{jl} \delta_{im}. \quad (\text{A.1})$$

2. The components of product of AB is defined by

$$(AB)_{ijlm} = A_{ij} B_{lm}. \quad (\text{A.2})$$

3. For vectors \mathbf{a} , \mathbf{b} , \mathbf{c} and \mathbf{d} , $\mathbf{ab} : \mathbf{cd} = (\mathbf{a} \cdot \mathbf{d})(\mathbf{b} \cdot \mathbf{c})$.

Proof:

$$\begin{aligned} \mathbf{ab} : \mathbf{cd} &= (\mathbf{ab})_{ij} (\mathbf{cd})_{lm} \delta_{jl} \delta_{im} \\ &= (\mathbf{ab})_{ij} (\mathbf{cd})_{ji} \\ &= (a_i b_j) (c_j d_i) \\ &= (\mathbf{b} \cdot \mathbf{c})(\mathbf{a} \cdot \mathbf{d}) \end{aligned} \quad (\text{A.3})$$

Proof of Eq. 2.41 Since

$$\lim_{t \rightarrow \infty} |e^{-it(a-ib)}| \leq \lim_{t \rightarrow \infty} |e^{-bt}| = 0, \quad (\text{A.4})$$

we can obtain

$$\int_0^\infty dt e^{-it(a-ib)} = \frac{1}{b + ia}, \quad (\text{A.5})$$

i.e.,

$$i \int_0^\infty dt e^{-it(a-ib)} = \frac{1}{a - ib}. \quad (\text{A.6})$$

Set $a = (\omega_{v'} - \omega_v) - \omega$, and $b = \gamma_{v'v}$, then we have

$$\int_0^\infty dt e^{-it[(\omega_{v'} - \omega_v) - \omega - i\gamma_{v'v}]} = \frac{-i}{(\omega_{v'} - \omega_v) - \omega - i\gamma_{v'v}}.$$

Molecular dipole moment and dipole polarizability derivatives The polarizability tensor α is defined by the relation

$$\delta \mu = \alpha \mathcal{E} \quad (\text{A.7})$$

where $\delta\boldsymbol{\mu}$ is the electric dipole moment (a vector) induced in the molecule by the electric field \mathcal{E} , with the components $\mathcal{E}_x, \mathcal{E}_y$ and \mathcal{E}_z . Now we describe the main algorithm to implement the parametrization of the molecular dipole moment derivative $\frac{\partial\mu_k}{\partial r}$ and dipole polarizability derivative $\frac{\partial\alpha_{\eta\xi}}{\partial r}$. This result can be used in the velocity ACF-based method for calculating the VSFG spectroscopy intensity.

Given a DFT MD trajectory of total length $\sim 10^2$ ps for bulk water, sampled with a frequency ~ 1 ps $^{-1}$. For the j -th water molecule in the n -th snapshot of the trajectory, we denote the two OH bonds as $\text{H}^{n,j,\epsilon=1}$ and $\text{H}^{n,j,\epsilon=-1}$. We will calculate statistical average over all time steps and all OH bonds, therefore, we just denote the corresponding OH bonds by $\epsilon = 1$ and $\epsilon = -1$, respectively. The H atoms in a water molecule are denoted by $\text{H}^{\epsilon=1}$ and $\text{H}^{\epsilon=-1}$, and the O atom by O^0 .

We used three different frameworks: the lab framework (x^l, y^l, z^l) , the molecular framework (x^m, y^m, z^m) and the bond framework (x^b, y^b, z^b) (see Fig. 2.2). In the lab framework, the z^l -axis is perpendicular to the interface. The molecular frame will be used to decompose the signal into normal modes of water monomers. For the j -th molecule, the z^m axis is along the bisector of the H-O-H angle, the x^m axis is in the molecular plane, and the y^m axis is out of the molecular plane. In the bond framework, $z^{b,\epsilon}$ axis is along the bond ϵ of a molecule, $z^{b,\epsilon}$ is in the molecular plane and $y^{b,\epsilon}$ is out of the molecular plane.

There are two direction cosine matrices between the bond frameworks and molecular framework, we name them as $\mathbf{D}^{b,\epsilon=-1}$ and $\mathbf{D}^{b,\epsilon=1}$, [120] or $\mathbf{D}^{b,-1}$ and $\mathbf{D}^{b,1}$ for short. Then the direction matrix $\mathbf{D}^{b,\epsilon}$ can be represented by direction cosines between $\mathbf{x}^{b,\epsilon}$ and \mathbf{x}^m , where $\epsilon = \pm 1$ and θ denotes the H-O-H angle in the j -th water molecule for the n -step:

$$\hat{x}_1^{b,\epsilon} = \epsilon \cos \frac{\theta}{2} \hat{x}_1^m + \sin \frac{\theta}{2} \hat{x}_3^m \quad (\text{A.8a})$$

$$\hat{x}_2^{b,\epsilon} = \epsilon \hat{x}_2^m \quad (\text{A.8b})$$

$$\hat{x}_3^{b,\epsilon} = -\epsilon \sin \frac{\theta}{2} \hat{x}_1^m + \cos \frac{\theta}{2} \hat{x}_3^m \quad (\text{A.8c})$$

i.e.,

$$\mathbf{D}^{b,\epsilon} = \begin{pmatrix} \epsilon \cos \frac{\theta}{2} & 0 & \sin \frac{\theta}{2} \\ 0 & \epsilon & 0 \\ -\epsilon \sin \frac{\theta}{2} & 0 & \cos \frac{\theta}{2} \end{pmatrix}. \quad (\text{A.9})$$

The molecular framework is given by the direction cosine matrix $\mathbf{D}^{m,1}$ (or \mathbf{D}^m) between molecular framework and the lab framework

$$\hat{\mathbf{x}}^m = \mathbf{D}^m \hat{\mathbf{x}}^l. \quad (\text{A.10a})$$

The dipole moment of each OH bond with different length is required to determine the dipole moment derivative. Therefore, we elongate (reduce) one bond ϵ by $\Delta r = 0.05$ Å ($\Delta r = -0.05$ Å), and keep other bonds in the total system still, then we obtain a updated coordinate. Then the MLWF centers for the system can be calculated from the updated coordinate, using force and energy calculation at the DFT level. From the Wannier centers of the j -th water molecule, we can calculate the dipole moment for the elongated (reduced) bond ϵ . In the bond frame, $|\mu^b| = |\mu_z^b|$. Therefore, we can calculate the $k = z$ component of the dipole moment for ϵ in water molecule j from the MLWF centers. [237] The MLWF centers are computed and the partial dipole

moment for a given molecular species I is defined as [132]

$$\mu^I = \sum_{i \in I} (Z_i \mathbf{R}_i - 2 \sum_{n \in i} \mathbf{r}_n^w). \quad (\text{A.11})$$

In particular, here it is expressed as

$$\mu^{b,r+\Delta r,\epsilon} = \frac{1}{2} Z_O \mathbf{R}^0 + Z_H \mathbf{R}^\epsilon - 2r^{w,\epsilon} - 2r^{w,0}, \quad (\text{A.12})$$

where $\epsilon = \pm 1$. In the ϵ frame, the $k = z$ component dipole moment derivative with respect to bond length [238] for the single OH bond ϵ in water molecule j is

$$\frac{\partial \mu^{b,\epsilon}}{\partial r} = (\mu^{b,r+\Delta r,\epsilon} - \mu^{b,r,\epsilon}) / \Delta r. \quad (\text{A.13})$$

Since the components of the dipole moment in the molecular framework are given by the transformation:

$$\begin{pmatrix} (\frac{\partial \mu^m}{\partial r})_1 \\ (\frac{\partial \mu^m}{\partial r})_2 \\ (\frac{\partial \mu^m}{\partial r})_3 \end{pmatrix} = \mathbf{D}^{b,\epsilon} \begin{pmatrix} 0 \\ 0 \\ \frac{\partial \mu^{b,\epsilon}}{\partial r} \end{pmatrix}, \quad (\text{A.14a})$$

then, to calculate the individual polarizability for a OH bond from Wannier centers, calculations involving finite electric fields (of 0.0001 au intensity) were performed independently along x , y , and z directions at each sampled time step. [130] For the electric field $\mathcal{E} \in \{\mathcal{E}_x, \mathcal{E}_y, \mathcal{E}_z\}$, like in the case of no external electric field, the MLWF centers are calculated. For a finite Δr , the dipole moment is given by

$$\mu^{b,r+\Delta r,\epsilon,\mathcal{E}} = Z_H \mathbf{R}^{\epsilon,\mathcal{E}} + \frac{1}{2} Z^0 \mathbf{R}^{0,\mathcal{E}} - 2\mathbf{r}^{w,\epsilon,\mathcal{E}} - 2\mathbf{r}^{w,0,\mathcal{E}}. \quad (\text{A.15})$$

From the relation (obtained from Eq. A.7)

$$0 = \alpha_{11}^{b,r+\Delta r} \mathcal{E}_1 + \alpha_{12}^{b,r+\Delta r} \mathcal{E}_2 + \alpha_{13}^{b,r+\Delta r} \mathcal{E}_3 \quad (\text{A.16a})$$

$$0 = \alpha_{21}^{b,r+\Delta r} \mathcal{E}_1 + \alpha_{22}^{b,r+\Delta r} \mathcal{E}_2 + \alpha_{23}^{b,r+\Delta r} \mathcal{E}_3 \quad (\text{A.16b})$$

$$\delta \mu_3^{b,r+\Delta r} = \alpha_{31}^{b,r+\Delta r} \mathcal{E}_1 + \alpha_{32}^{b,r+\Delta r} \mathcal{E}_2 + \alpha_{33}^{b,r+\Delta r} \mathcal{E}_3. \quad (\text{A.16c})$$

where

$$\delta \mu_3^{b,r+\Delta r} = \mu_3^{b,\epsilon,r+\Delta r,\mathcal{E}} - \mu_3^{b,\epsilon,r+\Delta r}. \quad (\text{A.17})$$

and the expressions of the electric field \mathcal{E}^b in a OH framework for the 3 cases of external electric field which is along x , y and z axis in the lab framework, respectively, we obtain 9 equations. For

$$\mathcal{E}^l = (\mathcal{E}_0, 0, 0)^T$$

where $\mathcal{E}_0 = 0.0001$ au, we can obtain the intensity of the external electric field in the molecular framework

$$\mathcal{E}_1^m = \mathbf{D}_{12}^m \mathcal{E}_2^l \quad (\text{A.18a})$$

$$\mathcal{E}_2^m = \mathbf{D}_{22}^m \mathcal{E}_2^l \quad (\text{A.18b})$$

$$\mathcal{E}_3^m = \mathbf{D}_{32}^m \mathcal{E}_2^l, \quad (\text{A.18c})$$

where \mathbf{D}_{pq}^m is the pq -component of \mathbf{D}^m . In OH bond framework,

$$\mathcal{E}^b = \mathbf{D}^b \mathcal{E}^m. \quad (\text{A.19})$$

Similarly, we obtain similar (but different) expansions of the intensity of the electric field for the other two cases: when $\mathcal{E}^1 = (0, \mathcal{E}_0, 0)^T$ and when $\mathcal{E}^1 = (0, 0, \mathcal{E}_0)^T$, respectively. Here, \mathcal{E}_x is the electric field along x -axis in the lab frame. Then the dipole polarizability for the bond ϵ is as follows:

$$\frac{\partial \alpha_{31}^{b,\epsilon}}{\partial r} = (\alpha_{31}^{b,\epsilon,r+\Delta r} - \alpha_{31}^{b,\epsilon,r})/\Delta r \quad (\text{A.20a})$$

$$\frac{\partial \alpha_{32}^{b,\epsilon}}{\partial r} = (\alpha_{32}^{b,\epsilon,r+\Delta r} - \alpha_{32}^{b,\epsilon,r})/\Delta r \quad (\text{A.20b})$$

$$\frac{\partial \alpha_{33}^{b,\epsilon}}{\partial r} = (\alpha_{33}^{b,\epsilon,r+\Delta r} - \alpha_{33}^{b,\epsilon,r})/\Delta r. \quad (\text{A.20c})$$

Therefore, the average for $(\frac{\partial \mu^{b,\epsilon}}{\partial r})_\kappa$ and $(\frac{\partial \alpha^{b,\epsilon}}{\partial r})_{\eta\xi}$ (The subscripts $\kappa, \eta, \xi = x^m, y^m, z^m$, or 1, 2, 3) over all OH bonds gives the molecular dipole and polarizability derivatives.

Appendix B

Computational details of the DFTMD simulations

The DFT calculations were done with the CP2K program[104, 105], which incorporates the Gaussian and Plane Waves (GPW) method[239]. Core electrons were described by Goedecker-Teter-Hutter pseudopotentials[240], while the valence electrons were expanded as a double-zeta Gaussian basis set. The double zeta basis sets optimized for the condensed phase[241] were used in conjunction with GTH pseudopotentials[242] and a 280 Ry cutoff for the auxiliary plane wave basis. The discretized integration time step Δt was set to 0.5 fs. The Brillouin zone was sampled at the Γ -point only and, the BLYP XC functional has been employed. All simulations for water/vapor interface and aqueous solutions were performed within the canonical NVT ensemble.

Bulk water To simulate the bulk water for testing the algorithm of IHB, we constructed the following model. The number of water molecules in the simulation system is 128, the temperature is still $T = 300$ K, and the box is a cube with a side length of 15.64 Å. In this simulation, we relax the value of the target accuracy for the SCF convergence to 10^{-6} . The size of the simulation box is obtained as follows: According to the experimentally obtained relations between water density, temperature and ion concentration (if ions are present), a nonlinear equation set is established, and then the equation set is solved to find the box size.

Lithium nitrate solutions The simulated interfacial system consisted of 127 water molecules and a Li^+ -nitrate pair in a periodic box of size $15.78 \times 15.78 \times 31.56$ Å³, which corresponds to a density of 0.997 g/cm³. At each DFTMD step the corrector was applied only once, which implies just one preconditioned gradient calculation. For a given molecular configuration, $\{\mathbf{r}_i(t)\}$, Eq. 6.17 can be solved through interpolation on a spatial grid.[211] We have taken $\{\mathbf{r}_i(t)\}$ to refer to the positions of all atoms except hydrogen atoms in the system, and because the bulk correlation length of liquid water is about one molecular diameter, we have used $\xi = 2.4$ Å; further, we have used $\rho_0 = 0.016$ Å⁻³, which is approximately one-half the bulk density of water.

This calculation of the $\chi^{(2,R)}$ is done for a model for the water/vapor interface where a slab of 117 water molecules containing one Li^+ and one NO_3^- is included in a period simulation box of $15.60 \text{ Å} \times 15.60 \text{ Å} \times 31.00 \text{ Å}$ at 300 K.

For the interface of the LiNO_3 solution, we performed the simulation on a system containing one Li^+ ion, one nitrate ion and 127 water molecules (concentration: ~ 0.4 M). The size of periodic box is $15.78 \times 15.78 \times 31.56$ Å³.

For the interface of the NaNO_3 solution, the size of periodic box is $15.65 \times 15.65 \times 31.31$ Å³. For the interface of the KNO_3 solution, the size of periodic box is $15.72 \times 15.72 \times 31.43$ Å³.

The simulated bulk alkali metal nitrate LiNO_3 , NaNO_3 , and KNO_3 solution consisted of one alkali metal ion, one nitrate ion and 127 water molecules in a periodic cubic box of length L , which corresponds to their density of $\sim 1.00 \text{ g cm}^{-3}$. Here, $L = 15.78$, 15.65 , and 15.72 for LiNO_3 , NaNO_3 , and KNO_3 solution, respectively.

Water/vapor interface For the calculation of the nonlinear susceptibility $\chi^{(2,\text{R})}$ of water/vapor interface, the water/vapor interface is modeled with a slab made of 121 water molecules in a simulation box of size $15.60 \times 15.60 \times 31.00 \text{ \AA}^3$. For this water/vapor interface, the DFTMD simulations at 300 and 330 K are also calculated.

Interface of alkali-iodine solution The calculation of the $\chi^{(2,\text{R})}$ is done for a model for water/vapor interface where a slab of 118 water molecules containing one Li^+ and one I^- is included in a period simulation box of $15.60 \text{ \AA} \times 15.60 \text{ \AA} \times 31.00 \text{ \AA}$.

Appendix C

Structural characterization of water clusters and solutions

C.1 Water clusters

The structural parameters of the considered water clusters are shown here. Table C.5 gives the average HB lengths r_a (with standard deviations) in $[\text{NO}_3 \cdot (\text{H}_2\text{O})_3]^-$. Table C.2 (C.3) reports the selected distances characterizing $[\text{NO}_3 \cdot (\text{H}_2\text{O})_3]^-$ ($\text{RNO}_3(\text{H}_2\text{O})_3$), and Table C.4 the selected parameters for $\text{RNO}_3(\text{H}_2\text{O})_3$ ($\text{R}=\text{Li}, \text{Na}, \text{K}$). The unit for length and angle are Å and degree ($^\circ$), respectively.

TABLE C.1: The HB lengths r_a in $[\text{NO}_3 \cdot (\text{H}_2\text{O})_3]^-$ at 300 K.

HB bound to	r_a
w1	2.40 ± 0.52 ; 3.02 ± 0.72
w2	2.56 ± 0.48 ; 3.20 ± 0.41
w3	2.29 ± 0.47 ; 3.11 ± 0.72

TABLE C.2: The parameters of water molecules and H-bonds in $[\text{NO}_3 \cdot (\text{H}_2\text{O})_3]^-$ at 300 K.

water	R_{OH}	$\angle\text{HOH}$	r_{OH}
w1	0.98 ± 0.02	101 ± 4	2.40 ± 0.52 , 3.02 ± 0.72
w2	0.98 ± 0.02	101 ± 5	2.56 ± 0.48 , 3.20 ± 0.41
w3	0.98 ± 0.02	101 ± 4	2.29 ± 0.47 , 3.11 ± 0.72

TABLE C.3: The structural parameters of $\text{RNO}_3(\text{H}_2\text{O})_3$ from geometry optimization.

Parameters	$\text{LiNO}_3(\text{H}_2\text{O})_3$	$\text{NaNO}_3(\text{H}_2\text{O})_3$	$\text{KNO}_3(\text{H}_2\text{O})_3$
r_{HB1}	1.67	1.71	1.82
r_{HB2}	1.91	1.78	1.92
r_{HB3}	1.82	1.69	1.94
$r_{\text{R-O(w1)}}$	1.91	2.31	2.70
$r_{\text{R-O(w2)}}$	1.90	2.26	2.70
$r_{\text{R-O}(\text{NO}_3^-)}$	1.84	2.29	2.69
$\angle\text{HOH(w1)}$	109	106	107
$\angle\text{HOH(w2)}$	106	105	105
$\angle\text{HOH(w3)}$	108	107	106

TABLE C.5: The lengths of H-bonds in $[\text{NO}_3 \cdot (\text{H}_2\text{O})_3]^-$. The indices of H atoms: H6, H7 in w1; H9, H10 in w2 and H12, H13 in w3.

HBs	$r_a \pm \delta$ (100 K)(Å)	$r_a \pm \delta$ (300 K) (Å)
H6-O2	2.75 ± 0.62	2.40 ± 0.52
H7-O4	2.79 ± 0.58	3.02 ± 0.72
H9-O3	2.89 ± 0.60	2.56 ± 0.48
H10-O4	2.74 ± 0.49	3.20 ± 0.41
H12-O3	2.46 ± 0.45	2.29 ± 0.47
H13-O2	2.75 ± 0.59	3.11 ± 0.72

TABLE C.4: The parameters of $\text{RNO}_3(\text{H}_2\text{O})_3$ at 300 K, obtained from the averaging during a DFTMD trajectory. For $\text{RNO}_3(\text{H}_2\text{O})_3$, R_{OH} and R'_{OH} denote the lengths of O-H bonds in which H atoms is H-bonded and is free, respectively.

Parameters	$\text{LiNO}_3(\text{H}_2\text{O})_3$	$\text{NaNO}_3(\text{H}_2\text{O})_3$	$\text{KNO}_3(\text{H}_2\text{O})_3$
r_{HB1}	1.83 ± 0.14	1.78 ± 0.09	1.82 ± 0.13
r_{HB2}	2.00 ± 0.25	1.91 ± 0.24	1.80 ± 0.12
r_{HB3}	1.79 ± 0.16	1.76 ± 0.11	1.89 ± 0.18
$R_{\text{OH}}(\text{w1})$	0.97 ± 0.01	0.98 ± 0.04	0.97 ± 0.03
$R'_{\text{OH}}(\text{w1})$	1.00 ± 0.02	1.00 ± 0.02	1.00 ± 0.03
$R_{\text{OH}}(\text{w2})$	0.97 ± 0.01	0.98 ± 0.02	0.97 ± 0.02
$R'_{\text{OH}}(\text{w2})$	0.99 ± 0.01	1.00 ± 0.02	1.00 ± 0.03
$R_{\text{OH}}(\text{w3})$	0.97 ± 0.01	0.97 ± 0.02	0.97 ± 0.03
$R'_{\text{OH}}(\text{w3})$	1.00 ± 0.02	1.00 ± 0.02	1.00 ± 0.03
$r_{\text{R-O}}(\text{w1})$	1.95 ± 0.09	2.34 ± 0.08	2.76 ± 0.11
$r_{\text{R-O}}(\text{w3})$	1.92 ± 0.07	2.32 ± 0.11	2.74 ± 0.13
$r_{\text{R-O}}(\text{NO}_3^-)$	1.91 ± 0.08	2.31 ± 0.09	2.74 ± 0.12
$\angle \text{HOH}(\text{w1})$	107 ± 4	106 ± 4	105 ± 5
$\angle \text{HOH}(\text{w2})$	106 ± 6	105 ± 4	106 ± 4
$\angle \text{HOH}(\text{w3})$	108 ± 5	106 ± 3	106 ± 3

Structural and vibrational properties of $[\text{NO}_3 \cdot (\text{H}_2\text{O})_3]^-$ To find the possible source of the different vibrational features of water molecules in the cluster $[\text{NO}_3 \cdot (\text{H}_2\text{O})_3]^-$, we considered the structural properties and VDOS for water molecules in the cluster $[\text{NO}_3 \cdot (\text{H}_2\text{O})_3]^-$.

The lengths of H-bonds in $[\text{NO}_3 \cdot (\text{H}_2\text{O})_3]^-$ is shown in Table C.5. The nitrate O (ON)–water O (OW) and nitrate O–water H (HW) RDFs for this cluster is shown in Fig. C.1.

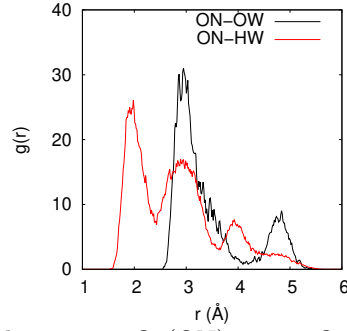


FIGURE C.1: The nitrate O (ON)–water O (OW) and nitrate O–water H (HW) RDFs for $[\text{NO}_3 \cdot (\text{H}_2\text{O})_3]^-$. The peaks for the former are 1.93, 2.95 and 3.95 Å, and for the later are 2.95 and 4.80 Å.

When $T = 300$ K, the difference r_a between different hydrogen atoms in one water molecule is $\Delta r_a = 0.69$ Å, while $\Delta r_a = 0.13$ Å for $T = 100$ K. It shows that the vibrational peaks for the three water molecules are much closer than that at the higher temperature 300 K.

The calculated VDOS for water molecules in the cluster at a lower temperature 100 K is given in Fig. C.2. This figure shows that the vibrational peaks for the three water molecules are very close to each other ($\Delta\nu < 10 \text{ cm}^{-1}$) for both vibrational and bending modes. At the lower temperature, the three water molecules are more symmetric distributed bound to the central nitrate. Therefore, the difference between H-bonds in the symmetric isomer of $[\text{NO}_3 \cdot (\text{H}_2\text{O})_3]^-$ is likely a finite temperature effect, which can be verified by the calculation of the VDOS for water molecules.

Both differences $\Delta\nu$ and Δd decrease as the temperature decrease, Therefore, the different vibrational features are temperature-dependent effect.

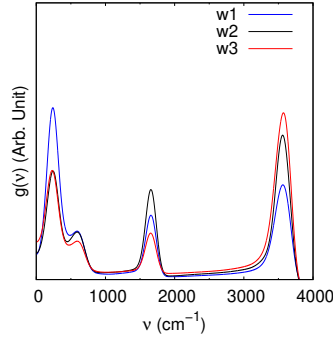


FIGURE C.2: The VDOS $g(\nu)$ for water molecules in the cluster $[\text{NO}_3 \cdot (\text{H}_2\text{O})_3]^-$ at 100 K.

In addition, the VDOS for H atoms and water molecules in $[\text{NO}_3 \cdot (\text{H}_2\text{O})_3]^-$ (Fig. C.3) shows that H's contribution dominates that of the water molecule.

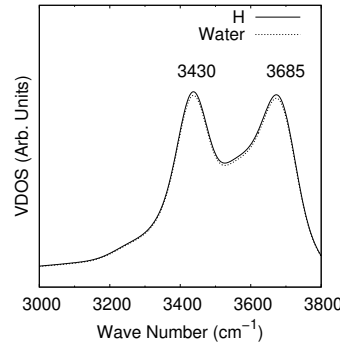


FIGURE C.3: The comparison between the VDOS for H and for a whole water molecule (w1, Fig. 4.1 a), in $[\text{NO}_3 \cdot (\text{H}_2\text{O})_3]^-$ at 300 K.

C.2 Soution/vapor interfaces

Dipole orientation distribution of water at aqueous/vapor interfaces Set θ as the angle between the dipole moment of water molecules and the normal vector of the interface, and $P(\theta)$ as the probability. The data used to statistics is the dipole tilt angle θ_i . We use the θ_i instead of $\langle \theta \rangle$ to do the statistics. With picking up θ_l , $l = 0, 10, 20, \dots$ from the series θ_i , we find that pure water's dipole moment tilt angle is smaller than that of water molecules at the salty water surface. This result means that on the pure water surface, water molecules have more p -polarization components than those in the salty water surface. However, the water molecules at the salty water surface has more s -polarization component. The result is shown in Fig. C.4.

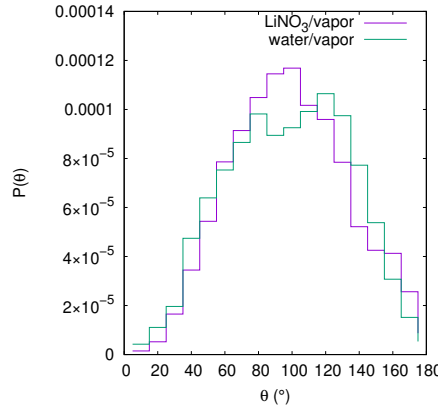


FIGURE C.4: The dipole orientation distribution of water molecules at the water/vapor and the LiNO_3 solution/vapor interfaces.

RDFs in alkali nitrate solutions The RDFs $g_{\text{Li-OW}}(r)$, $g_{\text{Li-HW}}(r)$, $g_{\text{ON-OW}}(r)$ and $g_{\text{ON-HW}}(r)$ in bulk LiNO_3 solution is shown in Fig. C.5.

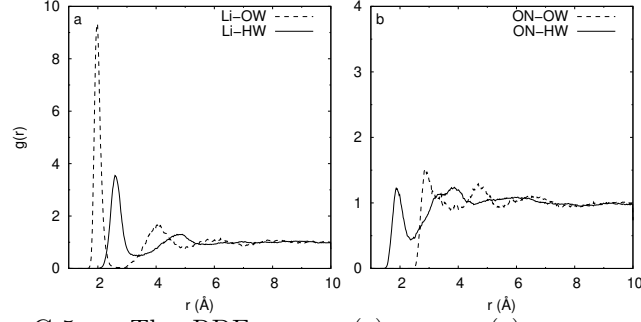


FIGURE C.5: The RDFs $g_{\text{Li-OW}}(r)$, $g_{\text{Li-HW}}(r)$, $g_{\text{ON-OW}}(r)$ and $g_{\text{ON-HW}}(r)$ in bulk LiNO_3 solution.

RDFs in alkali iodide solutions The RDFs $g_{\text{Li-OW}}(r)$, $g_{\text{Li-HW}}(r)$, $g_{\text{I-OW}}(r)$ and $g_{\text{I-HW}}(r)$ for the interface of the LiI solution is shown in Fig. C.6.

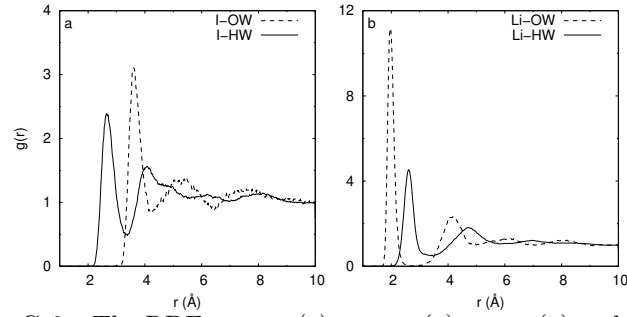


FIGURE C.6: The RDFs $g_{\text{Li-OW}}(r)$, $g_{\text{Li-HW}}(r)$, $g_{\text{I-OW}}(r)$ and $g_{\text{I-HW}}(r)$ for the interface of LiI solution.

The radii of second solvation shells are: 5.0 \AA for Li^+ , 5.38 \AA for Na^+ , and 6.0 \AA for I^- ions, which are obtained from the RDFs. The RDFs $g_{\text{X-O}}$ ($\text{X}=\text{Li}^+$, Na^+ , K^+) for the interfaces of LiI (NaI , KI) solutions are shown in Fig. C.7 (a), and the coordination numbers are in Fig. C.7 b.

From Fig. C.7, we see that the radius of the solvation shells of Li^+ ions, Na^+ ions, and K^+ ions increase sequentially, and the number of coordination molecules also increase sequentially. However, this order is not true for the relaxation time of HB dynamics between water molecules in the first solvation shell of the ion and other water molecules. As can be seen later (Fig. 7.5), the effects of the alkali metal ions and iodide ions are very similar, that is, the relaxation time of the HB dynamics in the outer layer is smaller than that in bulk water.

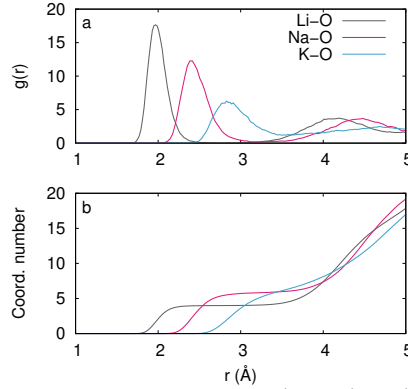


FIGURE C.7: (a) RDFs $g_{\text{X-O}}(r)$ ($\text{X}=\text{Li}^+, \text{Na}^+, \text{K}^+$) and (b) the coordination number of Li^+ (Na^+, K^+) ions at the interfaces of LiI (NaI, KI) solution. The coordination number $n_{\text{Li}^+}=4$, $n_{\text{Na}^+}=5$ and $n_{\text{K}^+}=6$.

TABLE C.6: The coordination number for ions in LiI (NaI) solution.

name	r_{shell} (Å)	coordination number
$n_{\text{Li-O}}$	3.0	4.0
$n_{\text{I-H}}$	3.3	5.5
$n_{\text{Na-O}}$	3.5	6.0
$n_{\text{I-O}}$	4.3	5.8

C.3 Classification of water molecules based on H-bonds

Here we discuss the relation between the reorientation relaxation time of water molecules and their environment. The basic method is as follows: classifying the water molecules at solution/vapor interfaces based on the types of H-bonds and the number of H-bonds. For both alkali nitrate and alkali iodide solutions, these two factors are main reasons to result in different reorientation relaxation time of water molecules.

Alkali nitrate solutions For alkali nitrate solution/vapor interfaces, we can classify the water molecules into three types. Because nitrate ions have more surface propensity (see Fig. 5.2), and we have studied the effect of alkali cations on the reorientation relaxation of water molecules, we only consider LiNO_3 solution/vapor interface.

The three types of water molecules are: nitrate-bound water, water at the water/vapor interface, and bulk water. We have known that nitrate-bound water are located at the solution/vapor interface (the thickness ~ 2 Å, see Fig. 5.4). Therefore, among the three types, the first two types of water molecules are interfacial ones. For each type of water molecules, we have chosen *six* water molecules for obtaining the correlation function $C_2(t)$. The MS sampling method (see paragraph E.1) is used to choose the water molecules for each type.

Lithium iodide solution Following the definition used in Ref.[14], we use the following labels to denote water molecules in an alkali iodide solution: D denotes that the water molecule donates a HB, D' donates a H-I bond, and A accepts a HB. [14] DDAA represents a water molecule with two H-Bonds donated to water molecules and two H-bonds accepted from water molecules (see Fig. C.8 a); DD'AA represents

a water molecule with two H-bonds donated to a water molecule and I^- (see Fig. C.8 b), and with two H-bonds accepted from other water molecules (see Fig. C.8 c), D'AA represents a water molecule bonded to I^- at the water/vapor interface and other H-bonds to water molecules (see Fig. C.8 d). Clearly, we found that D'AA molecules are of free OH stretching during the dynamics.

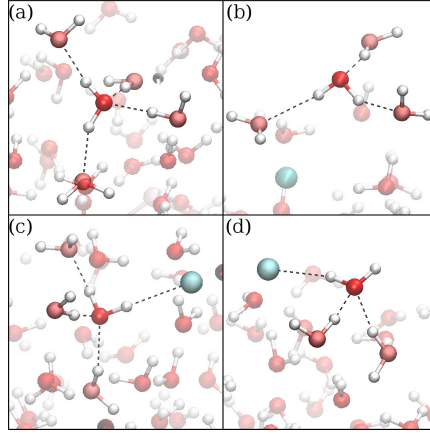


FIGURE C.8: Four types of water molecules at the LiI solution/vapor interface, regarding the HB environments: (a) DDAA; (b) DDA; (c) DD'AA; (d) D'AA. The cyan balls denote I^- ions.

It is evident that $C_2(t)$ for DDAA and DD'AA molecules do not decay exponentially (Fig. C.9 and Table C.7). This result is similar to the reactive flux function $k(t)$, i.e., the escaping rate kinetics of H-bonds in bulk water. [178] The relaxation of H-bonds in water appears complicated, with no simple characterization in terms of a few relaxation rate constants. Most of the authors believe that the cooperation between neighbouring H-bonds, [192, 243] or self evident coupling between translational diffusion and HB dynamics is the source of the complexity. [178] However, for D'AA molecules at the LiI solution/vapor interface, the $C_2(t)$ decays exponentially, i.e.

$$C_2(t) = Ce^{-t/\tau_2},$$

where the amplitude is $C = 0.76$, and the reorientation rate is $1/\tau_2 = 7.14 \text{ ps}^{-1}$. The single exponential decay of $C_2(t)$ for D'AA molecules, indicates that each D'AA molecule reorientate independently to each other.

Furthermore, the $C_2(t)$ for D'AA molecules decays much faster than that for DDAA or DD'AA molecules. From the definitions, the D'AA molecule accepts two H-bonds and donates only one H-bond, while both DDAA and DD'AA water molecules own *four* H-bonds. Therefore, the correlation between H-bonds around the D'AA molecule is weaker than those around the DDAA or DD'AA molecule. Faster decay of $C_2(t)$ for D'AA molecules shows that the reorientation process of D'AA molecules is faster than water molecules in bulk phase, e.g., DDAA or DD'AA molecules.

Additionally, a D'AA molecule has a free OH chemical bond, which can stretch and vibrate freely. This feature is not available in other types of molecules such as DDAA, DD'A, DD'AA, etc. Therefore, at the LiI solution/vapor interface, the most closely related feature of the molecular orientation relaxation process is the number of H-bonds *donated* by water molecules. The result that D'AA molecules have shortest relaxation time among the four types of water molecules implies that the factor $\langle n \rangle_{\text{HB}}$, the average number of H-bonds per water molecule, palys dominate

role. This conclusion is consistent with the one obtained from above discussion for $\text{LiNO}_3/\text{vapor}$ interface.

Besides, the type (or strength) of HB (water–water, or ion–water) also affects the orientation relaxation process, which is also consistent with the above conclusion about $\text{LiNO}_3/\text{vapor}$ interface. However, from our calculation, the number of H-bonds *accepted* by water molecules has no major effect on the orientation relaxation of the water molecules at the interface.

Finally, D'AA molecules' inertial-librational motion can not be seen in Fig. C.9. This result implies that the rotational anisotropy decay of D'AA molecules are of the same time scale of the inertial libration, i.e., ~ 0.2 ps. This conclusion can be verified from the value of τ_2 in Table C.7: $\tau_2 = 0.97$ for D'AA molecules, which is smaller than the τ_2 for DDAA, DD'A, and DD'AA molecules.

To summarize, rotational anisotropy decay of water molecules under different local environments is calculated at the LiI solution/vapor interface. The result comes from a different HB types from the usual DDAA HB type in bulk water. The faster anisotropy decay for D'AA molecules reflects the less correlation between different H-bonds for D'AA molecules, which comes from Hydrogen–Iodide bond at the interfaces and the existence of free OH stretching. As we already known from Fig. 5.7, in the LiI solution, I^- ions prefer to locate at the interface. Therefore, we infer that the reduction of the inter-correlations between H-bonds occurs at the interface. Slower rotational anisotropy decay exists for water molecules at the alkali-iodide solution/vapor interfaces, which is the result of a different H-Bond types (D'AA) from DDAA-type molecules in bulk water. The slowing down of anisotropy decay is the effect of Hydrogen-Iodide bonds at the interface. Since the iodide's surface propensity is high, this difference of HB structure from the water/vapor interface changed the $\text{Im}\chi^{(2)}$ spectrum and the total HB dynamics of the interface of alkali-iodide solutions.

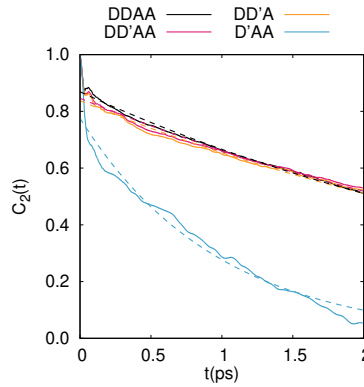


FIGURE C.9: Time dependence of $C_2(t)$ for DD'A, DD'AA, and D'AA water molecules at the LiI solution/vapor interface.

TABLE C.7: Biexponential fitting (2 ps) of $C_2(t)$ for water molecules in the LiI solution. The relative standard errors: $\Delta A/A \leq 10^{-2}$, $\Delta\tau_2/\tau_2 \leq 3 \times 10^{-2}$.

water molecules	A	τ_2 (ps)
DD'A	0.84	4.04
DD'AA	0.85	4.08
DDAA	0.87	3.76
D'AA	0.78	0.97

Appendix D

Propensities of ions

D.1 Free energy of the water separated and the contact ion pair

From the blue-moon ensemble method[244, 245], we can obtain the constraint force (unit: a.u.force) acting on the atoms. If the distance between the ion pair (unit: Å) is chosen as the reaction coordinate, the formula for calculating the free energy (unit: kcal/mol) is given as follows. The relative free energy is given by

$$F = \sum_i^N f_i \Delta r,$$

where i denote a point on the one-dimensional reaction coordinate, N is the number of the sampling points of the reaction coordinates, and f_i denotes the average force on atoms over the trajectory when i is fixed. Now we estimate the error of the free energy δF from the summation approximation. It reads

$$\delta F = \frac{1}{N} \sum_i^N \delta f_i \Delta r. \quad (\text{D.1})$$

Usually, $\delta f_i \approx \delta f$, thus

$$\delta F = \frac{1}{N} \delta f \sum_i^N \Delta r. \quad (\text{D.2})$$

Particularly, if $\Delta r = 0.2$ Å, $\delta f = 0.0075$ a.u.force, we get

$$\delta F \approx 1.78 \text{ kcal/mol.}$$

D.2 Ion–surface distance

The ion–surface distances for the aqueous solution/air interfaces are given below.

Figure D.1 shows the time dependence of K⁺–surface and I[−]–surface distances.

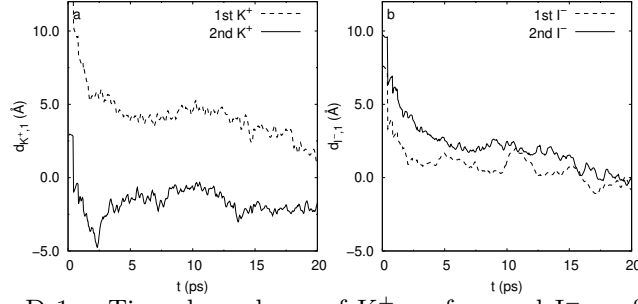


FIGURE D.1: Time dependence of K^+ -surface and I^- -surface distances for KI solution.

D.3 Surface tension increment

The surface tension increment $d\gamma/dm_2$ is derived as follows. At constant temperature T and constant pressure p , the Gibbs-Duhem equation is: [140]

$$Ad\gamma + n_1^\sigma d\mu_1 + n_+^\sigma d\mu_+ + n_-^\sigma d\mu_- = 0, \quad (D.3)$$

where water is component 1, and the chemical potential for the ionic species i ($i = +, -$) is defined as

$$\mu_i = \mu_i^0 + RT \ln a_i + z_i F \phi, \quad (D.4)$$

where F is Farady constant, ϕ is the electrical potential of this region (surface or bulk), and z_i is the valence of species i , with ionic activity $a_i = f_i m_i$ in that region, where f_i is the activity coefficient, and m_i is the surface or bulk molality of the ion.

Differentiate Eq. D.3 with respect to m_2 , then the surface tension increment is

$$\frac{d\gamma}{dm_2} = -\frac{1}{m_1^*} \frac{n_1^\sigma}{A} [(m_+^\sigma - m_+^b) \frac{d\mu_+}{dm_2} + (m_-^\sigma - m_-^b) \frac{d\mu_-}{dm_2}], \quad (D.5)$$

where m_1^* is the solvent molality.

For species i , distribution coefficient $K_{p,i}$, is defined as

$$K_{p,i} = \frac{m_i^\sigma}{m_i^b} \approx \frac{m_i^\sigma}{\nu_i m_2}. \quad (D.6)$$

$$\frac{d\mu_\pm}{dm_2} = \frac{RT}{m_2} (1 + \epsilon_\pm^b) + z_\pm F \frac{d\phi^b}{dm_2} \approx \frac{RT}{m_2} (1 + \epsilon_\pm^b), \quad (D.7)$$

where $\epsilon_\pm^b = d(\ln f_\pm^b)/d(\ln m_2)$.

The ion partition coefficients $K_{p,2}$ is defined:

$$\nu K_{p,2} = \nu_+ K_{p,+} + \nu_- K_{p,-}, \quad (D.8)$$

where ν_i is ions' stoichiometry.

In general, from Eq. D.5, Eq. D.6 and Eq. D.7, for solutions at sufficient low electrolyte concentrations, the surface tension increment is

$$\begin{aligned} \frac{d\gamma}{dm_2} &= -\frac{1}{m_1^*} \frac{n_1^\sigma}{A} \sum_{i=\pm} (m_i^\sigma - m_i^b) \frac{d\mu_i}{dm_2} \\ &= -\frac{RT\nu}{m_1^*} \frac{n_1^\sigma}{A} \sum_{i=\pm} \frac{\nu_i (K_{p,i} - 1) (1 + \epsilon_i^b)}{\nu} \end{aligned}$$

$$= -\frac{RT\nu}{m_1^*} \frac{n_1^\sigma}{A} [(K_{p,2} - 1) + \sum_{i=\pm} \frac{(K_{p,i} - 1)\nu_i \epsilon_i^b}{\nu}] \quad (\text{D.9})$$

Under the condition $\epsilon_\pm^b \ll 1$ or $\epsilon_+^b \approx \epsilon_-^b$ the surface tension increment is

$$\frac{d\gamma}{dm_2} = -\frac{RT\nu}{m_1^*} \frac{n_1^\sigma}{A} (1 + \epsilon_i^b)^0 \left[\frac{\nu_+ K_{p,+} + \nu_- K_{p,-}}{\nu} - 1 \right]. \quad (\text{D.10})$$

The approximations in Eq. D.10 regarding the self-interaction nonideality terms ϵ for the salt component, for the single ions, and as a geometric mean of the single ion terms, are given in Ref.[140]. Typically the mean ionic version of ϵ is of order ~ 0.1 , so smaller in magnitude than 1. (Thomas Record) Here, *nonideality* means the activity coefficient f_i is not much smaller than 1.

Appendix E

Thickness of the interface of aqueous solutions

E.1 Interfacial hydrogen bond dynamics

Instantaneous Surfaces Let us consider the interfacial system of pure water. At a certain time t , the instantaneous surface $\mathbf{s}^0(x(t), y(t))$ can be determined by calculating the coarse-graining density field: we can specify that the coarse-grained density is the reference density $\rho_{\text{ref}} = 0.016 \text{ \AA}^{-3}$, and those grid points constitute the surface $\mathbf{s}^0(x, y)$ of pure water. In our simulated pure water system, there are two such surfaces. The code for calculating the instantaneous surfaces of interfacial systems can be found on <https://github.com/hg08/interface>.

Griding and layering We assume that the normal is along the z -axis direction. First, we discretize the coordinates of the xy plane. We divide the edges along the x -axis direction and the edges along the y -axis direction of the simulated box into N parts uniformly, and the xy plane can be approximated by $N \times N$ discrete points. Then $N \times N$ ordinates of the surface $\mathbf{s}^0(x(t_0), y(t_0))$ at the initial time t_0 can be represented as components of an $N \times N$ -vector $\mathbf{z}^0(t_0)$. The surface $\mathbf{s}^0(x(t_0), y(t_0))$ is also the upper boundary of the interface. Secondly, we define a layering strategy, or define the thickness d of the interface layer. In this way, we then determine the lower boundary $\mathbf{s}^1(x(t_0), y(t_0))$ of the interface. It can be expressed as a $N \times N$ -vector $\mathbf{z}^1(t_0) = \mathbf{z}^0(t_0) - \mathbf{d}$, and \mathbf{d} is a $N \times N$ -dimensional constant vector in which all the entries are d . The superscripts 0 and 1 respectively identify the upper and lower boundaries of the interface. Similarly, the other interface can also be determined.

So far, our interfaces are still static, because we only considered the initial moment. But the instantaneous interfaces can be defined for different moments naturally. Therefore, according to the same method, for the molecular motion trajectory of an interface system, we can obtain the dynamically changing interface layer, i.e., $\mathbf{z}^1(t) = \mathbf{z}^0(t) - \mathbf{d}$. When the interfaces are determined, we can answer the question: For an atom with coordinates (x, y, z) at any time t , whether it is in the interface? To answer this question, we map the atom's coordinates (x, y) to an ordered integer pair (i, j) , $i, j \in \{0, \dots, N\}$, where $i = \text{int}(x/\Delta x)$, $j = \text{int}(y/\Delta y)$, $\Delta x = a/N$, and $\Delta y = b/N$.

At a certain time t , the ordinate z of an atom can be approximately represented as a function defined on point (i, j) , $z = z(i, j)$. Then we compare $z(i, j)$ and $z_{i,j}^l$, $l = 0, 1$ to determine if the atom is in the interface. That is, if $z_{i,j}^0(t) < z(i, j) < z_{i,j}^1(t)$, then the atom at (x, y, z) is located in the interface at time t .

Molecule Sampling (MS) from instantaneous interface The method of Molecule Sampling used to extract the interfacial molecules is as follows. 1) Determine the instantaneous surface of the water/vapor interface system; 2) Define a interfacial layer with a fixed thickness d below the surface; 3) Select the atoms which are near the instantaneous surface; 4) Calculate the HB dynamics for molecules in interface at different time t . Given the thickness of layer d , at any sampling time $t_0, t_1, t_2, \dots, t_n$, the set of molecules in the interface can be determined. Since the molecules are always in motion, generally, the set $S^0(t_i)$ of the molecules in the interface at time t_i and the set $S^0(t_j)$ of the molecules in the interface at a different time t_j is different. Therefore, to calculate the HB dynamics of molecules in the interface, we calculate the correlation functions of the HB population $h(t)$ of the molecules in the interface at different times, and calculate the *average* of the obtained correlation functions over the n functions, e.g., $C_{HB,j}(t), j = 1, \dots, n$.

Interfacial hydrogen bond population operator $h^{(s)}(t)$ The IHB method to extract the interfacial molecules is as follows. 1) Determine the instantaneous surface of a system; 2) Define a interface system with a fixed thickness below the instantaneous surface; 3) Define the interfacial hydrogen bond population operator $h^{(s)}(t)$. 4) Calculate the autocorrelation function of $h^{(s)}(t)$ and then the related observations.

If we want to calculate dynamical characteristics of the molecules located in the interface layer, the MS method will have a error in select correct molecules in interface. In chapter 6, we had combined the recognition technology of the instantaneous liquid interfaces [211] with the definition of H-bonds [178, 210] to define H-bonds that depend on the environment. With this method, we can have more understanding of the differences and commonalities in the kinetics of the breaking and reconstruction of the hydrogen bonds of the water molecules in the interface system. At the same time, we can compare the HB dynamics in the interface of different thicknesses with the HB dynamics in bulk water to obtain the thickness of the interface from the perspective of HB dynamics. In addition, for the interface system of different solutions, we can also use the layering technique to study the HB dynamics, so that we can understand the particularity of the interface of various solutions relative to pure water.

In fact, none of the above-mentioned two methods for obtaining the HB dynamics of the interface water molecules can give the true interface HB dynamics completely and accurately. But they respectively give an extreme case of interface HB dynamics. In the MS method, the formation and breaking of intermolecular H-bonds can be truly described, but the selection of interface water molecules is not accurate enough. Since the configuration of the molecule will change over time, the contribution of the H-bonds in the bulk phase will be included. In the IHB method, we are very accurate in choosing the interface water molecules and the H-bonds in the interface, but we may artificially destroy some H-bonds in the interface that were not broken. To a certain extent, the HB dynamics obtained by the IHB method is *accelerated*. Therefore, the comparison of the results obtained by these two methods may give a true picture of the interface HB dynamics. In particular, as the interface thickness increases, the two methods can achieve the same results. The code for calculating the HB dynamics for instantaneous interfaces can be found on https://github.com/hg08/hb_in_interface.

E.2 Thickness of the aqueous/vapor interfaces

To determine the thickness of the water/vapor interface of alkali solutions, we chose several different thickness values of slab of the interface and calculate the corresponding susceptibility for these slabs, respectively. Take the water/vapor interface of LiNO_3 solution as an example. We chose several different thickness values—from 2 to 8 Å, and calculate VSFG intensities $I_{SSP} \propto |\chi_{SSP}^{(2),R}|^2$ for the water/vapor interface with a thickness of each of these values. The result is given in Fig. E.1 a and b. It shows that $|\chi_{SSP}^{(2),R}|^2$ converges as the thickness increases.

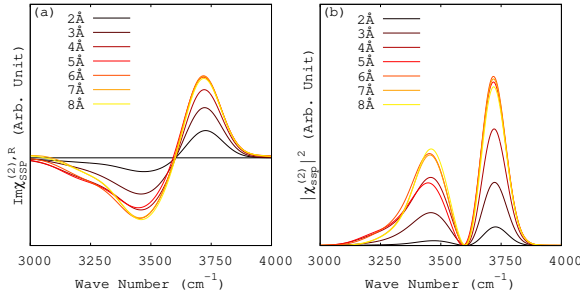


FIGURE E.1: The calculated $|\chi_{SSP}^{(2),R}|^2$, of water molecules at the aqueous/vapor interfaces with different thickness.

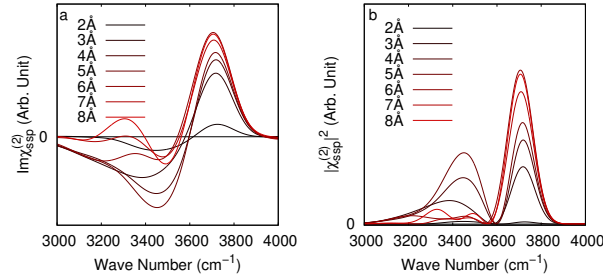


FIGURE E.2: The calculated $|\chi_{SSP}^{(2),R}|^2$, of water molecules at the interfaces of the LiI solution with different thickness.

The VSFG intensities $I_{SSP} \propto |\chi_{SSP}^{(2),R}|^2$ for the water/vapor interface of the LiI solution are given in Fig. E.2 a and b. The results show that $|\chi_{SSP}^{(2),R}|^2$ increases as the thickness increase from 0 to 8 Å.

Furthermore, we also estimated the thickness of a water/vapor interface by calculating the HB dynamics for it. Fig. E.3 shows the dependence of the logarithm of survival probability on the thickness of the water/vapor interface of the LiI solution. We found that when $d = 8$ Å the correlation function $\ln S_{HB}(t)$ of the interface converges as the thickness increases, indicating the thickness of the interface.

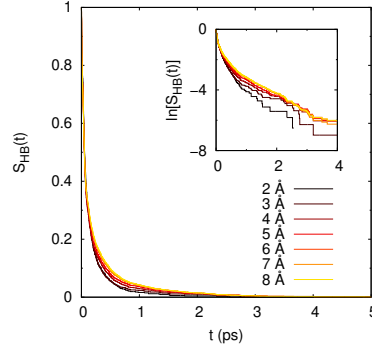


FIGURE E.3: The logarithms of the function $S_{\text{HB}}(t)$ for water-water H-bonds at interfaces with different thickness in the LiI solution.

In addition, the survival probability $S_{\text{HB}}(t)$ is dependent on the temporal resolution t_t , which is the time interval between two adjacent states in time used to calculate the survival probability. As an example, the t_t dependence of the τ_{HB} of the three alkali-iodine solution interfaces in AIMD simulations is reported in Fig. E.4. It shows that, if one take the t_t as small as possible, the number of times that H-bonds break and form again in this period of time (t_t) will be reduced. As shown in Fig. E.4, The value of τ_{HB} corresponding to the intersections of the $\tau_{\text{HB}}(t_t)$ functions and the line $t_t = 5$ fs approximately give the continuum HB lifetimes. For $t_t = 5$ fs, the calculated continuum HB lifetime is 0.30, 0.31 and 0.23 ps, for the interface of LiI, NaI and KI solution, respectively. Then, the estimated value of τ_a is ~ 0.2 ps. Moreover, we can obtain the continuum HB lifetime independent of the t_t : $\tau_{\text{HB}} = \lim_{t_t \rightarrow 0} \tau_{\text{HB}}(t_t)$.

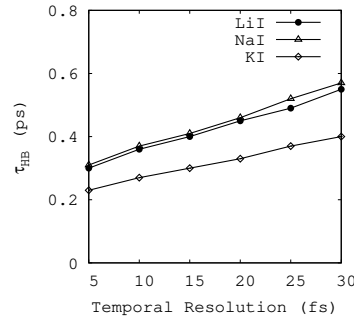


FIGURE E.4: The resolution dependence of the continuum lifetime τ_{HB} of water–water H-bonds at interfaces of different alkali-iodine solutions at 330 K, calculated for six temporal resolutions (t_t). [246–248]

PBC’s effect on $C_2(t)$ As an example, Figure E.5 shows the effect of PBC on $C_2(t)$. In our simulation, whether the PBC is considered or not will not have a substantial impact on the result that the orientation relaxation of OH bond depends on the thickness of the interface. Even without considering the PBC, we can still conclude that the orientation relaxation process of OH bonds at the water/vapor interface slows down obviously with the increase of interface thickness.

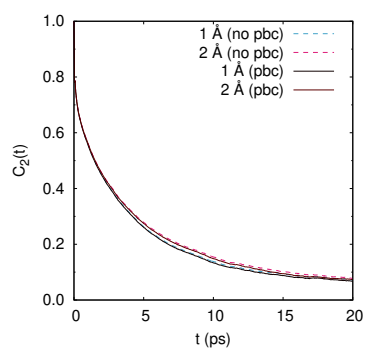


FIGURE E.5: The PBC's effect on the thickness-dependence of $C_2(t)$ for water molecules at the water/vapor interfaces.

Appendix F

HB dynamics and instantaneous interfaces

F.1 Relations between HB lifetime distributions

The HB lifetime is a significant feature of the HB dynamics in liquids. The peculiar properties of water are a direct consequence of water's H-bond lifetime distribution.[192, 199, 249] For example, understanding of HB dynamics is essential when investigating proton transfer reactions in protein environments.[250] The statistical properties of lifetime of H-bonds can be described by a variety of distribution functions.[195, 203, 251, 252] Below we discuss the three probability distribution functions of HB lifetime, so that we can study the dynamic characteristics of H-bonds in liquids and interfaces.

Probability distribution of HB lifetimes in a configuration Suppose that there are n_{tot} H-bonds in a system at time t , and we can distinguish a part of H-bonds from these H-bonds. The lifetime of this part of H-bonds is in a certain range $[\tau, \tau + d\tau]$. We can assume that their number of those bonds is n_τ . One can easily find that $n_{\text{tot}} > n_\tau$. If we observe this part of H-bonds in the next time period $[t, t + \tau]$, then they will be broken once during $[t, t + \tau]$. That is to say, within $[t, t + \tau]$, we will detect the breaking of all H-bonds with lifetime τ (see Fig. F.1). Therefore, in a very short period of time $d\tau$, the probability of detecting these H-bonds is $(1/\tau)d\tau$. Since the probability for the HB to have the lifetime $\in [\tau, \tau + d\tau]$ is $P_t(\tau)$. Therefore, the relation between $P_a(t)$ and $P_t(t)$ is

$$P_a(t) = \int_t^\infty P_t(\tau) \frac{d\tau}{\tau}, \quad (\text{F.1})$$

i.e., the probability of the HB breaking for the first time in the time t after detection at the initial moment depends on the number of those H-bonds whose lifetime exceeds the given time t . [202]

Different HB lifetime distributions From the probability $P_{tc}(t)$ of the total HB lifetime in a configuration, and the probability P_a of the first HB breaking in time t after it have been detected at the moment t , one can introduce the average time $\langle \tau_{tc} \rangle$ and $\langle \tau_a \rangle$:

$$\langle \tau_{tc} \rangle = \int_0^\infty t P_{tc}(t) dt, \quad (\text{F.2})$$

$$\langle \tau_a \rangle = \int_0^\infty t P_a(t) dt. \quad (\text{F.3})$$

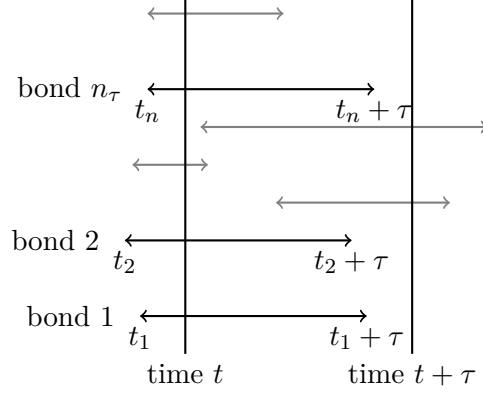


FIGURE F.1: The H-bonds with lifetime τ in a certain configuration. At time t , we assume that there are totally n_{tot} H-bonds can be detected, and n_τ H-bonds are of lifetime τ , therefore, the fraction of H-bonds that have the lifetime τ in the configuration at time t is $P_{\text{tc}}(\tau) = n_\tau/n_{\text{tot}}$. Let τ take all the values in the interval $[0, \infty]$, we can get the HB lifetime distribution $P_{\text{tc}}(t)$.

Since $P_a(t) = \int_t^\infty P_{\text{tc}}(\tau) \frac{d\tau}{\tau}$, i.e.,

$$P_{\text{tc}}(t) = -t \frac{dP_a(t)}{dt},$$

integrating by parts, we obtain

$$\begin{aligned} \langle \tau_{\text{tc}} \rangle &= - \int_0^\infty t^2 \frac{dP_a(t)}{dt} dt \\ &= - \int_0^\infty t^2 dP_a(t) \\ &= 2\langle \tau_a \rangle, \end{aligned}$$

in which we used $\int_0^\infty d(t^2 P_a) = 0$. Therefore, there is a relationship between $\langle \tau_{\text{tc}} \rangle$ and $\langle \tau_a \rangle$:

$$\langle \tau_{\text{tc}} \rangle = 2\langle \tau_a \rangle. \quad (\text{F.4})$$

We denote the probability of the total HB lifetime along a trajectory as $P_{\text{tt}}(t)$, then the average HB lifetime over the trajectory is

$$\langle \tau_{\text{tt}} \rangle = \int_0^\infty t P_{\text{tt}}(t) dt. \quad (\text{F.5})$$

Because $\int_0^\infty P_{\text{tc}}(t) dt = \frac{1}{\langle \tau_{\text{tt}} \rangle} \int_0^\infty t P_{\text{tt}}(t) dt = 1$, we get

$$P_{\text{tt}}(t) = \langle \tau_{\text{tt}} \rangle P_{\text{tc}}(t)/t. \quad (\text{F.6})$$

The difference between the two distribution functions, $P_{\text{tt}}(t)$ and $P_{\text{tc}}(t)$, can be described as follows. The $P_{\text{tt}}(t)$ represents the percentage of pairs of molecules that had a continuous H-bonds during time t , while the $P_{\text{tc}}(t)$ the percentage of the number of H-bonds with a given lifetime t to the number of all H-bonds in any configuration. [202]

Since $P_a(t) = \int_t^\infty P_{tc}(\tau) \frac{d\tau}{\tau}$, we can obtain

$$\begin{aligned} P_a(t) &= \int_t^\infty \frac{P_{tt}}{\langle \tau_{tt} \rangle} \frac{\tau}{\tau} d\tau \\ &= \int_t^\infty \frac{P_{tt}}{\langle \tau_{tt} \rangle} d\tau. \end{aligned}$$

Let $t = 0$, we obtain

$$P_a(0) = 1/\langle t_{tt} \rangle = 1/\langle t_{HB} \rangle. \quad (F.7)$$

From Eq. F.2 and the relation between $S_{HB}(t)$ and $P_a(t)$

$$S_{HB}(t) = \int_t^\infty P_a(\tau) d\tau, \quad (F.8)$$

we can obtain

$$\begin{aligned} \int_0^\infty \int_t^\infty P_a(\tau) d\tau dt &= \int_0^\infty \int_0^\tau P_a(\tau) dt d\tau \\ &= \int_0^\infty \tau P_a(\tau) d\tau \\ &= \langle \tau_a \rangle, \end{aligned}$$

i.e.,

$$\int_0^\infty S_{HB}(t) dt = \langle \tau_a \rangle. \quad (F.9)$$

Calculation of HB lifetime distributions In this paragraph, we describe the method to calculate the above lifetime distributions $P_{tc}(\tau)$, $P_a(\tau)$, and $P_{tt}(\tau)$.

First, we describe the method of calculating $P_{tc}(\tau)$. Theoretically speaking, in order to calculate $P_{tc}(\tau)$, our detection time t must meet the following conditions: $t - t_0 > \tau_{hb}^{\max}$, where t_0 is the initial time and τ_{hb}^{\max} is the maximum lifetime value of the H-bonds in the system. However, the value of τ_{hb} cannot be known in advance. In order to reduce the error, the method we can adopt is to set an empirical value as large as possible for τ_{hb}^{\max} if conditions permit. Since the value of τ_{hb}^{\max} is limited, in principle the lifetime value of the HB can always be greater than τ_{hb}^{\max} . Therefore, the average value of the HB lifetime distribution calculated in this approximate way will move to a shorter lifetime than the average value of the true HB lifetime distribution:

$$\int_0^\infty \tau P_{tc}^{\text{approx}}(\tau) d\tau < \langle \tau_{tc} \rangle. \quad (F.10)$$

Among the H-bonds detected at time t , if there are some H-bonds that have existed at the beginning t_0 and remain in existence until time t , then we can approximately express the lifetime of these H-bonds as $\delta t^{(j)} = t^{(j)} - t_0$, where $j = 1, \dots, m$ is the labels of the m H-bonds and $t^{(j)}$ is the moment when the j -th HB is broken. If we use $\tau^{(j)}$, $j = 1, \dots, m$ to represent the true lifetimes of these m H-bonds, then we can find that $\tau^{(j)} - \delta t^{(j)} > 0$. Since we cannot judge the true lifetime of these m hydrogen bonds, we can use $\delta t^{(j)}$ to approximate the lifetime of these m H-bonds, that is

$$\tau^{(j)} = \delta t^{(j)}. \quad (F.11)$$

For those H-bonds that did not exist at the beginning, the method of calculating their lifetime is very straightforward, the lifetime $\tau^{(j)}$ is equal to the time $t^{(j)}$ when the HB is broken minus the moment $t_0^{(j)}$ of its formation:

$$\tau^{(j)} = t^{(j)} - t_0^{(j)}, \quad (\text{F.12})$$

where the superscript $j = 1, \dots, m'$, identifies m' H-bonds detected at time t , and formed after t_0 and broken at $t^{(j)}$.

Specifically, for the DFTMD simulation results we obtained, we also approximate P_{tc} as follows: We select evenly distributed n time points $t = t_1, \dots, t_n$, from the trajectory obtained by the simulation, and count the HB lifetimes at each time point t_i . The distribution function $P_{tc}(\tau)$ can be obtained by the average of the lifetime distribution detected at a certain time t_i , $i = 1, \dots, n$, where $t_i - t_{i-1} = \tau_{\text{hb}}^{\text{max}}$.

If only from the perspective of simulation data, we have another way to obtain $P_{tc}(\tau)$: Count the lifetimes of H-bonds that are formed after the initial time t_0 and are broken before the end time t_f . Although the distribution obtained in this method cannot be verified experimentally, it is the true distribution of HB bonds in simulated systems.

F.2 Hydrogen bond population operator

Calculation of the reactive flux For dynamical variables $x_i(t)$ and $x_k(t)$, their correlation functions have the following relationship:[\[253\]](#)

$$\langle x_i(t') x_k(t) \rangle = -\langle x_i(t) x_k(t') \rangle, \quad (\text{F.13})$$

or

$$\phi_{ik}(t) = -\phi_{ki}(t).$$

Let $x_i = h$, $x_k = \dot{h}$, then, we obtain

$$\langle h(0) \dot{h}(t) \rangle = -\langle \dot{h}(0) h(t) \rangle. \quad (\text{F.14})$$

From the definition of the reactive flux $k(t) = -dc/dt$, we obtain

$$k(t) = -\langle h(0) \dot{h}(t) \rangle / \langle h \rangle. \quad (\text{F.15})$$

Then from Eq. [F.14](#), we get

$$k(t) = \langle \dot{h}(0) h(t) \rangle / \langle h \rangle.$$

Since $\langle \dot{h}(0) \rangle = 0$, $k(t)$ can be calculated by

$$k(t) = -\langle \dot{h}(0) [1 - h(t)] \rangle / \langle h \rangle. \quad (\text{F.16})$$

Relaxation time of hydrogen bonds in bulk water For the dynamic trajectory of such a system, we also calculated the self-correlation function $c(t)$ of the HB population operator, and the functions $k(t)$ and $n(t)$ derived from it. Table [F.1](#) and [F.2](#) shows the rate constant k , k' and the relaxation time τ_{HB} obtained by the least squares fit method. It can be seen from the tables that the accuracy of the calculation of k , k' are accurate to at least two decimal places.

TABLE F.1: The k and k' for the bulk water. We carried on the short time region $0.2 \text{ ps} < t < 2 \text{ ps}$. The unit for k (k') is ps^{-1} , and that for τ_{HB} ($= 1/k$) is ps. The $h(t)$ is bond-based.

Criterion	k (bulk)	k' (bulk)	τ_{HB} (bulk)
ADH	0.299	1.029	3.347
AHD	0.288	1.121	3.468

TABLE F.2: The k and k' for the bulk water. We carried on the long time region $2 \text{ ps} < t < 12 \text{ ps}$. The unit for k (k') is ps^{-1} , and that for τ_{HB} ($= 1/k$) is ps. The $h(t)$ is bond-based.

Criterion	k (bulk)	k' (bulk)	τ_{HB} (bulk)
ADH	0.103	0.028	9.728
AHD	0.103	0.040	9.702

F.3 Reorientation dynamics of water molecules at solution/vapor interfaces

Double exponential fit In general, the rotational motion of water molecules are not simply characterized by a well-defined rate constant. Similar non-single-exponential kinetics is also obtained in the HB kinetics in liquid water [188, 254] and in the time variation of the average frequency shifts of the remaining modes after excitation in hole burning technique.[255, 256] We can understand the non-single-exponential kinetics of rotational anisotropy decay by fitting the rotational anisotropy decay by a biexponential function.

To obtain the effects of diffusion and HB decay of water molecules in solutions respectively, we assume that the correlation function $C_2(t)$ has the form [257]

$$C_2(t) = A_1 e^{-t/\tau_{2,1}} + A_2 e^{-t/\tau_{2,2}}, \quad (\text{F.17})$$

where A_i are amplitudes and $1/\tau_{2,i}$ ($i = 1, 2$) are decay rates of $C_2(t)$, and the $\tau_{2,i}$ represent the relaxation times of the $C_2(t)$. The form of this expression means: We assume that the orientation relaxation $C_2(t)$ is composed of two independent relaxation processes with different time scales, and they can be described by an exponential decay function, respectively. For alkali-iodine solutions (LiI and NaI), the A_i and $\tau_{2,i}$ of the biexponentials fits for functions $C_2(t)$ are shown in Table F.3. We found that Eq. F.17, the biexponential kinetics is sufficiently accurate to describe the characteristics of anisotropy decay.

Then we considered the effect of ion species in solution/vapor interfaces on the anisotropy decay of water molecules. From Table F.3, we found that for both LiI and NaI solutions, there are two decay processes — amplitude ~ 1 , decay time $\tau_{2,2} \sim 10.0$ ps, and for the other describe the initial fast decay of the anisotropy, with amplitude ~ 0.1 , decay time $\tau_{2,1} \sim 0.1\text{--}1.0$ ps, due to the inertial-librational motion preceding the orientational diffusion.

TABLE F.3: The fitted parameters of anisotropy decay of water molecules at the LiI (NaI, KI) solution/vapor interface according to Eq. F.17 for the time range [0,10] ps. The standard errors: $\delta A_i \sim 0.01$, $\delta \tau_{2,i} \sim 0.1$ ps ($i = 1, 2$).

H ₂ O	A_1	$\tau_{2,1}$ (ps)	A_2	$\tau_{2,2}$ (ps)
Li ⁺ -shell	0.56	8.3	0.33	50.0
I ⁻ -shell	0.86	7.1	0.08	0.1
Na ⁺ -shell	0.71	16.7	0.19	1.3
LiI/vapor	0.84	4.9	0.09	0.6
NaI/vapor	0.77	9.1	0.13	0.4
KI/vapor	0.80	6.1	0.12	1.1

The orientation relaxation time constants $\tau_{2,i}$ and amplitudes A_i ($i = 1, 2$) of the single exponentials fits (10 ps) for $C_2(t)$ are in Table F.3. For comparison, we also fit the $C_2(t)$ function of the water molecules in each interface in Table 1 with a single exponential. The results are shown in table F.4. It can be seen that the value of τ_2 is between the two characteristic times $\tau_{2,1}$ and $\tau_{2,2}$, obtained by biexponential fitting. At the same time, we can see the obvious difference in water molecules under various conditions: the reorientation characteristic time τ_2 in the first solvation shell of alkali metal ions is 2 to 3 times that of I⁻ ion. This is a reasonable result. However, the single exponential model describes the reorientation of water molecules as an exponential decay process. Our above biexponential function model (Eq. F.17) can be explained as: the reorientation dynamics of each water molecule is composed of two independent decay processes. One has the amplitude ~ 1 , decay time ~ 10 ps, which describes the initial fast decay of the anisotropy, and the other is of amplitude ~ 0.1 , decay time ~ 0.1 ps, due to the inertial-librational motion preceding the orientational diffusion.

TABLE F.4: The fitted (single exponential) parameters of anisotropy decay of water molecules at the LiI (NaI, KI) solution/vapor interface according to Eq. F.17 for the time range [0,10] ps. The standard errors: $\delta A \sim 0.01$, $\delta \tau_2 \sim 0.1$ ps.

H ₂ O	A	τ_2 (ps)
Li ⁺ -shell	0.88	13.7
I ⁻ -shell	0.83	3.9
Na ⁺ -shell	0.84	10.1
LiI/vapor	0.80	3.0
NaI/vapor	0.86	4.2
KI/vapor	0.86	5.7

Bibliography

- [1] S. Yamamoto et al. “In Situ X-ray Photoelectron Spectroscopy Studies of Water on Metals and Oxides at Ambient Conditions”. In: *J. Phys.: Condens. Matter* 20.18 (2008), p. 184025. DOI: <https://doi.org/10.1088/0953-8984/20/18/184025>. URL: <https://iopscience.iop.org/article/10.1088/0953-8984/20/18/184025/meta>.
- [2] M. Salmeron et al. “Water Growth on Metals and Oxides: Binding, Dissociation and Role of Hydroxyl Groups”. In: *Faraday Discuss.* 141 (2009), pp. 221–229.
- [3] J. Balajka et al. “High-Affinity Adsorption Leads to Molecularly Ordered Interfaces on TiO₂ in Air and Solution”. In: *Science* 361 (2018), pp. 786–789. DOI: [10.1126/science.aat6752](https://doi.org/10.1126/science.aat6752). URL: <https://science.sciencemag.org/content/361/6404/786>.
- [4] D. J. Tobias. “A Workshop on MD Simulations”. In: *NATO Sci. Ser., Ser. A* 305 (1999), pp. 293–310.
- [5] A. V. Benderskii and K. B. Eisenthal. “Effect of Organic Surfactant on Femtosecond Solvation Dynamics at the Air-water Interface”. In: *J. Phys. Chem. B* 104 (2000), pp. 11723–11728. DOI: [10.1021/jp0025429](https://doi.org/10.1021/jp0025429). URL: <https://pubs.acs.org/doi/abs/10.1021/jp0025429>.
- [6] A. V. Benderskii and K. B. Eisenthal. “Dynamical Time Scales of Aqueous Solvation at Negatively Charged Lipid/Water Interfaces”. In: *J. Phys. Chem. A* 106 (2002), pp. 7482–7490. DOI: [10.1021/jp0120155](https://doi.org/10.1021/jp0120155). URL: <https://pubs.acs.org/doi/abs/10.1021/jp0120155>.
- [7] P. Ball. “Water as an Active Constituent in Cell Biology”. In: *Chem. Rev.* 108 (2008), pp. 74–108. DOI: [10.1021/cr068037a](https://doi.org/10.1021/cr068037a). URL: <https://pubs.acs.org/doi/abs/10.1021/cr068037a>.
- [8] I.-F. W. Kuo and C. J. Mundy. “An Ab Initio Molecular Dynamics Study of the Aqueous Liquid-Vapor Interface”. In: *Science* 303 (2004), p. 658. DOI: [10.1126/science.1092787](https://doi.org/10.1126/science.1092787). URL: <https://science.sciencemag.org/content/303/5658/658>.
- [9] L. Y. Zhang et al. “Protein Hydration Dynamics and Molecular Mechanism of Coupled Water-Protein Fluctuations”. In: *J. Am. Chem. Soc.* 131 (2009), pp. 10677–10691. DOI: [10.1021/ja902918p](https://doi.org/10.1021/ja902918p). URL: <https://pubs.acs.org/doi/pdf/10.1021/ja902918p>.
- [10] P. Lo Nostro and B. W. Ninham. “Hofmeister Phenomena: An Update on Ion Specificity in Biology”. In: *Chem. Rev.* 112 (2012), pp. 2286–2322. DOI: <https://doi.org/10.1021/cr200271j>. URL: <https://pubs.acs.org/doi/pdf/10.1021/cr200271j>.

- [11] G. L. Richmond. "Molecular Bonding and Interactions at Aqueous Surfaces as Probed by Vibrational Sum Frequency Spectroscopy". In: *Chem. Rev.* 102 (2002), pp. 2693–2724. DOI: [10.1021/cr0006876](https://doi.org/10.1021/cr0006876). URL: <https://doi.org/10.1021/cr0006876>.
- [12] H. Liu and B. E. Logan. "Electricity Generation Using an Air-Cathode Single Chamber Microbial Fuel Cell in the Presence and Absence of a Proton Exchange Membrane". In: *Environ. Sci. Technol.* 38 (2004), p. 4040. DOI: [10.1021/es0499344](https://pubs.acs.org/doi/abs/10.1021/es0499344). URL: <https://pubs.acs.org/doi/abs/10.1021/es0499344>.
- [13] R. Asahi et al. "Visible-Light Photocatalysis in Nitrogen-Doped Titanium Oxides". In: *Science* 293 (2001), pp. 269–271. DOI: [10.1126/science.1061051](https://science.sciencemag.org/content/293/5528/269.abstract). URL: <https://science.sciencemag.org/content/293/5528/269.abstract>.
- [14] C. Tian et al. "Interfacial Structures of Acidic and Basic Aqueous Solutions". In: *J. Am. Chem. Soc.* 130.39 (2008), pp. 13033–13039. DOI: [10.1021/ja8021297](http://dx.doi.org/10.1021/ja8021297). eprint: <http://dx.doi.org/10.1021/ja8021297>. URL: <http://dx.doi.org/10.1021/ja8021297>.
- [15] J. G. Irwin and M. L. Williams. "Acid Rain: Chemistry and Transport". In: *Environ. Pollut.* 50 (1988), pp. 29–59. DOI: [https://doi.org/10.1016/0269-7491\(88\)90184-4](https://doi.org/10.1016/0269-7491(88)90184-4). URL: <https://www.sciencedirect.com/science/article/pii/0269749188901844>.
- [16] J. H. Hu et al. "Reactive Uptake of Cl₂(g) and Br₂(g) by Aqueous Surfaces as a Function of Br[−] and I[−] Ion Concentration: The Effect of Chemical Reaction at the Interface". In: *J. Phys. Chem.* 99 (1995), pp. 8768–8776. DOI: [10.1021/j100021a050](https://pubs.acs.org/doi/abs/10.1021/j100021a050). URL: <https://pubs.acs.org/doi/abs/10.1021/j100021a050>.
- [17] D. F. Liu et al. "Vibrational Spectroscopy of Aqueous Sodium Halide Solutions and Air-Liquid Interfaces: Observation of Increased Interfacial Depth". In: *J. Phys. Chem. B* 108 (2004), pp. 2252–2260. DOI: [10.1021/jp036169r](https://pubs.acs.org/doi/abs/10.1021/jp036169r). URL: <https://pubs.acs.org/doi/abs/10.1021/jp036169r>.
- [18] D. Clifford and D. J. Donaldson. "Direct Experimental Evidence for a Heterogeneous Reaction of Ozone with Bromide at the Air-Aqueous Interface". In: *J. Phys. Chem. A* 111(39) (2007), pp. 9809–9814. DOI: [10.1021/jp074315d](https://pubs.acs.org/doi/abs/10.1021/jp074315d). URL: <https://pubs.acs.org/doi/abs/10.1021/jp074315d>.
- [19] A. Manna and A. Kumar. "Why Does Water Accelerate Organic Reactions under Heterogeneous Condition?" In: *J. Phys. Chem. A* 117(12) (2013), pp. 2446–2454. DOI: <https://doi.org/10.1021/jp4002934>. URL: <https://pubs.acs.org/doi/abs/10.1021/jp4002934>.
- [20] E. A. Pillar, R. C. Camm, and M. I. Guzman. "Catechol Oxidation by Ozone and Hydroxyl Radicals at the Air-Water Interface". In: *Environ. Sci. Technol. Lett.* 48.20 (2014), pp. 14352–14360. DOI: [10.1021/es504094x](https://doi.org/10.1021/es504094x). URL: <https://doi.org/10.1021/es504094x>.
- [21] D. Eisenberg and W. Kauzmann. *The Structure and Properties of Water*. Oxford University press, Oxford, 1969. ISBN: ISBN: 9780198570264. URL: <https://global.oup.com/academic/product/the-structure-and-properties-of-water-9780198570264?cc=cn&lang=en#>.

- [22] R. J. Speedy and C. A. Angell. “Isothermal Compressibility of Supercooled Water and Evidence for a Thermodynamic Singularity at -45°C ”. In: *J. Chem. Phys.* 65.3 (1976), pp. 851–858. DOI: [10.1063/1.433153](https://doi.org/10.1063/1.433153). eprint: <https://doi.org/10.1063/1.433153>. URL: <https://doi.org/10.1063/1.433153>.
- [23] Peter H. Poole et al. “Effect of Hydrogen Bonds on the Thermodynamic Behavior of Liquid Water”. In: *Phys. Rev. Lett.* 73 (12 1994), pp. 1632–1635. DOI: [10.1103/PhysRevLett.73.1632](https://link.aps.org/doi/10.1103/PhysRevLett.73.1632). URL: <https://link.aps.org/doi/10.1103/PhysRevLett.73.1632>.
- [24] A. K. Soper. “Structural Transformations in Amorphous Ice and Supercooled Water and Their Relevance to the Phase Diagram of Water”. In: *Molecular Physics* 106.16–18 (2008), pp. 2053–2076. DOI: [10.1080/00268970802116146](https://doi.org/10.1080/00268970802116146). eprint: <https://doi.org/10.1080/00268970802116146>. URL: <https://doi.org/10.1080/00268970802116146>.
- [25] A. Nilsson and L. G. M. Pettersson. “Perspective on the Structure of Liquid Water”. In: *Chem. Phys.* 389.1 (2011), pp. 1–34. ISSN: 0301-0104. DOI: <https://doi.org/10.1016/j.chemphys.2011.07.021>. URL: <http://www.sciencedirect.com/science/article/pii/S0301010411003247>.
- [26] P. Ball. *Life’s Matrix: A Biography of Water*. Berkeley and Los Angeles, California: University of California Press, 2001.
- [27] L. G. M. Pettersson and A. Nilsson. “The Structure of Water: from Ambient to Deeply Supercooled”. In: *Journal of Non-Crystalline Solids* 407 (2015). 7th IDMRCs: Relaxation in Complex Systems, pp. 399–417. ISSN: 0022-3093. DOI: <https://doi.org/10.1016/j.jnoncrysol.2014.08.026>. URL: <http://www.sciencedirect.com/science/article/pii/S0022309314004104>.
- [28] E. A. Raymond and G. L. Richmond. “Probing the Molecular Structure and Bonding of the Surface of Aqueous Salt Solutions”. In: *J. Phys. Chem. B* 108 (2004), p. 5051. DOI: [10.1021/jp037725k](https://pubs.acs.org/doi/10.1021/jp037725k). URL: <https://pubs.acs.org/doi/10.1021/jp037725k>.
- [29] S. E. McLain and A. K. Soper. “Structural Studies on the Hydration of l-Glutamic Acid in Solution”. In: *J. Phys. Chem. B* 110 (2006), pp. 21251–21258. DOI: [10.1021/jp062383e](https://pubs.acs.org/doi/abs/10.1021/jp062383e). URL: <https://pubs.acs.org/doi/abs/10.1021/jp062383e>.
- [30] A. Morita and T. Ishiyama. “Recent Progress in Theoretical Analysis of Vibrational Sum Frequency Generation Spectroscopy”. In: *Phys. Chem. Chem. Phys.* 10 (38 2008), pp. 5801–5816. DOI: [10.1039/B808110G](https://dx.doi.org/10.1039/B808110G). URL: <http://dx.doi.org/10.1039/B808110G>.
- [31] H.-F. Wang et al. “Quantitative Sum-Frequency Generation Vibrational Spectroscopy of Molecular Surfaces and Interfaces: Lineshape, Polarization, and Orientation”. In: *Annual Review of Physical Chemistry* 66.1 (2015), pp. 189–216. DOI: [10.1146/annurev-physchem-040214-121322](https://doi.org/10.1146/annurev-physchem-040214-121322).
- [32] Yu-Chieh. Wen et al. “Unveiling Microscopic Structures of Charged Water Interfaces by Surface-Specific Vibrational Spectroscopy”. In: *Phys. Rev. Lett.* 116.1 (2016), p. 016101. DOI: [10.1103/physrevlett.116.016101](https://doi.org/10.1103/physrevlett.116.016101).
- [33] Tatsuya Ishiyama and Akihiro Morita. “Computational Analysis of Vibrational Sum Frequency Generation Spectroscopy”. In: *Annual Review of Physical Chemistry* 68.1 (2017), pp. 355–377. DOI: [10.1146/annurev-physchem-052516-044806](https://doi.org/10.1146/annurev-physchem-052516-044806).

- [34] Chariz Peñalber-Johnstone et al. “Sum Frequency Generation Spectroscopy of Tetraalkylphosphonium Ionic Liquids at the Air-Liquid Interface”. In: *J. Chem. Phys.* 148.19 (2018), p. 193841. DOI: [10.1063/1.5009674](https://doi.org/10.1063/1.5009674). eprint: <https://doi.org/10.1063/1.5009674>. URL: <https://doi.org/10.1063/1.5009674>.
- [35] F. Vidal and A. Tadjeddine. “Sum-Frequency Generation Spectroscopy of Interfaces”. In: *Rep. Prog. Phys.* 68 (2005), pp. 1095–1127. DOI: [10.1088/0034-4885/68/5/r03](https://doi.org/10.1088/0034-4885/68/5/r03). URL: https://www.onacademic.com/detail/journal_1000035594033610_0ae5.html.
- [36] Xing Wei et al. “Sum-Frequency Spectroscopic Studies of Ice Interfaces”. In: *Phys. Rev. B* 66 (8 2002), p. 085401. DOI: [10.1103/PhysRevB.66.085401](https://doi.org/10.1103/PhysRevB.66.085401). URL: <https://link.aps.org/doi/10.1103/PhysRevB.66.085401>.
- [37] P. Guyot-Sionnest, J. H. Hunt, and Y. R. Shen. “Sum-Frequency Vibrational Spectroscopy of a Langmuir Film: Study of Molecular Orientation of a Two-Dimensional System”. In: *Phys. Rev. Lett.* 59 (14 1987), pp. 1597–1600. DOI: [10.1103/PhysRevLett.59.1597](https://doi.org/10.1103/PhysRevLett.59.1597). URL: <https://link.aps.org/doi/10.1103/PhysRevLett.59.1597>.
- [38] R. Superfine, J. H. Huang, and Y. R. Shen. “Nonlinear Optical Studies of the Pure Liquid/Vapor Interface: Vibrational Spectra and Polar Ordering”. In: *Phys. Rev. Lett.* 66 (1991), pp. 1066–1069. DOI: [10.1103/PhysRevLett.66.1066](https://doi.org/10.1103/PhysRevLett.66.1066). URL: <https://ui.adsabs.harvard.edu/abs/1991PhRvL..66.1066S>.
- [39] Q. Du et al. “Vibrational Spectroscopy of Water at the Vapor/Water Interface”. In: *Phys. Rev. Lett.* 70 (15 1993), pp. 2313–2316. DOI: [10.1103/PhysRevLett.70.2313](https://doi.org/10.1103/PhysRevLett.70.2313). URL: <https://link.aps.org/doi/10.1103/PhysRevLett.70.2313>.
- [40] Q. Du, E. Freysz, and Y. R. Shen. “Vibrational Spectra of Water Molecules at Quartz/Water Interfaces”. In: *Phys. Rev. Lett.* 72 (2 1994), pp. 238–241. DOI: [10.1103/PhysRevLett.72.238](https://doi.org/10.1103/PhysRevLett.72.238). URL: <http://link.aps.org/doi/10.1103/PhysRevLett.72.238>.
- [41] S. Gopalakrishnan et al. “Vibrational Spectroscopic Studies of Aqueous Interfaces: Salts, Acids, Bases, and Nanodrops”. In: *Chem. Rev.* 106 (2006), pp. 1155–1175. DOI: [10.1021/cr040361n](https://doi.org/10.1021/cr040361n). URL: <http://www.ncbi.nlm.nih.gov/pubmed/16608176>.
- [42] Y. R. Shen and V. Ostroverkhov. “Sum-Frequency Vibrational Spectroscopy on Water Interfaces: Polar Orientation of Water Molecules at Interfaces”. In: *Chem. Rev.* 106 (2006), pp. 1140–1154. DOI: [10.1021/cr040377d](https://doi.org/10.1021/cr040377d). URL: <https://www.ncbi.nlm.nih.gov/pubmed/16608175>.
- [43] M Che and J. C. Védrine (Ed.) *Characterization of Solid Materials and Heterogeneous Catalysts: From Structure to Surface Reactivity*. Vol. 1. Wiley-VCH, 2012, pp. 1075–1117.
- [44] Peer Fischer et al. “Three-Wave Mixing in Chiral Liquids”. In: *Phys. Rev. Lett.* 85 (20 2000), pp. 4253–4256. DOI: [10.1103/PhysRevLett.85.4253](https://doi.org/10.1103/PhysRevLett.85.4253). URL: <https://link.aps.org/doi/10.1103/PhysRevLett.85.4253>.
- [45] A. L. Harris et al. “Monolayer Vibrational Spectroscopy by Infrared-Visible Sum Generation at Metal and Semiconductor Surfaces”. In: *Chem Phys. Lett.* 141 (1987), pp. 350–356. DOI: [10.1016/0009-2614\(87\)85037-6](https://doi.org/10.1016/0009-2614(87)85037-6). URL: <https://www.sciencedirect.com/science/article/abs/pii/0009261487850376>.

- [46] R. Superfine et al. "Surface vibrational spectroscopy of molecular adsorbates on metals and semiconductors by infrared-visible sum-frequency generation". In: *Surf. Sci.* 200 (1988), pp. L445–L450. DOI: [10.1016/0039-6028\(88\)90422-0](https://doi.org/10.1016/0039-6028(88)90422-0). URL: <https://www.sciencedirect.com/science/article/pii/0039602888904220>.
- [47] B. Rotenberg. "Water in Clay Nanopores". In: *MRS Bulletin* 39.12 (2014), pp. 1074–1081. DOI: [10.1557/mrs.2014.251](https://doi.org/10.1557/mrs.2014.251). URL: <https://doi.org/10.1557/mrs.2014.251>.
- [48] P. Jungwirth and D. J. Tobias. "Specific Ion Effects at the Air/Water Interface". In: *Chem. Rev.* 106 (2006), pp. 1259–1281. DOI: [10.1021/cr0403741](https://doi.org/10.1021/cr0403741). URL: <https://pubs.acs.org/doi/abs/10.1021/cr0403741>.
- [49] Y. J. Zhang and P. S. Cremer. "Chemistry of Hofmeister Anions and Osmolytes". In: *Annu. Rev. Phys. Chem.* 61 (2010), pp. 63–83. DOI: [10.1146/annurev.physchem.59.032607.093635](https://doi.org/10.1146/annurev.physchem.59.032607.093635). URL: <https://www.annualreviews.org/doi/abs/10.1146/annurev.physchem.59.032607.093635>.
- [50] D. Tobias and J. C. Hemminger. "Getting specific about specific ion effects". In: *Science* 319 (2008), pp. 1197–1198. DOI: [10.1126/science.1152799](https://doi.org/10.1126/science.1152799). URL: <https://www.jstor.org/stable/20053465>.
- [51] D. F. Parsons et al. "Hofmeister Effects: Interplay of Hydration, Nonelectrostatic Potentials, and Ion Size". In: *Phys. Chem. Chem. Phys.* 13 (27 2011), pp. 12352–12367. DOI: [10.1039/C1CP20538B](https://doi.org/10.1039/C1CP20538B). URL: <http://dx.doi.org/10.1039/C1CP20538B>.
- [52] P. Jungwirth and D. J. Tobias. "Molecular Structure of Salt Solutions: A New View of the Interface with Implications for Heterogeneous Atmospheric Chemistry". In: *J. Phys. Chem. B* 105 (2001), pp. 10468–10472. DOI: [10.1021/jp012750g](https://doi.org/10.1021/jp012750g). URL: <https://pubs.acs.org/doi/abs/10.1021/jp012750g>.
- [53] P. Jungwirth and D. J. Tobias. "Ions at Air/Water Interface". In: *J. Phys. Chem. B* 106 (2002), pp. 6361–6373. DOI: [10.1021/jp020242g](https://doi.org/10.1021/jp020242g). URL: <https://pubs.acs.org/doi/abs/10.1021/jp020242g>.
- [54] C. Tian et al. "Surface Propensities of Atmospherically Relevant Ions in Salt Solutions Revealed by Phase-Sensitive Sum Frequency Vibrational Spectroscopy". In: *J. Phys. Chem. Lett.* 2 (2011), p. 1946.
- [55] P. Jungwirth and D. J. Tobias. "Ions at Air/Water Interface". In: *J. Phys. Chem. B* 106 (2002), pp. 6361–6373.
- [56] M. Xu et al. "Nitrate Anions and Ion Pairing at the Air-Aqueous Interface". In: *J. Phys. Chem. C* 113 (2009), pp. 2082–2087. DOI: [10.1021/jp805376x](https://doi.org/10.1021/jp805376x). URL: <https://pubs.acs.org/doi/abs/10.1021/jp805376x>.
- [57] A. M. Jubb, W. Hua, and H. C. Allen. "Organization of Water and Atmospherically Relevant Ions and Solutes: Vibrational Sum Frequency Spectroscopy at the Vapor/Liquid and Liquid/Solid Interfaces". In: *Accounts of Chemical Research* 45.1 (2012), pp. 110–119. DOI: [10.1021/ar200152v](https://doi.org/10.1021/ar200152v). URL: <https://pubs.acs.org/doi/abs/10.1021/ar200152v>.
- [58] K. Mizoguchi, T. Ujike, and Y. Tominaga. "Dynamics Structure of Water in NaCl Aqueous Solution". In: *J. Chem. Phys.* 109.5 (1998), pp. 1867–1872. DOI: [10.1063/1.476763](https://doi.org/10.1063/1.476763). eprint: <https://doi.org/10.1063/1.476763>. URL: <https://doi.org/10.1063/1.476763>.

- [59] C. M. Johnson and S. Baldelli. “Vibrational Sum Frequency Spectroscopy Studies of the Influence of Solutes and Phospholipids at Vapor/Water Interfaces Relevant to Biological and Environmental systems”. In: *Chem. Rev.* 114 (2014), pp. 8416–8446. DOI: <https://doi.org/10.1021/cr4004902>. URL: <https://pubs.acs.org/doi/abs/10.1021/cr4004902>.
- [60] T. Ishiyama, T. Imamura, and A. Morita. “Theoretical Studies of Structures and Vibrational Sum Frequency Generation Spectra at Aqueous Interfaces”. In: *Chem. Rev.* 114 (2014), pp. 8447–8470. DOI: [10.1021/cr4004133](https://doi.org/10.1021/cr4004133). URL: <https://pubs.acs.org/doi/abs/10.1021/cr4004133>.
- [61] L. X. Dang. “Solvation of the Hydronium Ion at the Water Liquid/Vapor Interface”. In: *J. Chem. Phys.* 119 (2003), p. 6351. DOI: <https://doi.org/10.1063/1.1599274>. URL: <https://aip.scitation.org/doi/abs/10.1063/1.1599274>.
- [62] M. K. Petersen et al. “The Hydrated Proton at the Water Liquid/Vapor Interface”. In: *J. Phys. Chem. B* 108 (2004), pp. 14804–14806. DOI: [10.1021/jp046716o](https://doi.org/10.1021/jp046716o). URL: <https://pubs.acs.org/doi/abs/10.1021/jp046716o>.
- [63] T. Ishiyama and A. Morita. “Molecular Dynamics Analysis of Interfacial Structures and Sum Frequency Generation Spectra of Aqueous Hydrogen Halide Solutions”. In: *J. Phys. Chem. A* 111.38 (2007), pp. 9277–9285. DOI: [10.1021/jp072997z](https://doi.org/10.1021/jp072997z). eprint: <http://dx.doi.org/10.1021/jp072997z>. URL: <http://dx.doi.org/10.1021/jp072997z>.
- [64] M. Mucha et al. “Unified Molecular Picture of the Surfaces of Aqueous Acid, Base, and Salt Solutions”. In: *J. Phys. Chem. B* 109 (2005), pp. 7617–7623. DOI: [10.1021/jp0445730](https://doi.org/10.1021/jp0445730). URL: <https://pubs.acs.org/doi/abs/10.1021/jp0445730>.
- [65] Ivan S. Ufimtsev, Nathan Luehr, and Todd J. Martinez. “Charge Transfer and Polarization in Solvated Proteins from Ab Initio Molecular Dynamics”. In: *J. Phys. Chem. Lett.* 2.14 (2011), pp. 1789–1793. DOI: <https://doi.org/10.1021/jz200697c>. URL: <https://pubs.acs.org/doi/abs/10.1021/jz200697c>.
- [66] Stefan Grimme. “Accurate Description of Van der Waals Complexes by Density Functional Theory Including Empirical Corrections”. In: *J. Comp. Chem.* 25.12 (2004), pp. 1463–1473. ISSN: 01928651. DOI: [10.1002/jcc.20078](https://doi.org/10.1002/jcc.20078). URL: <https://onlinelibrary.wiley.com/doi/abs/10.1002/jcc.20078>.
- [67] S. Grimme. “Semiempirical GGA-Type Density Functional Constructed with a Long-Range Dispersion Correction”. In: *J. Comput. Chem.* 27 (2006), pp. 1787–1799. DOI: [10.1002/jcc.20495](https://doi.org/10.1002/jcc.20495). URL: <https://onlinelibrary.wiley.com/doi/abs/10.1002/jcc.20495>.
- [68] Stefan Grimme et al. “Density Functional Theory with Dispersion Corrections for Supramolecular Structures, Aggregates, and Complexes of (Bio)Organic Molecules”. In: *Org. Biomol. Chem.* 5 (5 2007), pp. 741–758. DOI: [10.1039/B615319B](https://doi.org/10.1039/B615319B). URL: <http://dx.doi.org/10.1039/B615319B>.
- [69] S. Grimme et al. “A Consistent and Accurate Ab Initio Parametrization of Density Functional Dispersion Correction (DFT-D) for the 94 Elements H–Pu”. In: *J. Chem. Phys.* 132 (2010), p. 154104. DOI: [10.1063/1.3382344](https://doi.org/10.1063/1.3382344). URL: <https://aip.scitation.org/doi/abs/10.1063/1.3382344>.

- [70] Marcel D. Baer et al. “Re-examining the Properties of the Aqueous Vapor-Liquid Interface using Dispersion Corrected Density Functional Theory”. In: *J. Chem. Phys.* 135 (2011), p. 124712. DOI: [10.1063/1.3633239](https://doi.org/10.1063/1.3633239). URL: <https://aip.scitation.org/doi/abs/10.1063/1.3633239>.
- [71] Teresa Fornaro et al. “Dispersion Corrected DFT Approaches for Anharmonic Vibrational Frequency Calculations: Nucleobases and Their Dimers”. In: *Phys. Chem. Chem. Phys.* 16 (21 2014), pp. 10112–10128. DOI: [10.1039/C3CP54724H](https://doi.org/10.1039/C3CP54724H). URL: <http://dx.doi.org/10.1039/C3CP54724H>.
- [72] F. H. Stillinger. “Water Revisited”. In: *Science* 209 (1980), p. 451. DOI: [10.1126/science.209.4455.451](https://doi.org/10.1126/science.209.4455.451). URL: <https://science.sciencemag.org/content/209/4455/451.abstract>.
- [73] M. E. Tuckerman. *Statistical Mechanics: Theory and Molecular Simulation*. Oxford University Express, 2010.
- [74] S. W. Rick, S. J. Stuart, and B. J. Berne. “Dynamical Fluctuating Force Fields: Application to Liquid Water”. In: *J. Chem. Phys.* 101(7) (1994), p. 6141. DOI: [10.1063/1.468398](https://doi.org/10.1063/1.468398). URL: [arXiv:chem-ph/9406002](https://arxiv.org/abs/chem-ph/9406002).
- [75] S. W. Rick and S. J. Stuart. “Potentials and Algorithms for Incorporating Polarizability in Computer Simulations”. In: *Rev. Comput. Chem.* 18 (2002), pp. 89–146. DOI: [10.1002/0471433519.ch3](https://doi.org/10.1002/0471433519.ch3). URL: <https://onlinelibrary.wiley.com/doi/abs/10.1002/0471433519.ch3>.
- [76] G. Lamoureux, A. D. MacKerell, Jr., and B. Roux. “A Simple Polarizable Model of Water Based on Classical Drude Oscillators”. In: *J. Chem. Phys.* 119 (2003), p. 5185. DOI: [10.1063/1.1598191](https://doi.org/10.1063/1.1598191). URL: <https://aip.scitation.org/doi/abs/10.1063/1.1598191>.
- [77] M. E. Tuckerman. “Ab Initio Molecular Dynamics: Basic Concepts, Current Trends and Novel Applications”. In: *J. Phys.: Condens. Matter* 14 (2002), R1297–R1355. DOI: [10.1088/0953-8984/14/50/202](https://doi.org/10.1088/0953-8984/14/50/202). URL: <https://ui.adsabs.harvard.edu/abs/2002JPCM...14R1297T>.
- [78] A. Warshel and R. M. Weiss. “An Empirical Valence Bond Approach for Comparing Reactions in Solutions and in Enzymes”. In: *J. Am. Chem. Soc.* 102 (1980), pp. 6218–6226. DOI: [10.1021/ja00540a008](https://doi.org/10.1021/ja00540a008). URL: <http://pubs.acs.org/doi/10.1021/ja00540a008>.
- [79] D. K. Remler and P. A. Madden. “Molecular Dynamics Without Effective Potentials via the Car-Parrinello Approach”. In: *Mol. Phys.* 70 (1990), pp. 921–966. DOI: [10.1080/00268979000101451](https://doi.org/10.1080/00268979000101451). URL: <https://doi.org/10.1080/00268979000101451>.
- [80] M. C. Payne et al. “Iterative Minimization Techniques for Ab Initio Total-Energy Calculations: Molecular Dynamics and Conjugate Gradients”. In: *Rev. Mod. Phys.* 64 (4 1992), pp. 1045–1097. DOI: [10.1103/RevModPhys.64.1045](https://doi.org/10.1103/RevModPhys.64.1045). URL: <https://link.aps.org/doi/10.1103/RevModPhys.64.1045>.
- [81] M. P. Allen and D. J. Tildesley (Ed.) *Computer Simulation in Chemical Physics, chapter 8, First-Principles Molecular Dynamics*. NATO ASI Series C, 1993, p. 261. URL: https://link.springer.com/chapter/10.1007/978-94-011-1679-4_8.
- [82] M. E. Tuckerman et al. “Ab Initio Molecular Dynamics Simulations”. In: *J. Phys. Chem.* 100 (1996), pp. 12878–12887. DOI: [10.1021/jp960480+](https://doi.org/10.1021/jp960480+). URL: <https://pubs.acs.org/doi/abs/10.1021/jp960480+>.

- [83] M. Parrinello. “From Silicon to RNA: The Coming of Age of Ab Initio Molecular Dynamics”. In: *Solid State Commun.* 102 (1997), pp. 107–120. DOI: [10.1016/S0038-1098\(96\)00723-5](https://doi.org/10.1016/S0038-1098(96)00723-5). URL: <https://www.sciencedirect.com/science/article/abs/pii/S0038109896007235>.
- [84] Marx D. and J. Hutter. “Ab Initio Molecular Dynamics: Theory and Implementation”. In: *Modern Methods and Algorithms of Quantum Chemistry (NIC Series) ed J Grotendorst (Forschungszentrum Juelich)* 1 (2000). URL: <https://juser.fz-juelich.de/record/44687/files/NIC-Band-1.pdf#page=311>.
- [85] R. Car. “Introduction to Density-Functional Theory and Ab-Initio Molecular Dynamics”. In: *Quant. Struct. Act. Rel.* 21 (2002), pp. 97–104. URL: [https://onlinelibrary.wiley.com/doi/abs/10.1002/1521-3838\(200207\)21:2%3C97::AID-QSAR97%3E3.0.CO;2-6](https://onlinelibrary.wiley.com/doi/abs/10.1002/1521-3838(200207)21:2%3C97::AID-QSAR97%3E3.0.CO;2-6).
- [86] R. P. Feynman and A. R. Hibbs. *Quantum Mechanics and Path Integrals*. New York: McGraw-Hill, 1965.
- [87] R. P. Feynman. *Statistical Mechanics: A Set of Lectures*. Benjamin, 1972.
- [88] D. Marx and M. Parrinello. “Ab Initio Path Integral Molecular Dynamics: Basic Ideas”. In: *J. Chem. Phys.* 104 (1996), p. 4077. DOI: [10.1063/1.471221](https://doi.org/10.1063/1.471221). URL: <https://aip.scitation.org/doi/abs/10.1063/1.471221>.
- [89] M. Tuckerman et al. “Efficient and General Algorithms for Path Integral Car-Parrinello Molecular Dynamics”. In: *J. Chem. Phys.* 104 (1996), pp. 5579–5588. DOI: [10.1063/1.471771](https://doi.org/10.1063/1.471771). URL: <https://doi.org/10.1063/1.471771>.
- [90] Marx D., Tuckerman M. E., and Martyna G. J. “Quantum Dynamics via Adiabatic Ab Initio Centroid Molecular Dynamics”. In: *Comput. Phys. Commun.* 118 (1999), p. 166. DOI: [10.1016/S0010-4655\(99\)00208-8](https://doi.org/10.1016/S0010-4655(99)00208-8). URL: <https://www.sciencedirect.com/science/article/pii/S0010465599002088>.
- [91] J. VandeVondele et al. “QUICKSTEP: Fast and Accurate Density Functional Calculations using a Mixed Gaussian and Plane Waves Approach”. In: *Computer Physics Communications* 167 (2004), pp. 103–128. DOI: [10.1016/j.cpc.2004.12.014](https://doi.org/10.1016/j.cpc.2004.12.014). URL: <https://www.sciencedirect.com/science/article/pii/S0010465505000615>.
- [92] P. Hohenberg and W. Kohn. “Inhomogeneous Electron Gas”. In: *Phys. Rev.* 136 (3B 1964), B864–B871. DOI: [10.1103/PhysRev.136.B864](https://doi.org/10.1103/PhysRev.136.B864). URL: <https://link.aps.org/doi/10.1103/PhysRev.136.B864>.
- [93] W. Kohn and L. J. Sham. “Quantum Density Oscillations in an Inhomogeneous Electron Gas”. In: *Phys. Rev.* 137 (6A 1965), A1697–A1705. DOI: [10.1103/PhysRev.137.A1697](https://doi.org/10.1103/PhysRev.137.A1697). URL: <https://link.aps.org/doi/10.1103/PhysRev.137.A1697>.
- [94] M. Levy. “Universal Variational Functionals of Electron Densities, First-Order Density Matrices, and Natural Spin-Orbitals and Solution of the v-Representability Problem”. In: *Proc. Natl. Acad. Sci. USA.* 76 (1979), pp. 6062–6065. DOI: <https://doi.org/10.1073/pnas.76.12.6062>. URL: <https://www.pnas.org/content/76/12/6062.short>.
- [95] Kieron Burke. *ABC of Density Functional Theory*. Department of Chemistry, University of California, Irvine, 2007.

- [96] J. P. Perdew, K. Burke, and M. Ernzerhof. “Generalized Gradient Approximation Made Simple”. In: *Phys. Rev. Lett.* 77 (18 1996), pp. 3865–3868. DOI: [10.1103/PhysRevLett.77.3865](https://doi.org/10.1103/PhysRevLett.77.3865). URL: <http://link.aps.org/doi/10.1103/PhysRevLett.77.3865>.
- [97] J. Kohanoff. *Electronic Structure Calculations for Solids and Materials: Theory and Computational Methods*. Cambridge University Press, 2006.
- [98] X. Wu et al. “Towards extending the applicability of density functional theory to weakly bound systems”. In: *J. Chem. Phys.* 115 (2001), pp. 8748–8757. DOI: [10.1063/1.1412004](https://doi.org/10.1063/1.1412004). URL: <https://doi.org/10.1063/1.1412004>.
- [99] Q. Wu and W. Yang. “Empirical Correction to Density Functional Theory for Van der Waals Interactions”. In: *J. Chem. Phys.* 116 (2002), pp. 515–524. DOI: [10.1063/1.1424928](https://doi.org/10.1063/1.1424928). URL: <https://aip.scitation.org/doi/abs/10.1063/1.1424928>.
- [100] U. Zimmerli, M. Parrinello, and P. Koumoutsakos. “Dispersion Corrections to Density Functionals for Water Aromatic Interactions”. In: *J. Chem. Phys.* 120 (2004), p. 2693. DOI: [10.1063/1.1637034](https://doi.org/10.1063/1.1637034). URL: <https://aip.scitation.org/doi/abs/10.1063/1.1637034>.
- [101] J. Klimeš and A. Michaelides. “Perspective: Advances and Challenges in Treating van der Waals Dispersion Forces in Density Functional Theory”. In: *J. Chem. Phys.* 137.1 (2012), pp. 120901–120912. DOI: [10.1063/1.4754130](https://doi.org/10.1063/1.4754130). URL: <https://aip.scitation.org/doi/full/10.1063/1.4754130>.
- [102] P. Pulay. “Ab Initio Calculation of Force Constants and Equilibrium Geometries in Polyatomic Molecules: I. Theory”. In: *Mol. Phys.* 17.2 (1969), pp. 197–204. DOI: [10.1080/00268976900100941](https://doi.org/10.1080/00268976900100941). URL: <https://doi.org/10.1080/00268976900100941>.
- [103] R. Car and M. Parrinello. “Unified Approach for Molecular Dynamics and Density Functional Theory”. In: *Phys. Rev. Lett.* 55 (22 1985), pp. 2471–2474. DOI: [10.1103/PhysRevLett.55.2471](https://doi.org/10.1103/PhysRevLett.55.2471). URL: <https://link.aps.org/doi/10.1103/PhysRevLett.55.2471>.
- [104] J. VandeVondele et al. “Quickstep: Fast and Accurate Density Functional Calculations using a Mixed Gaussian and Plane Waves Approach”. In: *Comput. Phys. Commun.* 167.2 (2005), pp. 103–128. ISSN: 0010-4655.
- [105] Thomas D. Kühne et al. “CP2K: An electronic structure and molecular dynamics software package - Quickstep: Efficient and accurate electronic structure calculations”. In: *J. Chem. Phys.* 152.19 (2020), p. 194103. DOI: [10.1063/5.0007045](https://doi.org/10.1063/5.0007045). eprint: <https://doi.org/10.1063/5.0007045>. URL: <https://doi.org/10.1063/5.0007045>.
- [106] D. Frenkel and B. Smit. *Understanding Molecular Simulation*. Computational Science Series (Academic Press), 2nd ed, 2002.
- [107] G. Kresse and J. Hafner. “Ab Initio Molecular Dynamics for Liquid Metals”. In: *Phys. Rev. B* 47 (1 1993), pp. 558–561. DOI: [10.1103/PhysRevB.47.558](https://doi.org/10.1103/PhysRevB.47.558). URL: <https://link.aps.org/doi/10.1103/PhysRevB.47.558>.
- [108] M. T. Dove. *Introduction to Lattice Dynamics*. Cambridge: Cambridge University Press, 1993.
- [109] J. M. Dickey and A. Paskin. “Computer Simulation of the Lattice Dynamics of Solids”. In: *Phys. Rev.* 188 (1969), p. 1407.

- [110] M. P. Allen and D. J. Tildesley. *Computer Simulation of Liquid*. Clarendon Express, Oxford, 1986.
- [111] A. L. Harris et al. “Vibrational Energy Transfer to Metal Surfaces Probed by Sum Generation: CO/Cu(100) and CH₃S/Ag(111)”. In: *J. Electron Spec. Related Phenomena* 54155 (1990), pp. 5–16. DOI: [10.1016/0368-2048\(90\)80196-H](https://doi.org/10.1016/0368-2048(90)80196-H). URL: <https://www.sciencedirect.com/science/article/abs/pii/036820489080196H>.
- [112] A. L. Harris et al. “Molecular Vibrational Energy Relaxation at Metal Surfaces by Picosecond Infrared-Visible Sum Spectroscopy”. In:
- [113] H.-L. Dai and W. Ho. *Laser Spectroscopy and Photochemistry on Metal Surfaces: part 1*. World Scientific Publishing Co. Pte. Ltd., 1995.
- [114] P. Halevi (Ed.) *Photonic Probes of Surfaces*. Progress in Quantum Electronics, 1996, p. 255.
- [115] A. Wieckowski. *Interfacial Electrochemistry: Theory, Experiment and Applications*. CRC Press, 1999, p. 992.
- [116] Z. Chen, D. Gracias, and G. Somorjai. “Sum Frequency Generation (SFG)-Surface Vibrational Spectroscopy Studies of Buried Interfaces: Catalytic Reaction Intermediates on Transition Metal Crystal Surfaces at High Reactant Pressures; Polymer Surface Structures at the Solid-Gas and Solid-Liquid Interfaces”. In: *Appl. Phys. B* 68 (1999), p. 549. DOI: [10.1007/s003400050664](https://doi.org/10.1007/s003400050664). URL: <https://link.springer.com/article/10.1007/s003400050664>.
- [117] Z. Chen. “Understanding Surfaces and Buried Interfaces of Polymer Materials at the Molecular Level Using Sum Frequency Generation Vibrational Spectroscopy”. In: *Polymer International* 56(5) (2007), pp. 577–587.
- [118] R. Khatib et al. “Water Orientation and Hydrogen-Bond Structure at the Fluorite/Water Interface”. In: *Scientific Reports* 6 (2016), p. 24287. DOI: <https://doi.org/10.1038/srep24287>. URL: <https://www.nature.com/articles/srep24287>.
- [119] R. Khatib et al. “Molecular Dynamics Simulations of SFG Librational Modes Spectra of Water at the Water-Air Interface”. In: *J. Phys. Chem. C* 120 (2016), pp. 18665–18673. DOI: <https://doi.org/10.1021/acs.jpcc.6b06371>. URL: <https://pubs.acs.org/doi/abs/10.1021/acs.jpcc.6b06371>.
- [120] R. Khatib and M Sulpizi. “Sum Frequency Generation Spectra from Velocity-Velocity Correlation Functions”. In: *J. Phys. Chem. Lett.* 8 (2017), pp. 1310–1314. DOI: <https://doi.org/10.1021/acs.jpclett.7b00207>. URL: <https://pubs.acs.org/doi/abs/10.1021/acs.jpclett.7b00207>.
- [121] A. Morita. “Theory of Sum Frequency Generation Spectroscopy”. In: Singapore: Springer Nature Singapore Pte Ltd., 2018. Chap. 1, p. 2.
- [122] For OH vibrations at room temperature, the energy difference between vibrational states $|\nu = 0\rangle$ and $|\nu = 1\rangle$ is about 4500 K, or 0.4 eV, which is much larger than $k_B T$. Therefore, we can treat the OH like a linear harmonic oscillator.
- [123] S. Mukamel. *Principles of Nonlinear Optical Spectroscopy*. Oxford University Press, Oxford, 1995.
- [124] C. M. Pradier and Y. J. Chabal (Ed.) *Biointerface Characterization by Advanced IR Spectroscopy*. Elsevier, 2011, p. 344.

- [125] R. Vanselow and R. Howe. *Chemistry and Physics of Solid Surfaces VIII*. Springer Science + Business Media, 2012, p. 464.
- [126] A. Morita and J. T. Hynes. “A Theoretical Analysis of the Sum Frequency Generation Spectrum of the Water Surface. II. Time-Dependent Approach”. In: *J. Phys. Chem. B* 106 (2002), pp. 673–685. DOI: [10.1021/jp0133438](https://pubs.acs.org/doi/abs/10.1021/jp0133438). URL: <https://pubs.acs.org/doi/abs/10.1021/jp0133438>.
- [127] A. Morita and J. T. Hynes. “A Theoretical Analysis of the Sum Frequency Generation Spectrum of the Water Surface”. In: *J. Chem. Phys.* 258 (2000), pp. 371–390. DOI: [http://dx.doi.org/10.1016/S0301-0104\(00\)00127-0](http://dx.doi.org/10.1016/S0301-0104(00)00127-0). URL: <http://www.sciencedirect.com/science/article/pii/S0301010400001270>.
- [128] S. Nihonyanagi et al. “Unified Molecular View of the Air/Water Interface Based on Experimental and Theoretical $\chi^{(2)}$ Spectra of an Isotopically Diluted Water Surface”. In: *J. Am. Chem. Soc.* 133 (2011), pp. 16875–16880. DOI: [10.1021/ja2053754](https://pubs.acs.org/doi/abs/10.1021/ja2053754). URL: <https://pubs.acs.org/doi/abs/10.1021/ja2053754>.
- [129] S. A. Corcelli and J. L. Skinner. “Infrared and Raman Line Shapes of Dilute HOD in Liquid H₂O and D₂O from 10 to 90 °C”. In: *J. Phys. Chem. A* 109 (2005), pp. 6154–6165. DOI: <https://doi.org/10.1021/jp0506540>. URL: <https://pubs.acs.org/doi/abs/10.1021/jp0506540>.
- [130] M. Sulpizi et al. “Vibrational Sum Frequency Generation Spectroscopy of the Water Liquid-Vapor Interface from Density Functional Theory-Based Molecular Dynamics Simulations”. In: *J. Phys. Chem. Lett.* 4.1 (2013), pp. 83–87. DOI: [10.1021/jz301858g](http://dx.doi.org/10.1021/jz301858g). eprint: <http://dx.doi.org/10.1021/jz301858g>. URL: <http://dx.doi.org/10.1021/jz301858g>.
- [131] N. Marzari and D. Vanderbilt. “Maximally Localized Generalized Wannier Functions for Composite Energy Bands”. In: *Phys. Rev. B* 56 (20 1997), pp. 12847–12865. DOI: [10.1103/PhysRevB.56.12847](https://link.aps.org/doi/10.1103/PhysRevB.56.12847). URL: <https://link.aps.org/doi/10.1103/PhysRevB.56.12847>.
- [132] M. Salanne et al. “Polarizabilities of individual molecules and ions in liquids from first principles”. In: *J. Phys. Condens. Matter.* 20.49 (2008), p. 494207. URL: <http://stacks.iop.org/0953-8984/20/i=49/a=494207>.
- [133] P. Salvador et al. “Polarizability of the Nitrate Anion and Its Solvation at the Air/Water Interface”. In: *Phys. Chem. Chem. Phys.* 5 (17 2003), pp. 3752–3757. DOI: [10.1039/B304537D](http://dx.doi.org/10.1039/B304537D). URL: <http://dx.doi.org/10.1039/B304537D>.
- [134] A. M. Jubb, W. Hua, and H. Allen. “Environmental Chemistry at Vapor/Water Interfaces: Insights from Vibrational Sum Frequency Generation Spectroscopy”. In: *Ann. Rev. Phys. Chem.* 63 (2012), pp. 107–130. DOI: [10.1146/annurev-physchem-032511-143811](https://www.annualreviews.org/doi/abs/10.1146/annurev-physchem-032511-143811). URL: <https://www.annualreviews.org/doi/abs/10.1146/annurev-physchem-032511-143811>.
- [135] W. Hua, D. Verreault, and H. C. Allen. “Surface Electric Fields of Aqueous Solutions of NH₄NO₃, Mg(NO₃)₂, NaNO₃, and LiNO₃: Implications of Atmospheric Aerosol Chemistry”. In: *J. Phys. Chem. C* 118 (2014), pp. 24941–24949. DOI: <https://doi.org/10.1021/jp505770t>. URL: <https://pubs.acs.org/doi/abs/10.1021/jp505770t>.
- [136] P. K. Weissenborn and R. J. Pugh. “Surface Tension and Bubble Coalescence Phenomena of Aqueous Solutions of Electrolytes”. In: *Langmuir* 11.5 (1995), pp. 1422–1426. DOI: [10.1021/la00005a002](https://pubs.acs.org/doi/abs/10.1021/la00005a002). URL: <https://pubs.acs.org/doi/abs/10.1021/la00005a002>.

- [137] Michael J. Hey et al. "Surface Tensions of Aqueous Solutions of Some 1:1 Electrolytes". In: *J. Chem. Soc., Faraday Trans. 1* 77 (1 1981), pp. 123–128. DOI: [10.1039/F19817700123](https://doi.org/10.1039/F19817700123). URL: <http://dx.doi.org/10.1039/F19817700123>.
- [138] N. L. Jarvis and M. A. Scheiman. "Surface Potentials of Aqueous Electrolyte Solution". In: *J. Phys. Chem.* 72.1 (1968), pp. 74–78. ISSN: 00223654. DOI: [10.1021/j100847a014](https://doi.org/10.1021/j100847a014). URL: <https://pubs.acs.org/doi/abs/10.1021/j100847a014>.
- [139] N L Jarvis. "Effect of Various Salts on the Surface Potential of Water-Air Interface". In: 77.27 (1972), pp. 5177–5182. DOI: [10.1029/JC077i027p05177](https://doi.org/10.1029/JC077i027p05177). URL: <https://agupubs.onlinelibrary.wiley.com/doi/abs/10.1029/JC077i027p05177>.
- [140] L. M. Pegram and M. T. Record, Jr. "Partitioning of Atmospherically Relevant Ions between Bulk Water and the Water/Vapor Interface". In: *Proceedings of the National Academy of Sciences* 103.39 (2006), pp. 14278–14281. ISSN: 0027-8424. DOI: [10.1073/pnas.0606256103](https://doi.org/10.1073/pnas.0606256103). eprint: NIHMS150003. URL: <http://www.pnas.org/cgi/doi/10.1073/pnas.0606256103>.
- [141] W. Hua, A. M. Jubb, and H. C. Allen. "Electric Field Reversal of Na_2SO_4 , $(\text{NH}_4)_2\text{SO}_4$, and Na_2CO_3 Relative to CaCl_2 and NaCl at the Air/Aqueous Interface Revealed by Heterodyne Detected Phase-Sensitive Sum Frequency". In: *J. Phys. Chem. Lett.* 2 (2011), pp. 2515–2520. DOI: <https://doi.org/10.1021/jz200888t>. URL: <https://pubs.acs.org/doi/abs/10.1021/jz200888t>.
- [142] W. Hua, X. Chen, and H. C. Allen. "Phase-Sensitive Sum Frequency Revealing Accommodation of Bicarbonate Ions, and Charge Separation of Sodium and Carbonate Ions within the Air/Water Interface". In: *J. Phys. Chem. A* 115 (2011), pp. 6233–6238. DOI: [10.1021/jp111552f](https://doi.org/10.1021/jp111552f). URL: <https://pubs.acs.org/doi/abs/10.1021/jp111552f>.
- [143] X. Chen, W. Hua, and H. C. Allen. "Interfacial Water Structure Associated with Phospholipid Membranes Studied by Phase-Sensitive Vibrational Sum Frequency Generation Spectroscopy". In: *J. Am. Chem. Soc.* 132.32 (2010), pp. 11336–11342. DOI: [10.1021/ja1048237](https://doi.org/10.1021/ja1048237). URL: <https://pubs.acs.org/doi/abs/10.1021/ja1048237>.
- [144] D. Verreault and H. C. Allen. "Bridging the Gap between Microscopic and Macroscopic Views of Air/Aqueous Salt Interfaces". In: *Chem. Phys. Lett.* 586 (2013), pp. 1–9. DOI: [10.1016/j.cplett.2013.08.054](https://doi.org/10.1016/j.cplett.2013.08.054). URL: <http://www.sciencedirect.com/science/article/pii/S0009261413010646>.
- [145] D. Verreault and H. C. Allen. "Reactions at Surfaces in the Atmosphere: Integration of Experiments and Theory as Necessary (But Not Necessarily Sufficient) for Predicting the Physical Chemistry of Aerosols". In: *Phys. Chem. Chem. Phys.* 11 (2009), pp. 7760–7779. DOI: [10.1039/b906540g](https://doi.org/10.1039/b906540g). URL: <http://pubs.rsc.org/en/content/articlepdf/2009/cp/b906540g>.
- [146] J. Mathias Weber et al. "Isolating the Spectroscopic Signature of a Hydration Shell With the Use of Clusters: Superoxide Tetrahydrate". In: *Science* 287.5462 (2000), pp. 2461–2463. ISSN: 0036-8075. DOI: [10.1126/science.287.5462.2461](https://doi.org/10.1126/science.287.5462.2461). eprint: <https://science.sciencemag.org/content/287/5462/2461.full.pdf>. URL: <https://science.sciencemag.org/content/287/5462/2461>.

- [147] M. F. Kropman and H. J. Bakker. “Negligible Effect of Ions on the Hydrogen-Bond Structure in Liquid Water”. In: *Science* 291 (2001), p. 2118. DOI: [10.1126/science.1084801](https://doi.org/10.1126/science.1084801). URL: <https://science.sciencemag.org/content/301/5631/347>.
- [148] R. Jimenez et al. “Femtosecond Solvation Dynamics of Water”. In: *Nature* 369 (1994), pp. 471–473. DOI: <https://doi.org/10.1038/369471a0>.
- [149] David E. Smith and Liem X. Dang. “Computer simulations of NaCl association in polarizable water”. In: *J. Chem. Phys.* 100.5 (1994), pp. 3757–3766. DOI: [10.1063/1.466363](https://doi.org/10.1063/1.466363). URL: <https://doi.org/10.1063/1.466363>.
- [150] Amalendu Chandra. “Effects of Ion Atmosphere on Hydrogen-Bond Dynamics in Aqueous Electrolyte Solutions”. In: *Phys. Rev. Lett.* 85 (4 2000), pp. 768–771. DOI: [10.1103/PhysRevLett.85.768](https://doi.org/10.1103/PhysRevLett.85.768). URL: <https://link.aps.org/doi/10.1103/PhysRevLett.85.768>.
- [151] L. Jiang et al. “Gas-Phase Vibrational Spectroscopy of Microhydrated Magnesium Nitrate Ions $[\text{MgNO}_3(\text{H}_2\text{O})_{1-4}]^+$ ”. In: *J. Am. Chem. Soc.* 132 (2010), pp. 7398–7404. DOI: [10.1021/ja1011806](https://doi.org/10.1021/ja1011806). URL: <https://pubs.acs.org/doi/abs/10.1021/ja1011806>.
- [152] N. Heine and K. R. Asmis. “Cryogenic Ion Trap Vibrational Spectroscopy of Hydrogen-Bonded Clusters Relevant to Atmospheric Chemistry”. In: *J. Am. Chem. Soc.* 137 (2015), pp. 1–34. DOI: [https://doi.org/10.1080/0144235X.2014.979659](https://doi.org/10.1021/ja1011806). URL: <https://www.tandfonline.com/doi/full/10.1080/0144235X.2014.979659>.
- [153] J. Teixeira, M. C. Bellisent-Funel, and S. H. Chen. “Dynamics of Water Studied by Neutron Scattering”. In: *J. Phys. Condens. Matter* 2 (1990), SA105. DOI: [10.1088/0953-8984/2/S/011](https://doi.org/10.1088/0953-8984/2/S/011). URL: <http://iopscience.iop.org/0953-8984/2/S/011>.
- [154] Sundaram Balasubramanian, Subrata Pal, and Biman Bagchi. “Hydrogen-Bond Dynamics Near a Micellar Surface: Origin of the Universal Slow Relaxation at Complex Aqueous Interfaces”. In: *Phys. Rev. Lett.* 89 (11 2002), p. 115505. DOI: [10.1103/PhysRevLett.89.115505](https://doi.org/10.1103/PhysRevLett.89.115505). URL: <https://link.aps.org/doi/10.1103/PhysRevLett.89.115505>.
- [155] Jr. O. Rodriguez and J. M. Lisy. “Revisiting $\text{Li}^+(\text{H}_2\text{O})_{3-4}\text{Ar}_1$ Clusters: Evidence of High-Energy Conformers from Infrared Spectra”. In: *J. Phys. Chem. Lett.* 2 (2011), p. 1444. DOI: [10.1021/jp112087e](https://doi.org/10.1021/jp112087e). URL: <https://doi.org/10.1021/jp112087e>.
- [156] D. J. Miller and J. M. Lisy. “Hydrated Alkali-Metal Cations: Infrared Spectroscopy and Ab Initio Calculations of $\text{M}^+(\text{H}_2\text{O})_{x=2-5}\text{Ar}$ Cluster Ions for $\text{M} = \text{Li, Na, K, and Cs}$ ”. In: *J. Am. Chem. Soc.* 130 (2008), pp. 15381–15392. DOI: [10.1021/ja803665q](https://doi.org/10.1021/ja803665q). URL: <https://pubs.acs.org/doi/abs/10.1021/ja803665q>.
- [157] D. J. Miller and J. M. Lisy. “Entropic Effects on Hydrated Alkali-Metal Cations: Infrared Spectroscopy and Ab Initio Calculations of $\text{M}^+(\text{H}_2\text{O})_{x=2-5}$ Cluster Ions for $\text{M} = \text{Li, Na, K, and Cs}$ ”. In: *J. Am. Chem. Soc.* 130 (2008), p. 15393. DOI: [10.1021/ja803666m](https://doi.org/10.1021/ja803666m). URL: <https://pubs.acs.org/doi/abs/10.1021/ja803666m>.

- [158] J. P. Beck and J. M. Lisy. “Infrared Spectroscopy of Hydrated Alkali Metal Cations: Evidence of Multiple Photon Absorption”. In: *J. Chem. Phys.* 135 (2011), p. 044302. DOI: [10.1063/1.3609760](https://doi.org/10.1063/1.3609760). URL: <https://aip.scitation.org/doi/abs/10.1063/1.3609760>.
- [159] D. E. Otten, P. B. Petersen, and R. Saykally. “Observation of Nitrate Ions at the Air/Water Interface by UV-Second Harmonic Generation”. In: *J. Chem. Phys. Lett.* 449 (4-6 2007), pp. 261–265.
- [160] D. J. Tobias et al. “Simulation and Theory of Ions at Atmospherically Relevant Aqueous Liquid-Air Interfaces”. In: *Annu. Rev. Phys. Chem.* 64 (2013), pp. 339–359. DOI: [10.1146/annurev-physchem-040412-110049](https://doi.org/10.1146/annurev-physchem-040412-110049). URL: <http://www.annualreviews.org/doi/pdf/10.1146/annurev-physchem-040412-110049>.
- [161] E. S. Shamay et al. “At the Water’s Edge: Nitric Acid as Weak Acid”. In: *J. Am. Chem. Soc.* 129.43 (2007), p. 12910. DOI: [10.1021/ja074811f](https://doi.org/10.1021/ja074811f). URL: <https://doi.org/10.1021/ja074811f>.
- [162] G. C. Pimentel and A. L. McClellan. *The Hydrogen Bond*. W. H. Freeman, San Francisco, 1960.
- [163] Y. Marechal. “The Molecular Structure of Liquid Water Delivered by Absorption Spectroscopy in the Whole IR Region Completed with Thermodynamics Data”. In: *J. molecular structure* 1004 (2011), pp. 146–155. DOI: [10.1016/j.molstruc.2011.07.054](https://doi.org/10.1016/j.molstruc.2011.07.054). URL: <https://www.sciencedirect.com/science/article/abs/pii/S0022286011006247>.
- [164] S. Baldelli, C. Schnitzer, and M. J. Shultz. “Sum Frequency Generation Investigation of Water at the Surface of H₂O/H₂SO₄ Binary Systems”. In: *J. Phys. Chem. B* 101 (1997), pp. 10435–10441. DOI: [10.1021/jp972376d](https://doi.org/10.1021/jp972376d). URL: <https://pubs.acs.org/doi/abs/10.1021/jp972376d>.
- [165] L. M. Pegram and M. T. Record Jr. “Partitioning of Atmospherically Relevant Ions between Bulk Water and the Water/Vapor Interface”. In: *Proc. Natl. Acad. Sci. USA* 103 (2006), pp. 14278–14281.
- [166] L. M. Pegram and M. T. Record, Jr. “Thermodynamic Origin of Hofmeister Ion Effects”. In: *J. Phys. Chem. B* 112 (2008), pp. 9428–9436. DOI: [10.1021/jp800816a](https://doi.org/10.1021/jp800816a). URL: <https://pubs.acs.org/doi/abs/10.1021/jp800816a>.
- [167] E. A. Carter et al. “Constrained Reaction Coordinate Dynamics for the Simulation of Rare Events”. In: *Chem. Phys. Lett.* 156 (1989), p. 472.
- [168] M. Sprik and G. Ciccotti. “Free energy from constrained molecular dynamics”. In: *J. Chem. Phys.* 109 (1998), p. 7737.
- [169] M. E. Tuckerman. *Statistical Mechanics: Theory and Molecular Simulation*. Oxford University Press, 2010.
- [170] S. Ghosal et al. “Electron Spectroscopy of Aqueous Solution Interfaces Reveals Surface Enhancement of Halides”. In: *Science* 307 (2005), p. 563. DOI: [10.1126/science.1106525](https://doi.org/10.1126/science.1106525). URL: <https://science.sciencemag.org/content/307/5709/563>.
- [171] P. Jungwirth and D. J. Tobias. “Molecular Structure of Salt Solutions: A New View of the Interface with Implications for Heterogeneous Atmospheric Chemistry”. In: *J. Phys. Chem. B* 105 (2001), pp. 10468–10472.

- [172] L. X. Dang and T.-M. Chang. “Molecular Mechanism of Ion Binding to the Liquid/Vapor Interface of Water”. In: *J. Phys. Chem. B* 106 (2002), pp. 235–238. DOI: <https://doi.org/10.1021/jp011853w>. URL: <https://pubs.acs.org/doi/abs/10.1021/jp011853w>.
- [173] L. Vrbka et al. “Propensity of Soft Ions for the Air/Water Interface”. In: *Current Opinion in Colloid and Interface Science* 9 (2004), pp. 67–73. DOI: [10.1016/j.cocis.2004.05.028](https://doi.org/10.1016/j.cocis.2004.05.028). URL: <https://www.sciencedirect.com/science/article/pii/S1359029404000330>.
- [174] B. C. Garrett. “Ions at the Air/Water Interface”. In: *Science* 303.5661 (2004), pp. 1146–1147. DOI: [10.1126/science.1089801](https://doi.org/10.1126/science.1089801). URL: <https://science.sciencemag.org/content/303/5661/1146>.
- [175] P. Bajaj, A. W. Götz, and F. Paesani. “Toward Chemical Accuracy in the Description of Ion-Water Interactions through Many-Body Representations. I. Halide-Water Dimer Potential Energy Surfaces”. In: *J. Chem. Theory Comput.* 12 (2016), pp. 2698–2705. DOI: [10.1021/acs.jctc.6b00302](https://doi.org/10.1021/acs.jctc.6b00302). URL: <https://pubs.acs.org/doi/abs/10.1021/acs.jctc.6b00302>.
- [176] D. F. Liu et al. “Vibrational Spectroscopy of Aqueous Sodium Halide Solutions and Air-Liquid Interfaces: Observation of Increased Interfacial Depth”. In: *J. Phys. Chem. B* 108 (2004), pp. 2252–2260. DOI: [10.1021/jp036169r](https://doi.org/10.1021/jp036169r). URL: <https://pubs.acs.org/doi/abs/10.1021/jp036169r>.
- [177] M. J. Shultz et al. “Sum Frequency Generation Spectroscopy of the Aqueous Interface: Ionic and Soluble Molecular Solutions”. In: *Int. Rev. Phys. Chem.* 19.1 (2010), pp. 123–153.
- [178] A. Luzar. “Water Hydrogen-Bond Dynamics Close to Hydrophobic and Hydrophilic groups”. In: *Faraday Discuss.* 103 (0 1996), pp. 29–40. DOI: [10.1039/FD9960300029](https://doi.org/10.1039/FD9960300029). URL: <http://dx.doi.org/10.1039/FD9960300029>.
- [179] Bernard Cabane and Rodolphe Vuilleumier. “The physics of liquid water”. In: 2005, pp. 159–171. DOI: [10.1016/j.crte.2004.09.018](https://doi.org/10.1016/j.crte.2004.09.018).
- [180] Janamejaya Chowdhary and Branka M. Ladanyi. “Hydrogen Bond Dynamics at the Water/Hydrocarbon Interface”. In: *J. Phys. Chem. B* 113 (13 Nov. 2008), pp. 4045–4053. DOI: [10.1021/jp8061509](https://doi.org/10.1021/jp8061509).
- [181] L.-Å. Näslund et al. “X-ray Absorption Spectroscopy Study of the Hydrogen Bond Network in the Bulk Water of Aqueous Solutions”. In: *J. Phys. Chem. A* 109.27 (2005), pp. 5995–6002. DOI: [10.1021/jp050413s](https://doi.org/10.1021/jp050413s). URL: <https://doi.org/10.1021/jp050413s>.
- [182] A. Tongraar, P. Tangkawanwanit, and B. M. Rode. “A Combined QM/MM Molecular Dynamics Simulations Study of Nitrate Anion (NO_3^-) in Aqueous Solution”. In: *J. Phys. Chem. A* 110.47 (2006), pp. 12918–12926. DOI: [10.1021/jp064779w](https://doi.org/10.1021/jp064779w). URL: <https://pubs.acs.org/doi/abs/10.1021/jp064779w>.
- [183] J. Chanda and S. Bandyopadhyay. “Hydrogen Bond Lifetime Dynamics at the Interface of a Surfactant Monolayer”. In: *J. Phys. Chem. B* 110.46 (2006), pp. 23443–23449.
- [184] A. Tongraar, S. Hannongbua, and B. M. Rode. “QM/MM MD Simulations of Iodide Ion (I^-) in Aqueous Solution: A Delicate Balance Between Ion-Water and Water-Water H-bond Interactions”. In: *J. Phys. Chem. A* 114.12 (2010), pp. 4334–4339. ISSN: 10895639. DOI: [10.1021/jp910435d](https://doi.org/10.1021/jp910435d). URL: <https://www.ncbi.nlm.nih.gov/pubmed/20196599>.

- [185] Puja Banerjee, Subramanian Yashonath, and Biman Bagchi. “Coupled jump rotational dynamics in aqueous nitrate solutions”. In: *J. Chem. Phys.* 145.23 (2016), p. 234502. DOI: [10.1063/1.4971864](https://doi.org/10.1063/1.4971864). eprint: <https://aip.scitation.org/doi/pdf/10.1063/1.4971864>. URL: <https://aip.scitation.org/doi/abs/10.1063/1.4971864>.
- [186] Jasper C. Werhahn et al. “Dynamics of Weak, Bifurcated, and Strong Hydrogen Bonds in Lithium Nitrate Trihydrate”. In: *J. Phys. Chem. Lett.* 2 (2011), pp. 1633–1638. DOI: [dx.doi.org/10.1021/jz200591v](https://doi.org/10.1021/jz200591v). URL: <https://pubs.acs.org/doi/abs/10.1021/jz200591v>.
- [187] Joseph A. Fournier et al. “Interplay of Ion-Water and Water-Water Interactions within the Hydration Shells of Nitrate and Carbonate Directly Probed with 2D IR Spectroscopy”. In: *J. Am. Chem. Soc.* 138.30 (2016), pp. 9634–9645. DOI: [10.1021/jacs.6b05122](https://doi.org/10.1021/jacs.6b05122). URL: <https://pubs.acs.org/doi/full/10.1021/jacs.6b05122>.
- [188] A. Luzar and D. Chandler. “Effect of Environment on Hydrogen Bond Dynamics in Liquid Water”. In: *Phys. Rev. Lett.* 76 (6 1996), pp. 928–931. DOI: [10.1103/PhysRevLett.76.928](https://doi.org/10.1103/PhysRevLett.76.928). URL: <https://link.aps.org/doi/10.1103/PhysRevLett.76.928>.
- [189] D. Chandler. *Introduction to Modern Statistical Mechanics*. Oxford University press, Oxford, 1987.
- [190] S. Pal, B. Bagchi, and S. Balasubramanian. “Hydration Layer of a Cationic Micelle, C₁₀TAB: Structure, Rigidity, Slow Reorientation, Hydrogen Bond Lifetime, and Solvation Dynamics”. In: *J. Phys. Chem. B* 109 (2005), pp. 12879–12890. DOI: [10.1021/jp0510793](https://doi.org/10.1021/jp0510793). URL: <https://pubs.acs.org/doi/abs/10.1021/jp0510793>.
- [191] R. Kumar, J. R. Schmidt, and J. L. Skinner. “Hydrogen Bonding Definitions and Dynamics in Liquid Water”. In: *J. Chem. Phys.* 126.20 (2007), p. 204107. DOI: [10.1063/1.2742385](https://doi.org/10.1063/1.2742385). eprint: <https://doi.org/10.1063/1.2742385>. URL: <https://doi.org/10.1063/1.2742385>.
- [192] F. Sciortino and S. L. Fornili. “Hydrogen Bond Cooperativity in Simulated Water: Time Dependence Analysis of Pair Interactions”. In: *J. Chem. Phys.* 90.5 (1989), pp. 2786–2792. DOI: [10.1063/1.455927](https://doi.org/10.1063/1.455927). URL: <https://doi.org/10.1063/1.455927>.
- [193] A. K. Soper and M. G. Phillips. “A New Determination of the Structure of Water at 25 ° C”. In: *Chem. Phys* 107 (1986), pp. 47–60. DOI: [10.1016/0301-0104\(86\)85058-3](https://doi.org/10.1016/0301-0104(86)85058-3). URL: <https://www.sciencedirect.com/science/article/abs/pii/0301010486850583>.
- [194] Alenka Luzar and David Chandler. “Structure and hydrogen bond dynamics of water-dimethyl sulfoxide mixtures by computer simulations”. In: *J. Chem. Phys.* 98.10 (1993), pp. 8160–8173. DOI: [10.1063/1.464521](https://doi.org/10.1063/1.464521). URL: <https://doi.org/10.1063/1.464521>.
- [195] D. C. Rapaport. “Hydrogen Bonds in Water: Network Organization and Lifetimes”. In: *Mol. Phys.* 50 (1983), pp. 1151–1162. DOI: [10.1080/00268978300102931](https://doi.org/10.1080/00268978300102931). URL: <https://doi.org/10.1080/00268978300102931>.
- [196] A Luzar and D Chandler. *Application of the Reactive Flux Formalism to Study Water Hydrogen Bond Dynamics*. In: Bellissent-Funel MC., Dore J. C. (eds) *Hydrogen Bond Networks*. Vol. 435. Springer, Dordrecht, 1994.

- [197] Rustam Z. Khaliullin and Thomas D. Kühne. “Microscopic Properties of Liquid Water from Combined Ab Initio Molecular Dynamics and Energy Decomposition Studies”. In: *Phys. Chem. Chem. Phys.* 15 (38 2013), pp. 15746–15766. DOI: [10.1039/C3CP51039E](https://doi.org/10.1039/C3CP51039E). URL: <http://dx.doi.org/10.1039/C3CP51039E>.
- [198] S. Chowdhuri and A. Chandra. “Dynamics of Halide Ion-Water Hydrogen Bonds in Aqueous Solutions: Dependence on Ion Size and Temperature”. In: *J. Phys. Chem. B* 110 (2006), pp. 9674–9680. DOI: [10.1021/jp057544d](https://doi.org/10.1021/jp057544d). URL: <https://pubs.acs.org/doi/abs/10.1021/jp057544d>.
- [199] F. Sciortino et al. “Lifetime of the Bond Network and Gel-Like Anomalies in Supercooled Water”. In: *Phys. Rev. Lett.* 64.14 (1990), pp. 1686–1689. DOI: [10.1103/PhysRevLett.64.1686](https://doi.org/10.1103/PhysRevLett.64.1686). URL: <https://link.aps.org/doi/10.1103/PhysRevLett.64.1686>.
- [200] T. Krausche and W. Nadler. “Statistical Mechanics of Hydrogen Bond Networks”. In: *Z. Phys. B: Condens. Matter* 86.5 (1992), p. 433. URL: <https://link.springer.com/content/pdf/10.1007/BF01323737.pdf>.
- [201] F. W. Starr, J. K. Nielsen, and H. E. Stanley. “Fast and Slow Dynamics of Hydrogen Bonds in Liquid Water”. In: *Phys. Rev. Lett.* 82.11 (1999), p. 2294.
- [202] V. P. Voloshin and Yu. I. Naberukhin. “Hydrogen Bond Lifetime Distributions in Computer-Simulated Water”. In: *J. Structural Chem.* 50 (2009), pp. 78–89.
- [203] A. Geiger et al. “Structure and Dynamics of the Hydrogen Bond Network in Water by Computer Simulations”. In: *J. Phys. (Paris)* 45 (1984), pp. C7–13–C7–30.
- [204] H. E. Stanley et al. “Unsolved Mysteries of Water in its Liquid and Glassy Phases”. In: *J. Phys.: Condens. Matter* 12 (2000), A403–A412. URL: <https://iopscience.iop.org/article/10.1088/0953-8984/12/8A/355/pdf>.
- [205] F. W. Starr, J. K. Nielsen, and H. Eugene Sta. “Hydrogen-Bond Dynamics for the Extended Simple Point-Charge Model of Water”. In: *Phys. Rev. E* 62 (2000), pp. 579–587. DOI: [10.1103/physreve.62.579](https://doi.org/10.1103/physreve.62.579). URL: <https://www.ncbi.nlm.nih.gov/pubmed/11088494>.
- [206] A. Luzar. “Resolving the Hydrogen Bond Dynamics Conundrum”. In: *J. Chem. Phys.* 113 (2000), p. 10663. DOI: [10.1063/1.1320826](https://doi.org/10.1063/1.1320826). URL: <https://aip.scitation.org/doi/abs/10.1063/1.1320826>.
- [207] D. Chandler. “Roles of Classical Dynamics and Quantum Dynamics on Activated Processes Occurring in Liquids”. In: *J. Stat. Phys.* 42 (1986), pp. 49–67. DOI: [10.1007/BF01010840](https://doi.org/10.1007/BF01010840). URL: <https://link.springer.com/article/10.1007/BF01010840>.
- [208] D. Chandler. “Statistical Mechanics of Isomerization Dynamics in Liquids and the Transition State Approximation”. In: *J. Chem. Phys.* 68 (1978), pp. 2959–2970. DOI: [10.1063/1.436049](https://doi.org/10.1063/1.436049). URL: <https://aip.scitation.org/doi/abs/10.1063/1.436049>.
- [209] J. Kessler et al. “Structure and Dynamics of the Instantaneous Water/Vapor Interface Revisited by Path-Integral and Ab Initio Molecular Dynamics Simulations”. In: *J. Phys. Chem. B* 119.31 (2015), pp. 10079–10086. DOI: [10.1021/acs.jpcc.5b04185](https://doi.org/10.1021/acs.jpcc.5b04185). URL: <https://pubs.acs.org/doi/10.1021/acs.jpcc.5b04185>.
- [210] A. Luzar and D. Chandler. “Hydrogen-Bond Kinetics in Liquid Water”. In: *Nature* 379 (1996), pp. 55–57.

- [211] A. P. Willard and D. Chandler. "Instantaneous Liquid Interfaces". In: *J. Phys. Chem. B* 114.5 (2010), p. 1954.
- [212] R. Michael Townsend, Jan Gryko, and Stuart A. Rice. "Structure of the Liquid–Vapor Interface of Water". In: *J. Chem. Phys.* 82.9 (1985), pp. 4391–4392. DOI: [10.1063/1.448808](https://doi.org/10.1063/1.448808). URL: <https://doi.org/10.1063/1.448808>.
- [213] Ramona S. Taylor, Liem X. Dang, and Bruce C. Garrett. "Molecular Dynamics Simulations of the Liquid/Vapor Interface of SPC/E Water". In: *J. Phys. Chem.* 100 (1996), pp. 11720–11725.
- [214] I. V. Stiopkin et al. "Hydrogen Bonding at the Water Surface Revealed by Isotopic Dilution Spectroscopy". In: *Nature* 474 (2011), p. 192. DOI: [10.1038/nature10173](https://doi.org/10.1038/nature10173). URL: <https://www.nature.com/articles/nature10173>.
- [215] Eric Tyrode and Jonathan F. D. Liljeblad. "Water Structure Next to Ordered and Disordered Hydrophobic Silane Monolayers: A Vibrational Sum Frequency Spectroscopy Study". In: *J. Phys. Chem. C* 117.4 (2013), pp. 1780–1790.
- [216] D. E. Otten, P. B. Petersen, and R. J. Saykally. "Observation of Nitrate Ions at the Air/Water Interface by UV-Second Harmonic Generation". In: *Chem. Phys. Lett.* 449 (4-6 2007), pp. 261–265. DOI: [10.1016/j.cplett.2007.10.081](https://doi.org/10.1016/j.cplett.2007.10.081). URL: <https://www.sciencedirect.com/science/article/abs/pii/S0009261407014017>.
- [217] K. Hashimoto and K. Morokuma. "Ab Initio Molecular Orbital Study of Na(H₂O)_n (n = 1-6) Clusters and Their Ions. Comparison of Electronic Structure of the "Surface" and "Interior" Complexes". In: *J. Am. Chem. Soc.* 116.25 (1994), pp. 11436–11443. DOI: [10.1021/ja00104a024](https://doi.org/10.1021/ja00104a024).
- [218] Lavanya M. Ramaniah, Marco Bernasconi, and Michele Parrinello. "Density-functional study of hydration of sodium in water clusters". In: *J. Chem. Phys.* 109.16 (1998), pp. 6839–6843. DOI: [10.1063/1.477250](https://doi.org/10.1063/1.477250). URL: <https://doi.org/10.1063/1.477250>.
- [219] A. W. Omta et al. "Negligible Effect of Ions on the Hydrogen-Bond Structure in Liquid Water". In: *Science* 301 (2003), p. 347. DOI: [10.1126/science.1084801](https://doi.org/10.1126/science.1084801). URL: <https://science.sciencemag.org/content/301/5631/347>.
- [220] Y. Zhang and P. S Cremer. "Interactions between Macromolecules and Ions: the Hofmeister Series". In: *Current Opinion in Chemical Biology* 10 (2006), p. 658.
- [221] T. Steinel et al. "Watching Hydrogen Bonds Break: A Transient Absorption Study of Water". In: *J. Phys. Chem. A* 108 (2004), pp. 10957–10964. DOI: [10.1021/jp046711r](https://doi.org/10.1021/jp046711r). URL: <https://pubs.acs.org/doi/abs/10.1021/jp046711r>.
- [222] S. Chowdhuri and A. Chandra. "Hydrogen Bonds in Aqueous Electrolyte Solutions: Statistics and Dynamics Based on Both Geometric and Energetic Criteria". In: *Phys. Rev. E* 66 (2002), p. 041203.
- [223] M. F. Kropman and H. J. Bakker. "Negligible effect of ions on the hydrogen-bond structure in liquid water". In: *Science* 291 (2001), p. 2118.
- [224] S. Yadav, A. Choudhary, and A. Chandra. "A First-Principles Molecular Dynamics Study of the Solvation Shell Structure, Vibrational Spectra, Polarity, and Dynamics around a Nitrate Ion in Aqueous Solution". In: *J. Phys. Chem. B* 121 (2017), pp. 9032–9044.

- [225] David M. Jonas et al. “Pump-Probe Polarization Anisotropy Study of Femtosecond Energy Transfer within the Photosynthetic Reaction Center of *Rhodospirillum rubrum* R26”. In: *J. Phys. Chem.* 100.20 (1996), pp. 12660–12673. DOI: [10.1021/jp960708t](https://doi.org/10.1021/jp960708t). URL: <https://doi.org/10.1021/jp960708t>.
- [226] Darcie A Farrow et al. “Polarized Pump-probe Measurements of Electronic Motion via a Conical Intersection”. In: *J. Chem. Phys.* 128 (2006), pp. 144510–144531.
- [227] Attila Szabo. “Theory of fluorescence depolarization in macromolecules and membranes”. In: *The Journal of Chemical Physics* 81.1 (1984), pp. 150–167. DOI: [10.1063/1.447378](https://doi.org/10.1063/1.447378). URL: <https://doi.org/10.1063/1.447378>.
- [228] G. R. Fleming. *Chemical Applications of Ultrafast Spectroscopy*. Oxford University Press, New York, 1986.
- [229] T. C. L. Jansen et al. “Two-Dimensional Infrared Spectroscopy and Ultrafast Anisotropy Decay of Water”. In: *J. Chem. Phys.* 132 (2010), p. 224503. DOI: [10.1063/1.3454733](https://aip.scitation.org/doi/abs/10.1063/1.3454733). URL: <https://aip.scitation.org/doi/abs/10.1063/1.3454733>.
- [230] T. C. L. Jansen and J. Knoester. “Nonadiabatic Effects in the Two-Dimensional Infrared Spectra of Peptides: Application to Alanine Dipeptide”. In: *J. Phys. Chem. B* 110 (2006), pp. 22910–22916. DOI: [10.1021/jp064795t](https://pubs.acs.org/doi/abs/10.1021/jp064795t). URL: <https://pubs.acs.org/doi/abs/10.1021/jp064795t>.
- [231] J. R. Schmidt, S. A. Corcelli, and J. L. Skinner. “Pronounced Non-Condon Effects in the Ultrafast Infrared Spectroscopy of Water”. In: *J. Chem. Phys.* 123 (2005), p. 044513. DOI: [10.1063/1.1961472](https://aip.scitation.org/doi/abs/10.1063/1.1961472). URL: <https://aip.scitation.org/doi/abs/10.1063/1.1961472>.
- [232] A. Tokmakoff. “Orientational correlation functions and polarization selectivity for nonlinear spectroscopy of isotropic media. I. Third order”. In: *The Journal of Chemical Physics* 105.1 (1996), pp. 1–12. DOI: [10.1063/1.471856](https://doi.org/10.1063/1.471856). URL: <https://doi.org/10.1063/1.471856>.
- [233] Y. L. A. Rezus and H. J. Bakker. “Orientational dynamics of isotopically diluted H₂O and D₂O”. In: *The Journal of Chemical Physics* 125.14 (2006), p. 144512. DOI: [10.1063/1.2353831](https://doi.org/10.1063/1.2353831). URL: <https://doi.org/10.1063/1.2353831>.
- [234] Takuma Yagasaki, Junichi Ono, and Shinji Saito. “Ultrafast energy relaxation and anisotropy decay of the librational motion in liquid water: A molecular dynamics study”. In: *J. Chem. Phys.* 131.16 (2009), p. 164511. DOI: [10.1063/1.3254518](https://doi.org/10.1063/1.3254518). eprint: <https://doi.org/10.1063/1.3254518>. URL: <https://doi.org/10.1063/1.3254518>.
- [235] H. Bakker and J. L. Skinner. “Vibrational Spectroscopy as a Probe of Structure and Dynamics in Liquid Water”. In: *Chem. Rev.* 110 (2010), p. 1498.
- [236] Y. S. Lin et al. “On the Calculation of Rotational Anisotropy Decay, as Measured by Ultrafast Polarization-Resolved Vibrational Pump-Probe Experiments”. In: *J. Chem. Phys.* 132 (2010), p. 174505. DOI: [10.1063/1.3409561](https://aip.scitation.org/doi/abs/10.1063/1.3409561). URL: <https://aip.scitation.org/doi/abs/10.1063/1.3409561>.
- [237] P. L. Silvestrelli and M. Parrinello. “Water Molecule Dipole in the Gas and in the Liquid Phase”. In: *Phys. Rev. Lett.* 82.16 (1999), pp. 3308–3311. DOI: <https://doi.org/10.1103/PhysRevLett.82.3308>. URL: <https://journals.aps.org/prl/abstract/10.1103/PhysRevLett.82.3308>.

- [238] E. B. Wilson. *Molecular Vibrations*. New York: McGraw-Hill Book Company, Inc., 1955.
- [239] G. Lippert, J. Hutter, and M. Parrinello. “The Gaussian and augmented-plane-wave density functional method for ab initio molecular dynamics simulations”. In: *Theor. Chem. Acc.* 103 (1999), p. 124.
- [240] M. Krack. “Pseudopotentials for H to Kr optimized for gradient-corrected exchange-correlation functionals”. In: *Theor. Chem. Acc.* 114 (2005), p. 145.
- [241] J. VandeVondele and J. Hutte. “Gaussian Basis Sets for Accurate Calculations on Molecular Systems in Gas and Condensed Phases”. In: *J. Chem. Phys.* 127 (2007), p. 114105.
- [242] S. Goedecker, M. Teter, and J. Hutter. “Separable Dual-Space Gaussian Pseudopotentials”. In: *Phys. Rev. B* 54 (3 1996), pp. 1703–1710. DOI: [10.1103/PhysRevB.54.1703](https://doi.org/10.1103/PhysRevB.54.1703). URL: <https://link.aps.org/doi/10.1103/PhysRevB.54.1703>.
- [243] I. Ohmine. “Liquid Water Dynamics: Collective Motions, Fluctuation, and Relaxation”. In: *J. Phys. Chem* 99.18 (1995), pp. 6767–6776. DOI: [10.1021/j100018a004](https://doi.org/10.1021/j100018a004). URL: <https://pubs.acs.org/doi/abs/10.1021/j100018a004>.
- [244] E. A. Carter et al. “Constrained Reaction Coordinate Dynamics for the Simulation of Rare Events”. In: *Chem. Phys. Lett.* 156 (1989), p. 472. DOI: [10.1016/S0009-2614\(89\)87314-2](https://doi.org/10.1016/S0009-2614(89)87314-2). URL: <https://www.sciencedirect.com/science/article/abs/pii/S0009261489873142>.
- [245] M. Sprik and G. Ciccotti. “Free Energy from Constrained Molecular Dynamics”. In: *J. Chem. Phys.* 109 (1998), pp. 7737–7744. DOI: [10.1063/1.477419](https://doi.org/10.1063/1.477419). URL: <https://ui.adsabs.harvard.edu/abs/1998JChPh.109.7737S>.
- [246] M. Ferrario, M. Haughney, and R. McDonald M. L. Klein. “Molecular-Dynamics Simulation of Aqueous Mixtures: Methanol Acetone, and Ammonia”. In: *J. Chem. Phys.* 93 (1990), p. 5156. DOI: [10.1063/1.458652](https://doi.org/10.1063/1.458652). URL: <https://aip.scitation.org/doi/abs/10.1063/1.458652>.
- [247] Raymond D. Mountain. “Comparison of a Fixed-Charge and a Polarizable Water Model”. In: *J. Chem. Phys.* 103.8 (1995), pp. 3084–3090. DOI: [10.1063/1.470497](https://doi.org/10.1063/1.470497). eprint: <https://doi.org/10.1063/1.470497>. URL: <https://doi.org/10.1063/1.470497>.
- [248] L. J. Root and B. J. Berne. “Effect of Pressure on Hydrogen Bonding in Glycerol: A Molecular Dynamics Investigation”. In: *J. Chem. Phys.* 107 (1997), pp. 4350–4357. DOI: [10.1063/1.474776](https://doi.org/10.1063/1.474776). URL: <https://doi.org/10.1063/1.474776>.
- [249] Hee-Seung Lee and Mark E. Tuckerman. “Dynamical Properties of Liquid Water from Ab Initio Molecular Dynamics Performed in the Complete Basis Set Limit”. In: *J. Chem. Phys.* 126.16 (2007), p. 164501. DOI: [10.1063/1.2718521](https://doi.org/10.1063/1.2718521). URL: <https://doi.org/10.1063/1.2718521>.
- [250] H. Ishikita and K. Saito. “Proton Transfer Reactions and Hydrogen-Bond Networks in Protein Environments”. In: *J. R. Soc. Interface* 11.91 (2013), p. 20130518. DOI: [10.1098/rsif.2013.0518](https://doi.org/10.1098/rsif.2013.0518). URL: <https://www.ncbi.nlm.nih.gov/pmc/articles/PMC3869154/>.

- [251] H. Tanaka, K. Nakanishi, and N. Watanabe. “Constant Temperature Molecular Dynamics Calculation on Lennard-Jones Fluid and Its Application to Water”. In: *J. Chem. Phys.* 78.5 (1983), pp. 2622–2634. DOI: <https://doi.org/10.1063/1.445020>. URL: <https://aip.scitation.org/doi/10.1063/1.445020>.
- [252] Yu. I. Naberukhin and V. P. Voloshin. “Distributions of Hydrogen Bond Lifetimes in Instantaneous and Inherent Structures of Water”. In: *Z. Phys. Chem.* 223 (2009), pp. 999–1011. DOI: [10.1524/zpch.2009.6062](https://doi.org/10.1524/zpch.2009.6062).
- [253] L. D. Landau and E. M. Lifshitz. *Statistical Physics: Part 1*. Elsevier Ltd, 3rd ed, 1980.
- [254] T. E. Dirama, G. A. Carri, and A. P. Sokolov. “Role of Hydrogen Bonds in the Fast Dynamics of Binary Glasses of Trehalose and Glycerol: A Molecular Dynamics Simulation Study”. In: *J. Chem. Phys.* 122 (2005), p. 114505. DOI: [10.1063/1.1870872](https://doi.org/10.1063/1.1870872). URL: <https://aip.scitation.org/doi/abs/10.1063/1.1870872>.
- [255] R. Rey, K. B. Møller, and J. T. Hynes. “Hydrogen Bond Dynamics in Water and Ultrafast Infrared Spectroscopy”. In: *J. Phys. Chem. A* 106.50 (2002), pp. 11993–11996. ISSN: 10895639. DOI: [10.1021/jp026419o](https://doi.org/10.1021/jp026419o). URL: <https://doi.org/10.1021/jp026419o>.
- [256] K. B. Møller, R. Rey, and J. T. Hynes. “Hydrogen Bond Dynamics in Water and Ultrafast Infrared Spectroscopy: A Theoretical Study”. In: *J. Phys. Chem. A* 108.7 (2004), pp. 1275–1289. ISSN: 10895639. DOI: [10.1021/jp035935r](https://doi.org/10.1021/jp035935r). URL: <https://pubs.acs.org/doi/abs/10.1021/jp035935r>.
- [257] H.-S. Tan et al. “Dynamics of Water Confined on a Nanometer Length Scale in Reverse Micelles: Ultrafast Infrared Vibrational Echo Spectroscopy”. In: *Phys. Rev. Lett.* 94 (2005), pp. 057405.1–057405.4. DOI: [10.1103/PhysRevLett.94.057405](https://doi.org/10.1103/PhysRevLett.94.057405). URL: <http://europaepmc.org/article/MED/15783696>.